



**HAL**  
open science

# Etude de la structure massive dans des alliages à base TiAl et de son évolution en cours de traitements thermiques

Ananthi Sankaran

► **To cite this version:**

Ananthi Sankaran. Etude de la structure massive dans des alliages à base TiAl et de son évolution en cours de traitements thermiques. Autre. Université Paul Verlaine - Metz, 2009. Français. NNT : 2009METZ008S . tel-01752622

**HAL Id: tel-01752622**

**<https://hal.univ-lorraine.fr/tel-01752622>**

Submitted on 29 Mar 2018

**HAL** is a multi-disciplinary open access archive for the deposit and dissemination of scientific research documents, whether they are published or not. The documents may come from teaching and research institutions in France or abroad, or from public or private research centers.

L'archive ouverte pluridisciplinaire **HAL**, est destinée au dépôt et à la diffusion de documents scientifiques de niveau recherche, publiés ou non, émanant des établissements d'enseignement et de recherche français ou étrangers, des laboratoires publics ou privés.



## AVERTISSEMENT

Ce document est le fruit d'un long travail approuvé par le jury de soutenance et mis à disposition de l'ensemble de la communauté universitaire élargie.

Il est soumis à la propriété intellectuelle de l'auteur. Ceci implique une obligation de citation et de référencement lors de l'utilisation de ce document.

D'autre part, toute contrefaçon, plagiat, reproduction illicite encourt une poursuite pénale.

Contact : [ddoc-theses-contact@univ-lorraine.fr](mailto:ddoc-theses-contact@univ-lorraine.fr)

## LIENS

Code de la Propriété Intellectuelle. articles L 122. 4

Code de la Propriété Intellectuelle. articles L 335.2- L 335.10

[http://www.cfcopies.com/V2/leg/leg\\_droi.php](http://www.cfcopies.com/V2/leg/leg_droi.php)

<http://www.culture.gouv.fr/culture/infos-pratiques/droits/protection.htm>

# THESE

Présentée à



L'UNIVERSITE PAUL VERLAINE DE METZ

Par

**Ananthi SANKARAN**

Pour l'obtention de grade de:

**Docteur de l'Université Paul-Verlaine de Metz**

*SPECIALITE* : Sciences des matériaux

*OPTION*: Physique

**Etude de la Structure Massive dans des Alliages à Base TiAl et de son Evolution en Cours de Traitements Thermiques**

Soutenue publiquement le 19 Juin 2009 à Metz, devant le jury compose de:

Mme. Muriel VERON	Professeur, SIMAP, Saint Martin d' Hères, France	Rapporteur
M. Marc THOMAS	Ingénieur de Recherche, ONERA, Châtillon, France	Rapporteur
M. Jacques LACAZE	Directeur de Recherche, CIRIMAT, ENSIACET Toulouse, France	Examiner
M. Dominique DALOZ	Maître de conférences, LSG2M, Ecole des Mines, Nancy, France	Examiner
M. Alain HAZOTTE	Professeur, LETAM, Université Paul-Verlaine, Metz, France	Directeur de thèse
M. Emmanuel BOUZY	Maître de conférences, LETAM, Université Paul- Verlaine, Metz, France	Co-directeur de thèse

# Sommaire

## Chapitre I. Les alliages de TiAl - Introduction générale

I.1. Introduction .....	3
I.2 Objectifs .....	8

## Chapitre II: Introduction à la transformation massive

II. 1. Introduction à la transformation massive .....	10
II. 1. 1. Effet de la vitesse de refroidissement .....	11
II. 1. 2. Effet de la composition .....	12

## Chapitre III : Mécanismes de la germination et de la croissance dans les grains $\gamma_m$

III. 1. Matériau initial .....	15
III. 2. Formation et développement de $\gamma_m$ .....	16
III. 3. Mécanismes de germination des grains $\gamma_m$ .....	17
III.4. Sélection de variantes pendant la germination .....	19
III. 5. Validation statistique du mécanisme de germination .....	22
III. 6. Mécanismes de croissance des grains $\gamma_m$ .....	24

## Chapitre IV : Évolution microstructurale et de texture des grains $\gamma_m$ par des traitements thermiques

IV. 1. Évolution microstructurale .....	30
IV. 1. 1 Matériau de départ .....	30
IV. 1. 2. Température de déstabilisation des grains $\gamma_m$ .....	31
IV. 1. 3. Changements microstructuraux dus à la déstabilisation de la phase $\gamma_m$ .....	32
IV.2. Évolution de texture du matériau brut de fonderie avec les traitements thermiques .....	36
IV. 2. 1. Matériau initial .....	36
IV. 2. 2. Évolution de texture avec divers traitements thermiques .....	39

## Chapitre V : Calcul théorique de la texture $\gamma_m$

V. 1. Matériau initial.....	42
V. 2. Relation d'orientation entre le parent hexagonal $\alpha_p$ et le grain tétragonal $\gamma$ .....	42

## Chapitre VI : Résumé et perspectives

VI. 1. Résultats principaux.....	47
VI. 2. Perspectives.....	49

<i>Références</i>	51
-------------------	----

---

## Annexes

<i>Annexe A1: Materials and Methods.....</i>	A1-1
<i>Annexe A2: Two original methodologies for characterizing the microstructure of <math>\gamma</math>-massive phase in TiAl based alloys.....</i>	A2-1
<i>Annexe B: Variant selection during nucleation and growth of gamma-massive phase in TiAl-based intermetallic alloys.....</i>	B-1
<i>Annexe C: Texture and microstructure evolution during tempering of gamma-massive phase in a TiAl-based alloy.....</i>	C-1
<i>Annexe D: First attempt to theoretically calculate the <math>\gamma</math>-massive texture in a TiAl based alloy.....</i>	D-1

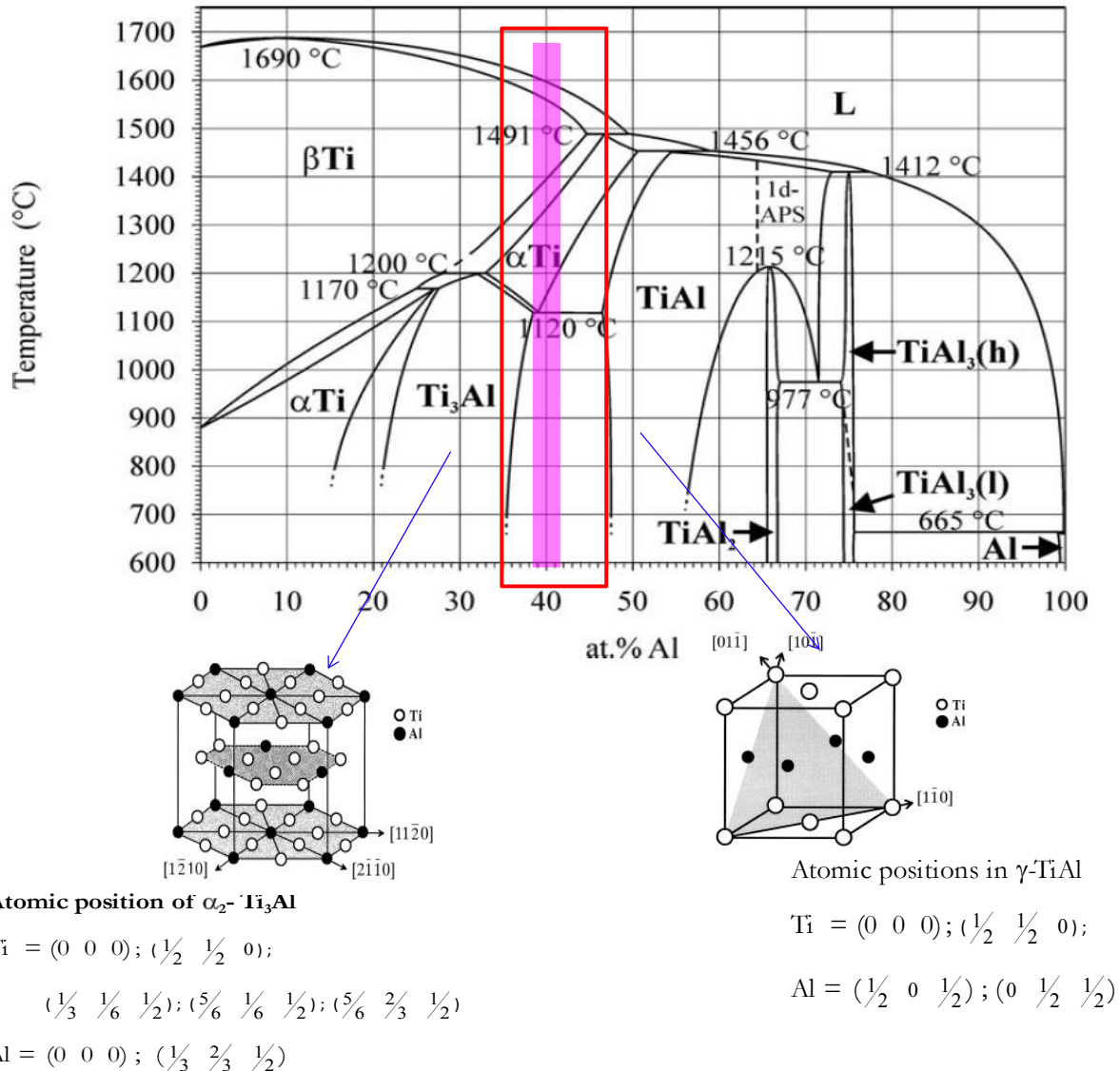
# Chapitre I. Les alliages de TiAl- Introduction générale

## I.1. Introduction

Le titane et les alliages de titane ont été introduits au début des années 1950 et ces matériaux, dans un temps relativement court, sont devenus des matériaux d'une importance primordiale pour l'industrie aérospatiale, l'industrie de l'énergie et l'industrie chimique. La combinaison de propriétés très recherchées telles qu'une **haute résistance mécanique spécifique, d'excellentes propriétés mécaniques et une forte résistance à la corrosion** fait que ce sont des matériaux de choix pour diverses applications de la plus haute importance. De nos jours, les alliages au titane sont utilisés pour des applications très exigeantes telles que **les composantes de turbines à gaz tant statiques que rotatives**. Certaines pièces des **avions civils et militaires**, soumis à des fortes contraintes et devant avoir des qualités du plus haut niveau sont fabriquées avec ces alliages.

Comme on peut le voir sur le diagramme de phases Ti-Al en Figure 1. 1, les aluminures de titane ont des composés intermétalliques majeurs tels que  $\gamma$ -TiAl,  $\alpha_2$ -Ti<sub>3</sub>Al, etc. Parmi eux,  $\gamma$ -TiAl a fait l'objet de beaucoup d'intérêt et de très nombreuses applications. Ceci est dû au fait que  $\gamma$ -TiAl a d'excellentes propriétés mécaniques et une excellente résistance à l'oxydation/corrosion à des températures élevées (plus de 600 C), ce qui en fait un substitut possible pour les superalliages à base Ni dans les turbines d'aéronefs. Cependant, le  $\gamma$ -TiAl seul, comme de nombreux autres matériaux intermétalliques, s'est avéré difficile à traiter car les possibilités de traitement sont limitées, il présente généralement une faible ductilité à température ambiante et une faible résistance à la rupture. Mais des améliorations considérables de la ductilité et de la résistance à la rupture peuvent être obtenues avec des alliages biphasés et ceci avec des compositions correspondant à celles du domaine de phase  $\alpha+\gamma$ . Ainsi, ces dernières années, beaucoup de recherches ont été faites pour développer un alliage biphasé :  $\gamma$ -TiAl (structure face-centrée quadratique L1<sub>0</sub>) et  $\alpha_2$ -Ti<sub>3</sub>Al (structure hexagonale DO<sub>19</sub>). Le fait d'ajouter des éléments d'alliage tels que Nb, B, Cr, W peut **grandement influencer la température du procédé et la microstructure et donc certaines propriétés mécaniques** car les propriétés mécaniques de ces alliages dépendent largement de la température. Le candidat qui a fait l'objet d'un maximum de recherches et qui est commercialement viable pour diverses applications industrielles est le 'GE alloy' dont la

composition Ti-48Al-2Cr-2Nb (at.%) a été brevetée par General Electric [Huang -a- 1989]. Cet alliage offre une très bonne combinaison entre ductilité, résistance à l'oxydation et résistance au fluage par rapport à d'autres alliages [Naka-1996]. Ces alliages ont fait l'objet de tests et sont aussi résistants que des alliages à base Ni jusqu'à 760°C tout en pesant moitié moins. On trouvera dans le Tableau 1. 1, une comparaison entre l'alliage le plus commun à base  $\gamma$ -TiAl et un super alliage base Ni.



**Figure 1. 1:-** Diagramme de phases Ti-Al [Schuster-2006]

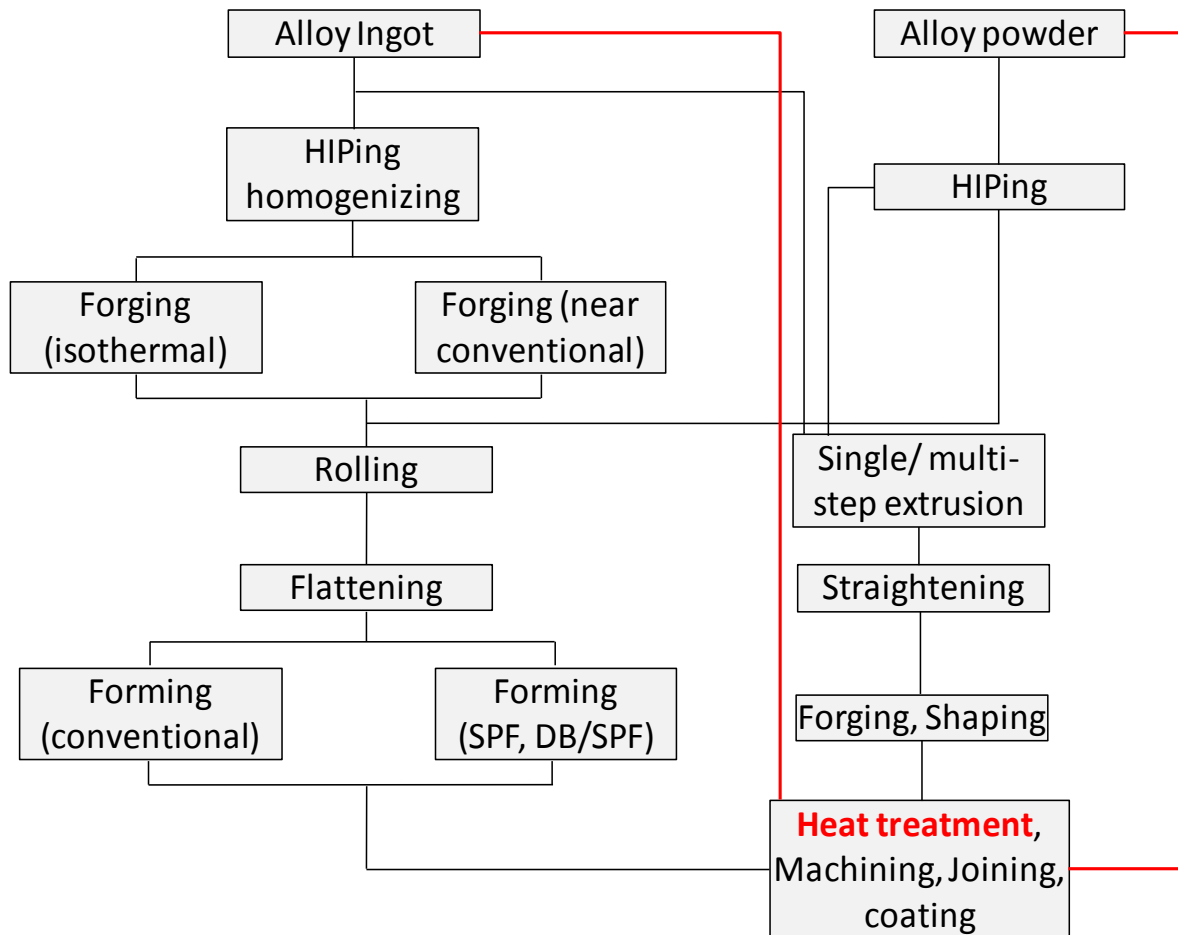
General Electric a récemment annoncé que des pales de turbine basse pression en  $\gamma$  TiAl sont appelées à être utilisés dans son moteur GEnx qui est monté sur les avions Boeing 787 et les Boeing 747-8. Ceci est la première utilisation à grande échelle de ce matériau sur un moteur d'avion à réaction civil. Pour le transport civil à grande vitesse, les alliages TiAl - en particulier l'alliage GE - est utilisé sous sa forme brute de coulée pour la buse d'échappement. TiAl a été retenu à cause de sa rigidité spécifique élevée (rapport module d'élasticité-poids) et sa bonne aptitude au traitement thermique [[Bartolotta- 1999].

**Tableau 1. 1:- Propriétés de résistance à la traction du Ti-48Al-2Cr-2Nb brut de coulée [Bartolotta- 1999, Boyer-1994, Huang-1994]**

Propriétés	Ti-48Al-2Cr-2Nb	Superalliages base Ni
Mass volumique (g/cm <sup>3</sup> )	3.7-3.9	8.3
Limite d'élasticité (MPa)	275-380	800-1200
Résistance à la traction (MPa)	360-500	1250-1450
Ductilité (%)	1-3	3-5
Module d'Young (GPa)	160-175	206
Ténacité (MPa√m)	22	30-100

A côté d'un grand nombre d'applications industrielles possibles, le principal critère pour qu'un alliage soit un candidat industriellement viable est qu'il offre un **bon compromis entre les propriétés mécaniques et un bon rapport qualité-prix**. Pour avoir cette bonne combinaison de propriétés mécaniques, à savoir ductilité et résistance, plusieurs procédés ont été étudiés pour la production des alliages à base  $\gamma$ -TiAl. Les différents types de procédés possibles sont donnés en Figure 1. 2. Le mode de coulée de pièces aux cotes finales par moulage à la cire perdue ou avec centrifugation représente l'une des meilleures méthodes du point de vue du rapport qualité-prix pour la production de pièce d'alliages à base  $\gamma$ -TiAl [Thomas- 2005]. Cependant, il présente des inconvénients tels que d'une part, l'hétérogénéité de composition due à la macro-ségrégation et à la micro-ségrégation, et d'autre part, la porosité liée au retrait. Cela conduit à une forte dispersion des propriétés mécaniques et à une moindre ductilité. Un autre inconvénient majeur est que l'on a une forte texture de solidification [Bartels -2002-].





**Figure 1. 2:-** Différents procédés d'élaboration des alliages TiAl (Adapté de [Clemens- 2002])  
 HIP (Hot isostatic pressing= pressage isostatique à chaud), SPF (super plastic forming = formage superplastique), DB (Diffusion bonding = soudage par diffusion)

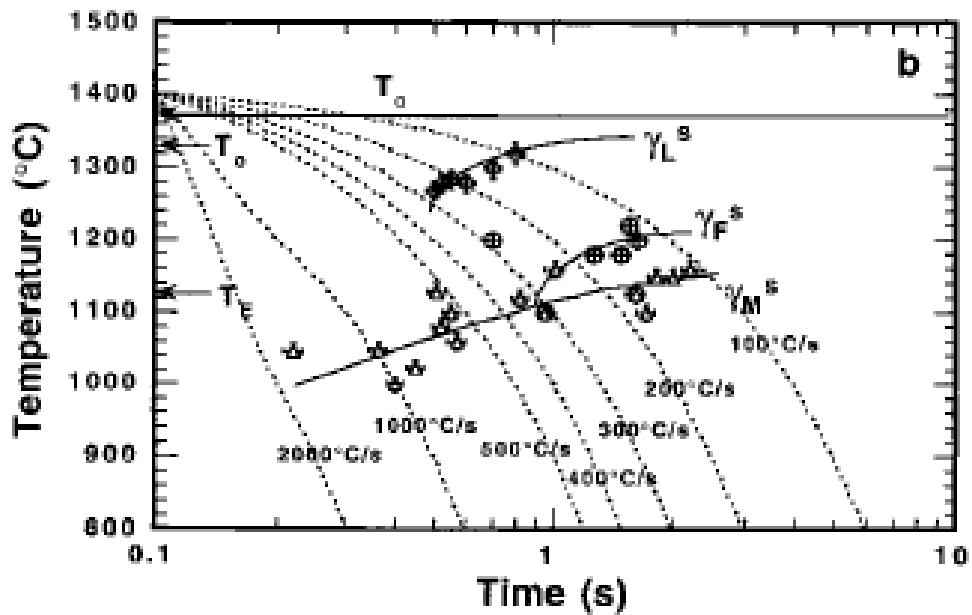
Dans l'alliage GE, la microstructure brute de coulée consiste généralement en une structure lamellaire avec des grains  $\gamma$  qui se forment secondairement le long des limites de grains à cause de la ségrégation d'Al. Par conséquent, il est nécessaire d'avoir un traitement d'homogénéisation afin d'améliorer les propriétés mécaniques [Huang-b- 1989]. Lorsque le chemin de solidification passe directement par le domaine de phase  $\alpha$ , les grains  $\alpha$  sont créés sous forme de dendrites. Ces dendrites croissent dans des directions cristallographiques préférentielles proches de  $\langle 0002 \rangle_{\alpha}$ . Au cours du refroidissement, les dendrites  $\alpha$  se transforment en une microstructure de lamelles  $\gamma$  avec une direction  $\langle 111 \rangle_{\gamma}$  parallèle à la direction initiale  $\langle 0002 \rangle_{\alpha}$ . Ceci est dû à ce que, pendant la transformation  $\alpha \rightarrow \gamma$ , les deux phases suivent une stricte Relation d'Orientation de type Blackburn [Blackburn-1970], à savoir

$$\begin{aligned} (0002)_{\alpha} // \{111\}_{\gamma} \\ \langle 11\bar{2}0 \rangle_{\alpha} // \langle 110 \rangle_{\gamma} \end{aligned}$$

Cela produit, en général, une forte texture de solidification avec pour conséquence une forte anisotropie mécanique. En outre, il est très important de réduire la taille des grains du matériau. Ceci peut se faire par apport d'éléments d'alliage tels que B et Y, lesquels agissent comme des inoculants pour la phase  $\alpha$  et modifient la microstructure de

solidification [Cheng- 2000]. Cependant, ces borures créent une morphologie en forme d'aiguilles dans la microstructure, laquelle a pour effet de dégrader les propriétés mécaniques [Hu-2005]. Une autre manière de réduire la taille des grains consiste à faire appel à des traitements thermo-mécaniques. Un certain nombre de traitements thermo-mécaniques possibles est présenté en Figure 1. 2. Mais l'inconvénient principal de ce type de traitement est qu'ils ne sont pas très rentables et, dans le cas de pièces moulées, ils ne permettent pas de conserver la forme moulée. La troisième manière possible - et la plus rentable pour affiner la taille des grains - consiste à simplement appliquer un traitement thermique en exploitant les différentes transformations de phase possibles à l'état solide.

Au cours du refroidissement d'un alliage de base-TiAl à partir d'une température de phase  $\alpha$  élevée, on peut obtenir, en fonction de la vitesse de refroidissement, un certain nombre de microstructures telles que les microstructures **lamellaire, de Widmanstätten, plumeau ou massive** [Dey-2006]. La structure lamellaire obtenue par refroidissement au four conservera la taille des grains de la phase  $\alpha$  à haute température. Il est donc nécessaire d'avoir des traitements thermiques multiples ou des traitements thermiques cycliques à des températures proches de la température de transformation de la phase  $\alpha$  pour affiner la taille des grains lamellaires [Clemens-2006]. Les microstructures du type Widmanstätten et plumeau sont des microstructures intermédiaires qui, normalement, coexistent avec les microstructures lamellaires et ne prennent pas réellement part au processus d'affinement. **La manière la plus efficace d'affiner la taille des grains par des traitements thermiques est de passer par une transformation massive.** Une transformation massive est une **transformation de phase sans diffusion qui se produit quand la vitesse de refroidissement est assez élevée pour empêcher tout autre type de transformation avec diffusion telle que la transformation en plumeau ou de Widmanstätten.** Cette transformation est fortement influencée par la vitesse de refroidissement et la composition. La courbe TRC de décomposition de  $\alpha$  pour Ti-48 Al est présentée en Figure 1. 3 et les effets de la composition sur la transformation massive sont donnés au Tableau 1. 2.



**Figure 1. 3:-** Courbe TRC du Ti- 47.5 Al (at %).  $\gamma_L^S$  – température de début de la transformation lamellaire,  $\gamma_M^S$  – température de début de la transformation massive,  $\gamma_F^S$  température de début de la transformation plumeau. Les symboles représentent la température de début mesurée [Veeraraghavan-1999].

**Tableau1. 2:-** Influence des différents éléments d'alliage sur les différentes propriétés et sur la transformation massive des alliages TiAl [Jones-1993, Huang- 1993, Hu- 2007, Charpentier- 2003].

Éléments	Influence des différents éléments d'alliage sur le	
	Propriétés (Effets connus)	Microstructure Massive
Al	Influence la ductilité, la ténacité diminue lorsque la teneur en Al augmente.	Haut % at. de Al, augmente la fraction volumique du la phase $\gamma_m$ .
Cr	Addition de 1-3 % at. augmentent la ductilité des alliages à structure duplexe. Additions >8% at. augmentent la résistance à l'oxydation	Il n'ya pas d'effet connu sur la structure massive
Nb	Augmentation considérable de la résistance à l'oxydation	Retarde la transformation diffusive et augmente la probabilité de la transformation massive..

## I.2 Objectifs

Bien que, dans la bibliographie, l'affinement des grains lamellaires ait été obtenu par un traitement thermique en une étape avec transformation massive, on n'a jamais fait d'étude complète sur les mécanismes d'affinement de grains par les traitements thermiques.

Les objectifs principaux de mon travail de recherche pour le doctorat sont les suivants

1. **Étudier les mécanismes de germination et de croissance des grains massifs:** - effectuer des traitements thermiques et obtenir les grains  $\gamma_m$  alors qu'ils sont encore au stade initial de leur formation, puis les caractériser en faisant appel à diverses techniques permettant de déterminer leur orientation cristallographique.
2. Analyser les **mécanismes de déstabilisation de la phase  $\gamma_m$  et étudier** l'évolution de la microstructure.
3. Analyser l'influence **de la transformation massive sur la texture globale** de l'échantillon ainsi que l'évolution de la texture de la phase massive avec différents traitements thermiques dans différents domaines de phase.
4. **Modéliser la texture des grains  $\gamma_m$**  en appliquant en théorie certains mécanismes de nucléation et de croissance.

# Chapitre II: Introduction à la transformation massive

Dans ce chapitre, nous présentons brièvement les caractéristiques principales de la transformation massive et discutons des paramètres influençant la formation des grains massifs. Dans les chapitres suivants, nous discuterons de chacun des objectifs énoncés au chapitre I.

La transformation massive est caractérisée depuis les stades initiaux de formation jusqu'aux différentes morphologies obtenues suite à la déstabilisation de cette phase hautement métastable. Nous avons essayé de proposer divers mécanismes de transformation à différents stades de la transformation massive et de sa déstabilisation à partir des données obtenues à partir de diverses méthodes de caractérisation morphologiques et cristallographiques.

## II. 1. Introduction à la transformation massive

La transformation massive est une transformation sans changement de composition chimique avec changement de la structure cristalline, de plus, elle est activée thermiquement et bien qu'elle soit sans diffusion à longue distance, le déplacement de l'interface se fait par des sauts atomiques à courte distance. L'interface en croissance est normalement en partie cohérente ou incohérente. Les grains massifs sont essentiellement équiaxes avec des joints de grain très irréguliers. Philips a été le premier à faire état de ce type de transformation dans un laiton à 60/40 Cu-Zn [Philips-1930]. Il a trouvé que, en trempant le laiton  $\beta$  à partir de températures élevées, on obtient, dans une zone très étroite de composition (62.5 pct Cu-37.5 pct Zn), des microstructures très différentes de celles attendues. En effet, il n'a obtenu qu'une seule phase de même structure que celle de la phase  $\alpha$  et présentant des variations de composition chimique très faibles par rapport à la phase  $\beta$  haute température dont elle est issue. Il a supposé que la transformation de la phase  $\beta$  en  $\alpha$  était un nouveau type de transformation qui se produisait sans changement de composition chimique et qui ne pouvait se faire que pour des vitesses de refroidissement élevées. De fait, il a été observé depuis, qu'un certain nombre d'alliages sont soumis à une transformation massive lorsque les cinétiques de refroidissement sont très rapides. Des

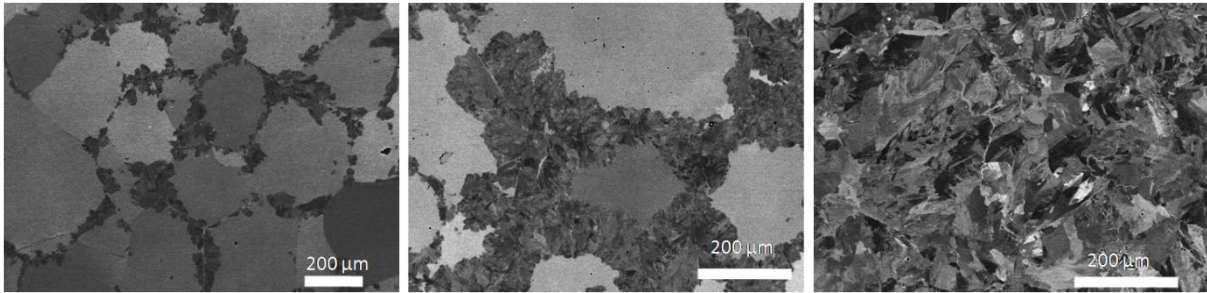
études approfondies sur la transformation massive ont été faites sur toute une gamme d'alliages au Cu par Massalski [Massalski- 1958]. Au cours de l'étude initiale sur la transformation massive, il a semblé relativement facile de définir les grains massifs avec leurs caractéristiques morphologiques bien distinctes, mais l'avènement de nouvelles méthodes de caractérisation cristallographique ont complètement changé la donne quant il s'est agi de définir les caractéristiques des grains massifs [Massalski- 1984]. L'analyse par diverses techniques de caractérisation a montré que la nucléation et les mécanismes de croissance des grains  $\gamma_m$  étaient très complexes. Bien que l'on ait proposé divers mécanismes de croissance, certaines ambiguïtés subsistent.

Dans notre étude, nous ne traitons que des alliages à base  $\gamma$ -TiAl. Tout comme pour les autres alliages, la formation des grains massifs dans  $\gamma$ -TiAl dépend fortement de la vitesse de refroidissement et de la composition [Veeraraghavan- 1999]. La phase  $\gamma$  qui est une structure quadratique - peut se présenter, en fonction de la vitesse de refroidissement, sous forme de quatre microstructures différentes au cours du refroidissement à partir du domaine  $\alpha$  : les structures lamellaires formées avec des vitesses de refroidissement plus faibles (structures lamellaires  $\gamma+\alpha_2$ ), les structures Widmanstätten ou plumeau (on trouve  $\alpha_2$  dans les interstices entre les grains  $\gamma$ ) se forment avec des vitesses de refroidissement modérées, et des structures massives (normalement la phase  $\alpha_2$  est presque absente à l'intérieur des grains massifs) sont formées avec des vitesses de refroidissement supérieures [Dey-2006]. Le deuxième critère qui influence la formation des structures massives dans un alliage  $\gamma$ -TiAl est la composition, particulièrement celle des éléments d'addition autres que Ti et Al. Selon la vitesse de refroidissement et la composition de l'alliage pendant la transformation massive, l'échantillon peut (i) être complètement recouvert avec des grains massifs  $\gamma$  (ii) coexister avec  $\alpha_2$  non transformé ou (iii) ne contenir que du  $\alpha_2$  non transformé.

### **II. 1. 1. Effet de la vitesse de refroidissement**

Une technique nouvelle fondée sur la mesure commandée par ordinateur et ultra-rapide des températures et de la résistivité électrique a été utilisée par Veeraraghavan [Veeraraghavan-1999] pour étudier l'influence de la vitesse de refroidissement sur la fraction volumique de grains massifs formés et les températures de déclenchement de la transformation dans un alliage Ti-47.5 Al at%. Il a été constaté que la fraction volumique de grains massifs décroissait et celle de la phase  $\alpha_2$  ordonnée augmentait à mesure que la vitesse de refroidissement à partir du domaine de phase  $\alpha$  croissait. Les échantillons ont été refroidis selon toute une gamme de vitesses de refroidissement entre 140°C/s et 1400°C/s. La température de la transformation massive commence à  $\sim 1050^\circ\text{C}$  pour une vitesse de refroidissement de 1400°C/s et à 1180°C pour une vitesse de refroidissement de 140°C/s.

Dans notre étude, pour obtenir différentes fractions en volume de grains massifs, nous avons trempé un alliage avec la composition suivante Ti-47Al-2Cr-2Nb (at. %), et ceci dans divers milieux de trempe allant de l'eau saumâtre glacée à l'eau simple. Les microstructures obtenues sont présentées en Figure 2. 1.



**Figure 2. 1:-** Images BSE de transformation massive effectuée dans divers milieux de refroidissement.

## **II. 1. 2. Effet de la composition**

### **👉 Alliage binaire:-**

La composition de l'alliage joue un rôle très important dans la transformation massive. Le % atomique d'Al lui-même peut modifier les caractéristiques durant la formation des grains massifs. On considère que la transformation massive est favorisée lorsque la composition de l'alliage Ti-Al est proche de la concentration d'équilibre de l'aluminium en phase  $\gamma$ . A mesure que la part d'Al diminue, à température ambiante, la fraction en volume de  $\alpha_2$  croît. Ainsi, il y a concurrence entre la transformation massive et la transformation désordre-ordre passant de  $\alpha$  à  $\alpha_2$ , ce qui conduit à une réduction de la fraction en volume des grains massifs  $\gamma$ . Cependant, avec une composition quasi-stœchiométrique, la fraction en volume de la phase  $\gamma$  est plus élevée et celle de la phase  $\alpha_2$  plus faible. Dans ce cas la transformation lamellaire commence très tôt et la transformation massive entre en concurrence avec la transformation lamellaire. En conséquence, pour ce type d'alliage, la vitesse de refroidissement doit être suffisamment rapide pour empêcher la transformation lamellaire et favoriser la transformation massive [Jones– 1993].

### **👉 Éléments d'alliage multiples:-**

L'ajout d'autres éléments tels qu'oxygène, bore, Cr, Nb, Mn dans le  $\gamma$ -TiAl modifie non seulement les propriétés du matériau mais aussi la formation des grains massifs. Les éléments d'addition dans l'alliage tels que l'oxygène - dont on sait qu'il est un bon stabilisateur de phase  $\alpha_2$  - peut inhiber la croissance des grains massifs. Ainsi, si l'oxygène est présent en quantité supérieure à 1.2 at% dans un alliage TiAl, il peut retarder la formation de grains massifs  $\gamma$  [Lefebvre- 2002]. L'influence de l'addition de toute une gamme d'éléments alliés sur la transformation massive a fait l'objet d'une étude par Hu et al [Hu-2007]. L'apport d'éléments alliés en petite quantité tels que Cr et Nb peut modifier de manière significative les propriétés mécaniques de l'échantillon. L'alliage bien connu qu'on appelle l'alliage GE alliage avec comme composition Ti-47Al-2Cr-2Nb (at %) est utilisé essentiellement pour un certain nombre d'applications à cause de ses propriétés mécaniques intéressantes. Selon le type des éléments d'alliage, la fraction en volume de grains massifs peut être contrôlée. Ceci est dû au fait que les éléments tels que Cr et Nb occupent préférentiellement soit les sites du Ti, soit, ceux de l'Al. Généralement, dans un échantillon refroidi en four, un % important de Cr (~85%) va se placer de préférence les sites de l'Al alors que le Nb n'occupe ceux du Ti [Miller- Unknown]. Cependant, à des plus hautes vitesses de refroidissement, on observe une tendance au désordre bien que cette tendance

soit moins marquée pour le Nb que pour le Cr, ainsi on obtient seulement ~70% des atomes de Cr occupant les sites d'Al et ~88% des atomes de Nb occupant les sites de Ti. Par conséquent, dans un alliage avec une concentration plus élevée de Nb, le Nb occupe les emplacements de Ti ce qui fait augmenter la concentration d'équilibre d'Al de la phase  $\gamma$ . Par ailleurs, le Nb - qui est un stabilisateur  $\beta$  - étend le domaine  $\beta$  à des concentrations en Al plus élevées, ce qui, en conséquence, réduit les domaines des phases  $\alpha$  et  $\alpha + \gamma$  [Wu- 2006, Chen- 1999]. Le fait d'ajouter du Nb à l'alliage binaire Ti-Al éloignera donc la composition d'équilibre de la phase  $\gamma$ , la limite de phase  $(\alpha+\gamma)/\gamma$  de la composition moyenne de l'alliage [Prasad -2003]. Si on tient compte de tout cela, le fait d'ajouter du Nb entrainera une diminution de la propension de l'alliage à aller vers une transformation massive. Cependant, il est important de noter que le fait d'ajouter du Nb à l'alliage Ti-Al pourrait faire baisser de façon importante la vitesse de diffusion et donc, à une vitesse de refroidissement donnée, il serait plus facile de prévenir une diffusion étendue dans un alliage ternaire avec x at. % de Nb et produire des structures  $\gamma$  massives par rapport à un Alliage TiAl sans Nb. Il a été montré par Hu et al [Hu-2007] qu'il est possible d'avoir une transformation massive de presque 100% dans un matériau avec du Nb à une vitesse de refroidissement plutôt plus faible. Dans un alliage GE avec environ 2 % de Nb et Cr, ces deux métaux ne provoquent pas beaucoup de changement dans la transformation massive car le Nb occupe préférentiellement les sites du Ti et le Cr occupe préférentiellement les sites d'Al. Considérant que le % at Al est supérieur à celui d'un alliage Ti-45Al, la transformation massive est en grande partie favorisée dans cet alliage. Cependant, des vitesses de refroidissement plus élevées sont nécessaires pour retarder la croissance des grains massifs et la maintenir au stade initial de la formation.

Divers types d'alliages TiAl ont été utilisés pour atteindre les différents objectifs de l'étude comme indiqué au Chapitre I. En conséquence, les caractéristiques et la nécessité de sélectionner différents matériaux seront expliqués à propos de chacun des objectifs.



## Chapitre III : Mécanismes de la germination et de la croissance dans les grains $\gamma_m$

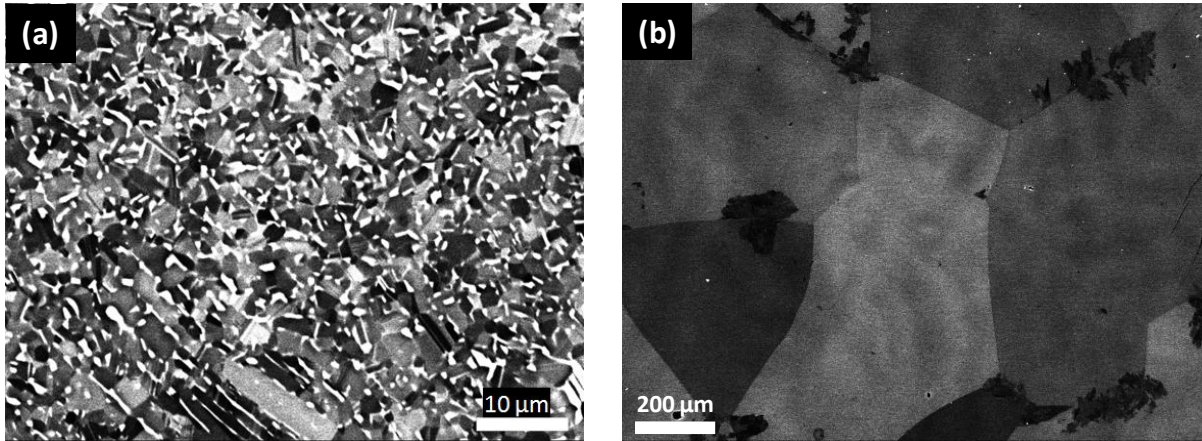
### Objectif I

**Étudier les mécanismes de germination et de croissance des grains massifs:** - Procéder à des traitements thermiques et obtenir les grains  $\gamma_m$  grains lors des stades initiaux de la formation, puis les caractériser en employant diverses techniques de la cristallographie.

Il a été bien établi que, pendant la transformation massive, les grains massifs sont formés par le processus de germination et de croissance. Comme la transformation massive est une transformation extrêmement rapide à des vitesses de refroidissement élevées, il est très difficile de les étudier, surtout pendant les stades initiaux de la germination et de la croissance. L'alliage GE subit la transformation massive très rapidement, ce qui donne une fraction en volume élevée de grains  $\gamma$  massifs, surtout à cause de sa composition. Par conséquent, un alliage capable de ralentir la transformation massive à une vitesse de refroidissement comparable est nécessaire pour étudier les stades initiaux de la germination et de la croissance. Un alliage de composition Ti-45.5Al-8Nb a été utilisé pour l'étude [Hu-2007]. La présence d'une grande quantité de Nb augmente la concentration en Al dans la phase  $\gamma$  par rapport à la concentration en Ti. La transformation massive est en concurrence avec la transformation désordre-ordre  $\alpha \rightarrow \alpha_2$ . De plus, le Nb empêche la transformation lamellaire à cause de sa faible vitesse de diffusion. Par conséquent, il est possible d'arrêter la transformation massive alors qu'elle est encore au stade initial de formation.

### III. 1. Matériau initial

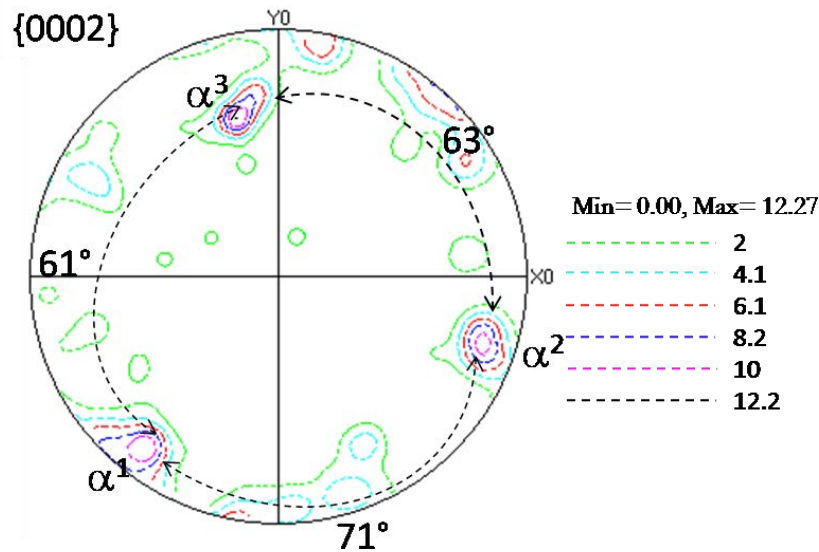
Nous avons reçu de TURBOMECA un disque circulaire de 60 mm de diamètre et 10 mm d'épaisseur. Le matériau en l'état avait été fabriqué par la méthode de fonderie à la cire perdue et il a été ensuite extrudé à haute température. La microstructure initiale du matériau est présentée en Figure 3.1 (a).



**Figure 3. 1:-** (a) micrographie BSE de l'échantillon initial de composition Ti-45.5Al-7Nb-0.2C avant traitement thermique (b) micrographie BSE de l'échantillon après le traitement thermique; la phase brillante correspond à la phase  $\alpha_2$  et la phase sombre correspond à la phase  $\gamma$ .

La microstructure est constituée principalement de grains équiaxes monolithiques  $\gamma$  avec la phase  $\alpha_2$  le long des joints de grains de la phase  $\gamma$ . Concernant la préparation métallographique, le disque dans l'état de réception a été découpé en échantillons plus petits de dimensions 7mm x 7mm x 10mm. Il a été traité thermiquement dans le domaine  $\alpha$  ( $\sim 1365^\circ\text{C}$ ) pendant 15 min et ensuite trempé dans de l'eau saturée glacée ( $\sim -5^\circ\text{C}$ ). La microstructure résultante comprenait principalement une phase  $\alpha_2$  non transformée, avec des petits îlots de grains massifs  $\gamma$  ( $\gamma_m$ ). La micrographie est présentée en Figure 3. 1(b). Il y a une légère différence au niveau de la fraction volumique des grains massifs en allant du bord vers le centre de l'échantillon qui est due au gradient de température auquel l'échantillon est soumis pendant le processus de refroidissement.

Considérant que le matériau avait été soumis à un processus d'extrusion avant le traitement thermique, la texture de la phase  $\alpha_2$  du matériau a été mesurée après le traitement thermique. La mesure de la texture sur les grains de phase  $\alpha_2$  brut que l'on voit sur la Figure 3. 1 (b) a été effectuée par des balayages en ligne EBSD à large pas (pour plus de détails voir Annexe A1). La Figure 3. 2 montre la texture (0002) de la phase  $\alpha_2$ . On peut voir qu'il y a trois pôles dominants de  $\alpha$  générés par le processus d'extrusion.

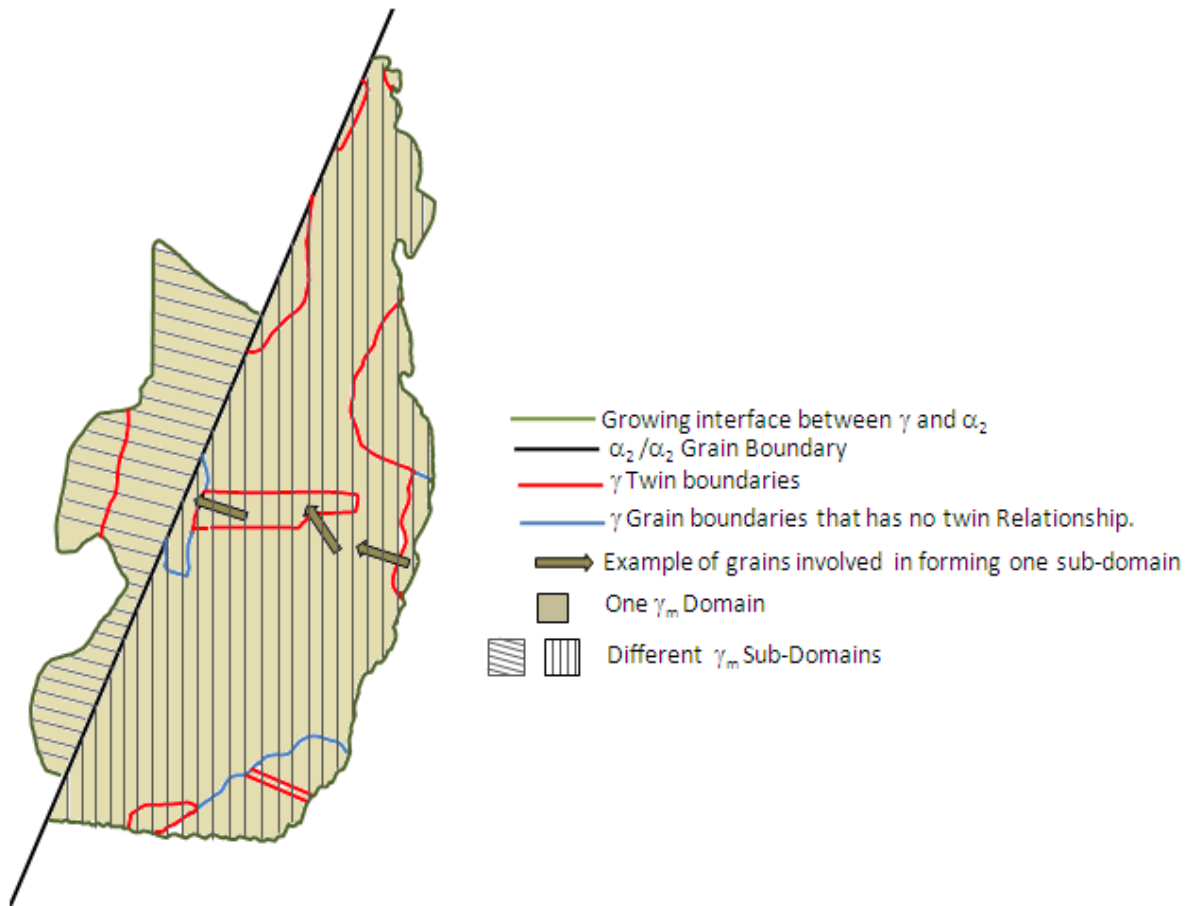


**Figure 3. 2:-**  $\{0002\}$  figures de pôle de la phase après traitement thermique de transformation massive.

### III. 2. Formation et développement de $\gamma_m$

Le traitement thermique de transformation massive dans un alliage Ti-45.5Al-7Nb-0.2C donne naissance à des grains  $\gamma_m$  qui ont une cristalline tétragonale et une phase  $\alpha_2$  non transformée. Ces grains  $\gamma_m$  sont présents en petits faisceaux dans la matrice  $\alpha_2$  et la fraction totale en volume des grains massifs présents dans les échantillons est d'environ 7%. Ceci nous donne l'opportunité d'étudier la transformation massive dans les premiers stades de son développement et dans le même temps la possibilité de déterminer la relation cristallographique que présentent les germes  $\gamma_m$  avec la phase  $\alpha_2$ .

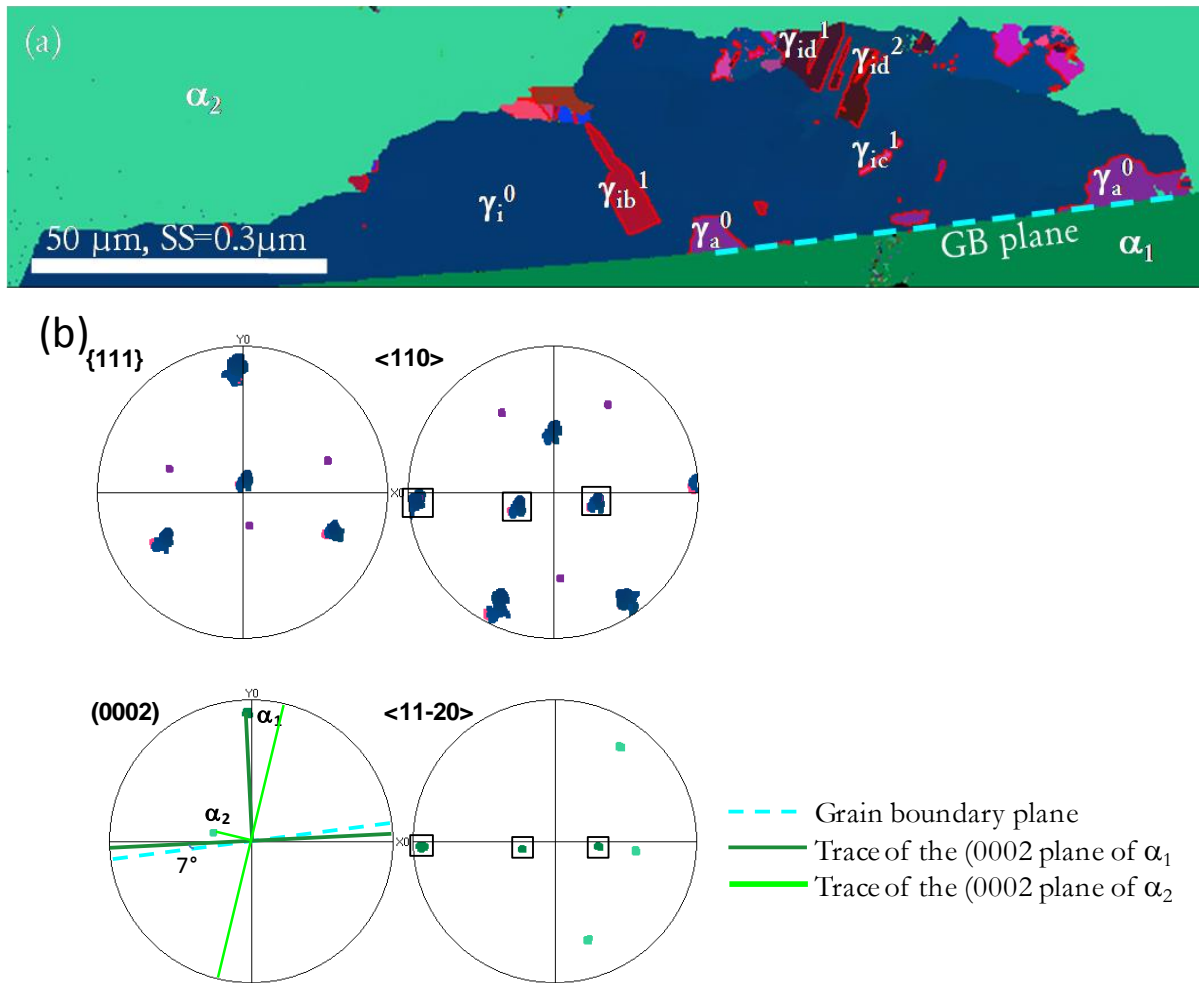
Un examen attentif par BSE prouve que la germination se produit principalement le long des joints triples constitués par trois grains de  $\alpha_2$  et les joints de grains  $\alpha_2/\alpha_2$ . L'ensemble des grains  $\gamma_m$  formé le long d'un joint de grain donné est considéré comme formant un domaine  $\gamma_m$ . Le classement des grains  $\gamma_m$  en domaines et sous-domaines est expliqué dans le schéma présenté en Figure 3. 3. Les grains  $\gamma_m$  dans ces régions ont été examinés avec l'aide de l'EBSA et différents types de mécanismes de germination les concernant sont proposés.



**Figure 3. 3:-** Représentation schématique expliquant la définition des domaines, sous-domaines et grains  $\gamma_m$ .

### III. 3. Mécanismes de germination des grains $\gamma_m$

Les investigations au MEB sur les échantillons obtenus par transformation massive montrent que les grains massifs ont germés le long des joints de grains et des joints triples, et qu'aucun ensemble de grains massifs n'a été observé provenant de l'intérieur des grains. Pour commencer l'étude et pour des raisons de simplicité, nous avons analysé d'abord les grains massifs formés sur les ex-joints de grain  $\alpha/\alpha$ . Une carte EBSD des grains massifs formés à partir de joints de grain  $\alpha/\alpha$  est présentée en Figure 3. 4 (a). La carte est présentée selon le code couleurs des angles d'Euler, en général, les différences de couleurs sur la carte représentent des grains de différentes orientations. Les lignes rouges séparent les grains qui ont une relation de maclage l'un avec l'autre.



**Figure 3. 4:-** (a) Germination à partir d'un joint de grain  $\alpha_2 / \alpha_2$  de la phase  $\gamma_m$ , (b) figures de pôles de  $\{111\}_\gamma$ ,  $\langle 110 \rangle_\gamma$  et  $\{0002\}_\alpha$ ,  $\langle 11-20 \rangle_\alpha$ , montrant le parallélisme de la trace du plan des joints de grains avec la trace de l'un des plans (0002) d'un  $\alpha_2$ .

Pendant la transformation d'équilibre (transformation lamellaire) passant du domaine  $\alpha$  au domaine  $\alpha+\gamma$ , la transformation  $\alpha \rightarrow \gamma$  se produit avec une relation d'orientation spécifique appelée "Blackburn Orientation Relationship" (BOR).

$$\text{à savoir } (0002)_\alpha // \{111\}_\gamma \text{ and } c_\alpha // \langle 110 \rangle_\gamma$$

Les plans  $(0002)_\alpha$  et  $\{111\}_\gamma$  et les directions  $\langle 11\bar{2}0 \rangle_\alpha$  et  $\langle 110 \rangle_\gamma$  sont parallèles entre eux. Suite à la tétragonalité de la phase  $\gamma$ , chaque orientation  $\alpha$  peut créer théoriquement au cours de la transformation six orientations  $\gamma$  différentes. Ces six orientations  $\gamma$  sont deux à deux en relation de macle (explications en Annexe A1) et ces orientations sont différenciées en utilisant leurs bandes de surstructures. Considérant que le ratio  $c/a$  des paramètres réticulaires de la phase  $\gamma$  est proche de 1 ( $c/a \approx 1.02$ ), il est difficile, lorsqu'on indexe par EBSD en appliquant les conditions standards, de distinguer les six orientations (cf. Annexe A1), en conséquence, cette phase est indexée comme une phase cubique avec seulement deux orientations en relation de macle entre elles. Chaque orientation  $\alpha$  donne deux orientations  $\gamma$  différentes qui sont en relation de maillage entre elles. Ce type de relation d'orientation pendant la transformation  $\alpha \rightarrow \gamma$  a été vérifié dans d'autres

microstructures obtenues avec différentes vitesses de refroidissement dans des systèmes d'alliages à base TiAl  $\gamma$  [Dey-2006].

Dans le cas de la transformation  $\gamma_m$ , bien qu'un certain nombre d'études aient été faites sur la relation cristallographique entre les grains  $\alpha$  et les grains  $\gamma_m$ , la BOR n'a pas été observée de manière systématique [Veeraraghavan-2003]. L'analyse des cartes EBSD et la comparaison des figures de pôle des grains  $\alpha$  et  $\gamma$  en Figure 3. montrent que le pôle (0002) de l'un des grains  $\alpha$  coïncide exactement avec l'un des pôles {111} de deux grains  $\gamma$  différents situés près de l'ex - joint de grains  $\alpha/\alpha$ . Cela vaut également pour les directions  $\langle 11\bar{2}0 \rangle_\alpha$  et  $\langle 110 \rangle_\gamma$ . Nous appelons ces grains  $\gamma_m$  germe ou  $\gamma_a^0$  et  $\gamma_i^0$ . Le '0' en exposant représente le germe, le 'i' représente le premier germe se formant le long du joint de grains tandis que le 'a' représente l'autre germe qui partage une BOR avec l'un des grains  $\alpha$  et qui a une relation de macles avec le premier germe. On peut voir que les grains  $\gamma$  partagent la BOR avec le grain  $\alpha$  adjacent mais qu'ils croissent au sein du grain  $\alpha$  opposé avec lequel ils ne partagent pas de relation d'orientation spécifique. Le grain  $\alpha$  avec lequel le  $\gamma_a^0$  partage la BOR est appelé  $\alpha$  parent ou  $\alpha_p$  et le grain  $\alpha$  à l'intérieur duquel les grains  $\gamma$  croissent est appelé  $\alpha$  hôte ou  $\alpha_h$ .

En cas de joints triples, en contradiction par rapport aux études antérieures faites par plusieurs auteurs [Veeraraghavan- 2003, Massalski-2002], nous avons constaté qu'il y a toujours un germe  $\gamma_m$  partageant une BOR avec l'un des trois grains  $\alpha$ .

#### III.4. Sélection de variantes pendant la germination

Lorsqu'on considère un joint de grains  $\alpha/\alpha$ , théoriquement chacun des deux grain  $\alpha$  formant le joint de grains  $\alpha/\alpha$  est susceptible de donner naissance à un  $\gamma_{germe}$  qui se développera à l'intérieur de  $\alpha_h$ . Cependant, comme on peut le voir dans la Figure 3. 4 (a), ce n'est pas le cas. Seul un grain  $\alpha$  a participé au processus de germination et a donné un  $\gamma_a^0$  et sa variante de macles ( $\gamma_i^0$ ). Par conséquent, il est clair que les germes  $\gamma$  sont soumis à des mécanismes de sélection. Généralement, pendant la précipitation d'une nouvelle phase le long d'un joint de grains, le germe qui est en mesure de former une interface de basse énergie avec le plan du joint de grains est celui qui est sélectionné pour la germination. On dit qu'un germe a une interface de basse énergie quand son plan d'habitat et le plan du joint de grains sont parallèles ou presque parallèles. Ce critère appelé **critère d'angle minimum** a été validé en théorie par Lee et Aaronson [ Lee-a-1975, Lee-b-1975 ]. Par conséquent, pour vérifier si ce critère fonctionne pour la germination du grain  $\gamma_m$ , la trace du plan du joint de grains et les traces des deux plans (0002) $_\alpha$  ont été représentées sur la Figure 3. 4 (b). Il est clair que la trace du plan du joint de grains et celle d'un des plans d'habitat {0002} $_\alpha$ <sup>1</sup> sont presque parallèles, avec un angle entre eux de 7°. Ce plan d'habitat est celui du grain  $\alpha$  qui a donné naissance au germe  $\gamma_m$ . Par conséquent, il apparaît clairement de ces observations que **les critères d'angle minimum** fonctionnent bien pour cette germination à partir des joint de grains. Sept autres cartes EBSD, semblables à celle de la Figure 3. (a), ont été prises, à chaque fois, seul un grain  $\alpha$  participe au processus de germination pour donner naissance

<sup>1</sup> Dans le cas de TiAl, à cause de la BOR entre la phase  $\gamma$  et la phase  $\alpha$ , le plan d'habitat est le plan {0002} de la phase  $\alpha$ .

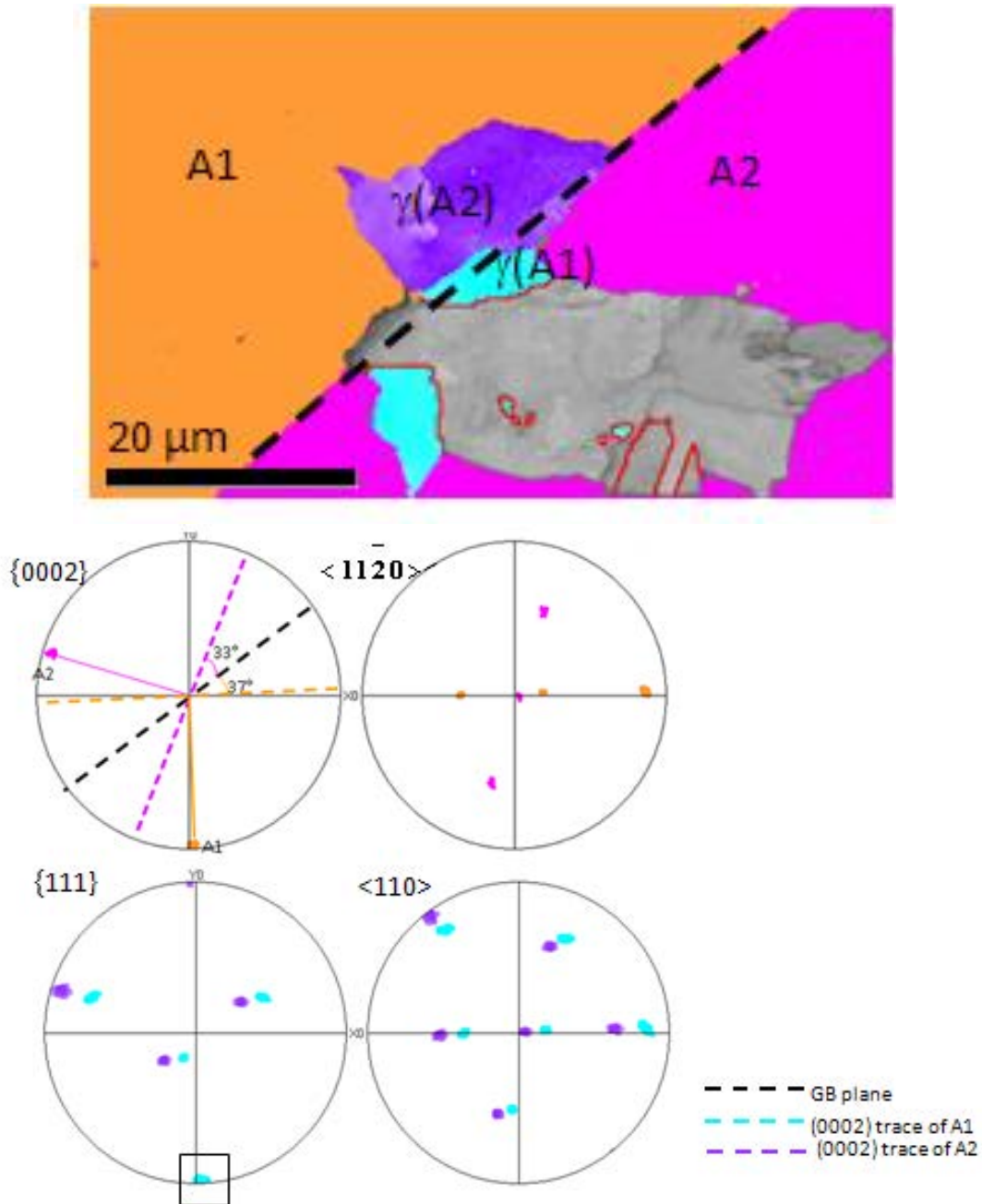
à un  $\gamma_n$ . L'analyse détaillée portant sur les sept cartes a montré que tous respectaient le critère d'angle minimum pour former un germe  $\gamma_m$ , ce qui prouve que ce critère est très important pour la germination des grains massifs. D'ailleurs, les calculs théoriques montrent que l'énergie interfaciale augmente à mesure que l'angle  $\theta$ , entre le plan du joint de grains et le plan d'habitat, croît jusqu'à une valeur critique au delà de laquelle l'énergie arrive à saturation.

Les observations ayant été faites sur une surface, nous avons été amenés à comparer les traces des plans et non les plans eux-mêmes. **Le critère « d'angle minimum » proposé comme mécanisme de germination pourrait ne pas s'avérer exact en volume.** En conséquence, une évaluation en tridimensionnel est nécessaire pour confirmer les résultats obtenus par l'analyse bidimensionnelle.

Pour analyser les domaines  $\gamma_m$  en tridimensionnel, nous avons enlevé des couches successives, pris une micrographie BSE, établi une carte EBSD et l'avons analysée. L'objet tridimensionnel reconstruit a montré que le plan du joint de grains, analysé en trois dimensions, était bien parallèle au plan d'habitat du germe  $\gamma$  (Annexe-A2).

Dans certains cas, nous avons constaté que les deux grains  $\alpha$  qui se forment au niveau d'un joint de grains participent au processus de germination. On trouvera un exemple de ce type en Figure 3. Dans les figures de pôle (0002), les traces des plans (0002) de  $A_1$  et de  $A_2$  sont tracées ainsi que celle du plan du joint de grains. La trace du plan (0002) des deux grains  $\alpha$  forme un angle de  $33^\circ$  et de  $37^\circ$  avec le plan du joint de grains. Nous pouvons voir que, bien que ni l'un ni l'autre des grains  $\alpha$  ne satisfasse le critère d'angle minimum,  $\gamma$  provient des deux grains  $\alpha$ . Ces grains  $\gamma$  provenant des deux côtés des grains  $\alpha$  suivent une BOR stricte par rapport à l'un des grains  $\alpha$ . Par conséquent, pour identifier le critère de germination, les grains  $\gamma$  sont comparés à leur grain hôte  $\alpha$ . Il ressort que  $\gamma(A_2)$  suit une BOR stricte avec  $\alpha_2$  grain  $A_2$  et qu'il a également un de ses plans {111} presque parallèle au plan (0002) de l'hôte  $\alpha A_1$ . Ce grain  $\gamma(A_2)$  a donc deux interfaces de basse énergie, l'une avec son parent et l'autre avec son hôte. Cela est appelé dans la littérature : germe à double facettes [Lee-a-1975, Adachi- 2005 ]. Nous dirons de cette forme de germe qu'il a **une SNOR (Secondary Near-Orientation Relationship)**. Un type comparable de germe a été étudié par [Lee-a-1975] et [ Adachi- 2005 ]. Ils ont calculé l'énergie d'activation nécessaire à la formation d'un germe à facette simple, à double facettes et sans facette. Ils en ont conclu que l'énergie d'activation pour la formation d'un germe à double facettes est plus faible que celle pour un germe à simple facette. On trouvera en Annexe B une représentation schématique de l'énergie d'activation exigée pour les différents types de germes. Ceci indique qu'une condition pour qu'un germe avec un angle  $\theta$  élevé se forme est de présenter une SNOR. Cependant, nous pouvons également noter que le  $\gamma(A_1)$  résultant du grain  $\alpha A_1$  s'est formé en dépit du fait qu'il n'avait pas d'interface à double facettes avec les deux grains  $\alpha$  en même temps. Ceci peut s'expliquer en considérant le fait que, comme le germe  $\gamma(A_2)$  présente une SNOR avec son grain hôte  $A_1$ , il peut former un joint d'interface de basse énergie avec le germe résultant du grain  $A_1$ . Cette interface de basse d'énergie entre deux grains  $\gamma$  peut se former quand l'angle entre deux de leurs pôles {111} est inférieur à  $10^\circ$ . En d'autres termes, le grain  $\gamma(A_2)$  favorise la formation du grain  $\gamma(A_1)$ . Ceci est dû au fait que  $\gamma(A_2)$ , qui a deux interfaces de basse énergie, souffre d'une faible mobilité d'interface et est donc stagnant. Cependant, cela contribue à la formation du second germe

$\gamma_m \gamma(A_1)$  lequel, en plus du BOR avec le grain  $\alpha$  parent, partage une autre interface de basse énergie avec  $\gamma(A_2)$ , comme on peut le voir sur la figure de pôle (figure 3. 5 (b)). Cependant, puisque le joint d'interphase entre le deuxième germe  $\gamma(A_1)$  et son grain hôte  $A_2$  n'est pas facetté, il peut croître rapidement pour donner des macles. Nous appelons ce type de mécanisme de germination '**Co-germination**'. On l'observe plus rarement que la germination juste sur un des côté du joint de grains.

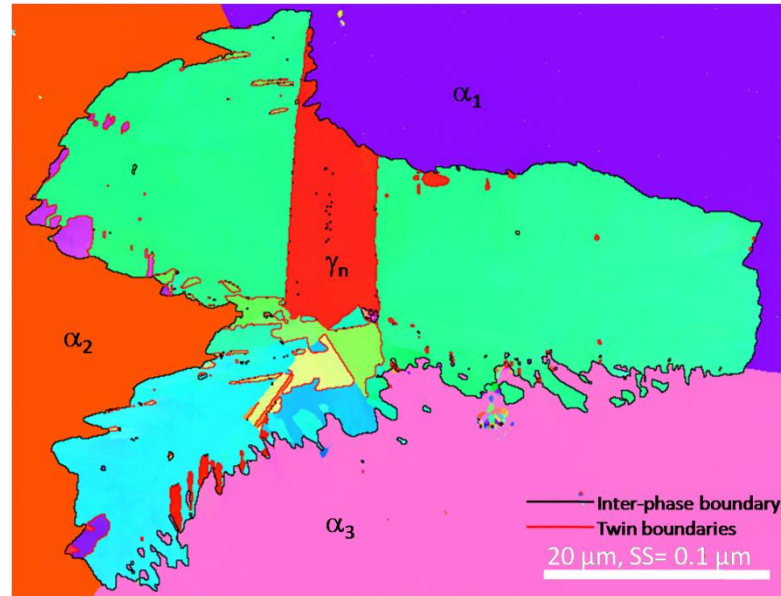


**Figure 3. 5:-** (a) Carte des angles d'Euler représentant la germination de joint de grains de type III. On voit aussi le germe émergeant de chaque grain  $\alpha_2$ . (b) Les figures de pôle du  $\{0002\}$  et  $\langle 11\bar{2}0 \rangle$  de la phase  $\alpha_2$  et de la phase  $\gamma\{111\}$  et  $\langle 110 \rangle$ .

Après identification des différents mécanismes de germination le long des joints de grains, nous avons étudié la germination du joint triple. Six cartes EBSD haute résolution ont été prises et étudiées. L'analyse de ces cartes a montré que le mécanisme dominant de



germination le long des joints triples était le critère « **d'angle minimum** ». On s'aperçoit souvent que les germes  $\gamma_m$  présentent une SNOR avec l'un des grains  $\alpha$ . La Figure 3. 6 est une carte EBSD montrant le grain  $\gamma_m$  le long du joint triple. Dans ce cas, il n'y a seulement qu'un grain  $\alpha$  qui participe au procédé de germination et le  $\gamma_n$  partage une BOR avec le grain  $\alpha_3$  et a une SNOR avec le grain  $\alpha_1$ .



**Figure 3. 6:-**  $\gamma_m$  Germination le long du joint triple.

### III. 5. Validation statistique du mécanisme de germination

Afin d'obtenir des données pertinentes du point de vue statistique sur les sites de germination  $\gamma_m$ , une grande carte EBSD a été faite sur une surface de  $5 \times 3 \text{ mm}^2$ . Le but principal recherché en faisant une carte était d'identifier tous les joints de grains et les joints triples qui portent des grains  $\gamma_m$  et de vérifier si les mécanismes proposés pour la germination est juste du point de vue statistique (Annexe-B).

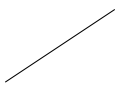
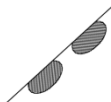
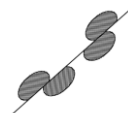
A partir de cette carte, nous avons constaté que presque 61% des joints triples sont couverts par des grains  $\gamma_m$  et seulement 15% des joints de grains contenaient des grains  $\gamma_m$ . Les orientations des deux grains  $\alpha$  voisins ont été tracées sur des figures de pôles (0002) et, ensuite, leurs traces ont été comparées avec les traces des plans de joints de grain.

On a examiné des joints de grains avec et sans grains  $\gamma_m$ , de même qu'on a aussi considéré seulement les joints de grains qui étaient droits à cause de la difficulté à dessiner la trace des joints courbes. Le Tableau 3. 1. donne la valeur moyenne des données échantillonnées à partir de 41 joints de grain ne donnant pas lieu à la formation de  $\gamma_m$ , 13 joints de grains avec  $\gamma_m$  se formant juste d'un côté du joint et 9 joints de grains avec  $\gamma_m$  présent sur les deux côtés. Ils ont été classés en type I, type II et type III de joints de grains.  $\theta_A$  et  $\theta_B$  représentent les angles entre la trace du plan de joint de grain et la trace du plan d'habitat des deux grains  $\alpha$  voisins. A partir des valeurs moyennes et de l'intervalle de confiance (explication détaillée en Annexe B) de  $\theta_A$  et  $\theta_B$  pour les trois types de joints de grains, on peut voir que les résultats obtenus pour le type II de germination de joint de grains sont cohérents avec le mécanisme de germination suggéré. La limite critique de

l'angle  $\theta$  en dessous de laquelle les critères de 'minimisation' de l'énergie interfaciale" s'appliquent et la germination peut se produire peut être donnée comme étant  $10^\circ$ . Par ailleurs, lorsqu'on compare les valeurs moyennes de  $\theta$  qui ont participé dans le processus de germination pour les joints de grains de type III et les valeurs  $\theta$  qui n'ont pas pris part au processus de germination pour les joints de grains de type I et II; nous pouvons dire qu'il est difficile de distinguer ces deux types. Par conséquent, nous avons procédé à une analyse soigneuse, on a obtenu les orientations  $\gamma$  possibles à partir de l'orientation  $\alpha$  pour le joint de grain sans germination (Type I) et on a établi leurs figures de pôles et les avons examinées.

Comme dit plus haut, une germination de grain  $\gamma_m$  avec SNOR peut exister si ce germe est capable de former une double facette, une avec son grain parent  $\alpha$  et l'autre avec son grain hôte  $\alpha$ . Pour que ce type de germe soit possible, les deux grains  $\alpha$  voisins doivent avoir leur désorientation de l'axe c aux environs de  $70^\circ$ . En effet, c'est l'angle de désorientation entre deux pôles  $\{111\}$  différents dans un cristal  $\gamma$ . Concernant le type III de joint de grains, en dehors des neuf joints analysés, sept grains  $\alpha$  voisins présentent une désorientation proche de  $70^\circ$  alors que, dans le cas du type I de joint de grain, le nombre de joints de grains  $\alpha/\alpha$  avec désorientation de l'axe c proche de  $70^\circ$  est bien inférieur. Par conséquent, un certain nombre de joints de grains  $\alpha/\alpha$  appartenant au type I qui ne satisfont pas les "critères d'angle minimum" ne satisfont pas non plus les critères pour former un germe  $\gamma$  avec SNOR.

**Tableau 3. 1:- Résumé des données pour les divers types des joints de grains analysés.**


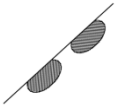
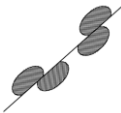
Type de joints de grains analysé	Type I: Joint de grains sans germe		Type II: Germe se formant d'un seul côté du joint de grain		Type III: Germe se formant des deux côtés du joint de grain	
						
Nombre de joints de grains analysé	41		14		9	
Angle entre les traces des joints de grains et le plan (0002) de $\alpha_2$	$\theta_A$	$\theta_B$	$\theta_A$	$\theta_B^*$	$\theta_A^*$	$\theta_B^*$
Valeur moyenne	44.68	57.2	57.1	7.4	42.4	39.0
Moyenne $\pm$ erreur standard	54.3 $\pm$ 7.1		7.4 $\pm$ 2.4		40.7 $\pm$ 10.8	

Le Tableau 3. 2 donne les informations sur le pourcentage de germes  $\gamma_m$  ayant une SNOR pour différents types de joints de grains. Nous pouvons voir qu'un joint de grain de type III n'a qu'un de ses germes en SNOR alors que

l'autre germe n'a aucune relation avec l'hôte. Dans ce genre de configuration il est plutôt facile pour le germe  $\gamma$  de former une double facette et de faire co-germer un autre germe  $\gamma$  de l'autre côté du joint de grains  $\alpha/\alpha$  qui peut ainsi participer au processus de croissance. Pour le type I de joint de grains, la majorité d'entre eux est capable de faire naître un germe SNOR, avec une chance de former deux germes différents avec SNOR émergeant à partir de chaque grain  $\alpha$ . Il est très difficile pour ce type de configuration de se former car les deux germes auront une double facette empêchant leur croissance. Nous avons des preuves statistiques du mécanisme de co-germination proposé pour le type III de germination des joints de grains.

Afin de savoir si la SNOR pourrait être un critère pour la germination des joints de grains, des calculs théoriques ont été faits sur l'échantillon texturé, en choisissant les paires de grains voisins de manière aléatoire. La fonction de densité d'orientation  $g(x)$  a été établie à partir des trois orientations principales de l' $\alpha$  obtenu de la figure de pôles dans la Figure 3. 2, lesquelles ont été considérées comme des fonctions gaussiennes (la dispersion est prise égale à  $g(x) = 30$ ). Les résultats des calculs théoriques sont donnés en Tableau 3. 2. On peut voir que les résultats théoriques et expérimentaux sont plus ou moins identiques pour les joints de grains susceptibles de présenter deux SNOR résultant des deux côtés du joint. Cependant, ce type de configuration n'a pas été repéré pour le joint de grains de type III, comme mentionné ci-dessus. Au contraire, le nombre de joints de grains présentant seulement une SNOR est plus élevé dans le cas des valeurs expérimentales lorsqu'on les compare aux théoriques, principalement pour le type III de joint de grains. Ceci indique que la germination SNOR et la "co-germination" peuvent effectivement être considérées comme des mécanismes valides de germination pour ce type de joint de grains.

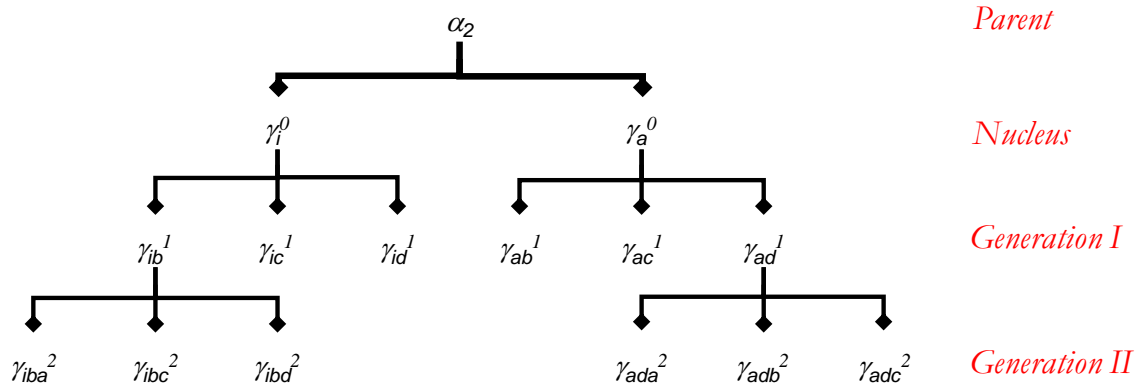
**Tableau 3. 2:- Occurrences expérimentales et théoriques de SNOR pour différents types de joints de grains**

	Type I	Type II	Type III	Calcul théorique
				Analyse de l'échantillon texturé
<b>Nombre de joints de grains analysés</b>	<b>41</b>	<b>14</b>	<b>9</b>	<b>10,000</b>
<b>2 SNOR (%)</b>	<b>10</b>	<b>14</b>	<b>0</b>	<b>10</b>
<b>Seulement 1 SNOR (%)</b>	<b>7</b>	<b>14</b>	<b>33</b>	<b>12</b>

### III. 6. Mécanismes de croissance des grains $\gamma_m$

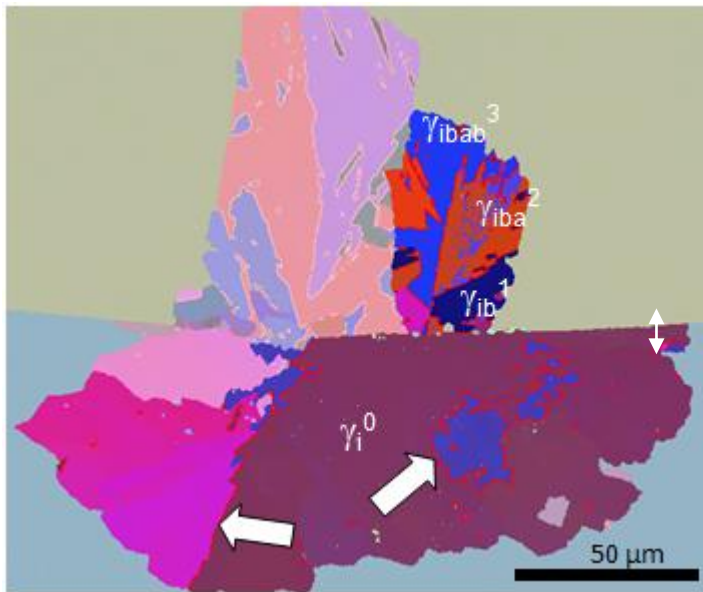
Dans la transformation massive, la germination est l'étape qui contrôle la vitesse du processus [Hawbolt-1970]. Car ensuite, la croissance des domaines massifs se produit très rapidement. Elle se produit toujours selon un maclage successif le long des plans  $\{111\}_\gamma$ . Par

conséquent, quelle que soit l'orientation donnée dans un ensemble de grains  $\gamma_m$ , il est toujours possible de remonter à son germe. La représentation schématique du processus de maclage est donnée en Figure 3. 7. Dans cette représentation nous supposons que la phase  $\gamma$  est cubique face centrée. 'i' dénote le premier germe formé le long du joint de grains qui partage un BOR avec le grain  $\alpha$  voisin. Les grains  $\gamma$  avec 'a', 'b', 'c' et 'd' sont les variantes émergeant du germe  $\gamma_i^0$ .



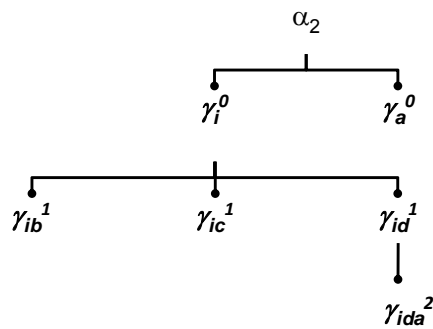
**Figure 3. 7:-** Représentation schématique de la croissance des grains  $\gamma_m$  par le processus de maclage

Le parent alpha  $\alpha_p$  donne naissance à deux variantes de  $\gamma_m$  qui sont en relation de maclage l'une avec l'autre et qui ont une BOR avec son  $\alpha_p$ . Ensuite ces deux germes peuvent donner quatre variantes chacune, la première correspond à un maclage le long des plans  $(111), (\bar{1}\bar{1}\bar{1}), (1\bar{1}\bar{1}), (\bar{1}\bar{1}1)$  avec  $(111)$  commun aux deux germes  $\gamma_m$ . Bien que ces quatre variantes soient en relation de maclage avec  $\gamma_i^0$ , il n'y a aucune relation d'orientation spécifique entre elles. Cet ensemble de six orientations de  $\gamma$  excluant les deux germes  $\gamma$  est appelée "première génération". Ensuite chaque orientation  $\gamma$  peut à son tour donner naissance à un autre ensemble de quatre orientations  $\gamma$  qui appartiendront à la "deuxième génération". La croissance de tous les grains  $\gamma_m$  se fait de cette manière et le nombre de générations possibles dépend de divers facteurs. La Figure 3. 8 donne un exemple montrant plusieurs générations de grains  $\gamma_m$  et la manière dont on peut remonter au  $\gamma_i^0$  à partir de la dernière génération. Après germination, les grains  $\gamma_m$  de première génération n'ont plus de relation d'orientation spécifique avec le grain  $\alpha_p$ . Par conséquent, les grains  $\gamma_m$  de la première génération peuvent croître dans les grains  $\alpha_p$ . Cependant, très souvent, la croissance des grains massifs est arrêtée par l'ex- joint  $\alpha/\alpha$  et le grain  $\gamma_m$  qui est arrêté par le joint de grains  $\alpha/\alpha$  soit donne naissance à un maclage de l'autre côté, soit cesse de se développer. Ceci est clairement montré en Figure 3. par une flèche blanche à deux têtes : le  $\gamma_i^0$  donne une macle  $\gamma_{ib}^1$  de l'autre côté du joint de grains à l'intérieur du grain  $\alpha_p$ .



**Figure 3. 8:-** Carte EBSD représentée en code couleurs d'angles d'Euler, qui fait ressortir le chemin de maillage qui peut être utilisé pour remonter au germe à partir de la variante  $\gamma$  finale qui s'est formée. La flèche blanche à deux têtes montre comment la variante de maillage se retransforme à l'intérieur de son grain parent  $\alpha$ .

Bien que la formation de diverses variantes de maillage à chaque étape soit clairement démontrée, une analyse EBSD approfondie montre que, à chaque génération, toutes les variantes de maillage  $\gamma$  ne sont pas présentes. Il y a toujours des variantes de maillage absentes. Ceci indique qu'il y a une tendance manifeste à une sélection de variantes pendant la croissance. Cette sélection lors de la croissance peut s'opérer à deux niveaux. D'abord, pendant le développement des deux germes, il y a toujours un germe qui se développe au détriment de l'autre. Ceci se voit en Figure 3. 4 avec la germination de joint de grains de type II. Dans ce cas, bien que les germes  $\gamma_i^0$  and  $\gamma_a^0$  se forment, la fraction en surface de  $\gamma_i^0$  est supérieure à celle de  $\gamma_a^0$ . La deuxième étape lors de laquelle la sélection de variante peut se faire, est pendant la formation des variantes de maillage  $\gamma$ . La formation de ces variantes n'est pas systématique. Dans la plupart des cas, certaines variantes de maillage sont absentes. Même si elles se sont toutes formées, les surfaces des variantes de maillage ne sont pas identiques. Certaines variantes sont préférées à d'autres. On trouvera en Figure 3. 9 un schéma des variantes formées en Figure 3. 4 (a).



**Figure 3. 9:-** Représentation schématique montrant les variantes formées dans la carte EBSD présentée en Figure 3. 4 (a).

D'autres auteurs [Dey-2006 ] ont fait état de cette tendance à la sélection de variantes bien que la mesure ait été toujours faite en bidimensionnel. Par conséquent, la sélection de variantes pendant la croissance du domaine massif est à vérifier en trois dimensions. Une analyse tridimensionnelle par EBSD et BSE a également été tentée le long d'un ex joint de grains  $\alpha/\alpha$  et le long d'un joint triple pour répondre aux questions suivantes :

“Pendant la croissance des grains massifs par maclage, les variantes apparemment absentes, sont-elles réellement absentes ou sont-elles présentes dans la zone au-dessus ou au-dessous de la surface analysée ? La variante dominante est-elle présente seulement en surface ou cette variante est-elle également réellement la variante dominante dans le matériau de cœur?”

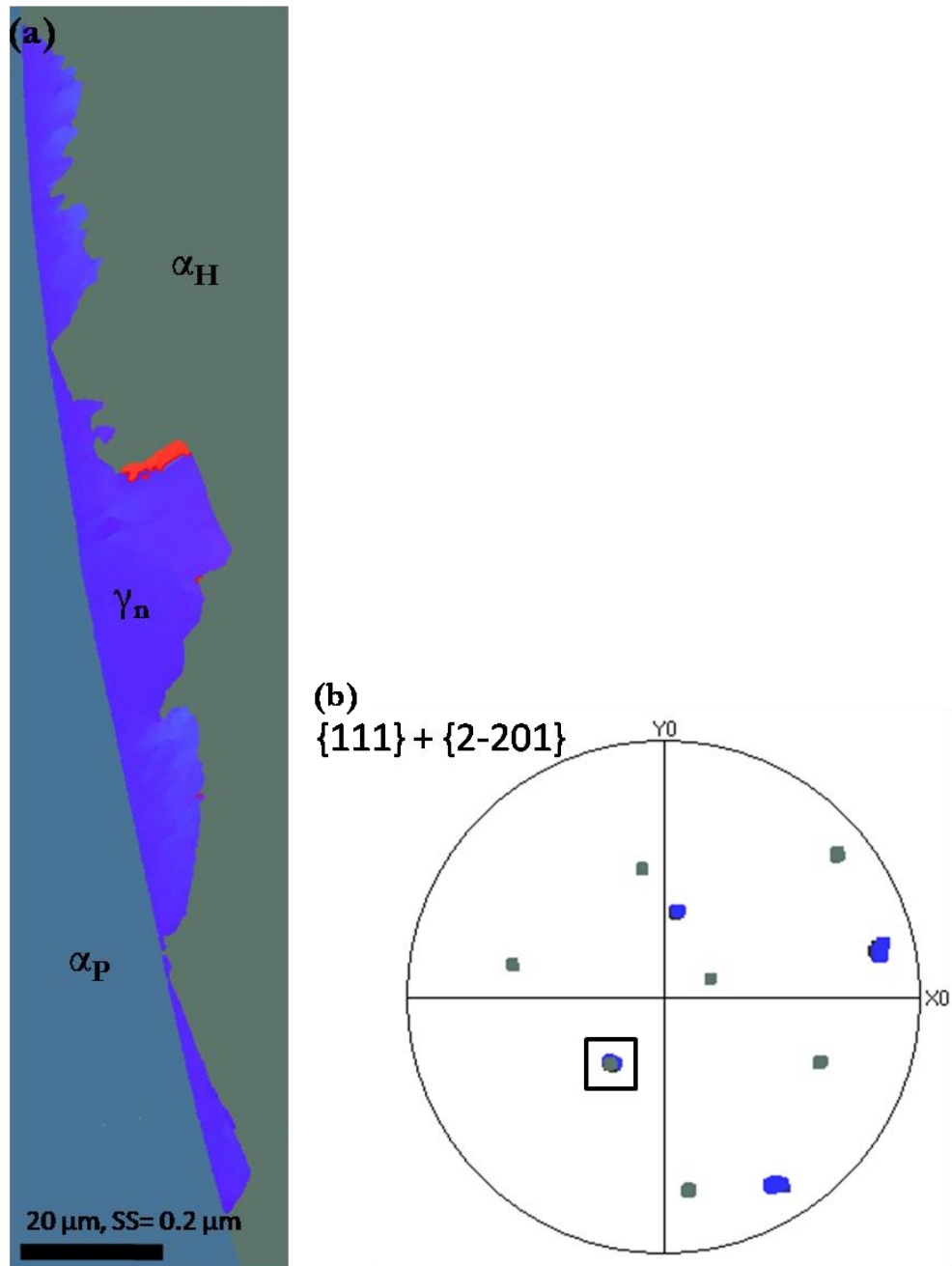
L'analyse de la série de cartes EBSD a montré qu'un grain  $\gamma$  peut produire toutes les variantes possibles bien que toutes ne soient généralement pas représentées dans une section donnée. Cependant, pendant la croissance, la variante qui est dominante en surface s'avère être aussi la variante dominante lorsqu'on analyse en tridimensionnel (Annexe A2). En conséquence, il semble qu'il y ait effectivement une sélection de variantes pendant la croissance des grains massifs.

Le développement des variantes  $\gamma_m$  à l'intérieur du grain  $\alpha$  peut être régi par deux facteurs ; l'un des ces facteurs est la minimisation de l'énergie élastique et le second est la mobilité des interfaces en croissance. La mobilité des interfaces  $\gamma_m/\alpha_H$  peut être considérée comme le facteur principal car, puisque le développement des grains  $\gamma_m$  est très rapide, leur croissance semble régie plutôt par des facteurs cinétiques que par des facteurs énergétiques. Le mouvement des interfaces  $\gamma_m/\alpha_H$  dépend d'un certain nombre de facteurs tels que la relation d'orientation entre les deux phases ( $\gamma$  et  $\alpha$ ) et le type d'interfaces  $\gamma_m/\alpha_H$  (planes ou irrégulières, cohérentes ou incohérentes). Dans notre étude, nous avons observé que les interfaces entre les phases  $\alpha$  et  $\gamma$  peuvent être fortement incurvées ou planes le long de plans de maclage  $\{111\}$ , comme on peut le voir dans la Figure 3. 8. Quand on a une interfaces incurvée ou incohérente, la probabilité pour le grain de donner naissance à une macle est plus grande par comparaison à une interface cohérente ou partiellement

cohérente [Mahajan- 1997]. Ceci est dû au fait que, si le rayon de courbure du joint est faible, la force motrice pour la migration de joint sera élevée. Par conséquent, la probabilité de former une macle en fonction des accidents de croissance est plus grande. Ces auteurs ont décrit la courbure du joint de grains en termes de marches et facettes. Plus le rayon de courbure est petit, plus la densité surfacique de ces caractéristiques est élevée. Pour des alliages de TiAl, on a fait état dans la bibliographie du fait qu'il y a toujours une relation d'orientation correspondant à une coïncidence de plans d'indices de Miller élevés entre les phases  $\gamma$  et  $\alpha$  [Massalski- 2002, Wang- 2002]. Dans notre cas, sauf pour le germe qui a un SNOR avec le (0002) de sa  $\alpha_H$ , les variantes ne partagent aucune relation d'orientation spécifique simple avec les plans (0002)  $\alpha_H$ . Cependant, bien souvent, les variantes qui sont sélectionnées, sont les variantes qui ont leur plan  $\{111\}$  parallèle ou presque parallèle à l'un des plans  $\{2-201\}_\alpha$  (type pyramidal I) du grain hôte  $\alpha_2$ . Un exemple de ce type se trouve en Figure 3. 10. Ici, le  $\gamma_n$  a sa  $\{111\}$  exactement parallèle par rapport au plan  $\{2-201\}$ ; il a participé à la germination et au processus de croissance. Au contraire, le  $\gamma_n^T$  qui ne partage aucune relation avec  $\{2-201\}$  ne s'est pas formé du tout. Mais le  $\gamma_n$  formé ne participe pas activement au processus de maclage, en ne formant qu'une variante de macle. Ainsi, il existe un rapport spécifique d'orientation entre  $\{111\}_\gamma$  et  $\{2\bar{2}01\}_\alpha$ .

Avec cette échelle d'observation, l'interface semble être générale et n'est pas limitée à ce plan particulier. Mais l'incapacité du  $\gamma$  grain à se développer librement et à produire des macles multiples suggère qu'il est possible qu'il se forme des nano-facettes à l'échelle atomique. Ces résultats sont en contradiction avec les théories du mouvement des joints de grains pour lesquelles quand deux grains forment un joint de grains d'interphase de basse énergie, le joint de grains a une mobilité extrêmement faible.

Ce type de cohérence ou de cohérence partielle de la phase du produit avec la phase de l'hôte n'avait jamais été identifié dans un alliage de TiAl. Howe et al. et Reynolds et al. [Howe- 2002, Reynolds 2003] ont repéré une coïncidence entre les rangées que forment les plans atomiques  $\{2-201\}_{\alpha_2}$  et  $\{111\}_\gamma$  lorsqu'ils se croisent au niveau de l'interface  $\alpha/\gamma$ . On appelle cela appariement bord-à-bord [Kelly 1999, Kelly 2006]. Les études HRTEM faites par Howe ont prouvé que les interfaces incurvées pouvaient être effectivement facettées le long de plans à faibles indices à l'échelle atomique. La présence de facettes peut provoquer un abaissement de l'énergie d'interface par rapport à une interface complètement non-facettée. Cependant, l'énergie d'interface n'est pas aussi basse que pour un joint de grains à simple facette ou à double facettes.



**Figure 3. 10:-** Relation d'orientation suivie par certains grains  $\gamma_m$  avec leurs grains hôtes  $\alpha$   $\alpha_H$ . (a) cas typique de germination de joint de grains de type II (b) figures de pôles de  $\{111\}\gamma$  et  $\{\alpha$  de  $2-201\}$  superposées.



# Chapitre IV : Évolution microstructurale et de texture des grains $\gamma_m$ par des traitements thermiques

## Objectif II

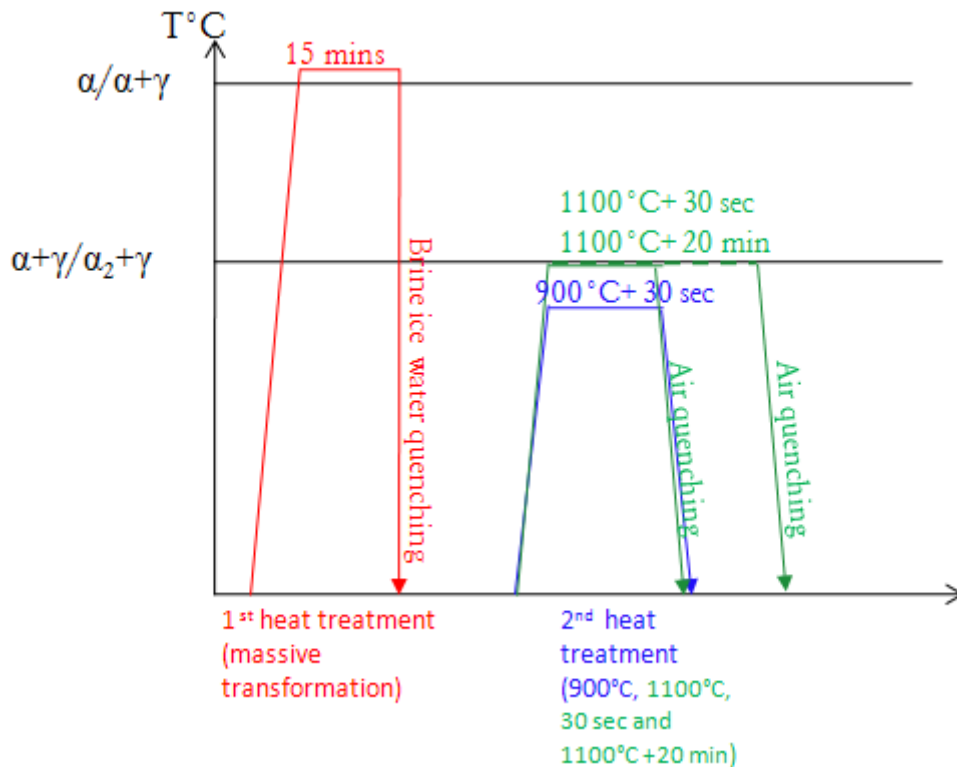
*Analyser les mécanismes de déstabilisation de la phase  $\gamma_m$  et étudier son évolution microstructurale.*

## IV. 1. Évolution microstructurale

### IV. 1. 1 Matériau de départ

Des échantillons fournis par l'ONERA ont été coupés à environ 15mm x15mm x40mm et trempés dans de la saumure glacée après un maintien isotherme de 15 minutes dans le domaine  $\alpha$ . Le matériau initial avait été fabriqué par le procédé de métallurgies des poudres (P.M.). Il a été choisi pour étudier les mécanismes de déstabilisation des grains  $\gamma_m$  afin d'éviter tout effet de texture. Après la trempe, la microstructure prédominante était la structure  $\gamma_m$ , avec un petit pourcentage de grains  $\alpha_2$  au bord de l'échantillon et de grains  $\gamma$  à plumeaux au centre de l'échantillon en raison du gradient thermique pendant le processus de refroidissement. Ces échantillons massivement transformés ont été soumis à des traitements thermiques à 900°C pendant 30 sec, 1100°C pendant 30 sec et à 1100°C pendant 20 minutes. Pour tous ces traitements thermiques, la vitesse de chauffage était de 5°/min. Ce régime a été choisi car un régime de chauffage plus élevé est susceptible de provoquer la formation de platelets  $\alpha$  qui ne subiraient aucun changement après le traitement thermique suivant [Ott- 1999]. Après les maintiens isothermes, les échantillons ont été trempés à l'air. Une représentation schématique des différents traitements thermiques effectués est donnée en Figure 4. 1. La température du traitement thermique a

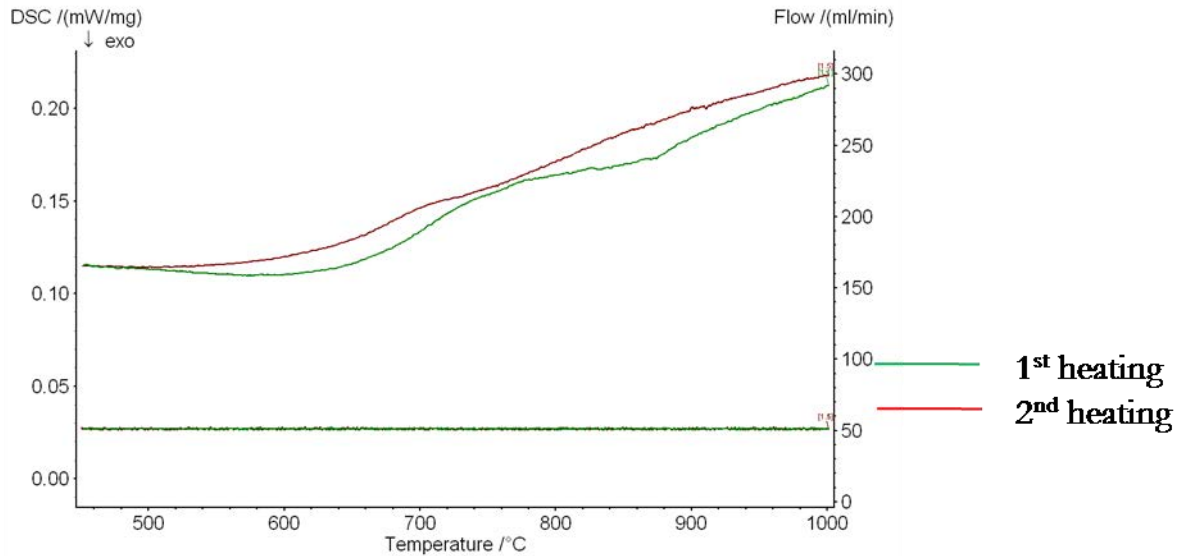
été décidée à partir des résultats livrés par les expériences en calorimétrie à balayage différentiel (DSC).



**Figure 4. 1:-** Représentation schématique des différents traitements thermiques effectués sur l'échantillon P.M. avec microstructure massive comme précurseur.

#### **IV. 1. 2. Température de déstabilisation des grains $\gamma_m$**

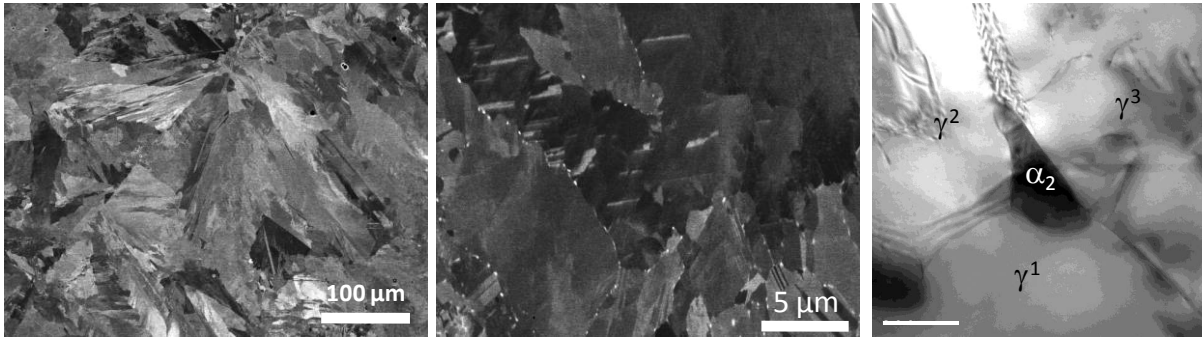
Les grains massifs sont fortement métastables et il s'avère qu'ils présentent un grand nombre de défauts cristallins tels que dislocations, fautes d'empilement et parois anti-phase [Wang- 2002]. L'identification du type de déstabilisation est essentielle. Des échantillons mesurant  $3\text{mm} \times 3\text{mm}$  ont été prélevés sur une zone complètement massive et soumis à un programme contrôlé de chauffage dans un appareil à balayage différentiel (DSC) (Pour plus ample information, se référer à l'Annexe A) en étant portés à une température allant jusqu' à  $1100^{\circ}\text{C}$ . La Figure 4. 2 montre qu'il y a une légère perturbation dans la zone de températures entre  $500^{\circ}$  et  $950^{\circ}\text{C}$ . L'observation de la microstructure massive à  $900^{\circ}\text{C}$  montre que la déstabilisation s'est déjà produite. Clemens et al. [Clemens- 2006] ont fait appel à une méthode différente pour étudier la température de déstabilisation de la phase  $\gamma_m$ . Ils ont mesuré la dureté sur l'échantillon massif soumis à un traitement thermique avec des paliers de  $100^{\circ}\text{C}$  à partir de  $400^{\circ}\text{C}$ . Ils ont observé une chute dans les valeurs de dureté à environ  $600^{\circ}\text{C}$  et ensuite une augmentation aux environs de  $800^{\circ}\text{C}$ . Avec la température de déstabilisation des grains massifs, différents traitements thermiques ont été effectués et les microstructures ont été analysées.



**Figure 4. 2:-** Courbes DSC pendant deux étapes successives de chauffage à 20°C/min pour un échantillon présentant au départ une microstructure gamma-massive : la ligne verte a été enregistrée pour les premières étapes de chauffage (structure  $\gamma_m$ ) alors que la ligne rouge correspond à la deuxième étape de chauffage (microstructure stabilisée)

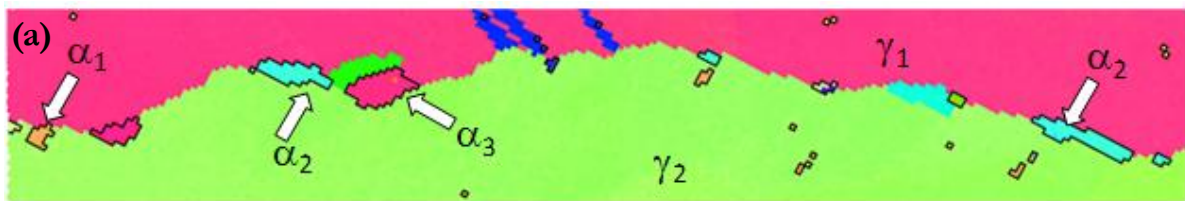
#### **IV. 1. 3. Changements microstructuraux dus à la déstabilisation de la phase $\gamma_m$**

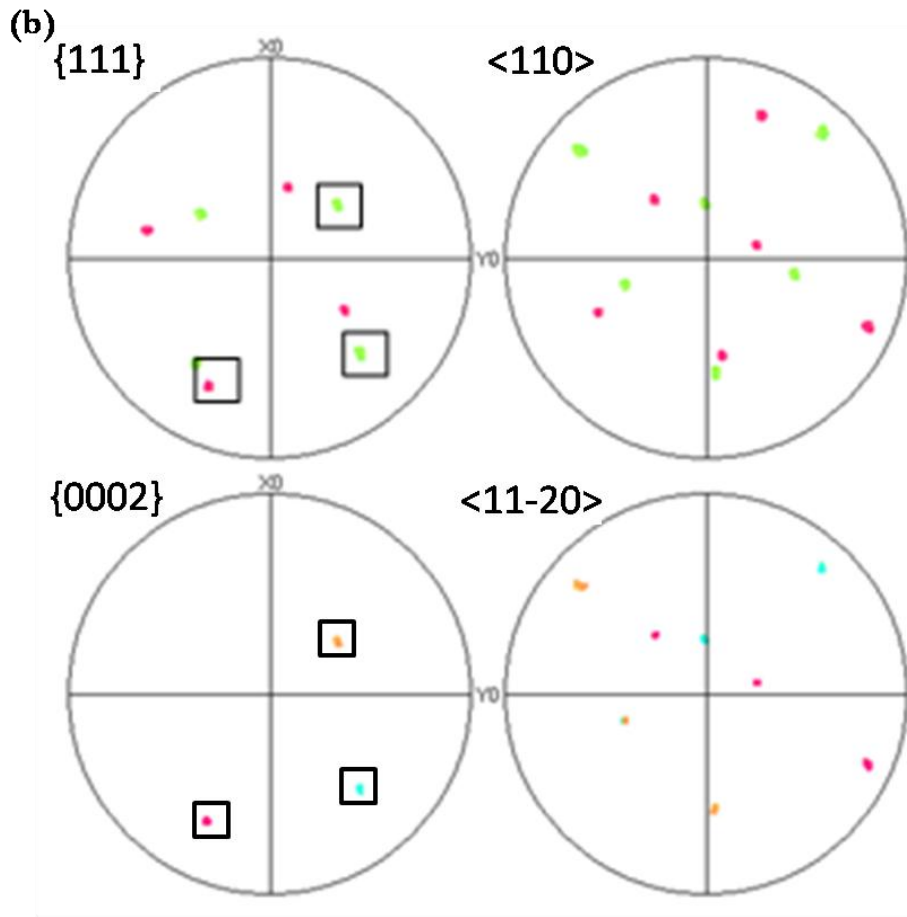
L'analyse MEB sur l'échantillon soumis à un traitement thermique à 900°C ne montre aucun changement dans la morphologie des grains  $\gamma_m$ . Cependant, à un grandissement plus élevé, on voit que la phase  $\alpha_2$  précipite le long des joints de grains. Ces précipités ont une morphologie globulaire et sont de l'ordre de quelques nanomètres. Bien que le FEG-MEB-EBSD ait une résolution spatiale de quelques dizaines de nanomètres, il est très difficile d'indexer ces précipités en utilisant des conditions standards. Par conséquent, l'analyse cristallographique a été effectuée en utilisant le TEM. La microstructure examinée à différents grandissements est donnée en Figure 4. 3. Les sites de germination des précipités globulaires  $\alpha_2$  se composent de joints triples constitués de joints de grain de forte désorientation ou de joints de domaines ordonnés, et de joints de grains à forte désorientation. De temps en temps, on voit la précipitation se faire sur les fautes d'empilement. Quelque soit le type de sites de germination, les précipités  $\alpha_2$  globulaires se forment toujours avec une facette le long d'un des grains  $\gamma$  et ils partagent une BOR avec ce grain  $\gamma$ . Pour la germination au joint de grains du précipité  $\alpha_2$  globulaire, le mécanisme de germination ressemble à celui de la germination  $\gamma_m$  sur des joints de grains de type II pour lesquels le "critère minimum d'angle" constituait la règle de sélection pour la précipitation.



**Figure 4. 3:-** Images BSE et MET de l'échantillon soumis à un traitement thermique à 900°C.

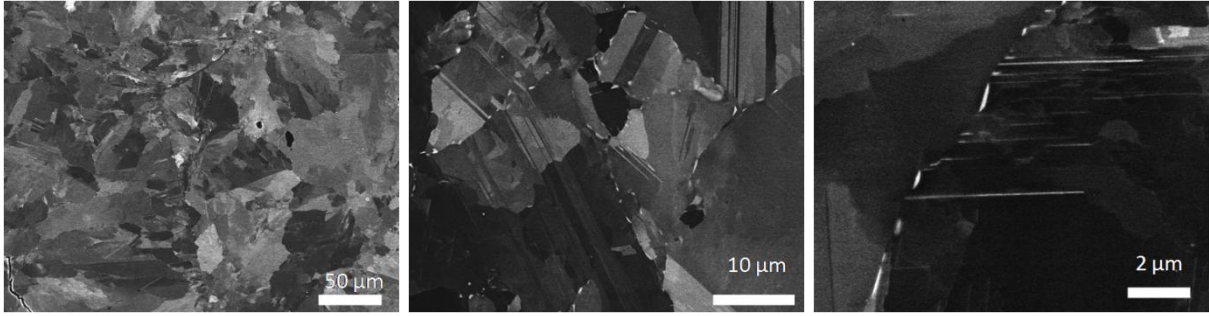
Un autre échantillon transformé massivement a été soumis à un traitement thermique à 1100°C pendant 30 sec. Ceci est proche de la limite de la transformation du domaine  $\alpha_2 + \gamma$  au domaine  $\alpha + \gamma$ . Quant à l'échantillon soumis à ce traitement thermique, on n'observe pas beaucoup de changement dans la morphologie des grains  $\gamma_m$ . Cependant, les précipités globulaires sont indéniablement devenus plus grossiers. La morphologie de ces  $\alpha_2$  globulaires semble être légèrement ovale quand on les compare aux précipités formés à 900°C, ce qui indique qu'il y a une possibilité de coalescence. Suite à cette coalescence, l'indexation de la phase  $\alpha$  par EBSD est possible. La carte EBSD le long d'un joint de grains  $\gamma/\gamma$  de forte désorientation est donnée en Figure 4. 4. Les figures de pôles des plans  $(0002)\alpha_2$  et  $\{111\}\gamma$  montrent que les précipités  $\alpha_2$  globulaires suivent toujours une BOR stricte avec l'un des deux grains  $\gamma$ . De multiples variantes se sont formées le long d'un joint de grains  $\gamma/\gamma$  (théoriquement, il existe huit orientations différentes de phase  $\alpha$  susceptibles de se former puisqu'il existe huit  $\{111\}$  différents à partir des deux grains  $\gamma$ ). Ceci est dû à la morphologie erratique du joint de grains  $\gamma_m$ . Le plan du joint des grains  $\gamma_m$  changent de place en place à cause de sa nature irrégulière. Par conséquent, il y a des chances pour que plusieurs variantes de  $\alpha_2$  participent au processus de germination bien que, localement, tous les précipités  $\alpha_2$  globulaires respectent la règle de sélection à savoir la règle de l'angle minimum.





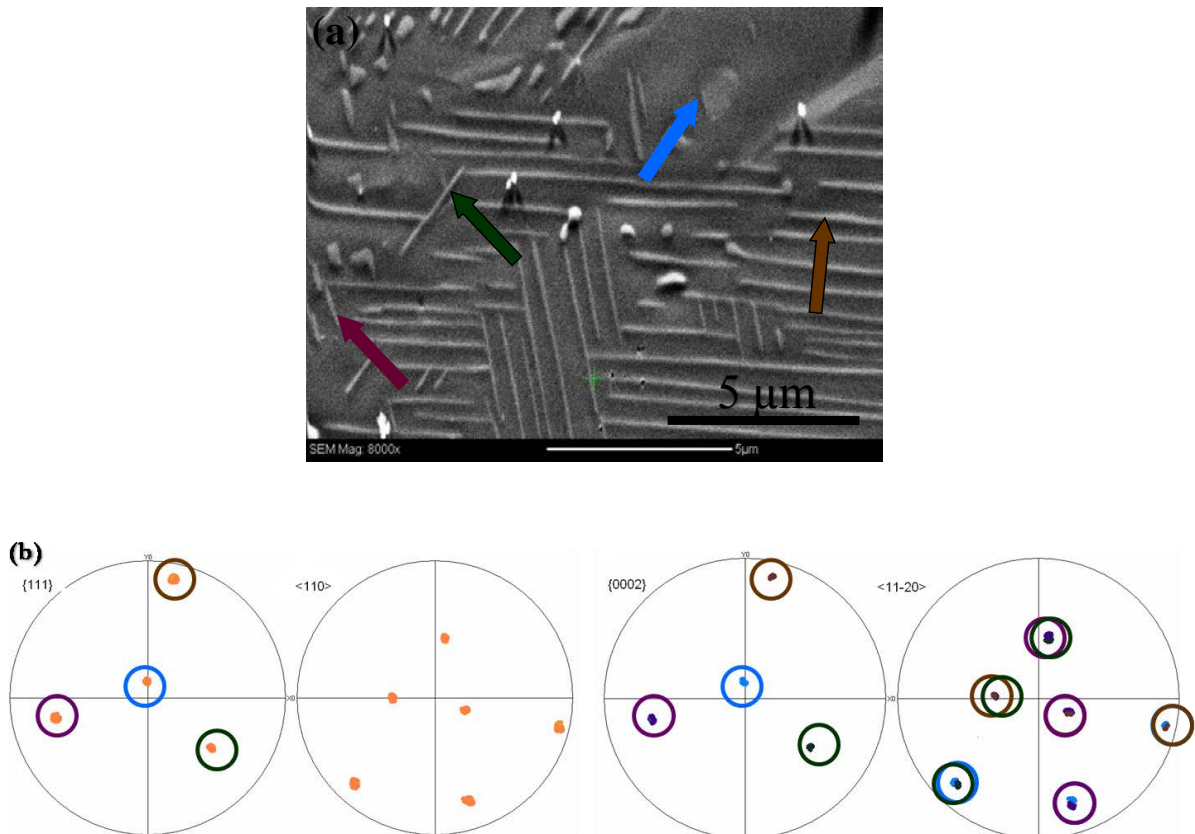
**Figure 4. 4:-** (a) joint de grains  $\gamma/\gamma$  avec différentes orientations des précipités  $\alpha_2$  globulaires (b) les figures de pôles  $\{111\}$  et  $\langle 110 \rangle$  de  $\gamma$  et  $\{0002\}$  et  $\langle 11-20 \rangle$  de  $\alpha$  montrant la relation de BOR entre les phases  $\gamma$  et  $\alpha_2$ .

Outre les précipités  $\alpha_2$  globulaires, on a pu observer que des précipités  $\alpha_2$  se développaient sous forme de platelets à l'intérieur des grains  $\gamma_m$ . Un platelet de  $\alpha_2$  à une largeur moyenne d'environ 200 nm et suit une BOR avec les grains  $\gamma$  à l'intérieur desquels il se forme. Il y a souvent seulement une ou deux orientations de platelets  $\alpha_2$  que l'on peut voir se former, bien qu'il y ait quatre orientations différentes de platelets  $\alpha_2$  qui sont susceptibles de le faire. L'étude MET de ces platelets montre qu'ils se sont formés sur les fautes d'empilement existantes. La croissance de ces platelets dans le sens de la longueur semble être entravée seulement par des joints de grains de forte désorientation, des platelets  $\alpha_2$  ayant des orientations différentes et certains joints de domaines ordonnés. La Figure 4. 5 présentes les différentes caractéristiques de la précipitation  $\alpha_2$  à différents grandissements. Les sites de germination des différents précipités  $\alpha_2$  rapportés ici sont cohérents par rapport aux conclusions de [Kumagai- 1997, Zhang- 1999] bien qu'ils aient travaillé à des températures et sur des périodes de temps différentes.



**Figure 4. 5:-** Images BSE prises à différents grossissements de l'échantillon soumis à un traitement thermique à 1100°C pendant 30 sec.

Le troisième traitement thermique consiste en un maintien isotherme à 1100°C mais pendant 20 minutes. Les études MEB montrent qu'il y a une tendance à la coalescence pour les deux types de précipités  $\alpha_2$ , bien que la croissance des platelets  $\alpha_2$  dans le sens de la largeur semble limitée. Le nombre d'orientations  $\alpha_2$  à l'intérieur des grains  $\gamma$  semble être hétérogène de grain à grain. Certains grains présentent les quatre orientations possibles de  $\alpha_2$  alors que d'autres n'ont qu'une orientation  $\alpha_2$  comme c'est le cas dans la microstructure lamellaire. La Figure 4. 6 est une carte EBSD prise à l'intérieur d'un grain  $\gamma_m$ . A partir des figures de pôles, nous pouvons voir que toutes les quatre orientations  $\alpha_2$  sont présentes sous forme de platelets.



**Figure 4. 6:-** (a) Carte EBSD haute résolution prise à l'intérieur d'un grain  $\gamma$  avec différentes orientations de platelets  $\alpha_2$ ; (b) Figures de pôles obtenues à partir des cartes EBSD, avec les quatre variantes possibles de  $\alpha_2$  qui se sont formées à l'intérieur du grain  $\gamma$ .

La taille de grain  $\gamma_m$  semble également être fortement hétérogène. On constate également que la fraction de précipités  $\alpha_2$  globulaires est plus élevée dans les zones où la taille de grains  $\gamma_m$  est plus petite. En raison de cette fraction volumique élevée de précipités  $\alpha_2$  globulaires, les grains  $\gamma_m$  correspondants sont appauvris en platelets  $\alpha_2$ . Un examen approfondi montre que ces grains  $\gamma$  plus petits se trouvent le long des joints de grains  $\alpha/\alpha$ . La taille plus petite des grains  $\gamma$  s'explique par le fait que de nombreux germes  $\gamma_m$  se sont développés le long de l'ex joint de grains  $\alpha/\alpha$  pendant la transformation massive, ainsi qu'on peut le voir dans la Figure 3. 4.

Nous avons procédé à la même étude sur un échantillon transformé massivement soumis à un traitement thermique à 1100°C pendant 20 minutes afin de suivre l'évolution de la microstructure des grains  $\gamma_m$ . Cependant, en raison de facteurs tels que l'oxydation, un certain nombre de changements que l'on avait pu voir dans l'échantillon soumis à un traitement thermique à 1100°C n'a pas été relevé ici. Une description plus détaillée de ceci est donnée en Annexe A2.

### - Objectif III

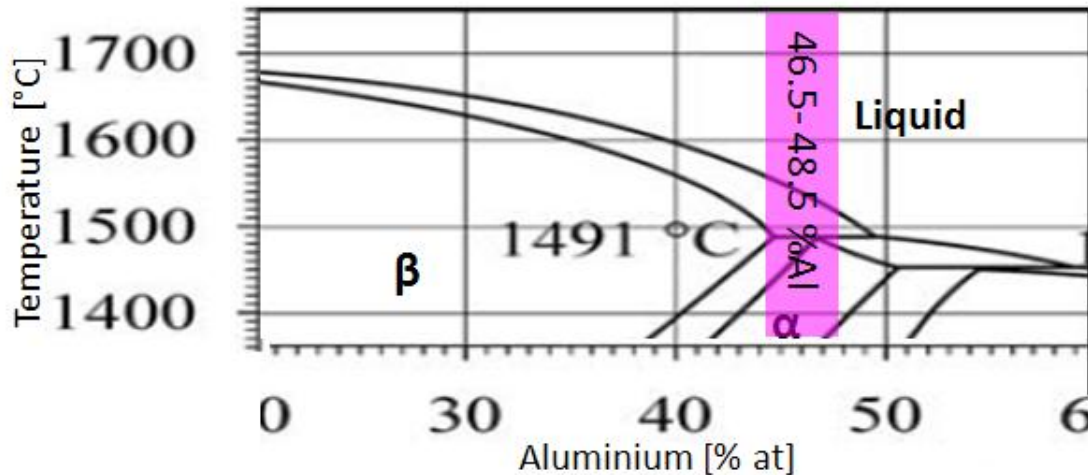
*Analyser l'influence de la transformation massive sur la texture globale de l'échantillon ainsi que l'évolution de la texture lors des traitements thermiques dans différents domaines de phases.*

## IV.2. Évolution de texture du matériau brut de fonderie avec les traitements thermiques

### IV. 2. 1. Matériau initial

On sait que le  $\gamma$ -TiAl produit par la technique de moulage à la cire perdue a une anisotropie mécanique très élevée [Bartels-2001]. En fait, pendant la solidification, il est très difficile de contrôler la taille des grains et l'orientation des grains colonnaires formés, lesquels ont parfois des longueurs allant jusqu'à 1mm. Nous avons reçu d'ONERA une barre cylindrique de 16mm de diamètre et 230 millimètres de hauteur produite par la technique de moulage à la cire perdue. La microstructure brute de fonderie montrait une zone équiaxe de 1.5 mm de diamètre au centre alors que le reste de l'échantillon était couvert de grains lamellaires colonnaires séparés par de petits grains  $\gamma$ -monolithiques. On peut voir que la majeure partie de la structure  $\gamma$ -monolithique s'est formée au-dessus des joints de grains colonnaires et les grains colonnaires présentent une structure lamellaire  $\alpha_2 + \gamma$ . Lorsque, au cours de la solidification, on passe de la phase liquide au domaine de phase  $\alpha$ , la direction de croissance du grain colonnaire est le long de la direction [0001] de la phase  $\alpha$  haute température. Il en résulte ultérieurement, à température ambiante, une microstructure lamellaire et quelques grains  $\gamma$ -monolithiques. Ce qui donne une texture de fibre {111}

perpendiculaire à la direction radiale. Les grains  $\gamma$ -monolithiques n'exercent aucune influence marquée sur la texture de l'échantillon brut de fonderie. La composition de l'alliage influence le chemin de solidification. La Figure 4. 7 présente une partie du diagramme de phase pour un alliage de TiAl [Schuster-2006].

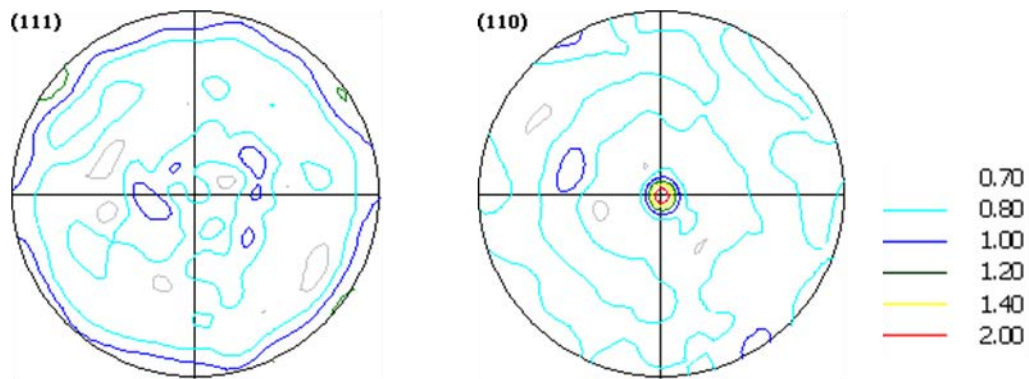


**Figure 4. 7** :-Diagramme de phase binaire partiel d'alliage TiAl selon [Schuster-2006].

Nous pouvons voir que le chemin de solidification n'est pas si simple. Il entre d'abord dans la phase  $\beta$  avant de passer par les domaines  $\alpha$  et  $\alpha + \gamma$ . Ce type de transformation est en fait assez complexe. Il a pour conséquence de rendre la texture plus isotrope. En effet, si une phase  $\beta$  suit la relation d'orientation de Burger ( $\{110\}_\beta // (0001)_\alpha$  and  $\langle 100 \rangle_\beta // \langle 11\bar{2}0 \rangle_\alpha$ ) avec la phase  $\alpha$ , chaque orientation  $\beta$  peut donner naissance à 12 orientations de  $\alpha$ , rendant de ce fait la texture plus isotrope [Kim- 1997].

Dans notre cas, il n'était pas possible de mesurer la texture obtenue en faisant une mesure parallèle à l'axe de la barre puisque la taille des grains était très grande et il n'y avait donc pas assez de grains pour donner des données exploitables statistiquement. En conséquence, la texture a été mesurée en transversal comme mentionné en Annexe A1 où la taille des grains  $\gamma$  est de l'ordre de 30  $\mu\text{m}$ . En outre, la zone mesurée est plus grande, ce qui permet aussi d'améliorer les résultats statistiques. Les mesures de texture en transversal montrent une texture de fibre  $\{110\}$ , comme on peut le voir en Figure 4. 8. En examinant la texture obtenue, il est clair que le chemin de solidification ne passe pas seulement par le domaine  $\alpha$ , il passe également par le domaine péritectique ( $\beta$  + liquide). Comme dit plus haut, le chemin de solidification passant par  $\beta$  peut entraîner une relative isotropie de la texture du matériau brut de fonderie. Dans notre cas, ceci est bien illustré par le fait que la densité de pôles maximale est seulement 2.00 fois celle correspondant à une texture complètement isotrope.

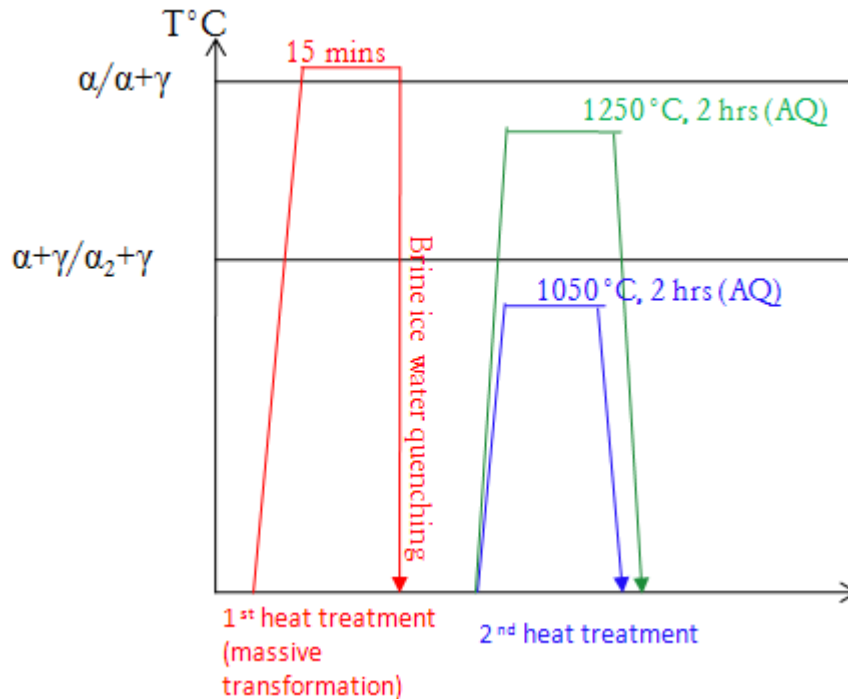




**Figure 4. 8:-** Figures de pôles  $\{111\}$  et  $\{110\}$  du spécimen brut de fonderie mesuré le long des tangentes

Puisque toutes les autres mesures de la texture ont été effectués parallèlement à l'axe de la barre, les figures de pôles  $\{111\}$  et  $\{110\}$  ont été simulées à partir des figures de pôles expérimentales obtenues pour le brut de fonderie en transversal, en tenant compte de la symétrie de l'échantillon cylindrique.

La barre brut de fonderie aux dimensions  $\phi 16$  millimètres X 40 mm a été trempée dans de la saumure glacée pour obtenir une microstructure massive complète. Le cylindre transformé massivement a été découpé en plusieurs morceaux pour procéder à des traitements thermiques. Les températures du traitement thermique ont été choisies de manière à ce qu'elles restent dans le cadre de différents domaines. Les traitements thermiques ont été effectués à 1050°C domaine ( $\alpha_2 + \gamma$ ), 1250°C domaine ( $\alpha + \gamma$ ) et 1365°C (domaine  $\alpha$ ). Les traitements thermiques effectués sont donnés en représentation schématique dans la Figure 4. 9.



**Figure 4. 9:-** Représentation schématique des différents traitements thermiques effectués sur l'échantillon brut de fonderie.

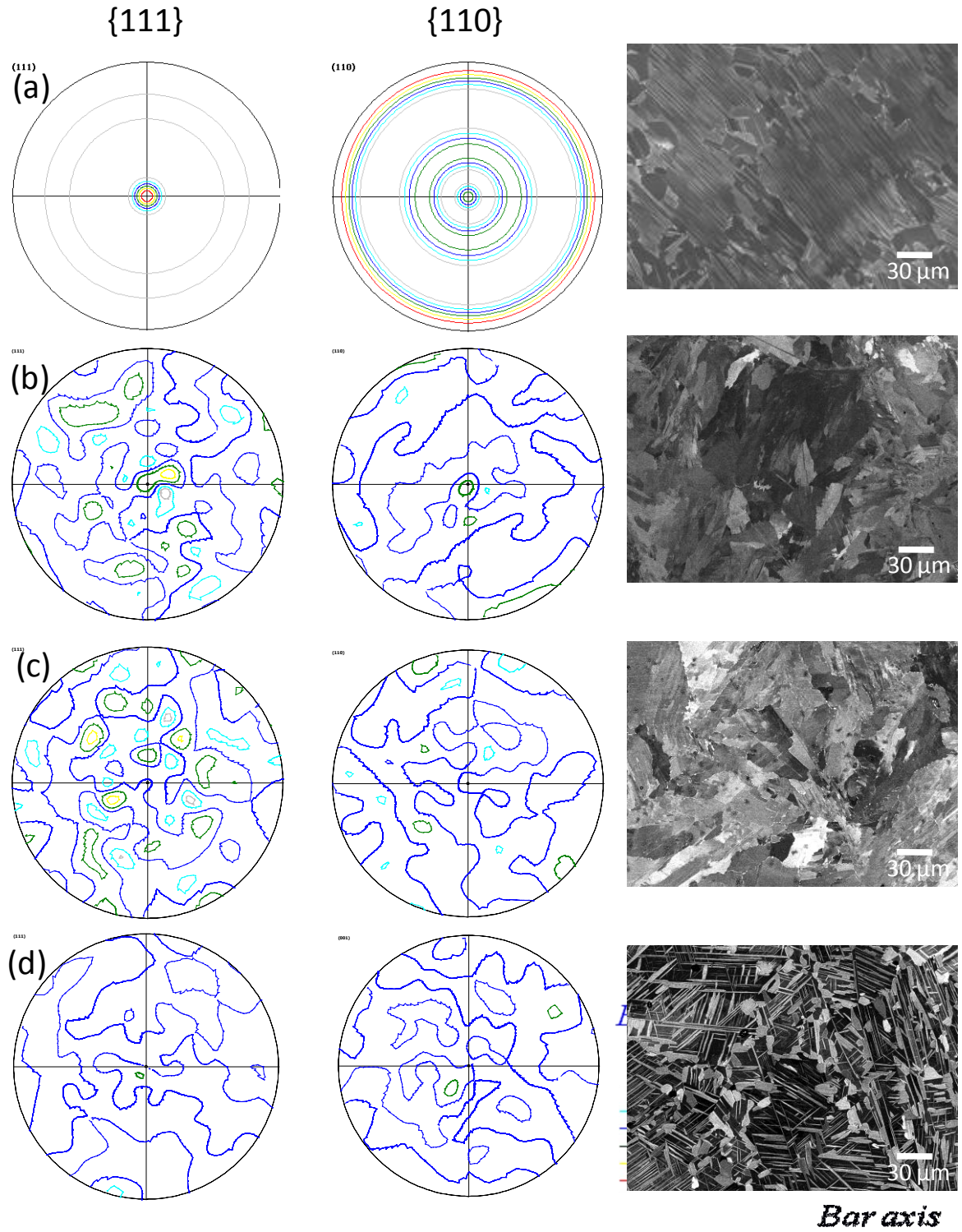
#### **IV. 2. 2. Évolution de texture avec divers traitements thermiques**

##### **- Microstructure massive :**

Les figures de pôles  $\{111\}$  et  $\{110\}$  de la microstructure  $\gamma_m$  montrent que la texture a été relativement affaiblie par la transformation massive. Ceci est évident quand on compare la densité de pôles maximale du brut de fonderie par rapport à celle de  $\gamma_m$ . Cependant, il reste des traces de la texture brute de fonderie, par exemple la densité de pôles est toujours maximum le long de l'axe de la barre pour  $\{111\}$ . Cet effet de lissage de la texture est le résultat des mécanismes de croissance des grains  $\gamma_m$  pour laquelle chaque grain  $\alpha$  présente de nombreuses orientations différentes de grains  $\gamma$  avec lesquels il ne partage aucune relation d'orientation.

##### **- Texture à 1050°C, 2 heures:**

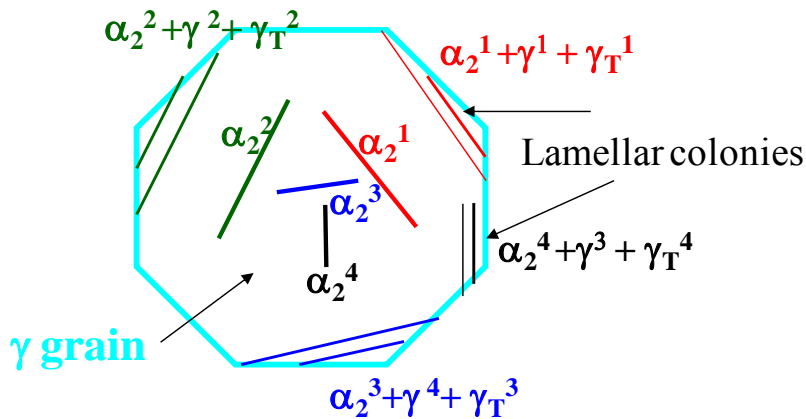
Le traitement thermique à 1050°C amène la précipitation  $\alpha_2$  mais ne change pas la morphologie des grains  $\gamma_m$ . Par conséquent, la texture  $\gamma$  n'est pas censée être beaucoup modifiée après ce traitement thermique. La Figure 3. 10 (c) montre les figures de pôles  $\{111\}$  et  $\{110\}$  de l'échantillon soumis à un traitement thermique à 1050°C pendant 2 heures. La texture obtenue est similaire à la texture obtenue dans l'échantillon massif.



**Figure 4.10** :- Figures de pôles  $\{111\}$  et  $\{110\}$  des échantillons avec divers traitements thermiques. (a) figures de pôles simulées de l'échantillon brut de fonderie parallèle à l'axe de la barre; (b) microstructure massive (c) échantillon soumis à un traitement thermique à 1050° C pendant 2 heures, (d) échantillon soumis à un traitement thermique à 1250° C pendant 2 heures.

- **Texture à 1250° C, 2 heures:**

Ce traitement thermique est semblable au traitement thermique appliqué pour obtenir la microstructure duplex. Les figures de pôles  $\{111\}$  et  $\{110\}$  en Figure 4. 10 (d) montrent une texture presque aléatoire. En termes de microstructure, nous pouvons voir que les précipités globulaire  $\alpha_2$  sont devenus très grossiers, il en est de même pour les platelets  $\alpha_2$  la fraction volumique de la phase  $\alpha$  est de presque 29%. Cette transformation provoque à nouveau un changement dans la texture de la phase  $\gamma$ . En effet, les différents précipités  $\alpha_2$  se sont retransformés en structures lamellaires pendant le refroidissement final. Pendant la précipitation globulaire le long des joints de grains  $\gamma/\gamma$ , comme on l'a vu plus haut, de multiples variantes de  $\alpha_2$  se sont formées et ces  $\alpha_2$  précipitent en se transformant en une phase  $\gamma$  avec deux orientations  $\gamma$  différentes. Sur ces deux orientations, l'une correspond à l'orientation des grains  $\gamma$  existants tandis que l'autre orientation est différente. Par conséquent, quatre nouvelles orientations de  $\gamma$  sont formées. Ce type de mécanismes de transformation est avéré pour les platelets  $\alpha_2$  présents à l'intérieur du grain  $\gamma$ . Par conséquent, elles provoquent le lissage de la texture. Une représentation schématique du mécanisme est donnée en Figure 4. 11.



**Figure 4. 11:-** Représentation schématique de la distribution des orientations  $\gamma$  dans un grain  $\gamma$ .

# Chapitre V : Calcul théorique de la texture $\gamma_m$

## Objectif IV:

*Modéliser la texture des grains  $\gamma_m$  en appliquant théoriquement certains mécanismes de germination et de croissance.*

## V. 1. Matériau initial

L'alliage TiAl obtenu par métallurgie des poudres (MDP) a été utilisé pour produire la microstructure massive. Des échantillons de dimensions 15mm x 15mm x 7mm ont été trempés dans l'eau glacée pour obtenir une structure massive non complètement transformée co-existant avec la phase  $\alpha_2$ . On a choisi un échantillon de MDP pour éviter l'influence de la texture. Comme prévu par les mécanismes de germination et de croissance de la phase massive, cette microstructure biphasée est caractérisée par la phase massive décorant les joints de grains de l'ex-phase  $\alpha$ , ainsi que la phase  $\alpha_2$  résiduelle présente au centre de chaque grain.

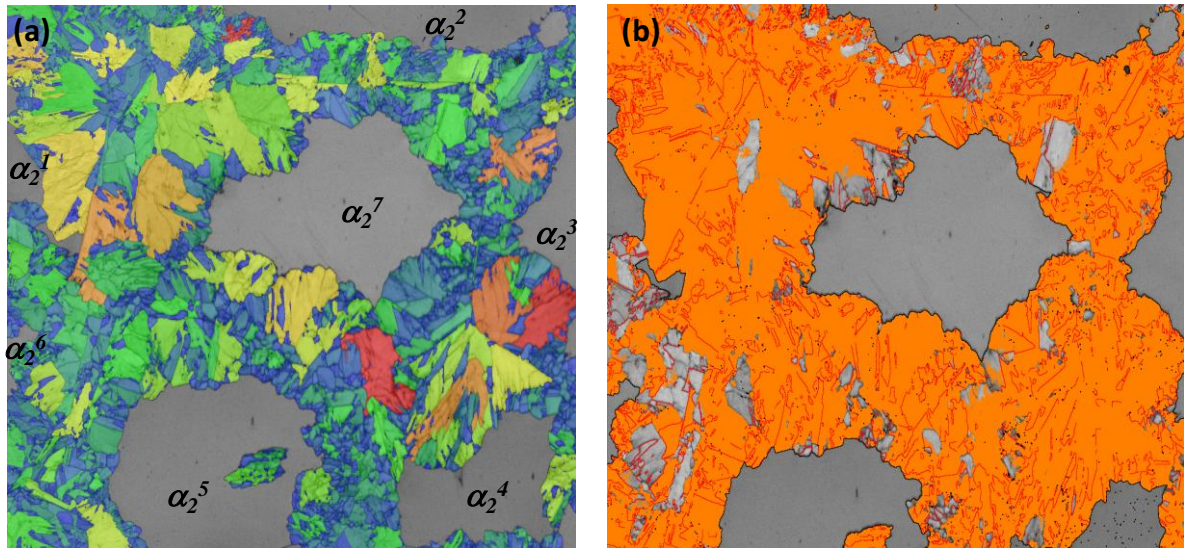
## V. 2. Relation d'orientation entre le parent hexagonal $\alpha_p$ et le grain tétragonal $\gamma$

Comme cela a été dit précédemment, pendant la transformation  $\alpha \rightarrow \gamma$ , le parent  $\alpha$  et le produit  $\gamma$  suivent une BOR stricte l'un avec l'autre. La phase  $\alpha$  peut donner naissance à six orientations de  $\gamma$ , qui apparaissent en raison de la tétragonalité de la phase  $\gamma$  [Zghal-1997]. Mais puisque la validation du modèle a été faite à partir d'une carte d'EBSD, la phase quadratique  $\gamma$  est considérée comme phase cubique, avec la phase  $\alpha_2$  donnant naissance à deux variantes de  $\gamma$  en relation de macles. Pour les calculs qui vont suivre, on a supposé que la phase  $\gamma$  était cubique.

L'orientation d'un cristal est représentée via les angles d'Euler ( $\phi_1, \phi, \phi_2$ ) [Bunge-1982]. La transformation de phase d'une structure cristalline à une autre structure cristalline s'exprime comme la rotation qui conduit à la superposition des deux systèmes de coordonnées orthonormés attachés à chacune des phases cristallines. Sachant que la transformation massive se fait avec une relation d'orientation entre la phase parente  $\alpha_{HCP}$  et la phase fille  $\gamma_{CFE}$  appelée BOR, la rotation associée à cette transformation  $\Delta g$ , exprimée en angles d'Euler, est

$$\Delta g = (30.0^\circ, 54.73^\circ, 45.0^\circ)$$

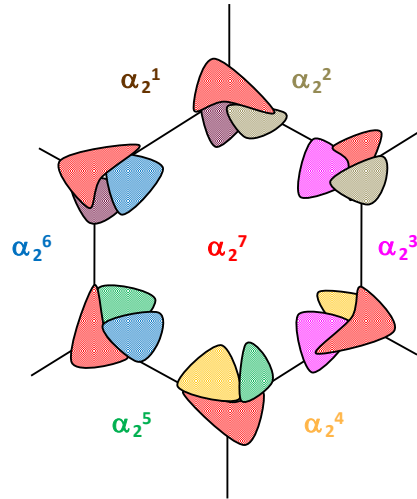
Avec cette transformation, un grain  $\alpha_2$  peut donner naissance à une orientation  $\gamma$ . A ce moment, nous pouvons rappeler une fois de plus les mécanismes de la transformation massive. Pendant la transformation massive le grain  $\alpha$  donne naissance à un grain  $\gamma$  selon la BOR, mais ce grain  $\gamma$  se développe au sein du grain  $\alpha$  opposé. Le premier grain formé ou germe est appelé  $\gamma_n$ . Après la formation du germe, la croissance s'effectue par le processus du maillage, ce qui correspond à une désorientation de  $60^\circ$  autour d'un des axes  $\langle 111 \rangle$ . Par conséquent, chaque germe  $\gamma$  peut donner par maillage quatre grains  $\gamma$  d'orientations différentes, ces quatre variantes ne partageant pas de relation de macle entre elles. L'orientation de l'une des quatre variantes est celle de l'autre germe  $\gamma_n^T$ . Par conséquent, la première génération comporte six variantes  $\gamma$  et chaque variante  $\gamma$  de la première génération participe au processus de maillage et donne la deuxième génération qui a 18 variantes différentes. Le processus continue ainsi de génération en génération. Un diagramme schématique du processus de maillage est donné en Figure 3. 7. Par conséquent, ayant la connaissance de l'orientation d'un grain parent  $\alpha$ , la texture  $\gamma$  de la phase massive peut être simulée à chaque génération. Afin de valider ce calcul de texture, il a été effectué sur un ensemble d'orientations de grains  $\alpha_2$  obtenues à partir d'une carte d'EBSD. Les grains  $\gamma_m$  se sont formés aux joints de grain  $\alpha/\alpha$  mais la transformation n'est pas totale et il subsiste de la phase  $\alpha$  au centre des grains. La carte d'EBSD utilisée pour le calcul est montrée à la Figure 5. 1 (a). Sur cette carte, nous pouvons voir qu'il y a sept orientations différentes de  $\alpha_2$  qui participent à la production de  $\gamma_m$ . Les analyses des cartes d'EBSD prouvent qu'il y a jusqu'à 2 générations de  $\gamma_m$  qui se sont formées avec très peu de variantes s'étendant jusqu'à la troisième génération.



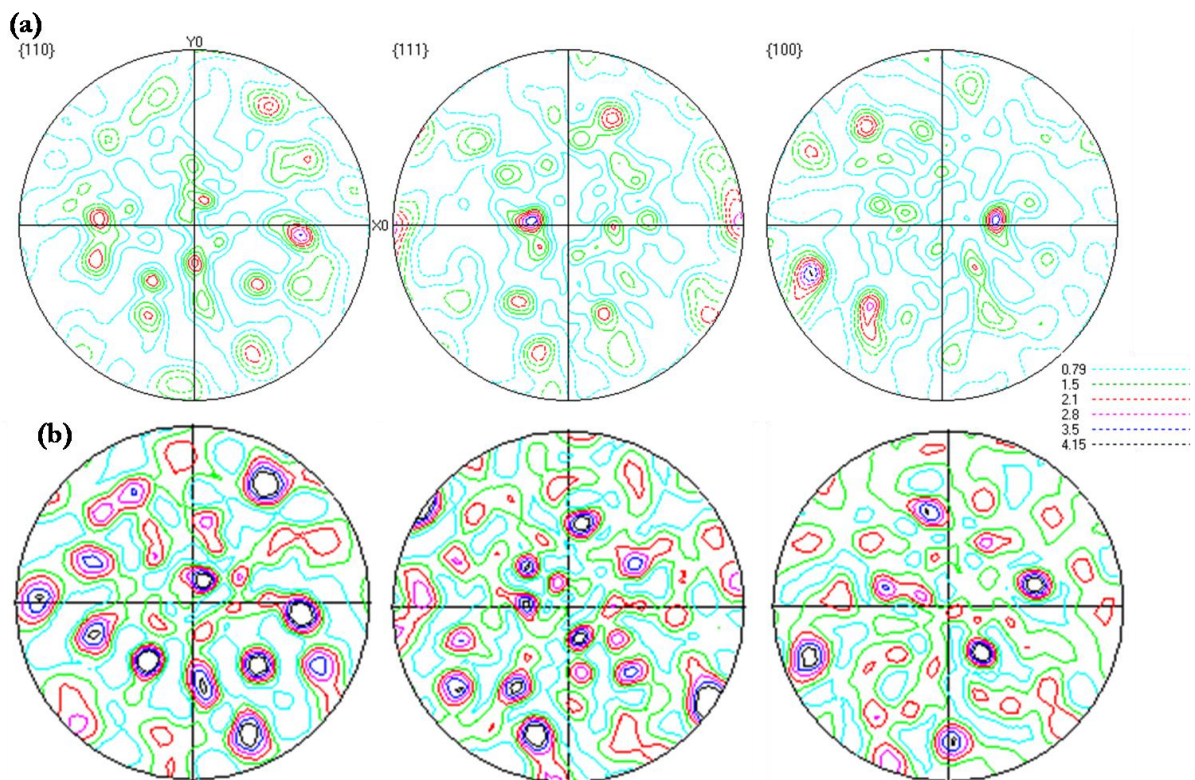
**Figure 5. 1:-** (a) carte d'EBSD utilisée pour calculer la texture locale de la phase  $\gamma$ .  
 (b) Contraste de bande EBSD de la phase avec théoriquement calculé l'orientation  $\gamma$ . La zone orange correspond aux grains  $\gamma$  dont les orientations ont été déduites du calcul théorique, les lignes rouges correspondent aux joints de macle et les lignes noires dénotent les interfaces entre phases  $\alpha/\gamma$ .

Le calcul des différentes orientations des grains  $\gamma$  a été effectué jusqu'à la deuxième génération. Ces orientations théoriques ont ensuite été rentrées dans le logiciel EBSD Channel 5 avec une tolérance en termes de désorientation de  $3^\circ$ . La carte EBSD est donnée dans la Figure 5. 1 (b). Il est évident sur cette carte qu'il est possible de retrouver presque toutes les orientations des variantes  $\gamma$  à partir des orientations calculées théoriquement. On voit des grains non-indexés partager une frontière de macle avec des grains indexés, ce qui s'expliquerait par le fait que ces grains appartiennent à la troisième génération de variantes  $\gamma$ , laquelle n'a pas été prise en compte dans le calcul..

Pour le calcul des figures de pôles, la même fraction volumique a été attribuée à toutes les orientations  $\gamma$  résultant de chaque grain  $\alpha$ . L'étude précédente a montré que, parmi les différents sites de germination des grains  $\gamma_m$ , les joints triples étaient les sites préférentiels. Par conséquent, dans ce calcul tous les joints triples ont été considérés comme prenant part au processus de germination. Les joints de grains n'ont pas été considérés, puisque seulement 15% d'entre eux participent à la germination. Le processus de germination dans cette carte particulière est expliqué schématiquement par le diagramme de la Figure 5. 2. Dans cette configuration particulière, le grain central  $\alpha^7$  donne un ensemble de germes six fois, alors que chacun des grains  $\alpha^{1\text{ à }6}$  ne donne un germe que deux fois. Ainsi, les variantes issues du grain  $\alpha^7$  sont pondérées d'un facteur trois par rapport aux variantes venant des autres grains  $\alpha$ . Les figures de pôles théoriques et calculées sont données dans la Figure 5. 3.



**Figure 5. 2 :-** Représentation schématique montrant la participation des différents grains  $\alpha$  à la naissance des germes  $\gamma$ . Le germe  $\gamma$  et son parent  $\alpha$  sont indiqués par la même couleur



**Figure 5. 3:-** (a) Figures de pôles expérimentales de la phase  $\gamma$  venant de la carte d'EBSD montrée en Figure 5. 1 (a), (b) figures de pôles théoriques calculées à partir de l'orientation des grains  $\alpha$  venant de la carte EBSD.

En comparant le jeu des figures de pôles expérimentales à celui des figures de pôles théoriques, nous pouvons voir que tous les pôles majeurs des figures de pôles expérimentales se retrouvent bien dans les figures de pôles théoriques. En revanche, un certain nombre de pôles apparaissant dans les figures de pôles théoriques ne sont pas



présents dans les figures de pôles expérimentales. Ceci peut être dû au fait que certaines variantes  $\gamma$  ne sont pas présentes sur la surface d'analyse, bien qu'elles puissent être présentes au-dessous ou au-dessus de cette surface. Ceci a été vérifié pendant les investigations tridimensionnelles sur les grains  $\gamma_m$  (annexe D). Par ailleurs, les densités de pôles des deux jeux de figures de pôles sont largement différentes. Ceci vient principalement du mécanisme de sélection de variantes lors de la croissance des grains  $\gamma_m$ . Puisqu'il n'était pas possible d'assigner un poids pour chacune des variantes particulières selon les divers critères de sélection, la simulation de la texture  $\gamma_m$  n'a pas pu être menée plus avant.

## Chapitre VI : Résumé et perspectives

L'objectif principal de ce travail de doctorat est l'amélioration des propriétés intrinsèques des alliages TiAl de manière rentable par des traitements thermiques. Le refroidissement de ces alliages à différentes vitesses à partir du domaine de haute température  $\alpha$  engendre un certain nombre de microstructures complexes, dont la taille de grain est réduite par rapport à celle de la phase  $\alpha$  haute température. Parmi les différentes transformations, la transformation massive, qui se produit pendant la trempe rapide à partir du domaine  $\alpha$ , est celle qui permet d'obtenir la microstructure la plus fine. Peu d'études ont été faites sur l'affinement des grains de l'alliage TiAl brut de fonderie suite à une transformation massive et aux traitements thermiques subséquents. Aussi, l'ambition de cette étude est-elle de contribuer à une compréhension fine et détaillée des mécanismes d'affinement des grains et de réduction de la texture.

L'objectif principal de ma thèse était de faire des caractérisations morphologiques et cristallographiques de la phase massive  $\gamma$  obtenue par trempe rapide depuis le domaine  $\alpha$  et d'étudier leur évolution microstructurale et de texture suite au traitement thermique à différentes températures. Pour ceci, différents alliages ont été sélectionnés pour répondre à ces différents objectifs, et des mécanismes de développement possibles ont été proposés.

### VI. 1. Résultats principaux

Pour l'étude de la formation de la phase massive  $\gamma$ , des échantillons présentant une faible fraction volumique de grains massifs  $\gamma$  ont été sélectionnés. Une analyse soignée de la morphologie et de la cristallographie des petits domaines  $\gamma_m$  se développant le long des joints de grains  $\alpha/\alpha$  et des joints triples par MEB et EBSD a montré qu'il existe toujours un germe  $\gamma_m$  qui présente une Relation d'Orientations de Blackburn, c'est-à-dire  $(0002)_\alpha // \{111\}_\gamma$  and  $\langle 11\bar{2}0 \rangle_\alpha // \langle 110 \rangle_\gamma$  avec son grain parent  $\alpha$ . Puis, il se développe au sein du grain  $\alpha$  opposé. On ne voit pas de germination intragranulaire dans ce cas-ci. La germination le long d'un joint de grains et d'un joint triple est favorisée si le plan du joint de grains est parallèle ou presque parallèle au plan d'habitat. Ceci a été vérifié sur un très grand nombre de cas en

comparant la trace du plan du joint de grains et la trace du plan (0002). Cette condition est appelée : "**critère minimum d'angle**". Une autre configuration pour laquelle un joint de grains peut donner naissance à un germe  $\gamma_m$  est quand le germe a une double relation d'orientation avec le parent et le grain hôte  $\alpha$ . Dans ce cas, la germination se produit des deux côtés du joint de grains puisque le germe doublement facetté peut donner naissance à un grain voisin  $\gamma$  qui a l'un de ses plans  $\{111\}$  étroitement parallèles à l'un des siens. Ce type de germination est nommé "**relation d'orientation proche secondaire**".

Tous les mécanismes proposés ci-dessus ont été validés statistiquement et les sites favorables de germination ont été classés comme suit:

a) a) Le joint triple est considéré comme le site de germination le plus favorable puisque la probabilité de germination avec les critères minimum d'angle est plus grande si il y a trois joints de grains intervenant dans le processus de germination. En outre, une perte plus élevée d'énergie de joint de grains est prévue lors de la germination d'un grain  $\gamma_m$  cohérent.

b) Le joint de grains dont le plan est proche du plan basal d'un des grains voisins  $\alpha$  est considéré comme deuxième site favorable de germination de la transformation massive. Ce critère provient de l'analyse statistique des surfaces sur lesquelles le plan du joint de grain est seulement visualisé par sa trace. Une observation en trois dimensions a aussi été faite à travers une coupe sériée et une reconstruction en 3 dimensions. La configuration observée s'est avérée être en accord avec notre proposition.

c) Le joint de grains pour lequel un germe  $\gamma_m$ , en BOR avec l'un des grains  $\alpha$ , a de surcroît l'un de ses plans  $\{111\}$  quasi-parallèle au plan basal de l'autre grain  $\alpha$ , est considéré comme étant le troisième site favorable pour la germination par ordre décroissant. Le nombre élevé de germes doublement facettés  $\gamma$  observés dans notre cas a été attribué à la texture initiale de l'échantillon qui a favorisé de telles configurations.

Les mécanismes de croissance des grains  $\gamma_m$  sont indépendants des sites de germination. La croissance se produit toujours par maclage successif le long des plans  $\{111\}_\gamma$ . Cela ne signifie pas pour autant que les quatre macles issues d'un germe  $\gamma_m$  sont en relation de macle entre elles. Il semble qu'au cours de la croissance, il y ait une sélection des variantes de maclage. En effet, sur la surface de recherche, on n'observe très souvent que l'un des deux germes possibles. De plus, parmi les variantes de macle possibles, le plus souvent, toutes ne se forment pas, et fréquemment, l'une des variantes est nettement prépondérante. Souvent, les variantes prépondérantes ont un de leurs plans  $\{111\}$  parallèles ou presque parallèles au plan  $\{2-201\}$  du grain hôte  $\alpha_2$ . Une analyse tridimensionnelle sur un domaine  $\gamma_m$  montre que les deux germes et toutes les variantes de macle sont formés, bien qu'ils ne soient pas tous présents sur la même section d'observation. Cependant, cette analyse confirme qu'il y a une variante nettement prépondérante par rapport aux autres.

Les grains  $\gamma_m$  sont fortement métastables, par conséquent ils vont évoluer lors de traitements thermiques à hautes températures. Des mesures de DSC ont été effectuées pour identifier leur température de déstabilisation. L'intervalle de température de déstabilisation s'étend de 500°C à 800°C, c.-à-d. dans le domaine  $(\alpha_2 + \gamma)$ . Les traitements thermiques sur un échantillon massif entièrement transformé montrent que la déstabilisation se produit premièrement par la précipitation de  $\alpha$  sous forme de globules le long de joints de grains  $\gamma/\gamma$  et de joints triples  $\gamma/\gamma/\gamma$ . De nouveau, on observe

systématiquement la Relation de Blackburn entre le précipité globulaire  $\alpha_2$  et l'un des grains  $\gamma$ . On observe généralement différentes orientations de précipités  $\alpha_2$  le long des joints de grains  $\gamma_m$  car ces derniers sont très irréguliers. Bien qu'il n'ait pas été statistiquement validé pour cette transformation, le "critère minimum d'angle" semble s'appliquer aussi dans ce cas.

Le traitement thermique dans le domaine ( $\alpha_2 + \gamma$ ) ou ( $\alpha + \gamma$ ) active également un autre type de germination pour la précipitation de  $\alpha$ . De longs platelets sont formés à l'intérieur des grains  $\gamma_m$ , en BOR avec leur grain hôte. Ils se développent sur la longueur entière du grain ou peuvent être arrêtés par d'autres platelets orientés différemment. Parfois, les quatre orientations possibles des platelets  $\alpha_2$  sont présentes à l'intérieur du grain  $\gamma$ , mais le plus souvent, une des orientations des platelets  $\alpha_2$  est dominante, formant une structure rappelant la structure lamellaire.

Un grain  $\alpha$  produit un nombre élevé de variantes de macles grâce à la transformation massive, il est donc logique de supposer que cela réduira la texture cristallographique issue du procédé de solidification. La mesure de la texture sur un échantillon massif obtenu à partir d'une microstructure brute de fonderie confirme clairement cette réduction de texture, bien que la texture initiale du matériau utilisé dans ce travail ait été malheureusement plutôt faible. Les traitements thermiques suivants effectués dans différents domaines de phase ont également eu comme conséquence de réduire encore davantage la texture  $\gamma$ . De toutes les microstructures obtenues dans cette étude, celle appelée "M-duplex", qui a été obtenue par traitement thermique des grains massifs pendant deux heures dans le domaine  $\alpha + \gamma$ , est celle qui présente la texture la plus isotrope et qui a la dureté la plus élevée.

A partir de la connaissance des mécanismes de transformation et des relations d'orientation, il est a priori possible de prévoir la texture finale résultant de traitements thermiques complexes, si ces traitements thermiques sont précisément connus. Comme exemple, une tentative a été faite pour calculer la texture massive  $\gamma_m$  connaissant l'orientation d'un ensemble de grains  $\alpha$  à partir d'une carte d'EBS. Bien que les tendances générales soient reproduites, on observe toujours des variations entre les figures de pôle mesurées et calculées. Ceci s'explique par la sélection des variantes lors de la croissance apparaissant à cette échelle. Le calcul de texture à partir d'informations plus globales serait certainement plus précis.

## VI. 2. Perspectives

Ce travail de doctorat a mis en lumière plusieurs questions qui nécessitent une attention particulière concernant les mécanismes cristallographiques et la transformation des grains massifs ainsi que leur évolution après traitement thermique. Cette étude a ouvert des portes sur d'autres questions qui doivent être traitées.

- L'existence de relations d'orientation possibles entre des grains à croissance rapide  $\gamma_m$  (variantes dominantes) avec leurs grains hôtes  $\alpha$  a été évoquée. L'analyse HRTEM des joints d'interface entre des grains plus grossiers  $\gamma_m$  et leur hôte  $\alpha$  pourraient nous apporter quelques réponses sur les mécanismes de sélection de variantes pendant la croissance.

- Lors des recherches sur les surfaces bidimensionnelles, certaines variantes de croissance n'étaient pas présentes, alors qu'elles ont été mises en évidence dans des coupes sériées. Cela pose un point d'interrogation sur la fiabilité des caractérisations bidimensionnelles. Avec l'arrivée de nombreuses techniques de caractérisation microstructurale tridimensionnelles, il est devenu nécessaire de revenir sur les premiers résultats proposés..
- Dans ce travail, la réduction de la texture par la transformation massive et les traitements thermiques ultérieurs crée une légère ambiguïté puisque la texture initiale n'était pas très forte. Par conséquent, il est important de vérifier nos conclusions dans le cas d'un alliage de TiAl ayant une forte texture de solidification.
- Pendant la formation des grains massifs par la trempe rapide, une quantité non négligeable de fissures s'est formée. Ceci est évidemment gênant au regard de l'utilisation potentielle de ces microstructures dans diverses applications industrielles. La solidification rapide permet d'éviter les transformations de phase avec diffusion. Mais l'ajout de certains éléments d'alliage comme Ta et Nb permet d'obtenir une microstructure 100% massive pour une vitesse de refroidissement plus lente. Un autre mode de traitement peut être de tremper l'échantillon pour l'amener à une température suffisamment haute pour limiter le comportement fragile de l'alliage mais suffisamment basse pour conserver la force motrice pour que la transformation massive se produise.
- En raison de la présence de fissures, les propriétés mécaniques des grains massifs et des microstructures obtenues par traitement thermique ont été mesurées seulement par des essais de dureté. Il est important de connaître d'autres propriétés structurales comme sa résistance à la traction, sa résistance au fluage et sa ductilité. Par conséquent, il est important d'étudier les propriétés mécaniques et les mécanismes de déformation principaux des microstructures massives et de celles qui ont subies des traitements thermiques ultérieurs.

## Références

- [Adachi- 2005] Adachi Y, Hakata K, Tsuzaki K, "Crystallographic analysis of grain boundary Bcc-precipitates in a Ni-Cr alloy by FESEM/EBSD and TEM/Kikuchi line methods", *Mat. Sci. Eng A*, 2005; 412: 252.
- [Bartels- 2001] Bartels A, Schillinger W, "Micromechanical mechanism of texture formation in  $\gamma$ -TiAl, *Intermetallics*" 2001; 9: 883.
- [Bartels- 2002] Arno Bartels, Heinrich Kestler, Helmut Clemens, "Deformation behavior of differently processed  $\gamma$ -titanium aluminides" *Mater. Sci. Eng. A*, 2002; 329-331: 153.
- [Bartolotta- 1999] Bartolotta PA and Krause DL, "Titanium Aluminide Applications in the high speed civil transport", NASA/TM-1999-209071.
- [Blackburn- 1970] Blackburn MJ, "The science, Technology and Applications of Titanium", Plenum Press, Newyork, 1970; 3: 633.
- [Boyer- 1994] Boyer R, Welsch G, Collings EW "Materials properties Handbook: Titanium Alloys, ASM International, 1994: 1009.
- [Bunge- 1982] Bunge HJ, "Texture analysis in materials science", Butterworths, London.
- [Charpentier- 2003] Charpentier M, "Heteroginities héritées de la solidification formation des microstructures dans l'alliage Ti- 48Al- 2Cr-2Nb : Contribution au développement des alliages intermétalliques de base  $\gamma$ -TiAl", Ecole Nationale Supérieure des Mines de Nancy, France, Ph. D. Thesis, 2003.
- [Chen- 1999] Chen G L, Zhang L. C, Zhang W. J, "Microstructural stability of lamellar TiAl-based alloys at high temperature" *Intermetallics*, 1999; 7: 1211.
- [Cheng- 2000] Cheng T T, "The mechanism of grain refinement in TiAl alloys by boron addition- an alternative hypothesis" *Intermetallics*, 2000; 8: 29.
- [Clemens-2002] Clemens H and Kestler H, "Processing and applications of Intermetallic  $\gamma$ -TiAl- based alloys", *Advanced Engineering Materials*, 2000; 2: 551.
- [Clemens- 2006] Clemens H, Bartels A, Bystrzanowski S, Chladil H, Leitner H, Dehm G, Gerling R, Schimansky FP, "Grain refinement in  $\gamma$ -TiAl-based alloys by solid state phase transformations", *Intermetallics*, 2006; 14: 1380.
- [Dey- 2006] Dey SR, "Crystallography and phase transformation mechanisms in TiAl-based intermetallic alloys" Paul Verlaine Univeriste – Metz, France, PhD. Thesis- 2005.
- [Hawbolt- 1970] Hawbolt EB and Massalski TB, "Massive transformations revisited" *Metall. Trans.* 1970; 1: 2315.

- [Howe- 2002] Howe JM, Reynolds WT, Vasudevan VK Metall. Mater. Trans. A, 2002; 33A:2391.
- [Hu-2005] Hu D, Wu X, Loretto MH, "Advances in optimization of mechanical properties in cast TiAl alloys" Intermetallics, 2005; 13: 914.
- [Hu- 2007] Hu D, Huang AJ, Wu X, "On the massive phase transformation regime in TiAl alloys: The alloying effect on massive/lamellar competition" Intermetallics, 2007; 15: 327.
- [Huang –a – 1989] Huang S.C U.S Patent 4.879.092, 1989
- [Huang –b – 1989] Huang SC, Siemers PA, "Characterization of high temperature phase fields near stoichiometric  $\gamma$ -TiAl" Metallurgical Transactions A, 1989; 20: 1899.
- [Huang- 1993] Huang SC, "Alloying considerations in gamma-based alloys" In: R. Darolia, J. Lewandowski, C.T. Liu, P. Martin, D. Miracle and M. Nathal, Editors, *Structural Intermetallics*, TMS, Warrendale, PA , 1993: 299.
- [Huang- 1994] Huang SC, Chesnutt JC "Gamma TiAl and its alloys", Intermetallics Compounds, Principles and Practice, Wiley New York, 1995; 2: 73.
- [Jones- 1993] Jones SA and Kaufman MJ, "Phase equilibria and transformations in intermediate titanium- aluminium alloys" Acta Metall. Mater, 1993; 41: 387.
- [Kelly- 1999] PM Kelly and M-X Zhang, "Edge-to-Edge Matching – A New Approach to the Morphology and Crystallography of Precipitates" Mat.Forum 1999; 23:41.
- [Kelly- 2006] PM Kelly and M-X Zhang "Edge-to –edge matching- The Fundamentals" Metall and Mater. Trans.2006; 37: 833.
- [Kim- 1997] Kim MC, Oh MH, Lee JH, Inui H, Yamaguchi M, Wee DM, Composition and growth rate effects in directionally solidified TiAl alloys, Mater. Sci. Eng., A, 239-240 (1997) 570-576.
- [Kumagai- 1997] Kumagai T, Abe E, Takeyama M, Nakamura M, "Microstructural evolution of massively transformed  $\gamma$ -TiAl during isothermal aging", Scripta Mater. 36 (1997) 523-529.
- [Lee-a-1975] Lee JK and Aaronson HI, "Influence of faceting upon the equilibrium shape of nuclei at grain boundaries-I. Two dimensions" Acta Metall. 1975; 23: 799.
- [Lee-b-1975] Lee JK and Aaronson HI, "Influence of faceting upon the equilibrium shape of nuclei at grain boundaries-I. Three dimensions" Acta Metall. 1975; 23: 809.
- [Lefebvre-2002] Lefebvre W, Loiseau A, Thomas M, Menand A, "Influence of oxygen on the  $\alpha \rightarrow \gamma$  massive transformation in a Ti-48 at% Al alloy" Phil. Mag. A,

- 2002; 82: 2341.
- [Mahajan- 1997] S. Mahajan, C. S. Pande, M. A. Imam, B. B. Rath, "Formation of annealing twins in f.c.c. crystals" *Acta Mater.*, 1997; 45: 2633.
- [Massalski- 1958] Massalski TB, "The mode and morphology of massive transformations in Cu---Ga, Cu---Zn, Cu---Zn---Ga and Cu---Ga---Ge alloys" *Acta Metall.* 1958; 6: 243.
- [Massalski- 1984] Massalski TB, "Distinguishing features of massive transformations" *Metall. Mater.Trans.A*, 1984; 15A: 421.
- [Massalski- 2002] Massalski TB, "Massive transformations revisited" *Metall. Mater.Trans.A*, 2002; 33A:2277.
- [Miller- unknown] Miller TM, Wang L, Hofmeister WH, Wittig JE, Anderson JM, "Site occupancy determination by ALCHEMI of Nb and Cr in  $\gamma$ - TiAl and their effects on the  $\alpha$  to  $\gamma$  massive phase transformation"
- [Naka- 1996] Naka A, "Advanced titanium-based alloys", *Current opinion in solid state and materials science*, 1996; 1: 333.
- [Ott- 1999] Ott EA, Pollock TM, "Development and structure of  $\alpha_2$  plates in  $\gamma$ -based titanium aluminides due to the  $\gamma$  to  $\alpha$  transformation on heating", *Scripta Mater.*, 1999; 40: 899.
- [Phillips- 1930] Phillips A. *Trans, AIME*, 1930 ; 89 : 194.
- [Prasad- 2003] Prasad U, Chaturvedi MC, "Influence of alloying elements on the kinetics of massive transformation in gamma titanium aluminides" *Metall. Mater.Trans.A*, 2003; 34A: 2053.
- [Reynolds- 2003] Reynolds Jr. WT, Nie JF, Zhang WZ, Howe JM, Aaronson HI, Purdy GR, "Atomic structure of high-index  $\alpha_2$  :  $\gamma$ m boundaries in a Ti-46.54 at.% Al alloy" *Scripta Mater.* 2003; 49 : 405.
- [Schuster- 2006] Schuster JC and Palm M, "Reassessment of binary Aluminium-Titanium phase diagram", *Basic and Applied Research: Section I*, 2006; 27: 255.
- [Thomas- 2005] Thomas M, Raviart JL, Popoff F "Cast and PM processing development in gamma aluminides" *Intermetallics*, 2005; 13: 944.
- [Veegaraghavan- 1999] Veeraraghavan D, Ping Wang, Vasudevan VK, "Kinetics and thermodynamics of the  $\alpha \rightarrow \gamma_m$  massive transformation in a Ti-47.5 at.% Al alloy", *Acta Mater.* 1999; 47: 3313.
- [Veegaraghavan- 2003] Veeraraghavan D, Wang P, Vasudevan VK, " Nucleation kinetics of the  $\alpha \rightarrow \gamma_M$  massive transformation in a Ti-47.5 at% Al alloy", *Acta Mater.* 2003; 51: 1721.
- [Wang- 2002] Wang P, Veeraraghavan D, Kumar M, Vasudevan VK, " Massive-parent interphase boundaries and their implications on the mechanisms of the  $(\alpha) \rightarrow (\gamma(m))$  massive transformation in Ti-Al alloys"



- Metall. Mater. Trans. A, 2002, 33A: 2353.
- [Wu- 2006] Wu Xinhua “Review of alloy and process development of TiAl alloys” *Intermetallics*; 14: 1114.
- [Zhang- 1999] Zhang WJ, Chen GL, Evangelista E, “Formation of alpha phase in the massive and feathery gamma-TiAl alloys during aging in the single alpha field”, *Metall. and Mater. Trans. A*, 1999; 30A: 2591.
- [Zghal- 1997] Zghal S, Naka S, Couret A, “A quantitative TEM analysis of the lamellar microstructure in TiAl based alloys” *Acta Mater.*1997; 45:3005.

# Annexes

Appendix A1  
Materials and Methods

# Materials and Methods

I. Introduction.....	2
II. Materials Elaboration and Heat Treatments.....	2
II. 1. Materials used.....	3
II. 2. Heat treatments.....	4
II. 3. Thermal stability measurements.....	5
III. Characterization techniques.....	6
III. 1. Metallographic Preparation.....	6
III. 2. Phase Determination.....	7
III. 3. Microstructure characterisation.....	8
III. 3. 1. Optical Microscopy.....	8
III. 3. 2. Scanning Electron Microscopy.....	9
III. 3. 2. 1. Phase determination and Quantification.....	9
III. 3. 3. Transmission Electron Microscopy.....	10
IV. Crystallography and Texture analysis.....	10
IV. 1. Global Texture measurement.....	12
IV. 1. 1. X-Ray Diffraction.....	12
IV. 2. Local Texture Analysis.....	16
IV. 2. 1. Electron Back Scattering Diffraction (EBSD).....	16
IV. 2. 1. 1. Acquisition of EBSD maps.....	17
IV. 2. 2. Three dimensional investigation of $\gamma$ grains and $\alpha/\alpha$ grain boundaries.....	19
IV. 2. 2. 3. Grain evolution analysis after different heat treatments.....	20
IV. 2. 2. Crystallographic analysis using TEM.....	21
IV. 2. 2. 1. Orientation and Crystallographic relationship determination.....	21
V. Mechanical properties determination.....	22
VI. References.....	23

## I. Introduction

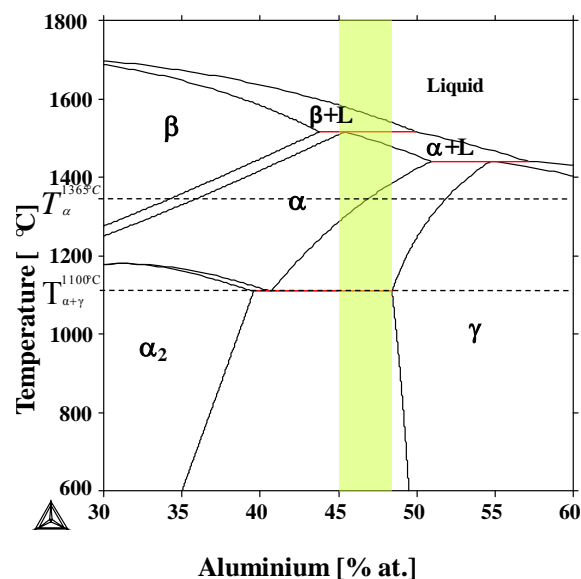
In this chapter, discussion about the materials used for the study, along with the different characterization techniques used to study them is elaborated. The experimental procedures used includes, several heat treatments, microstructural characterization, crystallographic orientation analysis, thermal stability investigation and study of mechanical properties using various techniques.

For this PhD study, two different TiAl-based alloys were used. A Large part of the study was done using a TiAl alloy with composition Ti-48-Al-2Cr-2Nb (at %). This alloy was first patented by Huang S-C for GENERAL ELECTRIC [Huang -1989] and hence also known as GE alloy. This alloy gives the best compromise between room temperature ductility and oxidation resistance.

The Nb content in a TiAl alloys is added depending on the oxidation resistance required. When GE alloy was introduced, the application targets were set for room temperature usage, such as low- pressure turbine blades from jet engines and exhaust valves for passenger vehicles, therefore oxidation resistance has not been a particular priority [Tetsui-2002]. However for high temperature applications such as turbochargers for passenger vehicles, oxidation resistance at high temperature is a necessity. Higher Nb content TiAl alloy provides a solution for this problem. Our second alloy studied has a composition of Ti-45.5Al-7Nb-0.2C. This alloy was provided by TURBOMECHA, during a collaborative project, for which different characterization techniques were used to characterize the microstructure of the alloy.

## II. Materials Elaboration and Heat Treatments

Both the alloys used for this study is a near  $\gamma$ -TiAl alloy. A part of the phase diagram belonging to  $\gamma$ -TiAl alloys is shown in Figure 1.



**Figure 1:-** Partial phase diagram of  $\gamma$ -TiAl alloy.

At room temperature, they have two stable phases: a  $\gamma$  phase which has a face centered tetragonal  $\gamma$  structure and  $\alpha_2$  phase which has an ordered Hexagonal Close Packed (HCP) structure. But the volume fraction of each phase depends on the composition of the alloy.

## **II. 1. Materials used**

### **GE Alloy:**

Alloy with composition Ti-46.8Al-1.7Cr-1.8Nb (at %), produced by two different processing techniques were used for the study. The alloy produced by investment casting was in the form of cylindrical bars with 16 mm diameter and 230 mm height. Chemical homogenization and compactness of these bars were achieved by further hot isostatic pressing (Hipping) at 1250°C and 125 MPa for 4 hours, followed by a heat treatment in furnace under vacuum at 1270°C for 24 hours. This as-cast GE-alloy was provided by ONERA. The microstructure which will be termed as 'as-cast microstructure' consists of columnar dendrites with  $\alpha_2 + \gamma$  lamellar grain, and patches of  $\gamma$ -monolithic grains in between.

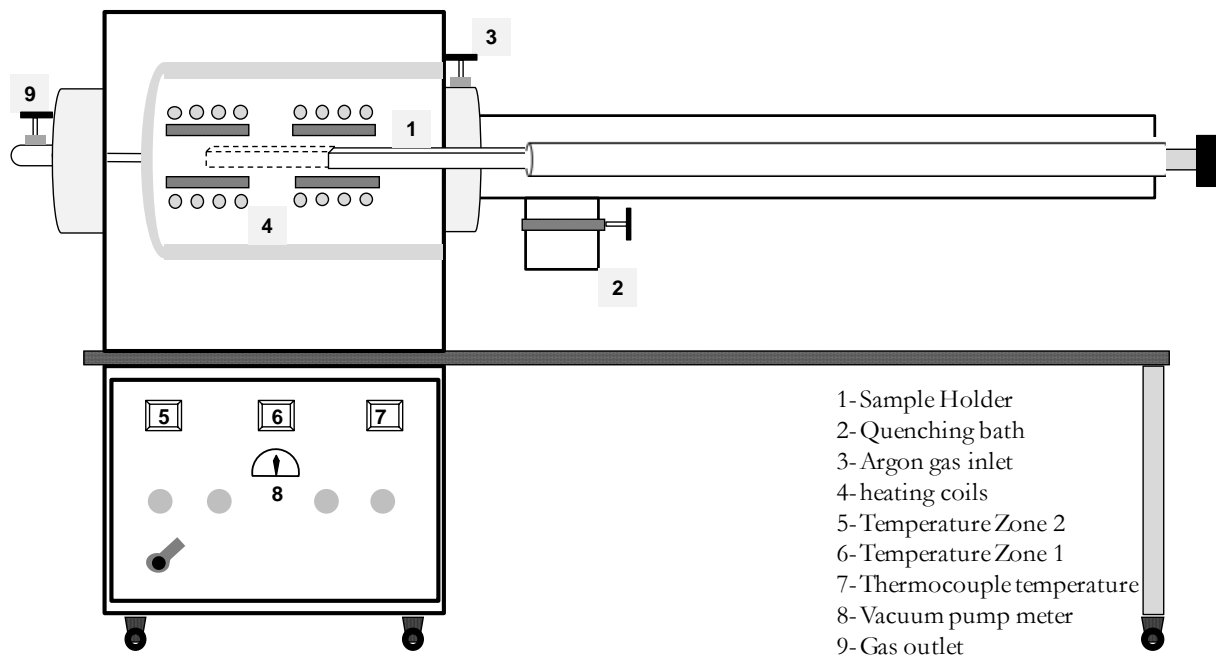
The second technique used for producing the GE alloy is by powder metallurgy. Cylinders with 60 mm diameter and 50 mm height were provided by ONERA. They were compacted at a temperature of 1300°C. The microstructure mainly consists of  $\gamma$ -monolithic grains with the  $\alpha_2$  formed along the grain boundaries and triple points of the  $\gamma$  grains.

### **Alloy with High Nb:**

Alloy with composition Ti- 45% Al-8%Nb-0.2%C (at %) were provided by TURBOMECA. The alloy with 60 mm diameter and 10 mm height was produced by the process of investment casting and then high temperature extrusion. The microstructure mainly consists of  $\gamma$ -monolithic with  $\alpha_2$  phases interspaced between the  $\gamma$  grains.

## **II. 2. Heat treatments**

All the heat treatments made during this study were done on a PYROX furnace, which was tailor made to meet the demands of our laboratory. A schematic representation of the furnace is given in Figure 2. The furnace is fitted with a molybdenum sample holder and the maximum working temperature is 1500°C. The furnace consists of two zones which can be maintained at two different temperatures at a difference of 300°C. The samples can be introduced and isolated from the furnace manually and at any temperature. The sample temperature is given by an S-type thermocouple soldered to the sample holder; the sample is placed as close as possible to the thermocouple to have the actual temperature of the sample. The furnace is also fitted with a quenching bath as can be seen from the figure. This quenching bath is separated from the body of the furnace by a valve. The sample when treated at high temperature can be immediately retreated and can be turned down to be quenched in the quenching bath. For all the heat treatment carried out, the furnace was first vacuumed up and then purged with Ar, three times and the heating were carried out with continuous flow of Ar. The sample dimensions and the heating program is given in Table 1. For the first heat treatment, the samples were heated at a heating rate of 5°/min until the  $T_\alpha$  temperature of 1365°C [Charpentier -2003]. The slow heating rate was chosen in order to avoid re-precipitation of  $\alpha$  or the  $\alpha_2$  laths inside the initial  $\gamma$  microstructure [Ott-1999].



**Figure 2:-** Schematic representation of the Furnace used for the heat treatments

At 1365°C, the samples were treated to an isothermal heat treatment for 15 min, and immediately quenched in 'Brine ice water' kept in the quenching bath, which was maintained at a temperature of around -5°C. The brine water quenched samples were again subjected to different heating programs for the study and the details are given in Table 1.

**Table 1:-** Different alloys used and different heat treatments performed for the study

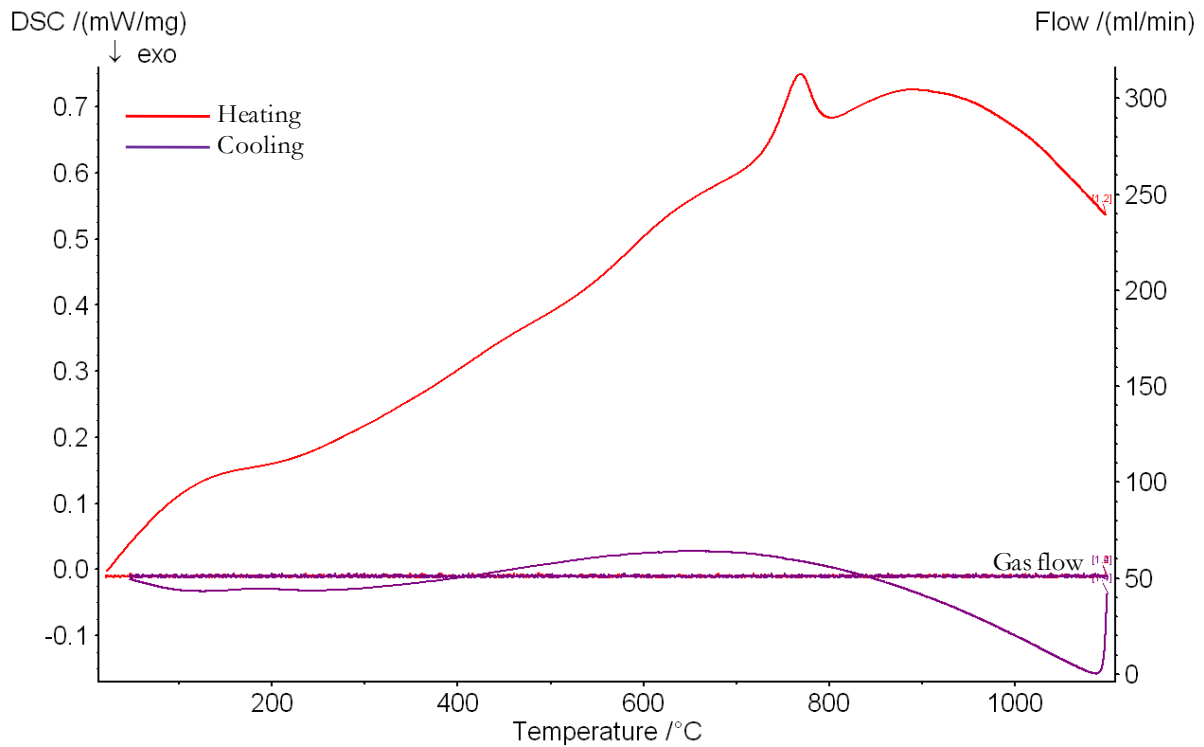
Alloys with composition	As-received samples and its dimensions	Processing conditions of the as-received sample	First heat treatment	Further processing	
				Temperature	Cooling conditions
<b>Ti- 45 Al- 8Nb-0.2C (at%)</b>	Disc with 60 mm diameter and 10mm height	Investment casting + High temperature extrusion	Constant heating rate of 5°/ min up to 1365, isotherm for 15 min, Quenching in Brine Ice water ( $\approx 5^{\circ}\text{C}$ )		
<b>GE alloy Ti- 46Al- 1.7Cr- 1.8 Nb (at %)</b>	Bar with 16 mm diameter and 230 mm height	Investment casting + HIPping at 1250°C, 125 MPa, 4hrs)	Constant heating rate of 5°/ min up to 1365, isotherm at this temperature for 15 min, Quenching in Brine Ice water ( $\approx 5^{\circ}\text{C}$ )	(a) 1050°C, isotherm for 2hrs	Air quenched
				(b) 1250°C, isotherm for 2hrs	Air quenched
	Bar with 60 mm diameter and 50 mm height	Compacted at 1300°C	Constant heating rate of 5°/ min up to 1365, isotherm at this temperature for 15 min, Quenching in Brine Ice water ( $\approx 5^{\circ}\text{C}$ )	(a) 900°C, isotherm for 30 sec	Air quenched
				(b) 1100°C, isotherm for 30 sec	Air quenched
				(c) 1100°C, isotherm for 20 min	Air quenched

### **II. 3. Thermal stability measurements**

The initial microstructures obtained from the heat treatments were highly metastable. Therefore, the stability of these microstructures was studied by a Differential Scanning Calorimetry (DSC) **DSC-404C** provided by NETZSCH systems. This is a technique in which the difference in energy input between the specimen of interest and a reference material is measured as a function of temperature, while the specimen of interest and the reference materials are subjected to a controlled temperature program. A high temperature furnace was used, which has a temperature range from Room Temperature (RT) to 1500°C.



The crucible used was a Pt-Rh/ $\text{Al}_2\text{O}_3$  crucible system and the thermocouple is a S-Type. Since the crucible has a diameter of 5mm and height 4mm, samples were prepared to fit in crucible. Powdered alumina was used as the reference material, approximately weighing the same as the sample. The system was purged with Argon for three times before performing the experiments with a continuous flow of Argon.



**Figure 3:-** DSC curve obtained from a metastable microstructure (massive+ untransformed  $\alpha_2$  microstructure) in a TiAl alloy.

An example is shown in Figure 3. The analysis is done on a metastable microstructure containing high temperature untransformed  $\alpha_2$  and  $\gamma$  phase. The sharp transformation at around 800°C corresponds to the de stabilization of the untransformed  $\alpha_2$  phase.

### III. Characterization techniques

Under this section, various characterization techniques used in this study, along with the sample preparation procedures for each characterization techniques is briefed.

#### III. 1. Metallographic Preparation

As a first step of metallographic preparation, all the samples were mechanically polished with an emery paper (Silicon carbide SiC granule paper), up to No. 4000 (granule size: 5 $\mu\text{m}$ ) followed by polishing with two different diamond paste with granule sizes, 3 $\mu\text{m}$  and 1 $\mu\text{m}$  respectively. After this initial sample preparation, the samples were etched with different etchant depending on the microscopes and techniques used.

For X-Ray Diffraction (XRD), the metallographically prepared samples, polished up to the diamond paste, can be used for the measurement.

For the initial characterization, optical microscopy was used. The mechanically polished samples were etched using modified Kroll's reagent (67% H<sub>2</sub>O (distilled), 23% H<sub>2</sub>O<sub>2</sub>, 7% HF (90% purity), 3% HNO<sub>3</sub>) [Charpentier -2003], for about 10 seconds. This reagent attacks the  $\gamma$  phase in the TiAl alloy rather than the  $\alpha_2$  phase, thereby helping us to discriminate the phase boundaries.

For higher magnification imaging, Scanning Electron Microscopy (SEM) was used. The mechanically polished sample was electropolished using an electrolytic solution of 90% Methanol and 10% perchloric acid. '**Struers Lectropol-5**' was the machine used for the electro polishing. The electrolyte was maintained at a temperature of 4°C and 17V was used for a polishing time of 70 sec. The electro polished samples were equally good for viewing under Back Scattered Electron (BSE) mode and for using Electron BackScatter Diffraction (EBSD) technique. In order to have a better phase contrast, electro polishing was not used, for this the samples were mechanically polished in a solution containing 70% OPS (colloidal solution of silica) and 30% hydrogen peroxide and rinsed repetitively with acetone and ethanol to be viewed under the microscope.

For higher magnification images, and precise and detailed information, Transmission Electron Microscopy (TEM) studies were carried out. TEM analysis demands for thin foils that are electron transparent. Therefore the samples were mechanically thinned up to 40 $\mu$ m thickness and 3mm circular discs were punched out. These discs were then polished using an electrolytic solution of 60 % Methanol, 35 % ethylene glycol and 5 % perchloric acid, until a small perforation appears in the centre of the sample. A '**Struers Tenupol-3**' twin jet polisher was used for polishing the discs using an operating voltage of 17V. The electrolyte was always maintained under sub-zero temperature. Certain samples that had numerous external defects in the material like cracks could not be prepared just by electro polishing, but were also ion milled. For ion milling, a Gatan Model 691 precision ion polishing system was used, with the working voltage of 3keV, the angle of two the ion guns maintained at 10°/10°. The sample was milled for a time of 30 mins.

### **III. 2. Phase Determination**

For the initial phase determination, XRD was used. The measurements were carried out using a texture goniometer called 'FSM' developed by LETAM. It uses an INEL detector. This detector allows us to measure the X-Ray Diffractogram within the range of 10° to 120. The X-ray beam produced, is passed through a Fe filter to allow Co-K $\alpha$  radiation with wavelength  $\lambda = 1.789 \text{ \AA}$ . The step size used in the  $2\theta$  direction is 0.05° and the integration time for each step is 5.00 sec.

An example of X-Ray diffraction pattern is given in Figure 4. This diffractogram is taken from the sample with high Nb. The indexed phases are the  $\gamma$ -TiAl phase which had a Face centred tetragonal structure and the  $\alpha$ -Ti<sub>3</sub>Al phase, which had a Hexagonal Closed packed (HCP) structure.

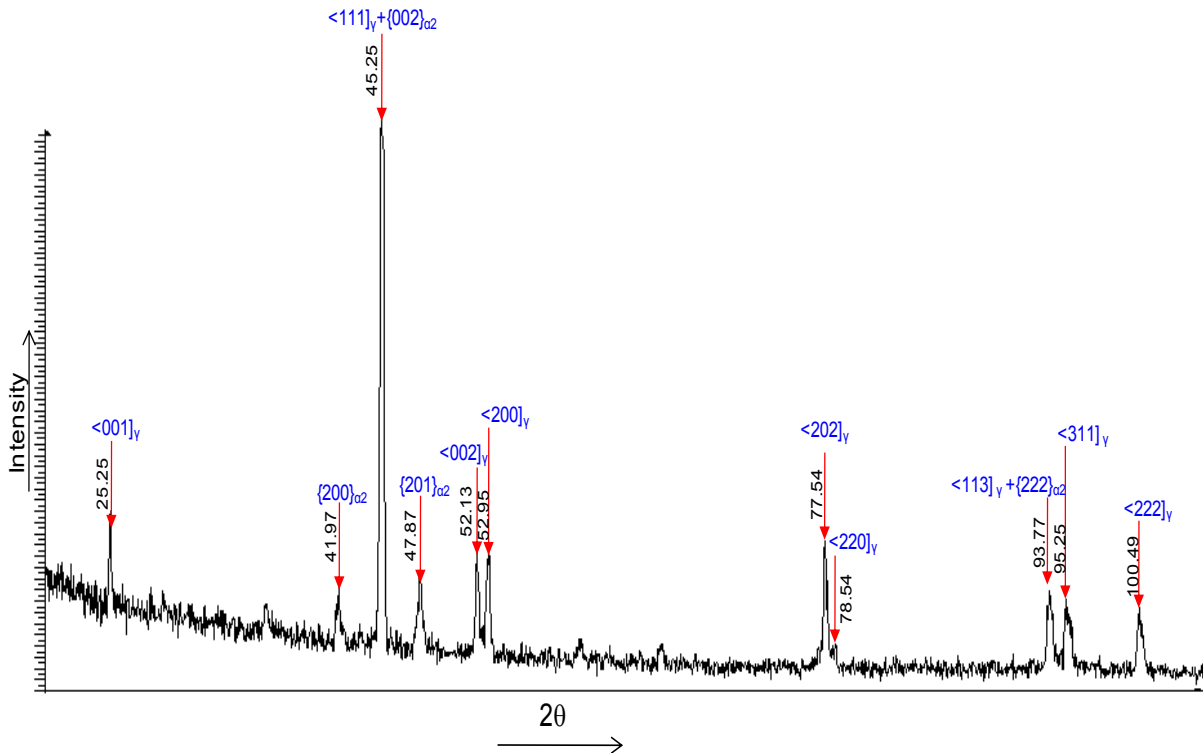


Figure 4:- X-Ray Diffractogram measured on high-Nb sample

### III. 3. Microstructure characterization

#### III. 3. 1. Optical Microscopy

The chemically etched samples are investigated under an optical microscope 'OLYMPUS BX61'. It uses a polychromatic light to reveal the microstructure depending on the type of etching and sample preparation. Figure 5 shows an example of an etched microstructure obtained from the as-cast GE alloy. The  $\gamma$ -monolithic grains and the lamellar grains are clearly distinguishable, although, the phase contrast between  $\gamma$  and the  $\alpha_2$  is not quite clear.

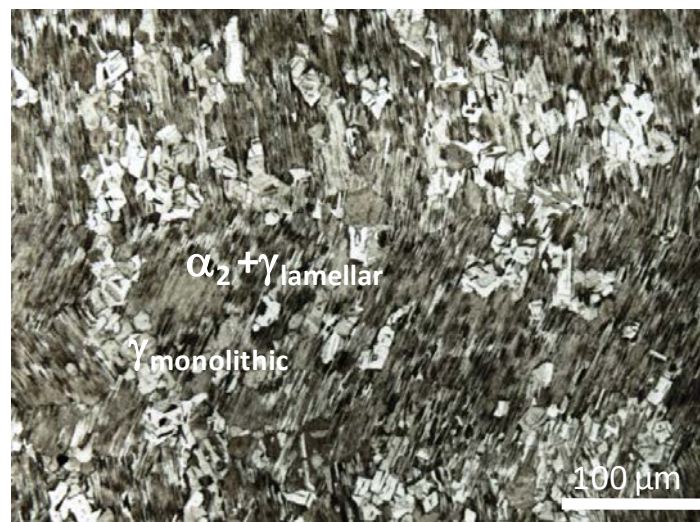


Figure 5:- Optical micrograph of GE alloy showing an as-cast microstructure

### **III. 3. 2. Scanning Electron Microscopy**

A 'JEOL JSM-6500F' Scanning Electron Microscope (SEM) equipped with a Field Emission Gun (FEG) was used from the microstructural imaging. FEG offers finer resolution and higher electron beam density than the conventional SEM. For microstructural imaging two different modes are available.

**Secondary electron imaging (SEI):** This is the best mode used to obtain higher resolution images having fine topological features.

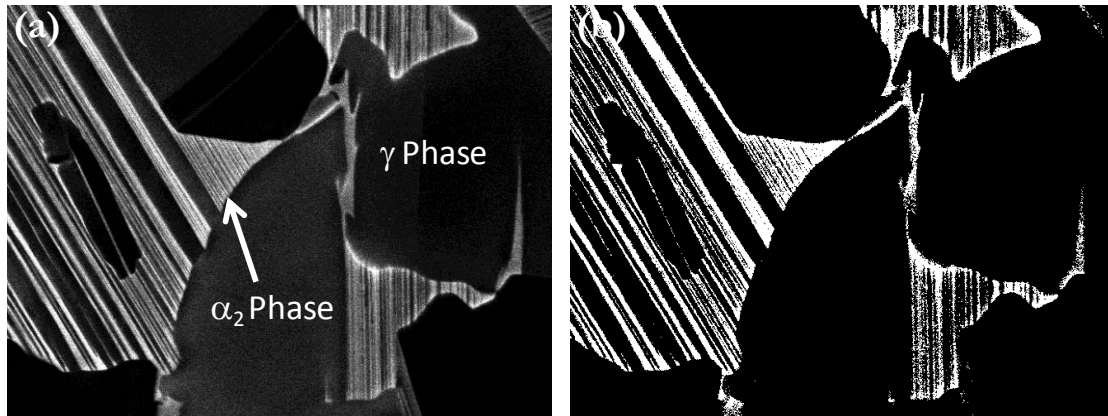
**Back Scattered Electron (BSE):** In this mode the detector collects the back scattered electrons reflected from the sample by the elastic scattering. This mode was used mainly for the orientation and composition or phase contrast.

**Working Conditions:** The general working conditions used for both the modes are the same. The accelerating voltage used is 15kV, and the probe current is 3 nA for a spot value of 13. The working distance is the distance between the electron gun and the sample and is mostly maintained at 10 mm. Depending on the information required during the microstructural imaging, the accelerating voltage, the probe current and the working distance were adjusted.

#### **III. 3. 2. 1. Phase determination and Quantification**

Backscattered electrons (BSE) consist of high-energy electrons originating in the electron beam that are back-scattered out of the specimen interaction volume by elastic scattering interactions with specimen atoms. Since heavy elements (high atomic number) backscatter electrons more strongly than light elements (low atomic number), and thus appear brighter in the image, BSE are used to detect contrast between areas with different chemical compositions [Goldstein-1981]. In a TiAl alloy a  $\alpha_2$  ( $\text{Ti}_3\text{Al}$ ) phase therefore will appear brighter than at  $\gamma$  phase (TiAl). The distinction between, the  $\alpha_2$  and  $\gamma$  phase is made by 'APHELION' image treatment software.

Figure 6 shows an example of a BSE micrograph treated by APHELION. This is a micrograph taken from the sample with high Nb. After the treatment of the image, the software gives a black and white image of the  $\alpha_2$  and  $\gamma$  phase. Sometimes due to the grey level transition (which is generally the  $\gamma$  phase, but can arise due to the change in orientation) some errors on the estimation can happen. Therefore to minimize the errors, 25 images with the magnification 5000 x was taken and processed.



**Figure 6:-** An example of a BSE micrograph treated to have the volume fraction of different phases using the APHELION software (a) Initial image (b) treated black-white image.

### III. 3. 3. Transmission Electron Microscopy

A 'PHILIPS CM200' Transmission Electron Microscopy with the maximum working voltage of 200 kV has been used of the study. The microscope is equipped with a 'Gatan CCD camera' and an image analysing software 'Digital Micrograph' was provided along with, for treating the images taken.

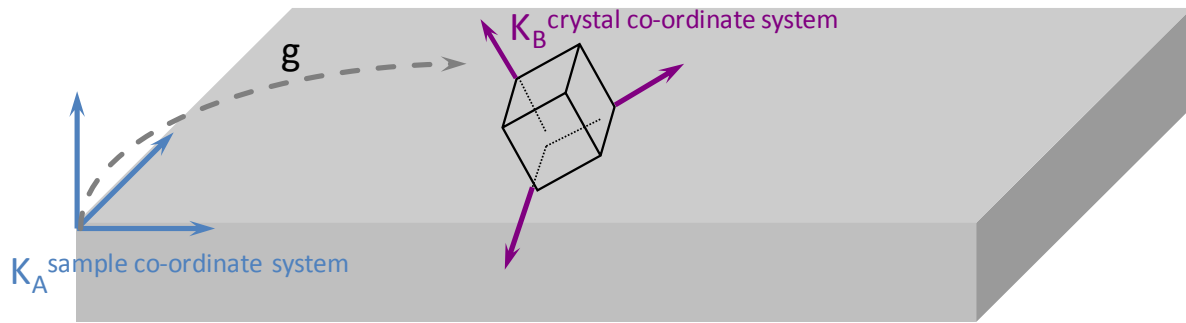
### IV. Crystallography and Texture analysis

This work mainly deals with the crystallographic characterization and texture studies of given TiAl alloys. The behaviour of the materials in terms of mechanical properties strongly depends on the texture of the material. Therefore, for this study different methods and crystallographic techniques has been used. X-ray diffraction analysis is a well known technique for qualitative study of a sample texture. This method is mainly used for global texture measurement.

The most often technique used in this study is Electron Backscattered Diffraction (EBSD). The texture along with the grain orientations and size of the grains can be automatically obtained by EBSD. A small introduction is given about this technique in the later part of this section. The third technique used is the crystallographic analysis through TEM. Although, TEM and EBSD-SEM related techniques deals mainly with local texture analysis.

#### **Texture:**

Texture is the distribution of crystallographic orientations of a sample. Depending on the preferred orientations of the grains in a material, the strength of the texture is termed as weak, strong or moderate. A polycrystalline material consisting of one or several phases is an aggregate of many grains of different orientations. The statistics of the orientation of grains, called crystallographic texture, is very important in terms of its effects on the anisotropic properties of the material [Bunge-1982]. The orientation of a certain grain can be defined by specifying different co-ordinate systems. Figure 7 shows two co-ordinates systems taken into consideration, one is the sample co-ordinate system ( $K_A$ ) and the second is the crystal co-ordinate system ( $K_B$ ).



**Figure 7:-** Relationship between the sample co-ordinate system and the crystal co-ordinate system

The co-ordinates of  $K_A$  depend on the sample geometry and its processing technique. While,  $K_B$  depends on the crystal co-ordinate having its axes taken on the basis of the symmetry of the considered crystal system. For example in a cubic crystal system, the axes  $K_B$  coincides with the  $\langle 100 \rangle$ ,  $\langle 010 \rangle$  and  $\langle 001 \rangle$  crystallographic directions. Whereas, in a hexagonal crystal system, the  $K_B$  axes coincides with  $\langle 10\bar{1}0 \rangle$ ,  $\langle \bar{1}2\bar{1}0 \rangle$  and  $\langle 0001 \rangle$  crystallographic directions.

The rotation of the crystal co-ordinate with respect to the sample co-ordinate is defined by a parameter ' $g$ '. For the same orientation there exist a set of equivalent rotations:

$$\{S_i \cdot g\}$$

Where  $\{S_i\}$  corresponds to the rotational symmetry elements of the chosen crystal group symmetry.

The rotation can be represented in different manners. The rotation  $g$  represented most conventionally and is used in present thesis, is explained below.

Euler angles as represented by [Bunge-1982] is given by

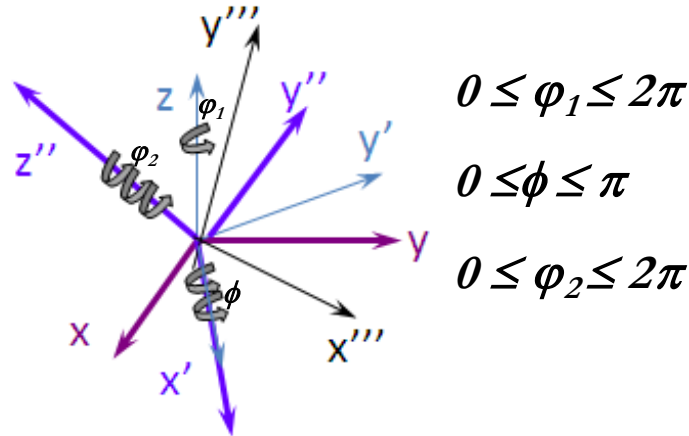
$$\text{Euler angles } g = \{\varphi_1, \Phi, \varphi_2\}$$

$\varphi_1$ - Rotation along the  $z$  axis: transforms  $x$  and  $y$  into new directions  $x'$  and  $y'$ .

$\Phi$ - Rotation along the  $x'$ : transforms  $x'$  and  $y'$  into new directions  $x''$  and  $y''$ .

$\varphi_2$ - Rotation along  $z''$ : transforms  $x''$  and  $y''$  into new directions  $x'''$  and  $y'''$ .

A schematic representation of the Bunge representation is shown in Figure 8.



**Figure 8:- Euler angle definition.**

The second type of representation of the component 'g' is by matrix representation. The matrix  $M(g)$  defines the vector needed to coincide the  $K_B$  co-ordinate with the  $K_A$  co-ordinate.

$$V_{KA} = M(g) \cdot V_{KB}$$

$$M(g) = \begin{pmatrix} c_1 c_2 - s_1 s_2 c & -c_1 s_2 - s_1 c_2 c & s_1 s \\ s_1 c_2 + c_1 s_2 c & -s_1 s_2 + c_1 c_2 c & -c_1 s \\ s_2 s & c_2 s & c \end{pmatrix}$$

Where:

$$c = \cos \Phi \quad s = \sin \Phi$$

$$c_1 = \cos \varphi_1 \quad s_1 = \sin \varphi_1$$

$$c_2 = \cos \varphi_2 \quad s_2 = \sin \varphi_2$$

In the present study, the Euler angles are represented in pole figures. A pole figure is a graphical representation of the orientation of specific crystals in space. Pole figures in the form of stereographic projections are used to represent the orientation distribution of crystallographic lattice planes.

#### **IV. 1. Global Texture measurement**

Two techniques were used for the global texture measurement. Grains with smaller grains (less than 100 $\mu$ m), X-ray diffraction goniometer was used, and for samples with larger grain sizes a method called multiple mapping in EBSD was used.

##### **IV. 1. 1. X-Ray Diffraction**

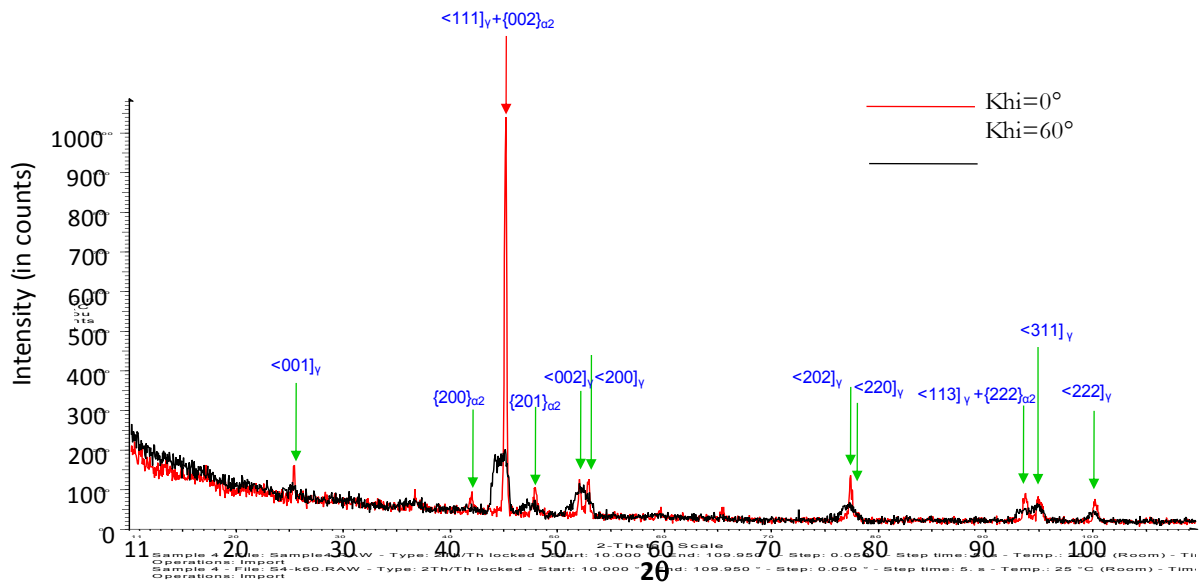
Two different goniometer's were used depending on the size of the sample. Their measurement specifications are given in Table 2.

**Table 2:-** Parameters used for the pole figure measurement depending on the sample requirements

Microstructure	Apparatus Type	Detector	Radiation	Step Size	Area scanned
As-Cast	Self built goniometer based on a Microcontrol-Nex port cradle and a RIGAKU rotating anode	INEC	Cu-K $\alpha$ ( $\lambda = 1.54\text{\AA}$ )	Azimuth: 5° Declination 5°	$\phi$ 0.8 mm x 5mm (on each face (ref. Fig 2) totally six faces)
Massive Massive + 1050°C Massive + 1250°C	Self- built Huber Goniometer	LYNXEYS Brucker	Co-K $\alpha$ ( $\lambda = 1.789\text{\AA}$ )	Azimuth: 5° Declination 2.5°	$\phi$ 0.8 mm x 10mm (on three different area)

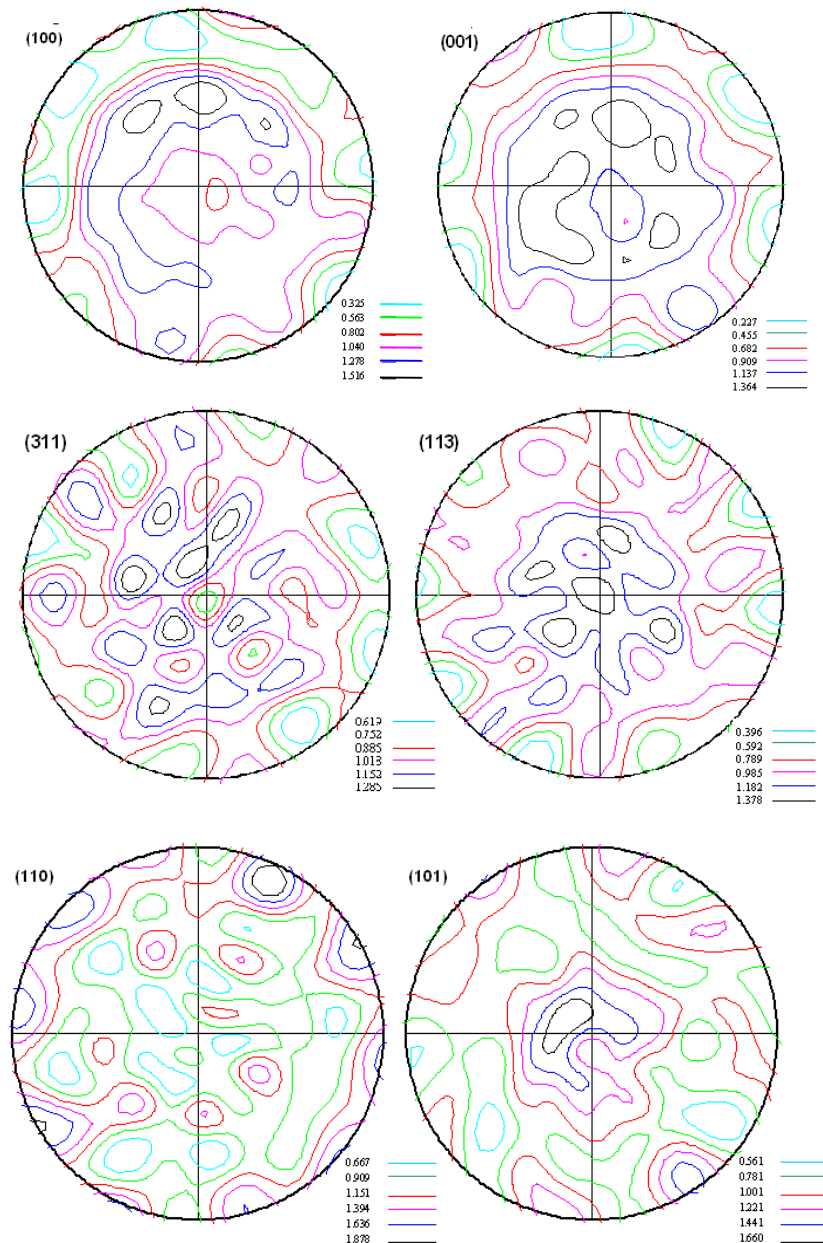
The declination angle was from 0° to 80° and the azimuth angle was from 0° to 360°. The duration of the measurement depends on the type of results required. The detector from the Huber goniometer is a curved detector covering a large range of  $2\theta$  angles. Thus the information from different planes can be calculated in one run. While for the INEC detector, the information from each plane is collected separately, therefore more time is required, but one can use samples of any sizes as we can adjust the sample-detector distance. From the Figure 4 one can see certain planes like (202) and (220), (113) and (311) have their  $2\theta$  angles very close to each other because of the tetragonality of the  $\gamma$  phase with it is  $c/a \sim 1$ . Although they are quite distinguishable when the  $\chi$  (declination angle) value is 0°, the peaks starts broadening when the  $\chi$  value increases. An example is show in Figure 9 (Here the two XRD patter taken at  $\chi = 0^\circ$  and  $\chi = 60^\circ$  is overlapped). This leads to erroneous and non-exact determination of texture at higher azimuth values. In order to overcome the above explained problem, a new technique has been developed for X-ray pole figure measurement [Juan-2007]. In this method, instead of measuring a broad range of X-ray diffracted spectra at different  $\chi$  angles, intensities of spectra at smaller regular intervals of  $2\theta$  values at each azimuth angle were recorded. Later on, these several measured intensities at smaller steps of  $2\theta$  values in different azimuth angles were integrated to produce the separate pole figures. This method not only distinguishes the two closely placed crystallographic planes, but also generate their texture separately. One of the main disadvantages of this method is, it is very time consuming. While the conventional method takes 16hrs to finish the texture measurement, this method takes nearly 52 hrs to complete texture measurement for one sample.





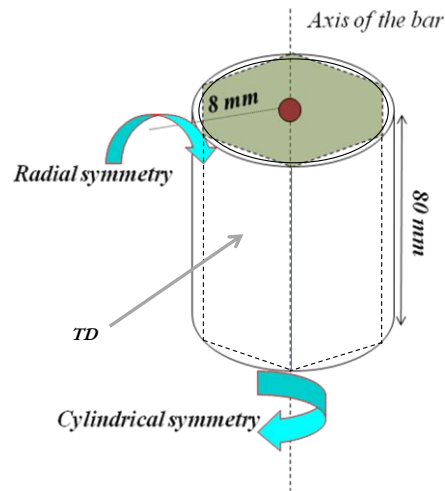
**Figure 9:-** Super imposed XRD pattern taken at  $K\chi_i = 0^\circ$  and  $K\chi_i = 60^\circ$ .

An example of calculated pole figures measure by this method is shown in Figure10. These pole figures were measured on the sample with high-Nb. With the tetragonal symmetry of the  $\gamma$  phase, at least four pole figures measurements are required to reconstruct and recalculate the pole figures. Calculated pole figures of  $\{100\}$ ,  $\{001\}$ ,  $\{311\}$ ,  $\{113\}$ ,  $\{110\}$ , and  $\{101\}$  are shown in Figure10.



**Figure 11:-** Calculated pole figures of High-Nb TiAl alloy

During the measurement of the as-cast sample, the conventional measurement of the pole figures was difficult, owing to their large grain size. The  $\gamma$  grain size of the as-cast columnar grains had a maximum grain size of 1mm on the surface perpendicular to the bar axis and the grain size along the tangential direction is around 30  $\mu\text{m}$ . Therefore, the cylindrical bar was cut at their border, making six faces forming a hexagon. This is schematized in Figure 11. The pole figures were measured along the tangential planes and they are measured six times along six different tangential planes. Assuming that all the tangential planes are equivalent because of the cylindrical specimen symmetry, the pole figures, represented in a tangential plane, are obtained by the integration of the six measured pole figures.



**Figure 11:-** Schematic diagram of the pole figure measurement done on as-cast sample.

## **IV. 2. Local Texture Analysis**

Two different techniques were used for the local texture analysis.

The first one is a technique called the EBSD whose principle is explained later is coupled with the SEM which allows us to obtain the crystallographic information of the sample locally with the help of diffraction patterns called the Kikuchi patterns [Schwarzer-1993].

The second technique is orientation determination by the transmitted Kikuchi patterns in TEM. In both cases Kikuchi patterns serve as the base for finding the crystallographic information from the sample.

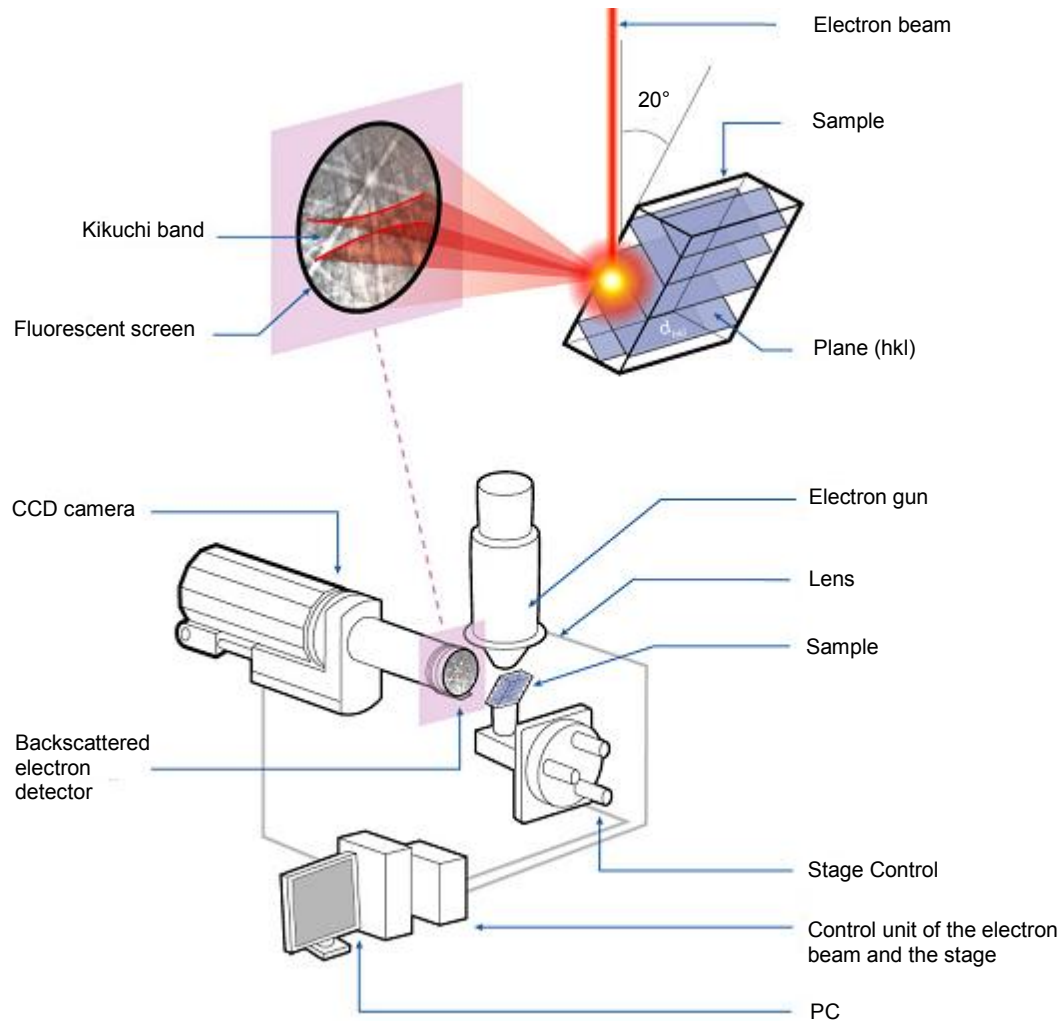
### ***Kikuchi lines:***

Kikuchi lines are formed in diffraction patterns by diffusely scattered electrons, e.g. as a result of thermal atom vibrations. The main features of their geometry can be deduced from a simple elastic mechanism proposed in 1928 by Kikuchi [Kikuchi-1928], although the dynamical theory of diffuse inelastic scattering is needed to understand them quantitatively. Because each Kikuchi line is associated with Bragg diffraction from one side of a single set of lattice planes, these lines can be labeled with the same Miller or reciprocal-lattice indices that are used to identify individual diffraction spots. Kikuchi band intersections, or zones, on the other hand are indexed with direct-lattice indices i.e. indices which represent integer multiples of the lattice basis vectors **a**, **b** and **c**.

### **IV. 2. 1. Electron Back Scattering Diffraction (EBSD)**

Electron Backscatter Diffraction (EBSD) is a technique which allows crystallographic information to be obtained from samples in the scanning electron microscope (SEM). In EBSD a stationary electron beam strikes a tilted, highly polished crystalline sample and the diffracted electrons form a Kikuchi pattern on a fluorescent screen. Figure 12 is a schematic representation of an EBSD set-up and how it is measured. The angle between the incident electron beam and the specimen normal is tilted to 70° to have better quality of Kikuchi patterns captured by the EBSD camera. This pattern is characteristic of the crystal structure and orientation of the sample region from which it was generated. The diffraction pattern

can be used to measure the crystal orientation, measure grain boundary misorientations, discriminate between different materials, and provide information about local crystalline perfection. When the beam is scanned in a grid across a polycrystalline sample and the crystal orientation measured at each point, the resulting map will reveal the constituent grain morphology, orientations, and boundaries. This data can also be used to show the preferred crystal orientations (texture) present in the material. A complete and quantitative representation of the sample microstructure can be established with EBSD. Knowing the crystal structure of the phase and feeding it into the software, an automatic indexing of the Kikuchi bands in Hough space, are achieved through the software routine.



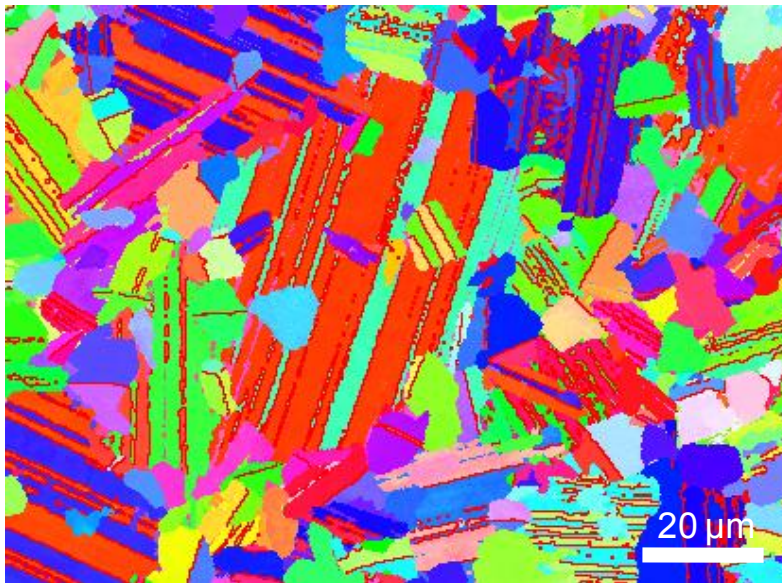
**Figure 10:-** Principle of EBSD technique [Germain -2005].

#### **IV. 2. 1. 1. Acquisition of EBSD maps**

To characterize the spatial resolution of the sample in co-relation with the microstructure, the EBSD system uses a mapping mode with the electron beam moving with respect to a pre-defined grill on the analyzed surface. The step size (which is also the pixel size) of the moving electron beam determines the resolution of the EBSD map. For measuring larger surfaces, it is necessary to acquire a number of maps by moving the stage on which the sample is fixed. These multiple maps are then stitched together to form an EBSD map. Each pixel or point in the grill has its corresponding Kikuchi pattern acquired and

indexed corresponding to its crystal structure. An indexed Kikuchi pattern has its coordinates, crystal structure, and corresponding orientation being saved.

An example of a high resolution EBSD map is show in Figure 11. The general working conditions during the map acquisition is similar to the SEM working conditions except for the working distance. The working distance used during the study for all the sample is 15 mm and the camera distance is 188.8 mm. the Hough resolution value is 70 and six to eight number of band detections was found sufficient to avoid any kind of mis-indexation between the two phases present. The step size used for this measurement is 0.3 $\mu\text{m}$ . The map after measurement can be treated and represented depending on the information need.



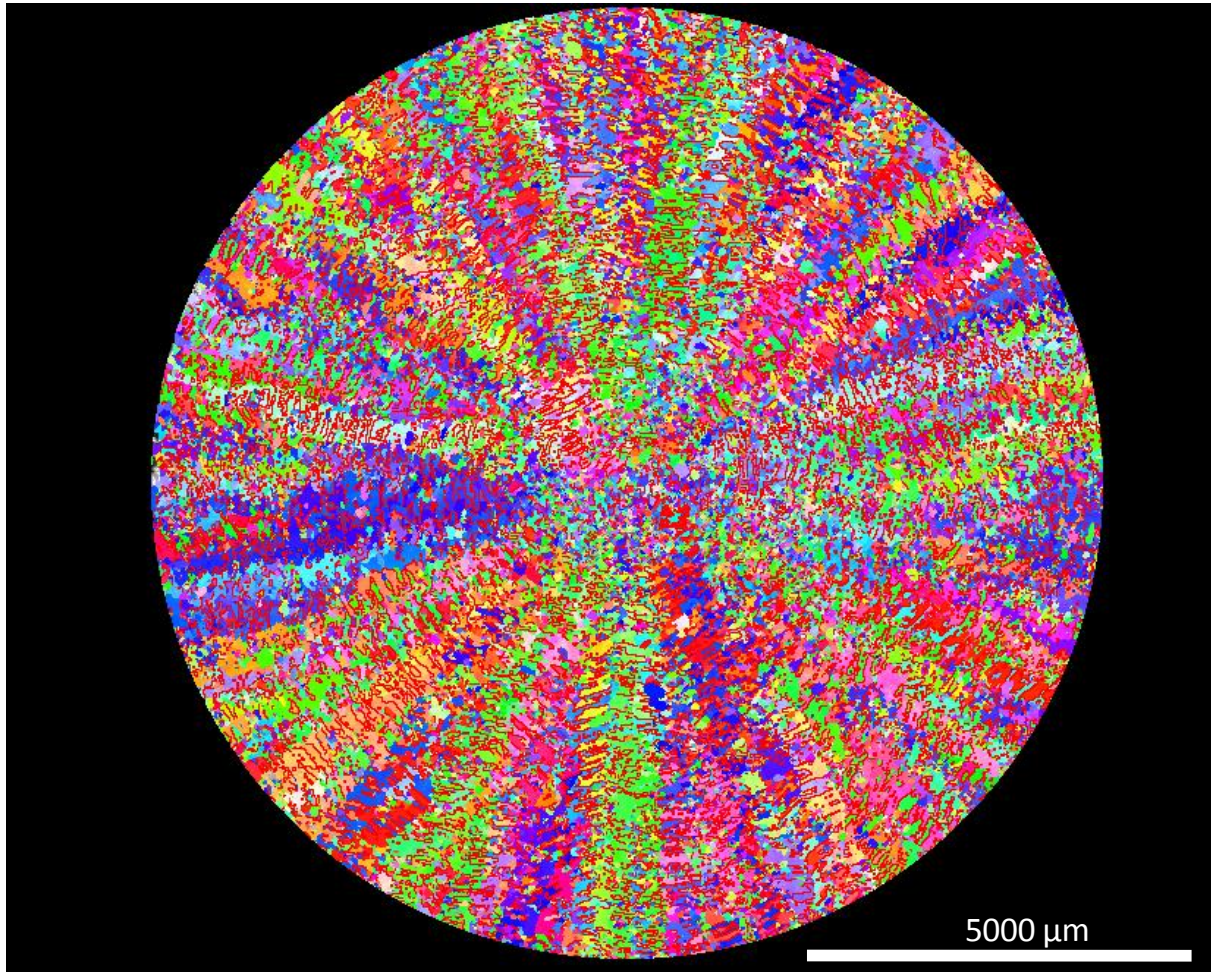
**Figure 11:-** High resolution EBSD of a duplex microstructure in high-Nb TiAl alloy.

The technique of EBSD is also used to map very large areas with the help of multiple mapping methods when it is difficult to obtain the texture of a sample by conventional XRD methods. This might be the case when the grain sizes are  $>100\mu\text{m}$ . The best example for using the EBSD technique for measuring the texture is in the case of as-cast sample as show in Figure 12. Here the complete sample is mapped with a step size of 19  $\mu\text{m}$ . A total of 180 maps were taken and stitched together. The figure is represented in inverse pole figures mode.

#### **Disadvantages:**

Although the technique of EBSD offers a number of advantages, there in one disadvantage which forces us to use other techniques for more precise crystallographic analysis. The two principle phases present in at  $\gamma$ -TiAl alloy is a  $\gamma$  phase which is tetragonal having the c/a ratio 1.016 and the  $\alpha_2$  phase a hexagonal close packed structure with its c/a ratio 0.8005. Crystallographically when the transformation from the  $\alpha^{\text{disordered}}$  and  $\alpha_2^{\text{ordered}}$  to the  $\gamma^{\text{ordered}}$  phase takes place every orientation of  $\alpha$  or  $\alpha_2$  can give rise to six different orientation of  $\gamma$ . These six orientation of  $\gamma$  are distinguished from each other with the help of their sub- lattice bands. The conventional mapping method in EBSD does not allow indexing these sub-lattice bands due to its too low signal/noise ratio and angular resolution. Instead,

we can only differentiate them as a set of two cubic variants, twin related to each other. Although it is possible to index all the six variants with the help of EBSD-SEM technique which has been demonstrated by [Pouchou-2002]. Compromising between various parameters like voltage, spot size, number of reflectors, acquisition time and camera distance, the sub-lattice bands can be indexed, although the time used for this type of indexation is very long.



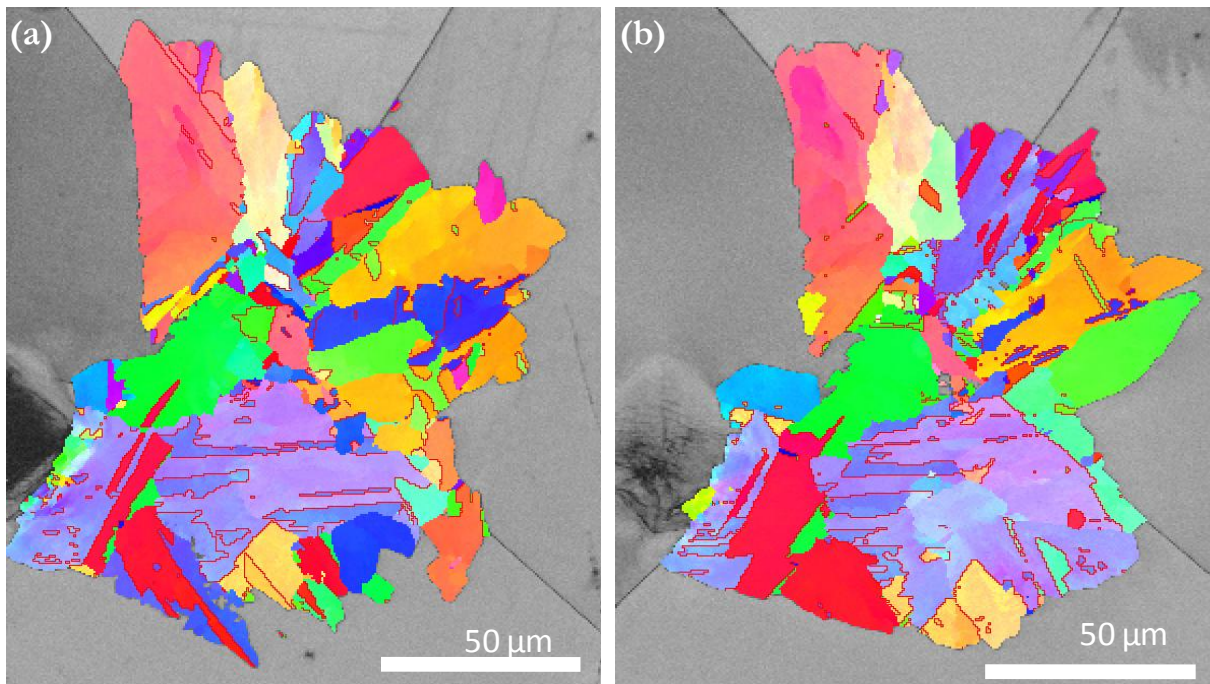
**Figure 12:-** Multiple mapping of a TiAl alloy with as-cast microstructure.

#### **IV. 2. 1. 2 Three dimensional investigation of $\gamma$ grains and $\alpha/\alpha$ grain boundaries**

In order to have information about the grain boundary plane and the grain evolution, several sectioning of the sample were performed. EBSD was used for the mapping of each section to have the orientation information and BSE images were also taken to avoid any experimental errors like slight rotation that could be formed because of the 70° tilt for the EBSD analysis. Two types of indentation were made on a sample prepared by OPS polishing to be viewed under SEM. An area was chosen closer to intent for mapping. After the first mapping, the sample was polished with a **Buehler Vibratory polisher**. A detailed explanation on this method is given in Appendix A2.

An example of an EBSD map done on GE-alloy is shown in Figure 13. The initial EBSD map before polishing and the final map taken after polishing up to certain depth is shown.

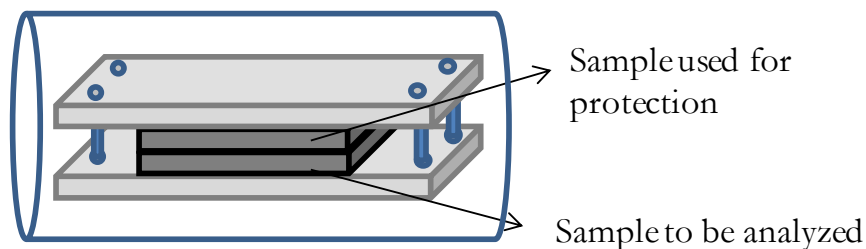
The maps are represented in Inverse pole figure mode and the colored grain represents the  $\gamma$  grains. The change in grain morphology is very evident when comparing the two maps.



**Figure 13:-** EBSD micrograph of a set of  $\gamma$  and  $\alpha_2$  taken at different depths. (a) Initial section (b) section at a depth of  $\approx 12 \mu\text{m}$ .

#### **IV. 2. 1. 3 Grain evolution analysis after different heat treatments**

During the second heat treatments performed in the GE alloy as can be seen from Table 1, the  $\gamma$  grains and the  $\alpha$  grain grains evolve itself at different temperature owing to the metastability of the microstructure obtained from the first heat treatment. In order to analyze the microstructure at different temperature, first the sample to be analyzed was polished OPS to be viewed under SEM. Two indentations were made using a Vicker's indenter, and EBSD maps were measured around this indent. Then another sample of the same size, from the same alloy with the same sample dimension was polished and placed over in order to prevent oxidation. Both the samples were then sandwiched with the help of two plates and screwed together. This set-up was then inserted inside a quartz tube and was purged with Argon. A schematic diagram of the set-up is show in Figure 14. The quartz tube was then placed in the furnace and heat treated at  $1100^\circ\text{C}$  for 20 min and air cooled. After the heat treatment, EBSD map was measured on the same area by tracing out the indents.



**Figure 14:-** Schematic representation of the set-up used for grain evolution studies.

## **IV. 2. 2 Crystallographic analysis using TEM**

Higher resolution studies on crystallographic and phase transformation can be achieved with the help of Transmission Electron Microscopy (TEM). A Philips CM200 TEM equipped with a CCD camera was used to analyze the transmitted Kikuchi patterns and were indexed automatically with the help of software called Euclid's Phantasies (EP). The detail about the software and the functionality is given elsewhere [Fundenburger-2003]. The acquired Kikuchi patterns are processed and filtered to be indexed by EP. It detects the Kikuchi bands through Hough transformation and then finally indexes them. The angular resolution is  $\approx 0.2^\circ$ .

### **IV. 2. 2. 1. Orientation and Crystallographic relationship determination:**

During this study, the technique of TEM was used for two purposes.

1. To determine the different orientation of the  $\gamma$  phase
2. To determine the volume fraction of  $\gamma$  and  $\alpha_2$  phase in the case of very fine lamellar structure.

The  $\gamma$  phase due to its tetragonality gives rise to six different orientations while transforming from the  $\alpha$  phase using Blackburn Orientation Relationship. All the  $\gamma$  lamellae share a twin orientation relationship with each other. Therefore in order to identify the orientation relationship between the  $\gamma/\alpha_2$  phase, first the grain boundary plane is made vertical i.e., exactly parallel to the transmitted beam. This can be identified from the interference fringes present in the grain boundary along the  $\gamma/\alpha_2$  and the  $\gamma/\gamma$  lamellae. When these fringes disappear, then we can say that the grain boundary plane is vertical. In this configuration, the diffracted Kikuchi patterns are taken from  $\gamma$  and  $\alpha_2$  phase. The six different variants of  $\gamma$  are distinguished from the presence of their sub-lattice bands as can be seen from Figure 15. These patterns are indexed with the help of the EP software; a detailed explanation about this method is given by [Dey -2005].

The lamellar structures in the duplex structures are very fine, owing to the faster rate of cooling from the  $\alpha+\gamma$  domain. To calculate the volume fraction of the  $\gamma$  and the  $\alpha_2$  phase in the lamellar structure using the APHELION software from the BSE images is quite difficult. Therefore, TEM was used to calculate the volume fraction of the  $\alpha_2$  phase in a lamellar grain. For this purpose, the grain boundary plane was made vertical to the transmitted beam and the  $\gamma$  and the  $\alpha_2$  phase was indexed for several lamellar grains and their volume fraction was deduced. An example of the TEM micrograph used for the volume fraction determination is given in Figure 15.





## VI. References

- [Bunge – 1982] H.J. Bunge: “Texture analysis in materials science”, Butterworths, London.
- [Charpentier -2003] M. Charpentier: “Heterogenities héritées de la solidification formation des microstructures dans l’alliage Ti-48Al-2Cr-2Nb: Contribution au developement des alliages intermétalliques de base  $\gamma$ -TiAl”, Ecole Nationale Supérieure des Mines de Nancy, France, Ph.D. Thesis, 2003.
- [Dey – 2006] S.R. Dey, A. Morawiec, E. Bouzy, A. Hazotte, J.J. Fundenberger: “A technique for determination of  $\gamma/\gamma$  interface relationships in a ( $\alpha_2 + \gamma$ ) TiAl base alloy using TEM Kikuchi patterns obtained by nanoprobe scanning”, Materials Letters 60, 2006 pp. 646-650.
- [Fundenburger-2003] J.J. Fundenberger, A. Morawiec, E. Bouzy, J.S. Lecomte: “Polycrystal orientation maps from TEM”, Ultramicroscopy 96, 2003, pp.127-137.
- [Germain-2005] L. Germain: “Contribution à l’étude des hétérogénéités de texture dans les billettes d’IMI 834”, Paul Verlaine, Université de Metz, France, Ph.D. Thesis, 2005.
- [Goldstein- 1981] *Goldstein, G. I.; Newbury, D. E.; Echlin, P.; Joy, D. C.; Fiori, C.; Lifshin, E. (1981). Scanning electron microscopy and x-ray microanalysis. New York: Plenum Press.*
- [Huang -1989] S.C. Huang: U.S. Patent 4.879.092, 1989.
- [Kikuchi- 1928] S. Kikuchi, “Diffraction of Cathode Rays by Mica”, Japanese Journal of Physics, 1928; 5: pp. 83-96
- [Ott-1999] Eric. A. Ott and Tresa M. Pollock, “Development and structures of  $\alpha_2$  plates in  $\gamma$ -based titanium aluminides due to the  $\gamma$  to  $\alpha$  transformation on heating” Scripta Materialia, 1999; 40: pp. 899-904.
- [Pouchou-2002] J.L. Pouchou, “L’Analyse EBSD : Principes et Applications”, EDP Sciences, Les Ulis (France) 2002: pp. 51.
- [Velasquez- 2007] J.D. Puerta Velasquez, B. Bolle, P. Chevrier, G. Geandier, A. Tidu, “Metallurgical study on chips obtained by high speed machining of a Ti-6 wt.%Al-4 wt.%V alloy” Materials science and engineering A, 452-453, 2007, pp. 469-474.
- [Schwarzer- 1993] R. A. Schwarzer, Review of Texture and Microstructure, 1993; 20: pp. 7.
- [Tetsui-2002] Toshimitsu Tetsui, “Effects of high niobium addition on the mechanical properties and high-temperature deformability of

gamma TiAl alloy”, *Intermetallics*, 2002; 10: pp. 239-245.

[Zghal – 1997]

S. Zghal, S. Naka, A. Couret, “A quantitative TEM analysis of the lamellar microstructure in TiAl based alloys”, *Acta Materialia*, 1997; 45: pp. 3005-3015.

## Appendix A2

Two original  
methodologies for  
characterizing the  
microstructure of  $\gamma$ -  
massive phase in TiAl  
based alloys

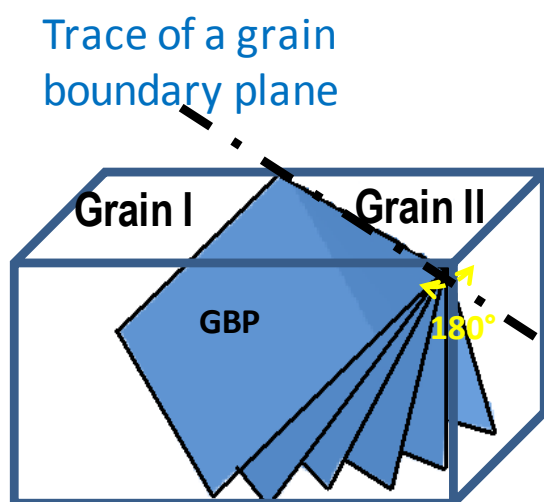
## **Two original methodologies for characterizing the microstructure of $\gamma$ -massive phase in TiAl based alloys**

### **Introduction**

Currently a number of characterization techniques and methods are been applied to understand the microstructure better, in order to tailor make the microstructure to suit various mechanical application. The mechanical properties of  $\gamma$ -TiAl alloys are well known to highly depend on their microstructure [1]. Hence, studying and optimizing the microstructure to have better mechanical properties is very important. Massive transformations are diffusionless transformation and they occur when  $\gamma$ -TiAl alloys are rapidly quenched [2,3]. This type of transformation has a number of advantages like refining the texture and grain size. Refining the lamellar grain through massive transformation is been studied widely [4, 5]. Hence it is important to understand and study the mechanisms of massive transformation more closely. Number theories have been proposed regarding the formation of the massive grains in TiAl-alloys, although, all the studies have been done on two dimensions [6-8]. Therefore this paper addresses two issues. First to analyse the  $\gamma$ -massive grains three-dimensionally and validate the nucleation and the growth mechanisms proposed. Secondly, to carry out same area investigation after tempering the massive grains, in order to study the microstructural evolution.

### **Back ground**

It is has been well established that the massive transformation occurs by the process of nucleation and growth [6, 7]. In TiAl alloys, during rapid quenching, the  $\alpha$  phase which has a HCP structure, massively transforms into  $\gamma$  phase which has a Tetragonal close packed structure. The nucleation of the  $\gamma_m$  grains preferentially occurs along the triple point of the  $\alpha$  grains and the  $\alpha/\alpha$  grains boundaries. In our earlier study [6, 7], the nucleation mechanisms have been closely investigated. From this extensive study it was established that during the nucleation of the  $\gamma_m$  grains along the grain boundary, the grain boundary that is capable of giving rise to a nucleus is the grain boundary that has it habit plane parallel or nearly parallel to the dense plane of one of the two neighbouring  $\alpha$  grains. This is because, nucleation of this type will lead to minimization of the interfacial energy [9]. This kind of criteria we termed as the 'minimum angle criteria'. Extensive studies have been made on this kind of grain boundary nuclei to see if they follow the minimum angle criteria. In the previous study, almost all the grain boundary nucleation with the  $\gamma_m$  grains developing on side of the grain boundary seems to follow this criterion. Although, statistically proved, the main disadvantage is, these studies are done in two-dimension and not in three dimensions. In two-dimension, only the trace of the grain boundary is obtained. In fact the actual grain boundary plane can have a rotational freedom of  $180^\circ$  and need not match with the trace of the grain boundary plane obtained in two dimensions. This situation is shown schematically in Figure 1.



**Figure 1:-** Schematic representation of the possible orientation of the grain boundary plane in three dimension.

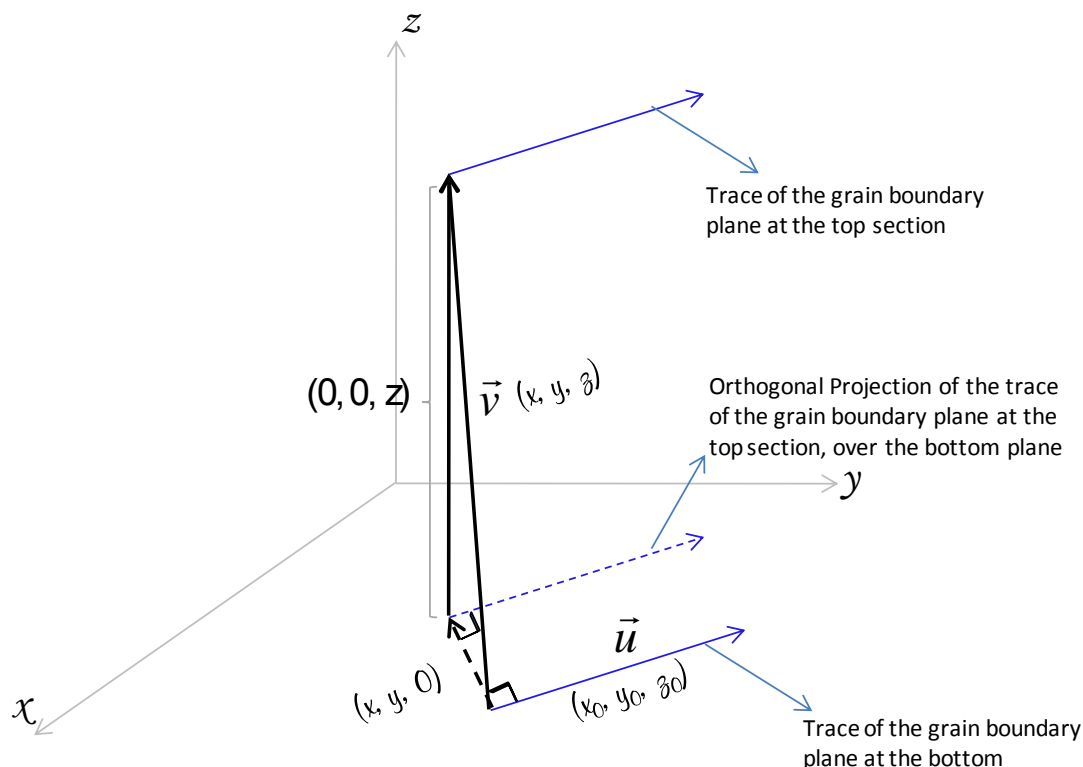
Once the nucleation occurs, the growth proceeds by the process of twinning. Each  $\gamma$  grain can give rise to four differently oriented  $\gamma$  variants which are in twin relation with the  $\gamma$  grain. This is because there are four different  $\{111\}$  planes present and each plane can give rise to four different variants [6, 7]. Therefore, in principle this process is effective and the formation of four  $\gamma$  variants is equiprobable. But in reality, it is not the case, while analysing an orientation map, very often, a number of variants are missing. Also, in many case, one variant grows as the dominant variant in detriment of the others. Therefore, it is important to verify if there is a strong variant selection mechanism taking place during the nucleation and the growth of the twin variants.

The second important study to be done is to understand the mechanisms of grain evolution during tempering of the  $\gamma_m$  grains. This is important because,  $\gamma$ -massive phase is a highly metastable phase, and when using these microstructures for high temperature applications, they de-stabilise, hence changing their mechanical properties [4, 10]. Generally it is hard to predict the grain evolution mechanisms by analysing the microstructure after subsequent heat treatments. Orientation maps have shown that the destabilisation of the  $\gamma$ -massive phase occurs by the precipitation of the globular precipitates of the  $\alpha_2$  along the high angle grain boundaries of the  $\gamma$  grains. And with increasing the tempering temperature, lenticular precipitates of  $\alpha_2$  are formed developing inside the  $\gamma$ -massive grains. After this heat treatment, the number of twin boundaries which is generally high among the massive grains has considerable reduced [10]. This indicates that the  $\gamma$  grains have evolved with increasing tempering temperature but the mechanism of the grain evolution is hard to predict. So, same area investigation using EBSD analysis can provide a solution in predicting the mechanisms of  $\gamma$ -massive grain evolution.

### Three dimensional evaluation of the $\gamma_m$ domains

In order to have information about the grain boundary plane and the grain evolution, several sectioning of the sample was performed. Successive thin layers of thickness  $\sim 2 \mu\text{m}$  were removed seven times and Back Scattered Electron (BSE) images and EBSD maps were taken on every layer. The method used here was to identify the grain boundary plane and is similar to the method used proposed by Randle [11]. Two types of indentation were made on a sample prepared by OPS polishing to be viewed under SEM; a macro indentation with 5kg and four micro indentations with 500g. The Vickers uses  $136^\circ$  pyramidal diamond indenter that forms a square indent. The size of the indent is obtained by measuring the diagonals of the indent. For Vickers's indents, normally the depth of the indent is the  $1/7$  the size of the value D. Therefore, for both the types of indents, the D value was measured to control the thickness of each section. An area was chosen closer to intend for mapping. After the first mapping, the sample was polished with a **Buehler Vibratory polisher**. A non-crystallizing colloidal silica polishing suspension was used. A time of 36 hrs was necessary to remove a thickness of  $\approx 2 \mu\text{m}$ . Since the depth of indentation for a 500g indenter is  $\approx 5.7 \mu\text{m}$ , new indents were made at regular intervals.

Later with all the BSE images taken from each section, they were overlapped to match with the indenter mark near the analyzed area and this overlapped image was used to identify the grain boundary plane. Figure 2 shows the method that we use to find the grain boundary plane.



**Figure 2:-** Method for calculating the grain boundary plane.

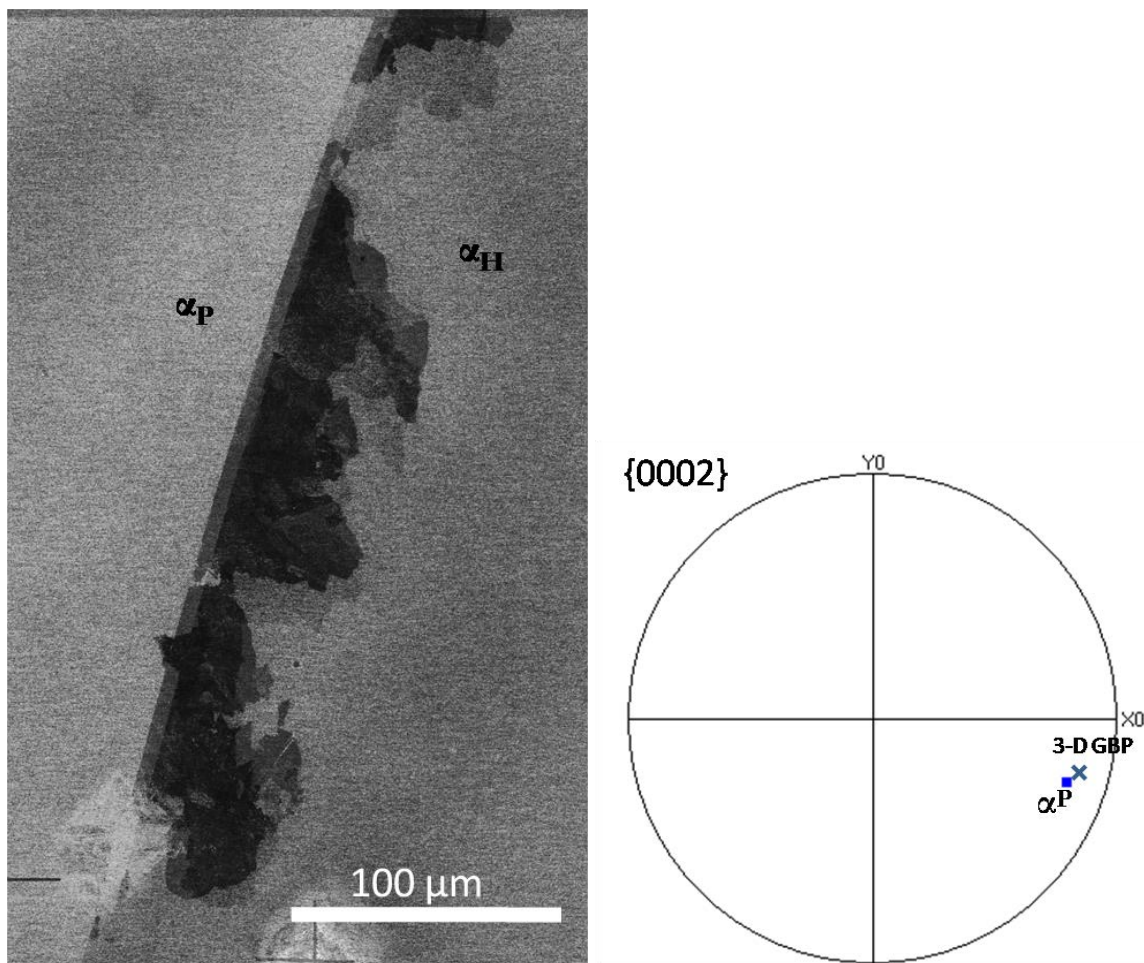
Here,  $(x_0, y_0, z_0)$  are the initial co-ordinates of the grain boundary plane and  $(x, y, z)$  are the final co-ordinates of the grain boundary plane.  $z$  represents the thickness of the sample

removed, therefore  $z_0$  is equal to zero. The co-ordinates of the grain boundary plane is given by (X, Y, Z) which is found by

$$\vec{u} \times \vec{v} = \begin{Bmatrix} X & Y & Z \\ x_0 & y_0 & z_0 \\ x & y & z \end{Bmatrix}$$

The obtained co-ordinates are plotted in the pole figure of (0002)  $\alpha_2$  (generally (0002) is considered to be the habit plane) to have the grain boundary plane.

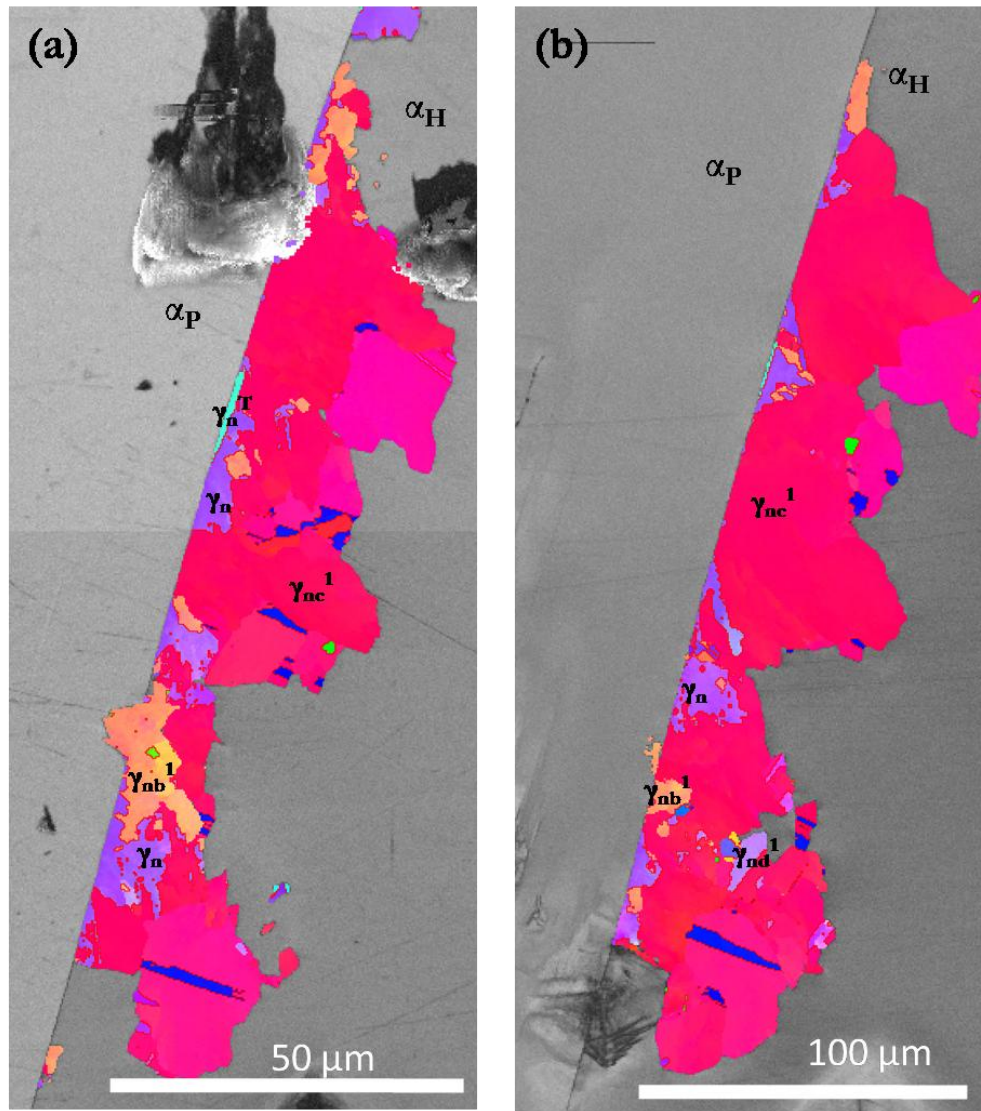
Figure 3 shows the super imposed images of a  $\gamma_m$  domain nucleating along the grain boundary. The grain boundary plane obtained was then plotted in the (0002) pole figure of the  $\alpha_p$  as can be seen from Figure 3 (b).



**Figure 3:-** (a) Three dimensional stacking of BSE images to identify the grain boundary plane.(b) {0002} pole figure of the  $\alpha_p$ , along with the calculated three dimensional grain boundary plane.

We can see that the trace of the grain boundary plane in the two-dimension is in fact the actual grain boundary plane in the three-dimension, with a very small difference. This affirms the fact that the analysis done for identifying the grain boundary plane by plotting its trace is indeed true for the bulk material too.





**Figure 4:-** (a) EBSD map taken at the first section (b) EBSD map taken at the last section of the serial sectioning  $\approx 12\mu\text{m}$ .

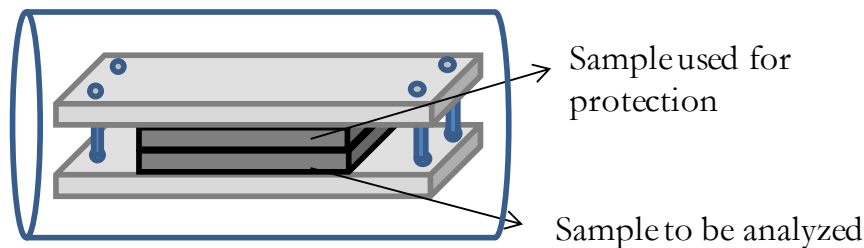
Figure 4 shows EBSD maps of grain boundary nucleation taken at (a) initial surface (b) at a depth of  $13\mu\text{m}$ . Even though, both the maps do not show any drastic changes in the  $\gamma_m$  grain morphology, the number of grains present in the analysed area is different. Also the surface areas of the grains that are found common in both the maps are different. For example the  $\gamma_n$  and the  $\gamma_n^T$  are the nuclei arising from the grain  $\alpha_p$ . As a result the  $\gamma_n$  gives rise to  $\gamma_{ib}^1$  and  $\gamma_{ic}^1$ , the third variant  $\gamma_{id}^1$ , is missing in Figure 4 (a). But when analysing the Figure 4 (b), all the three variants  $\gamma_{ib}^1$ ,  $\gamma_{ic}^1$  and  $\gamma_{id}^1$  are present, but the other twin of the nucleus  $\gamma_n^T$  is missing. This type of occurrence exists for the other twin generation of the  $\gamma_m$ . Therefore, we can say that the nucleation of all the different possible  $\gamma_m$  variants is equiprobable. However, not always are all the possible variants formed, present in the same surface of investigation.

The variant  $\gamma_{nc}^1$  arising from the nucleus  $\gamma_n$  is the dominant variant in Figure 4 (a). Also this variant still remains the dominant variant that is selected for growth even at certain depth of the sample Figure 4 (b). This pleads us to conclude that although all the possible twin  $\gamma_m$  variants are formed and can be indexed when analysing up to certain

depth, there is still a very strong selection of variant during growth, independent of the area analysed.

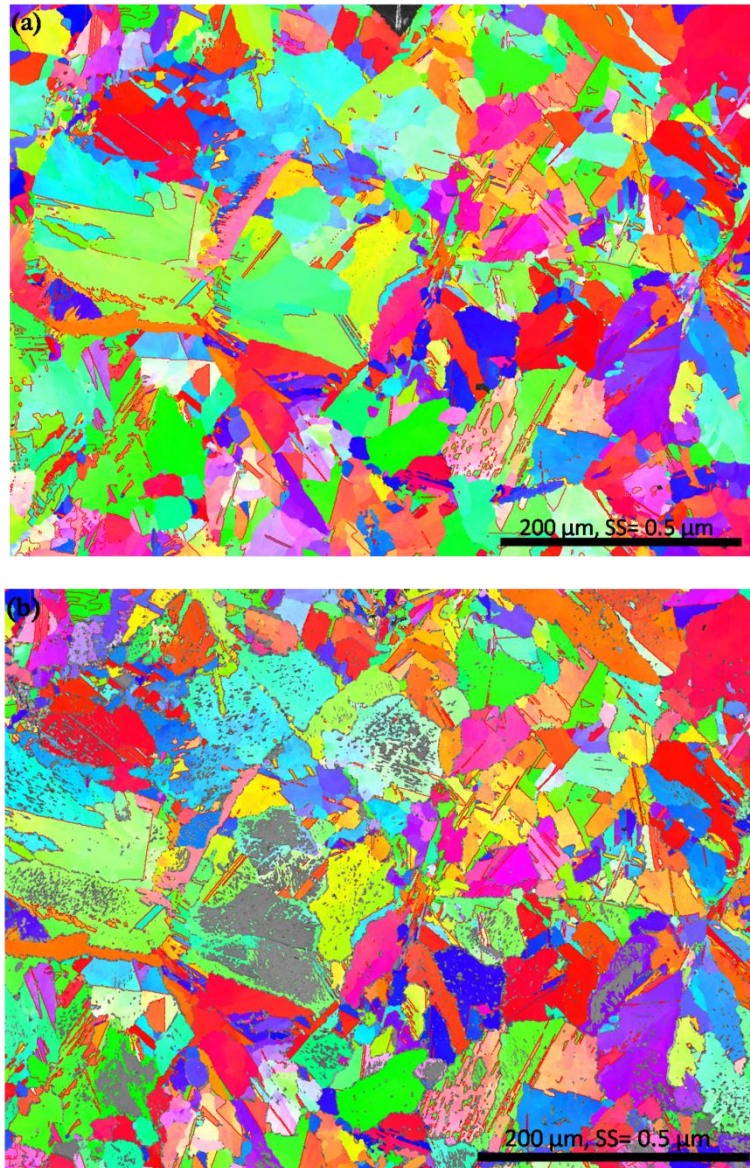
### **Grain evolution analysis after different heat treatments**

In order to analyze the microstructure at different temperature, first, the sample that was completely transformed into massive. Then it was polished with OPS to be viewed under SEM. Two indentations were made using a Vicker's indenter, and EBSD maps were measured around this indent. Then another sample of the same size, from the same alloy with the same sample dimension was polished and placed over in order to prevent oxidation. Both the samples were sandwiched with the help of two plates and screwed together. This set-up was then inserted inside a quartz tube and was purged with Argon. A schematic diagram of the set-up is show in Figure 5. The quartz tube was then placed in the furnace and heat treated at 1100°C for 20 min and air cooled. After the heat treatment, EBSD map was measured on the same area by tracing out the indents.



**Figure 5:-** Schematic representation of the set-up used for grain evolution studies.

Figure 6 (a) and (b) are the EBSD maps taken prior to the heat treatment and after the heat treatment. By comparing the EBSD maps, the following observations can be made:



**Figure 6:-** (a) EBSD map of a massively transformed sample (b) EBSD maps taken on the same area after a heat treatment at 1100°C, 20 mins. The grey phase corresponds to the  $\alpha_2$  phase.

1. Almost all the high angle grain boundaries bear the globular  $\alpha_2$  precipitates.
2. The next preferred site for the  $\alpha_2$  nucleation are the low angle grain boundaries
3. Most of the twin boundaries do not bear any  $\alpha_2$  precipitates, however certain twin boundaries takes part in the nucleation of the globular  $\alpha_2$ .
4. In certain grains the amount of  $\alpha_2$  present is very high.
5. Some of the  $\gamma$  grains are shrinking, while others seem to grow, although there has not been formation of any new  $\gamma$  grains.

Although, a number of points match well with the mechanisms on the  $\alpha_2$  precipitation, it is astonishing that the precipitation of the  $\alpha_2$  plates does not take place inside all the  $\gamma$  grains. Also, a number of twin boundaries are reduced in bulk of the sample,

but in the EBSD map seen in Figure 6 (b), we can see that most of the twin boundaries are preserved. The volume fraction of the  $\alpha_2$  phase is close to 16%. This is slightly higher than the volume fraction of the  $\alpha_2$  phase in the bulk. Also, the globular  $\alpha_2$  precipitation seems to be higher in the surface. These lead us to conclude that there are other factors that are responsible for slight change in the morphology of the microstructure. Since the surface of samples used of the same area investigation was protected by another sample of the same dimension, there are chances that there has been some oxidation. The oxygen being an  $\alpha$  stabilizer, helps in the formation of higher amount of  $\alpha_2$  precipitates, and these precipitates arrests the movements of the grain boundaries. Hence, the numbers of twin boundaries are preserved in this sample while it is different in the other sample.

### Summary

Two different and original characterization techniques have been used to understand the formation mechanisms and grain evolution mechanisms of the  $\gamma_m$  grains in TiAl based alloys.

For the three-dimensional analysis of the  $\gamma_m$  grains, it is clear that the trace of the grain boundary plane obtained in the two-dimensional case is in fact the real grain boundary plane. Therefore the minimum angle criterion is valid when considering the bulk material too. During the growth of the massive grains, all the four possible variants from one  $\gamma$ -grains are formed though all of them are not present in the same surface of investigation. However there are dominant variants that are formed which remain dominant even in three-dimensions.

As for the grain evolution, although, the nucleation sites of the  $\alpha_2$  precipitates are in agreement with the studies done earlier, the volume fraction of the  $\alpha_2$  phase seems to be slightly higher. This can be attributed to the oxidation of the surface during the heat treatment. Hence successfully predicting all the evolution mechanisms was not possible.

### References

- [1] Takeyama M, Microstructural evolution and tensile properties of titanium-rich TiAl alloy, Mater. Sci. and Eng., A, 152 (1992) 269-276.
- [2] Massalski TB, Soffa WA, Laughlin DE, Metall. Mater. Trans. A, 2006; 37A:825.
- [3] Plitcha MR and Aaronson HI, Acta Metall. 1980; 28:1041.
- [4] Clemens H, Bartels A, Bystrzanowski S, Chladil H, Leitner H, Dehm G, Gerling R, Schimansky FP, Grain refinement in  $\gamma$ -TiAl-based alloys by solid state phase transformations, Intermetallics, 14 (2006) 1380-1385.
- [5] Wu X, Hu D, Microstructural refinement in cast TiAl alloys by solid state transformations, Scripta Mater. 52(2005) 731-734.
- [6] Dey SR, Bouzy E, Hazotte A, EBSD characterisation of massive  $\gamma$  nucleation and growth in a TiAl-based alloy, Intermetallics, 14 (2006) 444-449.
- [7] Sankaran A, Bouzy E, Humbert M, Hazotte A, Variant selection during nucleation and growth of  $\gamma$ -massive phase in TiAl-based intermetallic alloys, Acta Mater., 57 (2009) 1230-1242.
- [8] Wang P, Veeraraghavan D, Kumar M, Vasudevan VK, Metall. Mater. Trans. A, 2002, 33A: 2353.
- [9] Lee JK and Aaronson HI, Acta Metall. 1975; 23: 799.

- [10] Sankaran A, Bouzy E, Funderberger JJ, Hazotte A, Accepted in Intermetallics.
- [11] Randle V, The measurement of grain boundary geometry, published by institute of physics publishing.

## Annexe B

**Variant selection  
during nucleation and  
growth of  
gamma-massive phase  
in TiAl-based  
intermetallic alloys**

## **Variant selection during nucleation and growth of gamma–massive phase in TiAl-based intermetallic alloys**

A.Sankaran, E. Bouzy, M. Humbert, A. Hazotte \*

Laboratoire d'Etude des Textures et Application aux Matériaux (LETAM)

UMR CNRS/UPV-M 7078, Ile du Saulcy, 57045 Metz Cedex 1, France

*Published in: Acta Materialia 57 (2009) 1230-1242*

### **Abstract**

This work deals with the mechanisms of nucleation and growth of gamma-massive phase in TiAl-based intermetallic alloys. In particular, it focuses on the process of variant selection operating at both stages of the transformation. Small gamma-massive domains produced by rapid cooling are extensively characterized by high-resolution Electron Back-Scatter Diffraction (EBSD). This large data set allows a statistical analysis of nucleation sites, according to different crystallographic configurations. It is established that, whatever the nucleation sites, i.e. grain boundaries or triple junctions, a coherent facet is always found presenting a Blackburn orientation relationship (BOR) between the gamma nucleus and the alpha parent grain. Moreover, some gamma nuclei can additionally present another semi-coherent facet with an approximate BOR with the alpha host grain. A new nucleation mechanism, called 'co-nucleation', is highlighted for this type of double faceted nucleus. Variant selection during nucleation are discussed for both types of nuclei, in terms of minimization of interface energy. In addition, it is showed that growth of gamma-massive domains from their initial nucleus always involves successive {111} twinning. Variant selection also occurs either at the nucleus growth stage or during the development of the successive twin generations. It is discussed in terms of interphase boundaries mobility.

**Keywords:** Massive transformation, Variant selection; Crystallography; Nucleation

### **1. Introduction**

Massive transformation, as defined by Massalski [1], is a "composition invariant, interface-controlled diffusional phase transformation, involving a characteristic irregular patchy microstructure and frequent faceting and ledges, but not necessarily involving lattice orientation relationships". This type of transformation was first observed by Phillips [2], and its main characteristics were initially established by Massalski in a range of Cu alloys [3]. Since then, massive-like transformations have been reported in a number of alloys [3-28, 31-34], with major contributions from Massalski and co-workers [1, 3-8] and Aaronson and co-workers [9-17, 28]. It is now generally admitted that the rate-controlling step is the germination of massive nuclei, whereas the subsequent development of massive grains occurs very rapidly [3, 5]. However, massive transformation is clearly a time-dependent phenomenon. Caretti et al., [20] performed continuous cooling experiments on several metallic systems and found that increasing the cooling rate leads to decrease the massive transformation temperature, to increase the nucleation density and to refine the final microstructure. It has also been established that nucleation of massive domains predominantly occurs at heterogeneous sites (grain boundaries and defects). However, the existence of specific orientation relationships between massive nuclei and parent grains has

been a subject of controversy. Several theories were put forward regarding the massive grain nucleation mechanisms and have been compared with experiments. It was concluded that a viable nucleus forming at a parent-grain boundary should have a low energy facet with one of the parent grains in order to minimize the activation energy of nucleation [11]. Mechanisms are far to be established for growth of massive domains. The moving interface between the growing massive grain and the host grain was often reported or considered to be incoherent. The nature of the incoherent interphase interfaces especially during massive transformation was discussed by Massalski et al [8] and was debated in a session during the TMS Hume – Rothery Symposium in 2004 [18]. Yanar et al., [21] and Howe et al., [22] have done some experiments using HRTEM on the growing massive interfaces. They concluded that these massive interfaces though consist of prominent facets along various length scale, they exhibit no specific orientation relationship with the matrix inside which it is growing. However, a few authors observed that certain dense planes of the two phases involved in the massive transformation could sometimes be nearly parallel [11, 19].

Massive transformation is also observed in near- $\gamma$  TiAl alloys, when rapidly transformed from the high-temperature  $\alpha$  solid solution. It was confirmed that it develops with no composition change, but involving short-range atomic jumps across the moving  $\gamma/\alpha$  interface [25]. In the case of continuous cooling, this transformation mode appears intermediate between modes controlled by long-range diffusion, as lamellar, Widmanstätten and ‘feathery’ transformations (occurring at lower cooling rates), and the direct  $\alpha \rightarrow \alpha_2$  ordering transformation (higher cooling rates). Consequently,  $\gamma$ -massive (hereafter noted  $\gamma_m$ ) colonies are often observed co-existing with other types of microstructures. Veeraraghavan et al., [24] measured the transformation temperatures and growth kinetics of massive transformation in several TiAl alloys. Hu et al., [34] located the domains of the different transformation modes as a function of cooling rate for TiAl alloys with different compositions. They showed that for some alloys there is an optimum cooling rate for which a 100% massive transformation takes place. Wittig [23] was able to arrest the initial stages of heterogeneous nucleation and growth and found that a  $\gamma$  nucleus forming along the  $\alpha/\alpha$  grain boundaries often follows a specific orientation relationship with one of the neighboring  $\alpha$  grains, i.e.,  $\{111\}_\gamma // (0002)_\alpha$  and  $\langle 110 \rangle_\gamma // \langle 11\bar{2}0 \rangle_\alpha$ . This relationship, known as the ‘Blackburn Orientation Relationship’ [35] (hereafter noted BOR), is very usual in TiAl alloys. Indeed, it is also observed between  $\gamma$  and  $\alpha_2$  phases developing through lamellar, Widmanstätten or feathery transformation modes [36-38]. Dey et al., [31] used EBSD to study the heterogeneous nucleation of  $\gamma_m$  nuclei along  $\alpha/\alpha$  boundaries. They confirmed that BOR is systematic, but they also noted that not all  $\alpha/\alpha$  grain boundaries give rise to  $\gamma_m$  nuclei. Intra-granular  $\gamma_m$  nucleation was also reported by some authors [23], but a careful examination of the nuclei shows that the nucleation is heterogeneous and occurs on twin boundaries present inside the  $\alpha$  grain [31].

Veeeraraghavan et al., [26] calculated the critical free energy ( $\Delta G^*$ ) associated with  $\gamma_m$  nuclei forming at grain boundaries, triple junctions or quadruple points (denoted as grain face, edge and corner sites in this reference). They found that sufficiently low  $\Delta G^*$  values can be expected for single faceted (having one low energy interface) grain boundary nucleation as well as for non-faceted and incoherent nucleation at grain edges and corners. In counterpart, formation of non-faceted nuclei along grain faces and formation of faceted nucleus with growth on both the sides of the grain boundary is unexpected. However, these



authors observed  $\gamma_m$  nuclei, which deviate from the BOR with respect to its parent  $\alpha$  grain, for both grain face and edge nucleation. Similar results have also been reported by Wang et al., [25] while analyzing orientation maps and TEM micrographs.

The purpose of the present work was to have a closer and more statistical look at the  $\gamma$ -massive nucleation in a near- $\gamma$  TiAl alloy, using an EBSD approach on large surfaces. The objectives were to identify the preferred sites for the formation of the nuclei and to analyze the orientation relationships between nuclei and host  $\alpha$  grains, in order to determine if some local crystallographic configurations appear favorable for  $\gamma_m$  nucleation. In the following, the results obtained will be described and analyzed. Nucleation and growth mechanisms will be proposed to explain the variant selection observed.

## **2. Experimental Procedure**

The material under study was a Ti-45Al-7Nb-0.2C (in at %) alloy. A sample of about  $6 \times 6 \times 10 \text{ mm}^3$  was cut from a cylinder prepared by conventional casting then high-temperature extrusion. This sample was heat treated up to  $1350^\circ\text{C}$  at a rate of  $5^\circ\text{C min}^{-1}$ . It was held at  $1350^\circ\text{C}$  ( $\alpha$  phase domain [39]) for 15 min under a constant flow of argon, and then quenched in cold brine water ( $\sim -10^\circ\text{C}$ ). This rapid cooling resulted in a microstructure containing small amounts of  $\gamma$ -massive ( $\gamma_m$ ) phase accompanied with coarse  $\alpha_2$  grains.

The specimen was mechanically and electrolytically polished, using a solution of 10% perchloric acid (70% pure) in methanol, at  $10^\circ\text{C}$  and 17V. A JEOL JSM-6500F Scanning Electron Microscope (SEM), equipped with a field emission gun (FEG), was used for the microstructure observation. Images of the microstructure were taken in Back Scattered Electron (BSE) mode.

Crystallographic information about  $\alpha_2$  and  $\gamma_m$  phases was obtained by Electron Back-Scatter Diffraction (EBSD), using Channel 5 software from HKL. In order to achieve a statistically pertaining analysis of the  $\gamma_m$  nucleation sites, one very large Orientation Image Mapping (OIM) was acquired over an area of  $5 \text{ mm} \times 3 \text{ mm}$ , with a step size of  $4.5 \mu\text{m}$ . Since this step size was large, compromise had to be made with the resolution. In order not to miss any grain boundaries and triple junctions with the  $\gamma_m$  domains, BSE images were also taken in the same area and used as reference.  $\alpha$ -Grains with area less than  $40 \mu\text{m}^2$  were ignored. Several other OIM's were also measured on particular grain boundaries and triple junctions, using a better spatial resolution (step size =  $0.2 \mu\text{m}$ ).

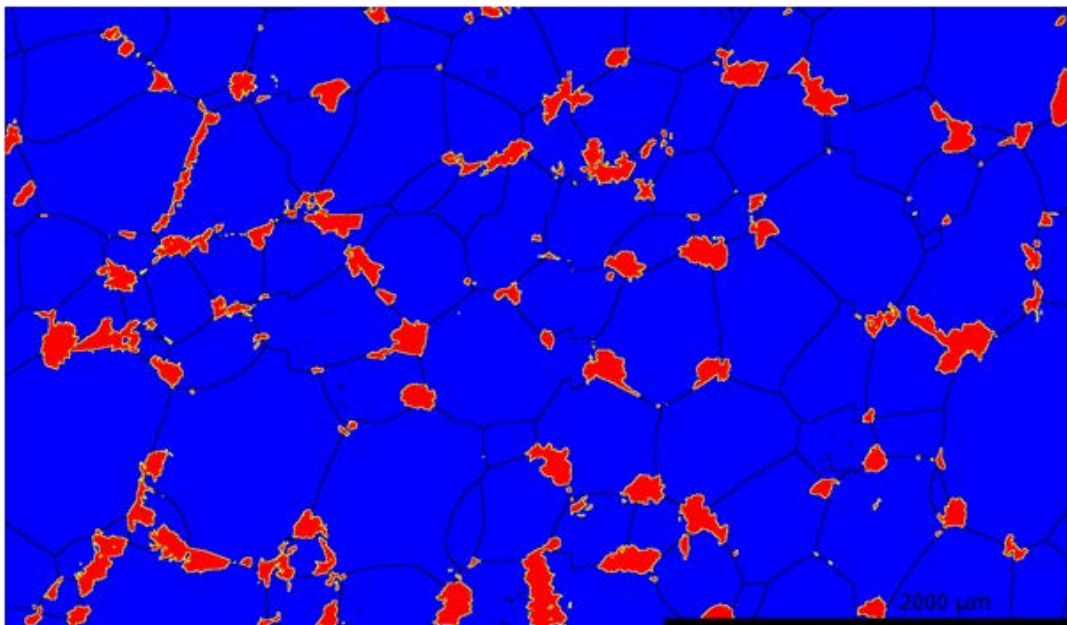
During the transformation of  $\alpha$  phase into  $\alpha_2 + \gamma_m$ , the orientation of the  $\alpha$  phase (disordered hexagonal structure, A3) is retained by the  $\alpha_2$  phase (ordered hexagonal structure,  $\text{DO}_{19}$ ). Therefore, indexing the room-temperature hexagonal phase gives the information about the orientation of the high-temperature  $\alpha$  phase (also, the substructure Kikuchi bands relative to the ordered  $\alpha_2$  structure are not detectable in the usual SEM/EBSD conditions). Moreover, it is known that the  $\alpha \rightarrow \gamma_m$  transformation takes place before  $\alpha \rightarrow \alpha_2$  ordering [40]. Consequently, when discussing massive-transformation mechanisms in the following, we will refer to crystallographic data relative to the  $\alpha$  phase (or to  $\alpha/\alpha$  grain boundaries), although they were actually measured on the  $\alpha_2$  phase. The  $\gamma$  phase has an ordered tetragonal structure ( $\text{L1}_0$ ) with a very small  $c/a$  ratio (about 1.016). As far as BOR, it applies between  $\gamma$  and  $\alpha$  phases, one  $\alpha$  parent orientation can give rise to six different orientations (tetragonal variants) of the  $\gamma$  phase [36, 41]. Unfortunately, due to its too low

signal/noise ratio and angular resolution, EBSD/SEM technique is not able to differentiate amongst these six possible variants (which is possible using transmission microscopy), neither through the position of their substructure bands nor through the rotation of their Kikuchi patterns. Instead, one can only differentiate them as a set of two cubic variants, twin related to each other. Hence, during EBSD mapping, the  $\gamma_m$  phase was considered to be FCC, rather than a face centered tetragonal. As far as the orientation relationships between  $\alpha/\alpha$  grain boundaries and  $\gamma_m$  nuclei are concerned, another limitation of SEM lies in the fact that the spatial information is only available over plane surfaces, which clearly limits data analysis, whatever their statistical weight. This point will be discussed below.

### 3. Results

#### 3.1 Morphology of massive domains

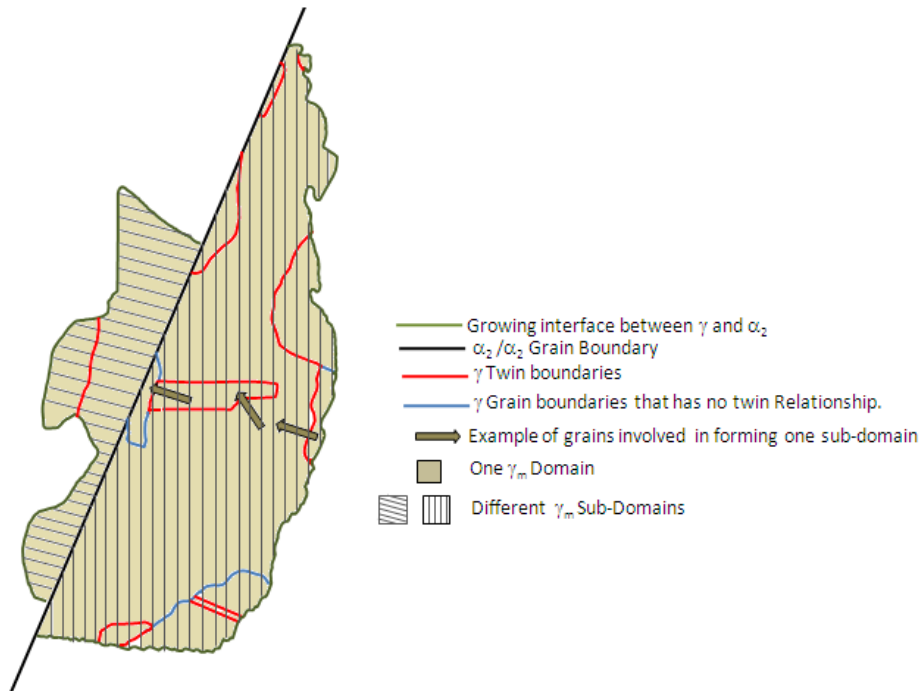
Brine-water quenching from the  $\alpha$  domain was quick enough to suppress the microstructures associated with long-range diffusion. Therefore it results in a two-phase microstructure formed by gamma-massive domains<sup>2</sup> (each connected group of massive phase will be termed as a ' $\gamma_m$  domain' in the following) and  $\alpha_2$  grains. This is illustrated in Figure 1, where the cubic and hexagonal phases identified by EBSD over a large surface area are represented in red and blue, respectively; together with the traces of grain boundaries in black (the criterion used to detect grain boundaries is a misorientation greater than  $3^\circ$  between two neighboring pixels).



**Figure 1:-** Phase contrast map obtained from the EBSD mapping. The red color regions correspond to the  $\gamma$  phase which is massively transformed and the blue region corresponds to the  $\alpha_2$  phase.

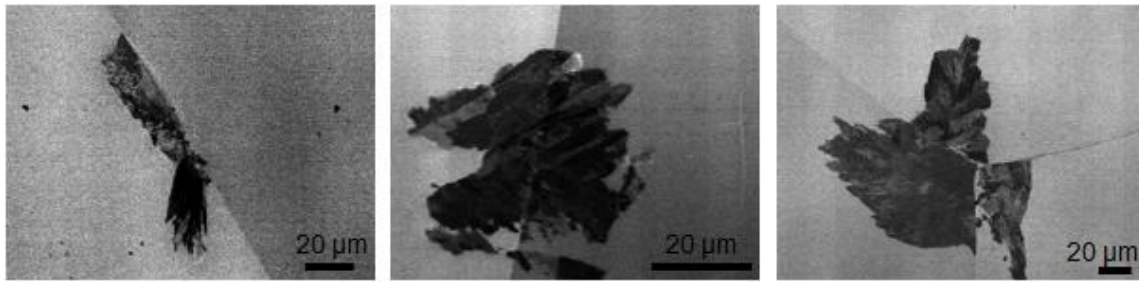
<sup>2</sup> In the following, we will call ' $\gamma_m$  domain' every block of gamma phase attached to a grain boundary or a triple junction. Figure 2 gives a schematic representation to explain the different terms used in the present paper. In the example, the domain is formed by two 'subdomains' which are constituted by a set of 'grains' all issued from the same nucleus by successive twinning.(cf paragraph 3-4)

$\gamma_m$  domains appear in the form of small bundles located along  $\alpha_2/\alpha_2$  grain boundaries and more often around triple junctions. In the area analyzed, the mean volume fraction of  $\gamma_m$  grains totals to only 7%. A slight variation was noted from the border of the sample, where the volume fraction is less, towards the centre of the sample, where it is slightly higher. This results from the difference in the cooling rate experienced by the specimen at different locations.



**Figure 2:-** Schematic representation explaining the definitions of  $\gamma_m$  domains, sub-domains and grains.

The boundary between a massive domain and the  $\alpha_2$  grain inside which it is growing appears mainly irregular. Three types of inter-granular  $\gamma_m$  morphologies can be distinguished, as illustrated in Figure 3 (a-c): along grain boundary  $\gamma_m$  develops on only one side (3.a). This configuration will be referred as 'Type II', 'Type I' being used for a grain boundary without  $\gamma_m$  domain.  $\gamma_m$  can also be observed on both sides of the grain boundary (3.b ; Type III). Development from triple-junction always results in massive equiaxed domains settling among the three neighboring grains (3 c).



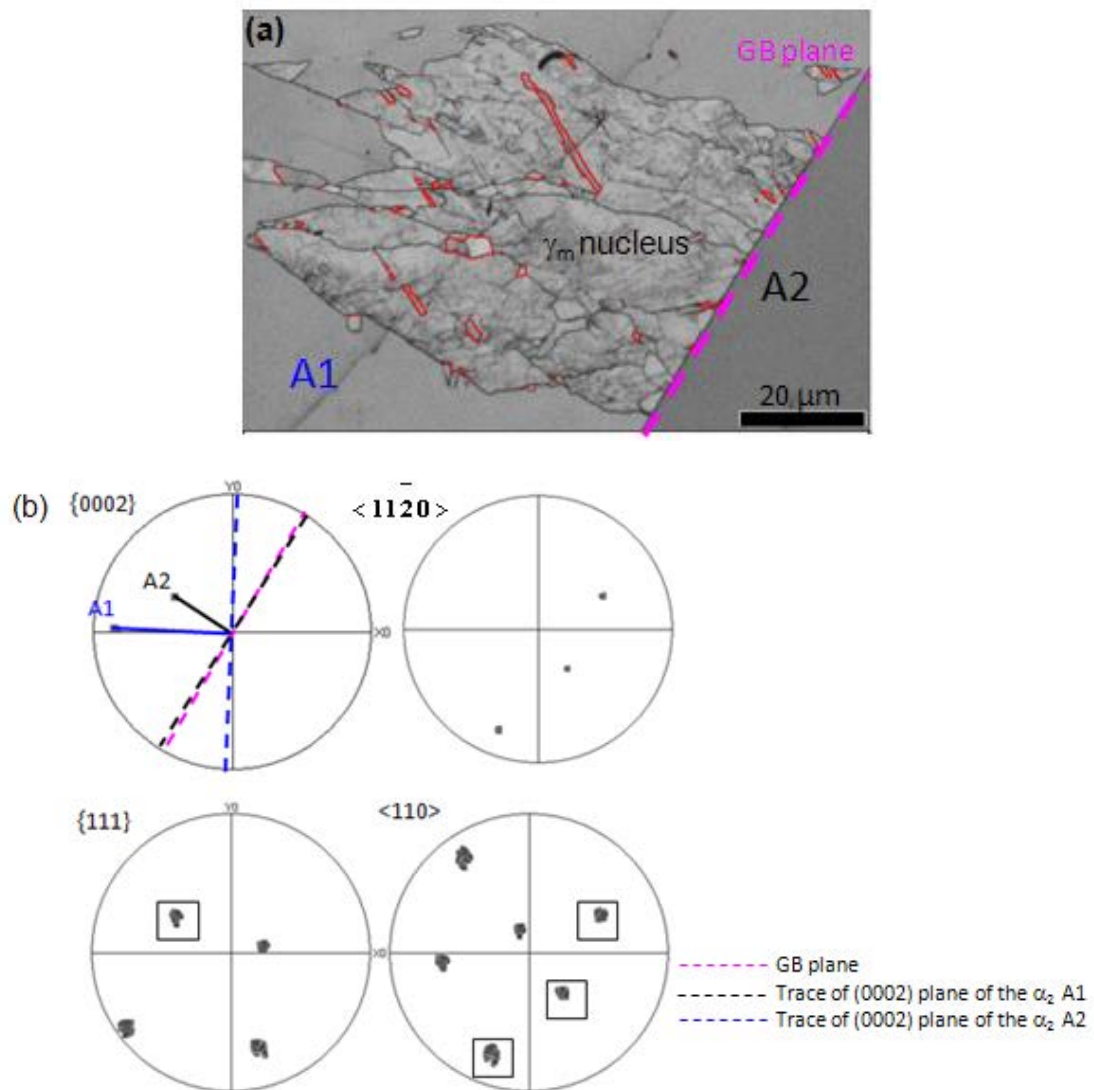
**Figure 3:-** BSE images of  $\gamma_m$  structures showing different types of inter-granular massive domains. (a) Domains developing across one side of the grain boundary (b) massive domains developing across both sides of the grain boundaries (c) massive domains along the triple junctions

Out of the 171 triple junctions obtained in the Figure 1, nearly 104 junctions bear a  $\gamma_m$  domain.  $\gamma_m$  domains were observed on about 15% grain boundaries, whereas around 150 show no nucleation.

### 3.2 Crystallography of $\gamma_m$ nuclei

Several high resolution OIM's of  $\gamma_m$  domains have been obtained along grain boundaries and at triple junctions. Six OIM maps with Type II grain boundary, three OIM maps with Type III grain boundary and six triple junctions were analyzed. As it will be discussed later, a  $\gamma_m$  domain is divided in several  $\gamma_m$  grains presenting different crystallographic orientations (see Figure 2 for definitions). For the present cooling conditions, the number of grains inside one domain is limited (sometimes the domain is even formed by only one grain) and the size of  $\gamma_m$  domains is small (the mean size of a massive grain is about  $5\mu\text{m}$ ). For all grain boundaries and triple junctions analyzed through EBSD maps, at least one of the  $\gamma_m$  grains was found to present a strict Blackburn orientation relationship (BOR ; i.e.  $(0002)_\alpha // \{111\}_\gamma$  and  $\langle 11\bar{2}0 \rangle_\alpha // \langle 110 \rangle_\gamma$ ) [35] with one of its neighboring  $\alpha_2$  grains. In the following, such a grain will be assumed as being the nucleus of the domain. As an example, Figure 4(a) shows a large  $\gamma_m$  nucleus on a Type II grain boundary. The strict BOR is visualized through the superimposition of the dots present in the pole figures of both  $\gamma_m$  nucleus and A2  $\alpha$  grain (cf. Figure 4(b)). It is seen that the  $\gamma_m$  develops inside the opposite  $\alpha$  grain, i.e. the grain with which it has no BOR (A1 grain). This mechanism was first reported by Smith [42], and by many other authors for massive transformation [23, 31]. In the following, the  $\alpha$  grain in BOR with a  $\gamma_m$  nucleus will be denoted as its 'parent  $\alpha$  grain', while the one in which the  $\gamma_m$  domain develops will be denoted as its 'host  $\alpha$  grain'.

Under the cubic assumption, two variants of  $\gamma_m$  nuclei can be generated in BOR with one ex- $\alpha$  grain. These two variants are twin related along the  $\{111\}$  plane parallel to the  $(0002)$   $\alpha$  plane. Knowing the orientation of one  $\alpha$  grain, the orientation of the two BOR  $\gamma_m$  nuclei can be deduced theoretically with the help of the transformation matrix in the form of Euler-angles ( $\Delta g = 90^\circ, 54.54^\circ, 45^\circ$ ). In the case of grain boundary nucleation, each  $\alpha$  grain can give rise to two nuclei, which results in four possible nuclei for each grain boundary. But very often, only two nuclei from the same parent  $\alpha$  grain are found for a given  $\gamma_m$  domain. As a confirmation, the ratio between grain boundaries of Type II (two nuclei) and of Type III (four nuclei) observed for the large EBSD map in Figure 1 is approximately 2:1. Clearly, particular  $\gamma_m$  variants appear to be selected at the nucleation stage.



**Figure 4:-** (a) Band contrast map representing the Type II grain boundary nucleation. (b)  $\{0002\}$  and  $\langle 11\bar{2}0 \rangle$  pole figures corresponding to the two neighboring  $\alpha_2$  grains and the  $\{111\}$  and  $\langle 110 \rangle$  pole figures of the  $\gamma_m$  nucleus.

### 3.3 Analysis of the different types of $\gamma_m$ domains

A large data set has been collected in order to analyze the crystallography and mechanism of nucleation. Totally 119  $\alpha_2$  grains were mapped and 170 grain boundaries were analyzed. As shown in Figure 1, a number of grain boundaries do not bear any  $\gamma_m$  domain, most of them being curved. Grain boundaries with and without  $\gamma_m$  domains were selected and the  $\{0002\}$  pole figures of their two adjacent  $\alpha_2$  grains were plotted. As illustrated in Figure 4(b), the traces of the  $\{0002\}$  planes were drawn and compared with the trace of the grain boundary, which allows to evaluate the angle  $\theta$  between the  $\alpha$  basal plane of each  $\alpha$  grain and the grain boundary plane. Obviously, this angle is an apparent one, since the orientation of the grain boundary is only known through its intersection with the observation surface. As  $\theta$  angle is difficult to define in the case of curved grain boundaries, only grain boundaries with straight morphology were considered for the analysis.

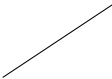
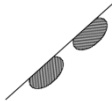
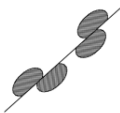
Table 1 reports the data collected from all the randomly-selected grain boundaries. It has been stated previously that an inter-granular  $\gamma_m$  domain nucleates in BOR with one of the two  $\alpha$  grains, but grows in the other. Consequently, the mean values of measured  $\theta$  angles have been reported in two ways in Table 1:  $\theta_i$  ( $i = A, B$ ) being the angle between the traces of the grain boundary and of the basal plane, those noted  $\theta_i^*$  correspond to  $\alpha$  grains giving rise to a  $\gamma_m$  nucleus (i.e., located on the other side of the grain boundary with respect to the  $\gamma_m$  domain), while those noted  $\theta_i$  are relative to the  $\alpha$  grains which does not give rise to a  $\gamma_m$  nucleus. In the following, these two different types of  $\alpha$  grains will also be denoted as 'fertile' and 'sterile' respectively. Three types of grain boundaries have been characterized in the present work, corresponding to the schematic representations given in Table 1 : for the straight grain boundaries without a  $\gamma_m$  domain (Type I: two sterile grains), 42 couples of  $\theta_A$  and  $\theta_B$  angles were measured ; measurements on grain boundaries of Type II (only one fertile grain) (exemplified in Figure 3(a)) led to 14 couples of  $\theta_A$  and  $\theta_B^*$  angles ; 9 couples of  $\theta_A^*$  and  $\theta_B^*$  angles are reported for Type III (two fertile grains) grain boundaries (exemplified in Figure 3(b)). When a confidence range,  $\pm \Delta\theta$ , is indicated, it is calculated using the formula,

$$\Delta\theta = z_{5\%} (\sigma^* / \sqrt{n}),$$

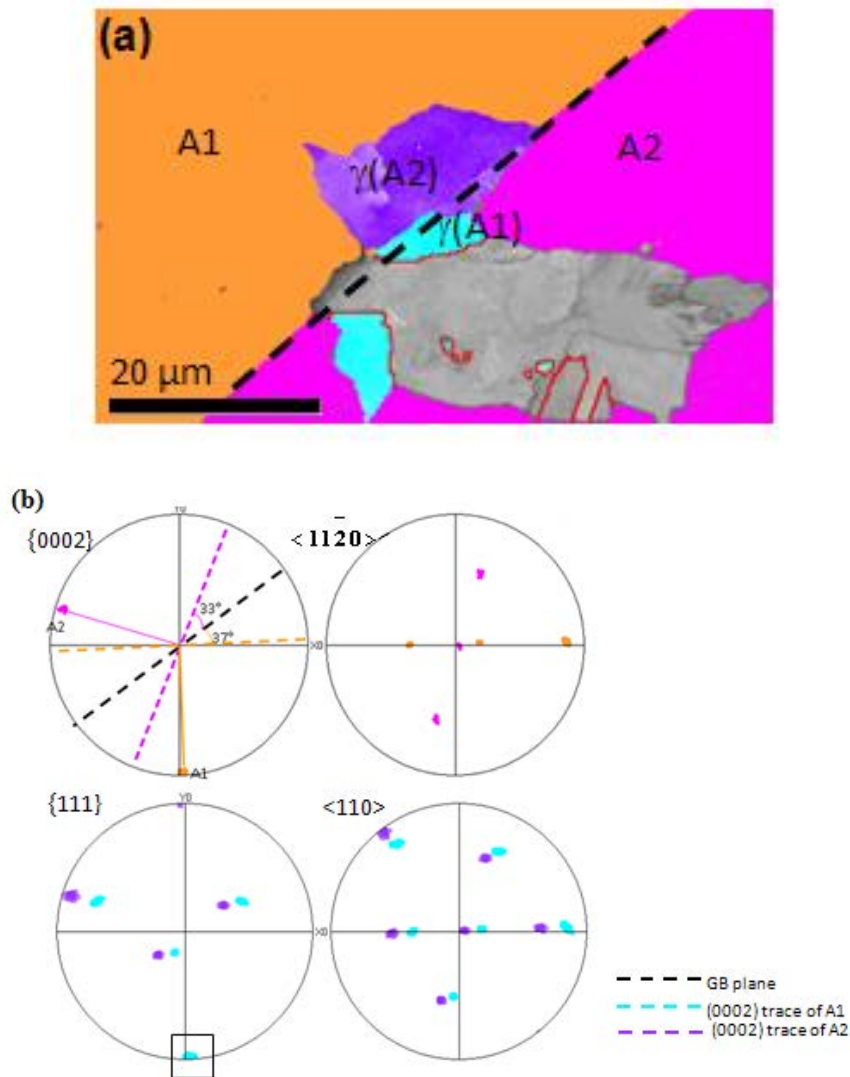
where  $\sigma^*$  is the estimated standard deviation of  $\theta$ ,  $n$  is the number of  $\theta$  values taken into account and  $z_{5\%}$  is obtained from a Student-Fischer table with  $(n-1)$  degrees of freedom and a symmetric risk of 5% ( $z_{5\%}$  is about 2 if  $n > 20$ ). Grouping the first three columns of Table 1 allows us to calculate the mean value and confidence range of the apparent angle between a grain boundary plane and the basal plane of a sterile  $\alpha$  grain. If comparing this mean value with the one relative to fertile grains of Type II grain boundaries (fourth column), it appears that the latter is significantly lower than the former. This analysis strongly plead for the idea that a  $\gamma_m$  nucleus is favored if its habit plane<sup>3</sup> –i.e. (0001) <sub>$\alpha$</sub> –is close to the grain boundary plane. This point will be discussed later. However, statistical analysis of 5<sup>th</sup> and 6<sup>th</sup> columns (fertile grains along Type III boundaries) suggests that nucleation mechanisms could be more complex. Indeed, in that case the estimated mean value of  $\theta^*$  angle appears to be intermediate between those calculated for fertile and sterile grains of Types I and II. With regard to the statistics collected in the present study, this value is even significantly higher than the mean value for fertile grains of Type II. This means that these grain boundaries have been active for nucleation, while their planes largely deviate from the nucleation habit planes. This apparent contradiction will be analyzed and explained in the discussion, at the light of the following observations relative to the crystallography of  $\gamma_m$  nuclei.

<sup>3</sup> Habit plane- Defined as the plane of interface between two phases ands represented by convention, by the plane of the parent phase, in our case, the  $\alpha$  phase.

**Table 1:-** Different types of grain boundaries analyzed from Figure 1.

Types of grain boundary analysed	<b>Type I: Grain boundary with no nucleus.</b>		<b>Type II: Nucleus forming on the single side of the grain boundary</b>		<b>Type III: Nucleus forming on both sides of the grain boundary</b>	
						
<b>Number of grain boundaries analyzed</b>	41		14		9	
<b>Angle between the GB trace and (0002) plane of <math>\alpha_2</math></b>	$\theta_A$	$\theta_B$	$\theta_A$	$\theta_B^*$	$\theta_A^*$	$\theta_B^*$
<b>mean value</b>	44.68	57.2	57.1	7.4	42.4	39.0
<b>Mean <math>\pm</math> standard Error</b>	54.3 $\pm$ 7.1		7.4 $\pm$ 2.4		40.7 $\pm$ 10.8	

In addition to BOR, the literature sparsely reports that a dense plane of the  $\gamma_m$  phase can be observed parallel to a dense plane of the  $\alpha$  grain in which it grows (host grain) [11, 19]. Therefore, we tried to detect this configuration using the following procedure : knowing the crystallographic orientations of both  $\alpha$  grains at a grain boundary, it is possible to check if one of the equivalent  $\{111\}$  plane of a  $\gamma_m$  nucleus in BOR with the parent  $\alpha$  grain, (whatever this grain is actually observed to be fertile or not) is nearly parallel to the (0002) plane of the host  $\alpha$  grain; here, the criterion chosen to consider that two planes are ‘nearly’ parallel is when the angle between their normal,  $\omega$ , is less than  $10^\circ$ , (Here, for the interphase boundary, we use the same criterion that is used to define a low angle grain boundary). In the following, this particular configuration will be denoted as ‘SNOR’, for Secondary Near-Orientation Relationship. One example of SNOR is shown in Figure 5. From the pole figures, we can see that one  $\{111\}$  pole of the nucleus  $\gamma_{n1}(A2)$  (colored in violet) forming from the A2  $\alpha$  grain (pink) is nearly parallel with the (0002) pole of the A1  $\alpha$  grain (orange) inside which it is growing. Note that, unlike  $\theta$ ,  $\omega$  is an unbiased angle.



**Figure 5:-** (a) Band contrast map representing the Type III grain boundary nucleation. The nuclei arising from each  $\alpha_2$  grain are highlighted along with their parent  $\alpha_2$  grains. (b) The pole figures of the  $\{0002\}$  and  $\langle 11\bar{2}0 \rangle$  of the  $\alpha_2$  grains: A1 and A2, and the pole figures of the  $\{111\}$  and  $\langle 110 \rangle$  of the  $\gamma_m$  nuclei:  $\gamma$  (A1) and  $\gamma$  (A2).

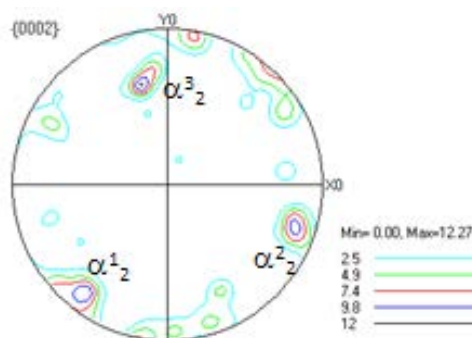
Table 2 reports the number of SNOR occurrences measured for the three types of grain boundaries present in Figure 1.



**Table 2:** Experimental and theoretical occurrences of SNOR for different types of grain boundaries

				<i>Theoretical calculation</i>	
				<i>Textured sample analyzed</i>	<i>Random texture</i>
<i>Number of grain boundaries analyzed</i>	41	14	9	10,000	10,000
<i>2 SNOR (%)</i>	10	14	0	10	4
<i>Only 1 SNOR (%)</i>	7	14	33	12	12

Two different configurations have been considered: a) when both  $\alpha$  grains could give a  $\gamma_m$  nucleus in SNOR with the other grain or b) when only one  $\alpha$  grain could give it. In order to decide if SNOR could favor nucleation or not, it is necessary to compare these experimental data to ‘normal’ statistics expected from the texture of the sample. These statistics were numerically calculated with an algorithm involving 10,000 draws of crystallographic orientations for couples of  $\alpha$  grains, then a search for the SNOR occurrence using the same criterion as presented before (see ref. [43] for more details on the algorithm). Two different orientation distributions were considered for the calculation, a random one and a textured one. The former considered randomly distributed crystallographic orientations, while the latter was used to take the actual texture of the sample into account. This texture was estimated from the orientations of  $\alpha_2$  grains present in the EBSD map of Figure 1. Their pole figure, reported in Figure 6, shows that three orientation poles – noted  $\alpha_2^1$ ,  $\alpha_2^2$  and  $\alpha_2^3$  – have been reinforced by the extrusion process. This strong specific texture was modeled by an orientation distribution presenting three equivalent orientations with a Gaussian dispersion around them.

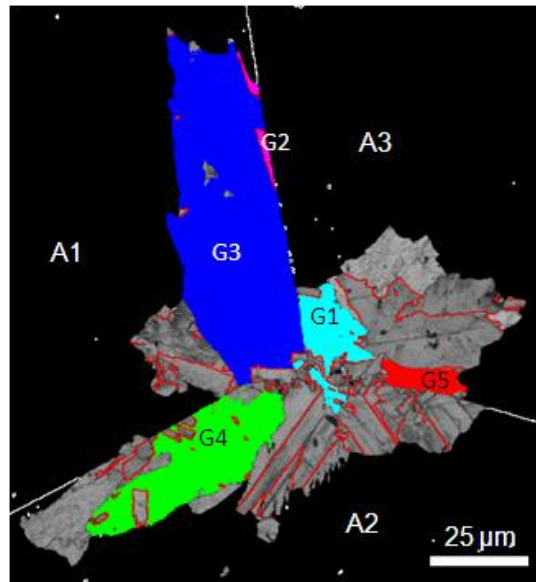


**Figure 6:-**  $\{0002\}$  pole figure of  $\alpha_2$  phase obtained from the EBSD texture measurements of the sample.

The last two columns in Table 2 report the theoretical percentages of SNOR occurrences calculated for both random and textured distributions. It can be seen that a higher ratio of SNOR is expected in the sample due to the extrusion texture. From Table 2, it appears that the ratio of SNORs measured for Types I and II grain boundaries is relatively close to the

expected one when taking the texture of the sample into account. On the contrary, the experimental number of Type III grain boundaries presenting only one SNOR seems to be much higher than the theoretical one, whereas no Type III grain boundaries with two SNOR were found at all. Although a definitive conclusion is difficult to assume with regard to the relatively small number Type III grain boundaries analyzed in Table 2, these results suggest that the existence of one SNOR could be associated with the development of  $\gamma_m$  domains on both sides of an  $\alpha/\alpha$  grain boundary. This point will be discussed later.

Such detailed statistical analysis has not been made for triple junctions, since in that case two neighboring grains are candidates for a  $\gamma_m$  domain developing in the third one. With the six EBSD maps done with high resolution, it is seen that the dominant nucleation mechanism is similar to the Type II case, though one of the nucleus often presents a SNOR with one of the  $\alpha$  grains. Figure 7 shows an EBSD map with the nucleus from each  $\alpha$  grain highlighted in different colors. The measured angles between the  $\{0002\}$  planes of the  $\alpha$  grains and the  $\{111\}$  planes of the  $\gamma_m$  nuclei are reported in Table 3. It appears that each  $\alpha$  grain has given at least one  $\gamma_m$  nucleus, and that the nucleus G1 is in SNOR with A3 grain.



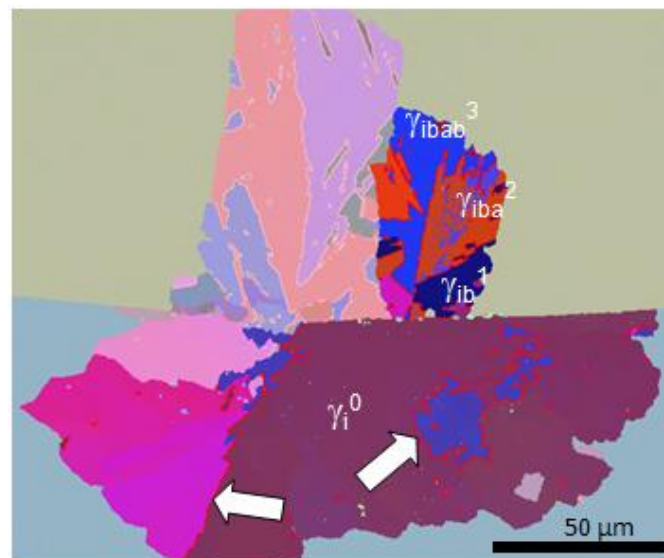
**Figure 7:-** Band contrast map, highlighting only the nucleus arising from each  $\alpha_2$  grain. The orientation relationship between the different  $\gamma$  nuclei with the three  $\alpha_2$  grain is given in Table 3.

**Table 3:** Measured angles between the  $\{0002\}$  planes of the  $\alpha$  grains and the  $\{111\}$  planes of the  $\gamma_m$  nuclei shown in Figure 7.

$\gamma_m$ nucleus/ $\alpha_2$ grain	Orientation relationship between the $\alpha$ and $\gamma_m$ grains
G1/A1	(111)//(0002)
G1/A3	(111) $\approx 5^\circ$ deviated from (0002)
G2/A3	(111)//(0002)
G2/A1	(111) $\approx 15^\circ$ deviated from (0002)
G3/A3	(111)//(0002)
G4/A1	(111) $\approx 2^\circ$ deviated from (0002)
G5/A2	(111)//(0002)

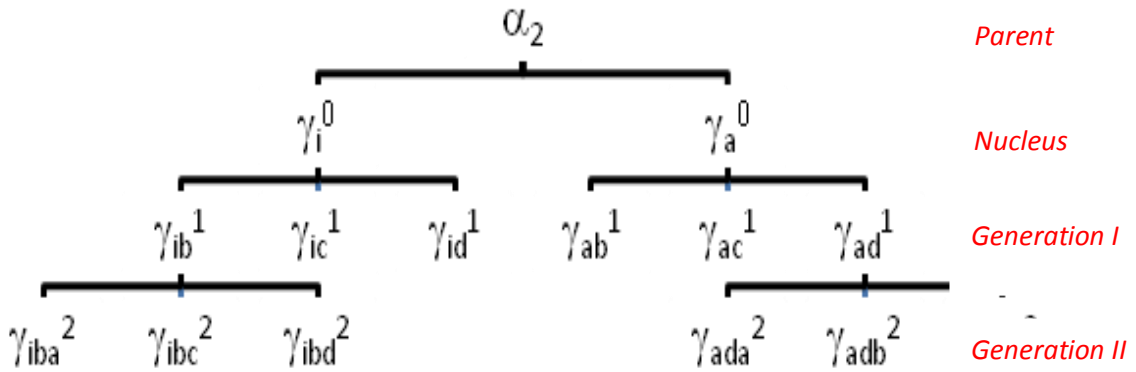
### 3.4 Crystallography of the growing massive sub-domains

After nucleation, massive phase develops rapidly. Extensive analysis of several OIM's of  $\gamma_m$  domains along grain boundaries and triple junctions shows that their growth always involves successive  $\{111\}$  twinning events. Indeed, for any grain in a given domain, it is always possible to find a path leading from the crystallographic orientation of one nucleus of the domain to the orientation of this grain by successive  $\{111\}$  twinning relations. For example, on the OIM in Figure 8 where the  $\{111\}$  twins boundaries are colored in red, the grain  $\gamma_{ibab}^3$  shows a twin relationship with  $\gamma_{iba}^2$ , which itself is a twin of  $\gamma_{ib}^1$ , which originates from the nucleus  $\gamma_i^0$  by twinning. By this process, what we will call a 'sub-domain' hereafter is a set of grains generated from a same nucleus though several generations of twin variants (cf. Figure 2). Note that the nucleus and the successive twin generations showed in Figure 8 developed on both sides of the Type III grain boundary. This point will be discussed later.

**Figure 8:-** An EBSD map showing a typical Type III grain boundary nucleation. The brighter region in the map corresponds to a sub-domain where all the grains are generated from the

nuclei by successive twinning. The two different arrows shows the curved and the planar interface of the grains having a  $\{111\}$  twinning relationship.

As schematized in Figure 9, the process of growth by  $\{111\}$  twinning generates different orientations (hereafter, called 'growth variants') at each twinning step. As explained earlier, there are two possible nuclei in BOR with a  $\alpha$  grain, which are  $\{111\}$  twin related. Noting their common twinning plane as (111), each nucleus can form three different variants with twinning planes:  $(\bar{1}11)$ ,  $(\bar{1}\bar{1}1)$ ,  $(1\bar{1}\bar{1})$ . Indeed, the (111) one is excluded from the four equivalent  $\{111\}$  twins because it restores the orientation of the other nucleus. The set of six new variants coming from the two nuclei constitutes the first generation of growth by twinning. In the same way, each variant of the first generation can give rise to three different variants. Consequently the second generation is formed by 18 variants. On the schema of Figure 9, the different variants are represented as a tree<sup>4</sup>. The twin orientation relationship between the parent variants is represented by a bold line and the different levels of branching correspond to the different generations of twins. It is clear that, except for the parent variants, two variants from the same generation are not twin related. Consequently, neighboring grains in a given sub-domain can show no particular twin relationship with each other, even though they all result from a chain of twinning events starting from the same nucleus.

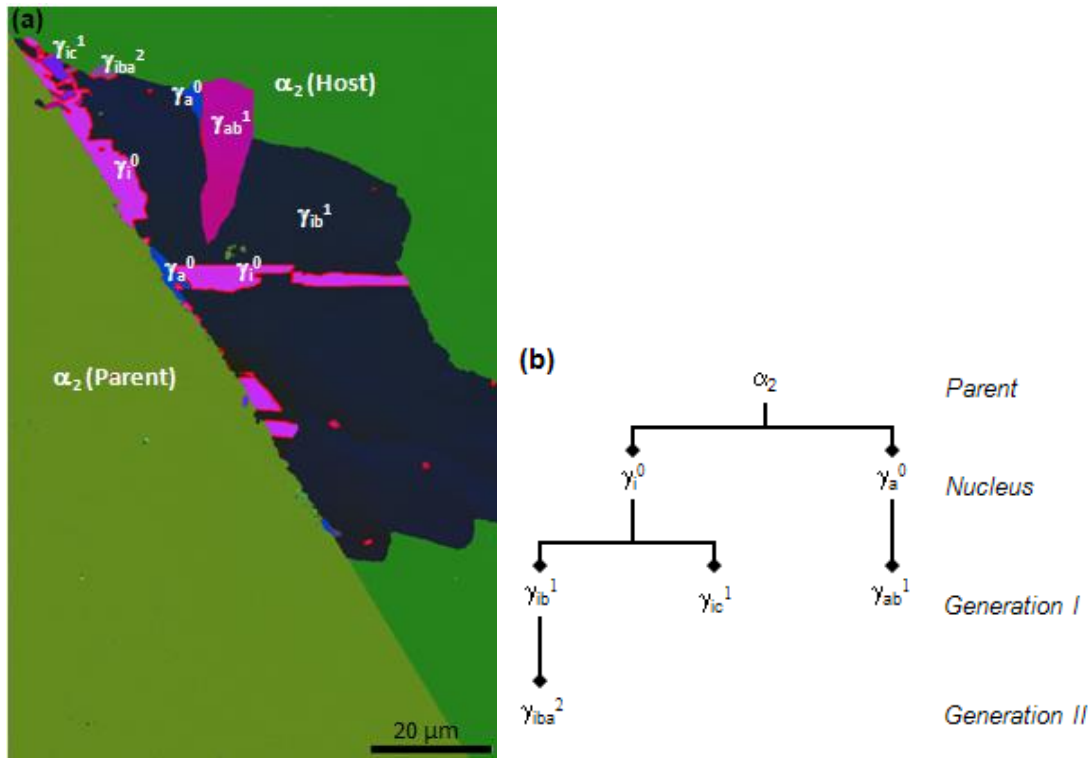


**Figure 9:-** Schematic representation showing the propagation of the massive domains forming different generations through twinning.

Although this process is clearly effective, analysis on the EBSD data shows that not all different possible  $\gamma_m$  twin variants are formed at a given generation, i.e., it seems that there is also a trend for variant selection during growth. This selection can be realized at two stages: first, during growth of the two twin-related  $\gamma_m$  nuclei, one often observe that one of these variants develops on the detriment of the other; second, there is also a selection among the  $\gamma_m$  variants appearing at the twinning stage. Usually, one or two out of the three equivalent  $\gamma$  variants are missing at each generation. To illustrate this variant selection, Figure 10(a) shows the Euler-angle image of a  $\gamma_m$  domain developed on a Type II grain boundary. Figure 10(b) classifies the different  $\gamma_m$  variants selected at each generation, which

<sup>4</sup> Notation of the different variants: the exponent is the number of generations and the index is formed by the identity or the twins in the order of increasing generations. (The identity and the twins with a twinning plane (111),  $(-111)$ ,  $(1-11)$  and  $(11-1)$  are noted, respectively, i, a, b, c and d). The generation 0 corresponding to the two nuclei is  $\gamma_i^0$  and  $\gamma_a^0$ . For the next generations,  $\gamma_{ibc}^2$  for example, corresponds to a variant obtained from the nucleus first by a twin  $(-111)$  and second by a  $(1-11)$  twin. Note that the order of the twins is important because the twinning operation is not commutative. So  $\gamma_{ibc}^2$  corresponds effectively to an orientation different from  $\gamma_{icb}^2$ .

are also indicated on the map. It is clear that the proportion of each twin variant arising from a  $\gamma_m$  grain is different. Also, in the first generation arising from the nucleus  $\gamma_i^0$ , one twin variant does not appear at all. In case of the other nucleus  $\gamma_a^0$ , only one twin variant out of the three possible forms. Hence the variant selection is realized in both the selection of the nucleus and the growth of the massive during twinning.



**Figure 10:-** (a) Euler angle map showing the different twin generations formed. (b) The twins selected for the growth are shown in the schema, though two generations of growth has taken place, not all the variants are formed.

## 4. Discussion

### 4.1 Nucleation in BOR

The nucleation of the massive transformation in TiAl alloys is heterogeneous. It is mainly inter-granular, either at triple junctions or at grain boundaries. Although it has not been observed in the present work, it can also sometimes be intra-granular, along elongated  $\alpha$  twins inside the prior  $\alpha$  grains, as established in a previous study [32]. From the large collection of data analyzed in the present paper, we can claim that, whatever the nucleation sites, there is always at least one nucleus which follows a strict Blackburn orientation relationship (BOR) with one of the  $\alpha$  grains (parent grain). Then, this nucleus grows into the adjacent  $\alpha$  grain with which it has no orientation relationship (host grain), forming an incoherent  $\alpha/\gamma$  interface. In the literature, there is some inconsistency among the different experimental studies regarding the orientation relationships followed by  $\gamma_m$  nuclei. Wittig [23], capturing the first stages of nucleation and growth, claimed that the  $\gamma_m$  nuclei have

always a BOR with an  $\alpha$  grain; Wang *et al.*, [25] reported that the  $\gamma_m$  nuclei often have a BOR with an  $\alpha$  grain but they also observed  $\gamma_m$  nuclei having substantial deviation from this exact BOR. This inconsistency could come from the criterion used to identify a  $\gamma_m$  grain as a nucleus. In the present study, after establishing that growth exclusively proceeds by twinning, we define the nuclei as the grain from which all the other grains of a  $\gamma_m$  sub-domain originate by successive twinning. Using this definition, a  $\gamma_m$  grain extending along an  $\alpha$  grain boundary is not necessarily a nucleus. For example, as we can see on Figure 10 (a), the pink colored grains noted  $\gamma_i^0$  and the light blue colored grains noted  $\gamma_a^0$  along the  $\alpha_2$  grain boundary have been identified as nuclei because all the other grains of the domain can be obtained from them by twinning. They are in BOR with the  $\alpha$  grain. On the contrary, the dark blue  $\gamma_m$  grain noted  $\gamma_{ib}^1$  also partly lies along the  $\alpha$  grain boundary. It has no specific orientation relationship with the  $\alpha$  grain but it is not considered as a nucleus because it comes from one of the nuclei (in red color) by twinning. Adopting this criterion to define a  $\gamma_m$  nucleus, a strict BOR is systematically found between a  $\alpha$  grain and any nucleus located along grain boundaries (Types II and III in Table 1) or triple junctions.

Plitcha and Aaronson [11] have done similar study on massive transformation in a different alloy, AgAl system. The fact that the nucleus has a coherent interface presenting a specific orientation relationship with its parent grain is in agreement with their work. They found that almost all the nuclei had a Burgers orientation relationship with the parent grains, with a very few numbers slightly deviating by 1–2°. Moreover, our results are in agreement with their nucleation kinetics calculations, the conclusion of which was that incoherent nucleation of the massive product is highly improbable [11]. On the contrary, our results are rather in disagreement with the nucleation kinetics calculation by Veeraraghavan *et al.*, [26] on a TiAl- based alloy. Indeed, they showed that incoherent nucleation is expected at triple junction (grain corner) and quadruple points (grain edge), though we experimentally found that, whatever be the nucleation sites including triple junctions, there is always one nuclei which follows a strict BOR with one of the  $\alpha$  grains.

## **4.2 Variant selection during nucleation**

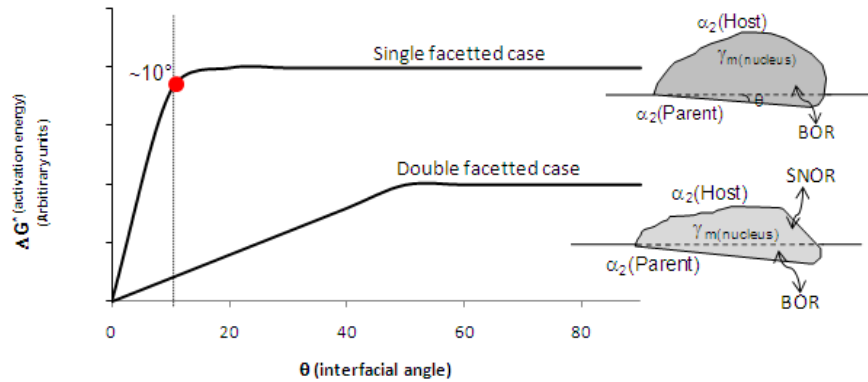
Theoretically, along the prior  $\alpha/\alpha$  grain boundaries, each  $\alpha_2$  grain can give rise to two  $\gamma_m$  nuclei in  $\{111\}$  twin relationship; hence, at each grain boundary four  $\gamma_m$  nuclei can be formed. However, in the OIM of Figure 1, a large fraction of grain boundaries and a few triple junctions do not bear any  $\gamma_m$  domain. Moreover the grain boundaries with  $\gamma_m$  domains do not present all the four possible nuclei: most often only one  $\alpha$  grain is fertile and consequently  $\gamma_m$  domain develops on only one side of the grain boundary. This means that there is a strong variant selection at the nucleation stage.

The most favorable nucleation sites and configurations are associated with the lowest values of activation energy for nucleus germination. Considering a coherent  $\gamma_m$  nucleus at a  $\alpha/\alpha$  grain boundary (also called single- faceted nucleus in the literature ), it is possible to neglect in a first approximation the strain energy because of the small volume fraction and of the small lattice mismatch through the coherent interface boundaries, as it is the case for the BOR between  $\alpha$  and  $\gamma$ . Thus, the activation energy for nucleation essentially depends on the interfacial energy. A nucleus will form if the interface energy balance - including the contributions of disordered  $\alpha/\alpha$  grain boundary, disordered nucleus/matrix  $\gamma/\alpha$  boundary and ordered faceted nucleus/matrix  $\gamma/\alpha$  boundary (ies)- becomes sufficiently low.

It has been theoretically showed by Lee and Aaronson [44, 45] that intergranular nucleation is at best possible when the grain boundary plane is parallel or nearly parallel to the habit plane corresponding to a low energy interphase boundary, as illustrated in Figure 11 for a single faceted nucleus. In the case of  $\alpha$  and  $\gamma$  phases in TiAl alloys, the lowest energy interphase boundary is the  $(0002)_\alpha // \{111\}_\gamma$  and  $\langle 11\bar{2}0 \rangle_\alpha // \langle 110 \rangle_\gamma$ . Consequently,  $\gamma_m$  nucleation is expected to be favorable when the grain boundary plane is parallel or nearly parallel to the (0002) plane. Moreover, these authors found that the interfacial energy increases with increasing angle between the grain boundary plane and the habit plane up to a critical value beyond which the energy saturates.

This type of variant selection for nucleation, also called “minimum angle criterion” is clearly effective in the nucleation of the  $\gamma_m$  massive transformation. A typical example of variant selection for nucleation is shown in Figure 4. The  $\alpha$  grain with  $\theta = 2^\circ$  is fertile, while the other (sterile)  $\alpha$  grain shows a very large value of  $\theta$ . More statistically, for the Type II grain boundaries (nucleation along one side; see Table 1), the apparent angles between the grain boundary traces and the  $\{00.2\}_\alpha$  habit plane of fertile grains ( $\theta_B^*$  mean value) are significantly lower than the angles between the grain boundary traces and the  $\{00.2\}_\alpha$  habit plane of sterile grains ( $\theta_A$  mean value). Large values of  $\theta$  are also measured in the case of Type I grain boundaries (no nucleation on any side;  $\theta_A$  and  $\theta_B$  mean values in Table 1). The value of the critical angle below which nucleation occurs,  $\theta_C$ , can be roughly estimated in the order of  $10^\circ$ .

However, this “minimum angle criterion” sometimes goes unsatisfied, i.e., the value of  $\theta$  for the  $\alpha$  grain which gives a nucleus can be higher than  $\theta_C$ . This kind of nucleation is reported in Table 1 under Type III nucleation, which corresponds to grain boundaries with nucleation on both sides; one example is shown in Figure 5. For this type of nucleation, the nucleus follows the BOR with its parent  $\alpha$  grain and has, in addition, a secondary near-orientation relationship (SNOR) with the grain inside which it is growing. It means that the nucleus has two coherent or semi-coherent low energy boundaries, one with its parent grain and the other with the host grain. This nucleus is often called double faceted nucleus in the literature [44, 46]. Lee and Aaronson [44] calculated the nucleation energy of such nucleus with two facets. Similar calculations were done by Adachi et al., [46], for the nucleation of inter-granular precipitates in Ni-Cr alloy. The Figure 15 from this reference [46] is reproduced here in Figure 11 for better understanding. From this figure, we can see that, for a given angle between the grain boundary plane and the habit plane, the activation energy of nucleation for a double faceted nucleus is smaller than for a single faceted nucleus, i.e., the critical angle over which no nucleation can occur is higher. A few nuclei of this type were also viewed by Plichta et al., [11] in Ag-Al alloy during massive transformation. Adachi et al., [46] analyzed the minimum-angle variant selection of inter-granular precipitates in a Ni-Cr alloy. They also noted that precipitates with the lower  $\theta$  values are not always the selected ones, but that sometimes precipitates with higher  $\theta$  values nucleate.



**Figure 11:-** A schematic representation of the activation energy for nucleation according to the angle between the habit plane and the grain boundary plane for the case of the single faceted nucleus and double faceted nucleus.

To observe two low energy facets during nucleation, one of the four equivalent  $\{111\}$  planes of the nucleus has to be parallel to the  $\{00.2\}_\alpha$  plane of the parent grain, and, in addition, another one has to be parallel with the  $\{00.2\}_\alpha$  plane of the host grain. Considering that a low energy interphase boundary is formed when the maximum deviation between one  $\{111\}$  pole of the  $\gamma_m$  nucleus and the  $(0002)$  pole of the matrix  $\alpha$  is lower than  $10^\circ$ , the angle between the  $(0002)$  poles for two neighboring  $\alpha$  grains must range between  $60^\circ$  and  $80^\circ$ . In our case, the probability to find two  $\alpha$  grains with this angle between their  $(0002)$  poles was relatively high because of the initial extrusion texture of the sample. Hence the chance of finding a nucleus with SNOR is high in comparison with a sample with random texture. An example is given in Figure 5. The angles between the grain boundary plane and the  $\{00.2\}_\alpha$  habit planes on both sides,  $\theta_A$  and  $\theta_B$  are higher than  $10^\circ$ , nevertheless in one side, a  $\gamma_m$  nucleus,  $\gamma$  (A2), is formed because it is double faceted. In addition with the BOR with one of the  $\alpha$  grain, A2, there is a SNOR with the other  $\alpha$  grain, A1.

However, as the coherent interphase boundaries are known to have a low mobility, a nucleus in SNOR is expected to be stagnant. Besides, this problem of interface mobility is also the reason why a nucleus in BOR does not grow into its parent  $\alpha$  grain but in the opposite  $\alpha$  grain with which it has, generally, an incoherent interphase boundary [42]. But if the interphase boundary, instead to be incoherent, is coherent or semi-coherent due to a specific SNOR, it will not be so mobile and the nucleus should be stagnant. EBSD maps as the one of Figure 5(a) have to be carefully analyzed to explain how  $\gamma_m$  domains can even develop in spite of this mobility limitation. Due to the SNOR, the first  $\gamma_m$  nucleus in Figure 5(a) is stagnant. But another  $\gamma_m$  nucleus  $\gamma$ (A1), can form on the other side of the  $\alpha$  grain boundary which, in addition to the BOR with the  $\alpha$  grain noted A1, has a low angle grain boundary and thus a low energy boundary with the previous  $\gamma_m$  nucleus, as we can see on the  $\{111\}$  poles figures in the Figure 5(b). This second nucleus is double faceted, but one facet is an interphase boundary between  $\alpha$  phase and the  $\gamma_m$  nucleus, whereas the other is a grain boundary between two  $\gamma_m$  grains. As the interphase boundary between this second nucleus and its host  $\alpha$  grain is incoherent, it can grow quickly and give different twin variants. To our knowledge, this mechanism of 'co-nucleation' where a nucleation occurs on a previous stagnant nucleus has never been identified.



On the contrary, if two SNOR's are found with both  $\alpha$  grains of a given grain boundary, both nuclei are expected to remain stagnant for reasons of interphase boundary mobility as mentioned above. This could explain why Type III grain boundaries seem to be associated with only-one-SNOR but not with two-SNOR configurations (cf. Table 2).

In summary, the mechanisms of nucleation explained above are consistent with the statistical results established from a large collection of data presented in the Table 2. It appears quite clearly that for Type II grain boundaries (nucleation along one side), the nucleation criterion is the "minimum angle criterion" i.e., the value of  $\theta$  for the  $\alpha$  grain which gives a nucleus is less than  $\theta_c$  which is estimated to be around  $10^\circ$ . For Type III grain boundaries (nucleation along both sides), the "minimum angle" appears not to be the dominant criterion. In that case, the favored nucleus has to have one SNOR with one of  $\alpha$  grains; the double faceted nucleus formed is stagnant but a second nucleus can form by co-nucleation on the other side of the  $\alpha$  grain boundary, then it grows and twins provided that there is not a SNOR with the other  $\alpha$  host grain. For both the criteria, the common character is the minimization of the interfacial energy which is the main factor governing the nucleation.

### **4.3 Variant selection during growth**

As mentioned previously, there is also a strong variant selection during growth. This selection operates at two stages: first, during growth of the two  $\gamma_m$  nuclei, often, one of these nuclei develops to the detriment of the other; second, during the twinning stage, one among the three equivalent  $\gamma$  variants is usually very predominant. But either for the nuclei or for the twin variants, growth is governed by the same factors. Among these factors, they are the elastic energy minimization and the mobility of the  $\alpha/\gamma$  interphase boundaries. The mobility of the interphase boundaries is likely the main factor because the growth of the massive transformation, which is very fast, is more dictated by kinetic factors than energetic factors. The mobility of the  $\alpha/\gamma$  interphase boundaries is dependent, among others, on the orientation relationship between the two phases, the nature of the boundary (i.e., coherent or incoherent) and the morphology of the boundary (i.e., planar or irregular). For the Ti-Al alloys, it is mentioned in the literature that there is often, although not always, a high-index/irrational orientation relationship between the  $\alpha$  parent and product  $\gamma$  phases; the habit plane is also often, but not always, high indexed [25]. These interfaces are essentially incoherent but they could also display one-dimensional matching of atom planes across the interface which is also called plane edge-to-edge/atom row matching [27-30]. Concerning the morphology of the interfaces, a cinematographic study of the massive transformation in Cu-Ga alloys has shown that growth of the massive phase occurs by the propagation of irregular as well as nearly planar interfaces [4]. We also observed that interfaces can be either highly curved or planar along the  $\{111\}$  twinning plane, as indicated by arrows in Figure 8. TEM observations by Howe *et al.*, [22] at the atomic scale have shown that apparently curved interfaces might be faceted along low index planes in the massive phase. Moreover, both ledge and continuous mechanisms of interface motion have been observed at the atomic level by Yanar *et al.*, [21] and during in-situ TEM studies by Howe *et al.*, [22]. From all these studies, it emerges that there is not still a clear picture of the structure of the interphase boundaries during the massive transformations and consequently, that the dependence of their mobility on the various crystallographic parameters is not fully understood. For these reasons, it is difficult, in the actual state of the knowledge, to

understand the mechanisms of the variant selection during growth. Further studies are necessary to bring out a rule for this selection.

## 5. Summary

In-depth examination of the morphology and crystallography of small  $\gamma_m$  domains developed along  $\alpha/\alpha$  grain boundaries or  $\alpha/\alpha/\alpha$  triple junctions in a TiAl-based alloy has been performed by SEM observations, high-resolution EBSD mapping as well as by statistical analysis of an EBSD map over a large and representative sample surface. This work allows to clarify the controversy concerning the existence or not of crystallographic relations between massive and parent phases. It clearly shows that strict crystallographic relationships are effective all along the massive-transformation process. Additionally, the statistical crystallographic analysis (i) enables classification of the different nucleation sites; (ii) points out the effectiveness of variant selection at both the nucleation and growth/twinning stages of the transformation; and (iii) proposes realistic mechanisms to explain it. These results are summarized hereafter by separating those regarding nucleation and growth stages of the  $\gamma$ -massive transformation.

### Nucleation:

- All nuclei of  $\gamma_m$  domains were systematically found to present a Blackburn Orientation Relationship (BOR, i.e.,  $(0002)_\alpha // \{111\}_\gamma$  and  $\langle 11\bar{2}0 \rangle_\alpha // \langle 110 \rangle_\gamma$  with one  $\alpha$  grain (parent grain) and to develop in the other (host grain).
- Favorable nucleation sites and configurations have been identified, which can be classified by decreasing order of efficiency: (a) triple junction; (b) grain boundary whose plane is close to the basal plane of one of the neighboring  $\alpha$  grains; (c) grain boundary for which one  $\gamma_m$  nucleus in BOR with one of the neighboring  $\alpha$  grains has another  $\{111\}$  plane closely parallel to the basal plane of the other  $\alpha$  grain (configuration denoted Secondary Near-Orientation Relationship or SNOR).
- Triple junctions are the most favorable sites due to i) the higher loss of  $\alpha/\alpha$  interface energy expected from  $\gamma_m$  nucleation and ii) the higher probability to fulfill one of the nucleation criteria associated with configurations b) or c).
- Configuration b) fulfils the “minimum-angle criterion” which has been theoretically proposed and already observed in others systems; it is associated with the development of the  $\gamma_m$  domain on only one side of the grain boundary.
- As well as we know, configuration c) is reported for the first time ; although favorable nucleation can be explained from interface energy considerations, the resulting nucleus is expected to be stagnant ; a ‘co-nucleation’ mechanism has been proposed, which explains how the  $\gamma_m$  domain can even develop and why its development takes place on both sides of the grain boundary.

### Growth:

- Whatever the nucleation process, further growth of  $\gamma_m$  phase always proceeds by successive twinning steps over  $\{111\}_\gamma$  planes ; consequently, each  $\gamma_m$  domain can be

divided in a limited number of subdomains in which every single grain originates from the same nucleus through twinning; in a given subdomain, no twin relationship exists between grains of the same generation, which could explain some inconsistency in the literature regarding the crystallography of  $\gamma_m$  phase.

- Selection of specific twin variants also takes place at each twin generation, either by sorting out some of the possible orientations at the twinning step or by promoting growth of only some activated variants; with regard to the complexity of microstructures and of the mechanisms involved, no clear selection criterion has been deduced at the present time, neither from observation nor from theoretical analysis.

## Acknowledgements

The authors are greatly indebted to Thibaut LARROUY of TURBOMECA for providing samples for the study. S. Sankaran would like to thank the research council of “Région Lorraine” for the financial support of her Ph.D.

## References

- [1] Massalski TB, Metall. Mater. Trans. A, 2002; 33A:2277.
- [2] Phillips A. Trans, AIME, 1930; 89: 194.
- [3] Massalski TB Acta Metall. 1958; 6: 243.
- [4] Kittl JE and Massalski TB, Acta Metall. 1967; 15: 161.
- [5] Hawbolt EB and Massalski TB, Metall. Trans. 1970; 1: 2315.
- [6] Bhattacharyya SK, Perepezko JH, Massalski TB Acta Metall. 1974; 22: 879.
- [7] Massalski TB, Metall. Mater. Trans. A, 1984; 15A: 421.
- [8] Massalski TB, Soffa WA, Laughlin DE, Metall. Mater. Trans. A, 2006; 37A:825.
- [9] Aaronson HI, Laird C, Kinsman KR, Scripta Metall. 1968; 2:259.
- [10] Plitcha MR, Rigsbee JM, Hall MG, Russell KC, Aaronson HI, Scripta Metall. 1976;10:1065.
- [11] Plitcha MR and Aaronson HI, Acta Metall. 1980; 28:1041.
- [12] Plitcha M. R, Clark W. A.T, Aaronson, Metall. Mater. Trans. A, 1984; 15: 427.
- [13] Plitcha MR Perepezko JH, Aaronson HI and Lange WF, Acta Metall. 1980; 28: 1031.
- [14] Aaronson HI, Metall. Mater. Trans A, 2002; 33A: 2285.
- [15] Aaronson HI, Mahajan S, Purdy GR and Hall MG, Metall. Mater. Trans. A, 2002; 33A:2347.
- [16] Aaronson HI, Metall. Mater. Trans. A, 2006; 37A: 803.
- [17] Aaronson HI, Vasudevan VK, Metall. Mater. Trans. A, 2002; 33A: 2445.
- [18] Aaronson HI, Reynolds W, Metall. Mater. Trans. A, 2006; 37A: 961.
- [19] Caretti JC, Kittl J E and Bertorello H R, Acta Metall. 1983; 31: 317.
- [20] Caretti JC and Bertorello HR, Acta Metall. 1983; 31: 325.
- [21] Yanar C, Wiezorek JMK, Radmilovic V, Soffa WA, Metall. Mater. Trans. A, 2002;33A:2413.
- [22] Howe JM, Reynolds WT, Vasudevan VK Metall. Mater. Trans. A, 2002; 33A:2391.
- [23] Wittig JE, Metall. Mater. Trans. A, 2002; 33A: 2373.
- [24] Veeraraghavan D, Ping Wang, Vasudevan VK, Acta Mater. 1999; 47: 3313.
- [25] Wang P, Veeraraghavan D, Kumar M, Vasudevan VK, Metall. Mater. Trans. A, 2002, 33A: 2353.
- [26] Veeraraghavan D, Wang P, Vasudevan VK, Acta Mater. 2003; 51: 1721.
- [27] Nie JF, Muddle BC, Metall. Mater. Trans. A, 2002; 33A:2381.
- [28] Reynolds Jr. WT, Nie JF, Zhang WZ, Howe JM, Aaronson HI, Purdy GR, Scripta Mater. 2003; 49: 405.

- [29]PM Kelly and M-X Zhang, Mat.Forum 1999; 23:41.
- [30]PM Kelly and M-X Zhang Metall and Mater. Trans.2006; 37: 833.
- [31]Dey SR, Bouzy E, Hazotte A, Intermetallics, 2006; 14: 444-449.
- [32]Dey SR, Bouzy E, Hazotte A, Scripta Mater. 2007; 57: 365.
- [33]Jones SA and Kaufman MJ, Acta Metall. Mater. 1993; 41:387.
- [34]Hu D, Huang AJ and Wu X, Intermetallics, 2007; 15: 327.
- [35]Blackburn M J, In: Jaffee, Promisel N E, editors. The Science, Technology and Applications of Titanium. Pergamon Press, Oxford; 1970: 633.
- [36]Dey SR, Morawiec A, Bouzy E, Hazotte A and Fundenberger JJ, Materials letters,2006; 60: 646-650.
- [37]Dey SR, Hazotte A, Bouzy E, Naka S, Acta Mater. 2005; 53: 3783.
- [38]Dey SR, Bouzy E, Hazotte A, Acta Mater. 2008; 56: 2051.
- [39]Chladil HF, Clemens H, Leitner H, Bartels A, Gerling R, Schimansky F.-P, Kremmer S, Intermetallics , 2006;14: 1194.
- [40]Charpentier M, Hazotte A, Daloz D, Mater. Sci. Eng. A, 2008; 491:321.
- [41]Zghal S, Naka S, Couret A, Acta Mater. 1997; 45: 3005.
- [42]Smith CS, Trans. ASM. 1953; 45:533
- [43]Humbert M, Germain L, Gey N, Bocher P, Jahari M, Mat. Sci. Eng. A, 2006; 430: 157.
- [44]Lee JK and Aaronson HI, Acta Metall. 1975; 23: 799.
- [45]Lee JK and Aaronson HI, Acta Metall. 1975; 23:809.
- [46]Adachi Y, Hakata K, Tsuzaki K, Mat. Sci. Eng A, 2005; 412: 252.

## Annexe C

# **Texture and microstructure evolution during tempering of gamma- massive phase in a TiAl-based alloy**

## **Texture and microstructure evolution during tempering of gamma-massive phase in a TiAl-based alloy**

A. Sankaran, E. Bouzy, J.J. Fundenberger, A. Hazotte \*

Laboratoire d'Etude des Textures et Application aux Matériaux (LETAM)  
CNRS/UPV-M/ENIM, Ile du Saulcy, 57045 Metz Cedex 1, France

*Published: Intermetallics*

### **Abstract**

This work focuses on the mechanisms of microstructure and crystallographic texture evolution during gamma-massive transformation and subsequent tempering treatments, in the case of the Ti-48Al-2Nb-2Cr (at %) TiAl-based alloy. A complete massive structure is obtained by iced-water quenching. The temperature range for the destabilization of this massive structure is estimated from DSC measurement. Then, tempering is performed in both  $\alpha_2 \rightarrow \gamma$  and  $\alpha \rightarrow \gamma$  phase fields. Microstructure evolution is studied by transmission and scanning electron microscopy observation of samples from different stages of the heat treatments. Isotropic samples resulting from a powder-metallurgy route are used for this purpose. Then, working on samples from investment-casting, the reduction of solidification texture through massive then tempering treatments is analyzed at the light of the mechanisms of microstructure evolution identified previously.

### **1. Introduction**

TiAl-based intermetallics alloys have been studied for a long time owing to their attractive structural properties like high specific strength and stiffness at high temperatures. However, they also present certain disadvantages like poor ductility and low toughness at room temperature. Actually, the mechanical behavior of these alloys strongly depends on their microstructure and crystallographic texture [1, 2]. For instance, grain refinement obtained through thermo-mechanical routes was shown to produce more attractive mechanical properties [3-6]. However, these processes are expensive and difficult to control, due to the high strength and reactivity of these alloys. On the other hand, near-shape casting appears as an attractive and direct elaboration process, but it results in coarse-grained microstructures and large mechanical anisotropy due to a sharp solidification texture. Heat treatments inducing gamma-massive ( $\gamma_m$ ) transformation are now considered as a possible way to refine the grains and to smooth the texture without modifying the original shape of the cast component [7, 9].

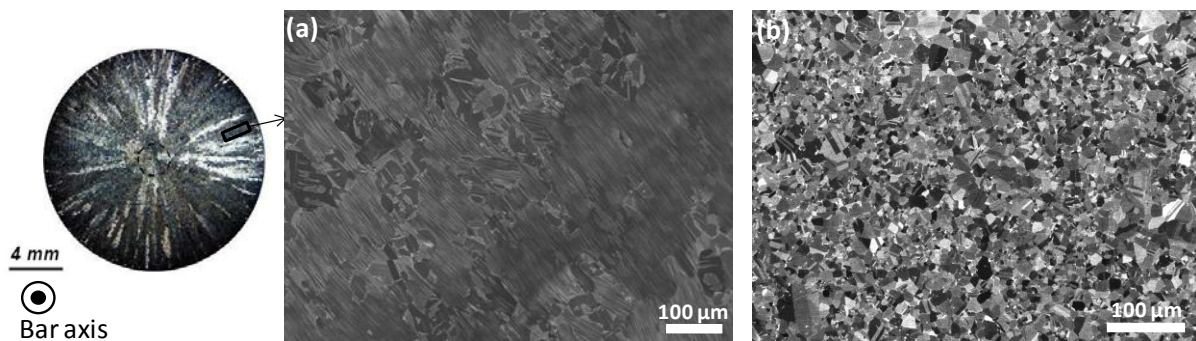
Different types of microstructures can be obtained by continuously cooling TiAl-based alloys from their high-temperature  $\alpha$  domain, depending on the cooling rate used. Whereas  $\alpha_2$ - $\gamma$  lamellar, Widmanstätten and feathery structures develop over large distances in orientation relationship with their  $\alpha$  host grains [10-12], gamma-massive phase is constituted of numerous small  $\gamma$  grains showing no specific orientation relationship with the  $\alpha$  grain inside which they develop [13-16]. Therefore,  $\gamma_m$  transformation is expected to induce grain refinement and texture reduction. However, massive grains are highly out-of-equilibrium and contain high internal stresses [7-8] and defects such as dislocations, stacking faults and anti-phase boundaries [15]. Some works have been performed to obtain stable microstructures by tempering of massive phase, while retaining low grain sizes [7-8,

17-19]. For instance, H. Clemens *et al.* [7] achieved grain sizes of 30 – 65 $\mu\text{m}$  starting from coarse lamellar grains, by means of multiple heat treatments including massive transformation then tempering in the  $\alpha$ - $\gamma$  domain. Destabilization of massive phase starts by the precipitation of  $\alpha$  particles either within the  $\gamma_m$  grains or at the  $\gamma_m/\gamma_m$  grain boundaries [17, 18]. These  $\alpha$  precipitates coarsen during the isothermal heat treatment, and then eventually decompose into  $\alpha_2$ - $\gamma$  lamellae during cooling to room temperature. This finally results in complex microstructures which strongly depend on the tempering parameters (heating and cooling rates, temperature and duration of isothermal treatment, etc). Only fewer studies are devoted to this field and they are mostly focused on the optimization of these process parameters only, whereas the mechanisms of precipitation are not very well known. In particular, it has not been clearly established if the destabilization of the massive phase can also take place in the low-temperature  $\alpha_2$ - $\gamma$  domain. If it would be the case, tempering heat treatments within this field would be expected to promote finer microstructures by using longer –thus easier to control- heat treatments. Moreover, though it is often stated that massive transformation also reduce the crystallographic texture of as-cast TiAl alloys, there has not been any study on the texture of the massive phase and on its evolution during subsequent tempering heat treatments.

The aims of the present work are a) to detect the earlier stage of destabilization of the gamma-massive phase during heating from room temperature, b) to analyze the  $\alpha_2/\alpha$  precipitation mechanisms during tempering in both  $\alpha_2$ - $\gamma$  and  $\alpha$ - $\gamma$  domains and c) to follow the crystallographic texture evolution of a cast product at every steps of complete (massive transformation then tempering) optimizing heat treatments.

## 2. Materials and Methods

The material under study was the Ti-48Al-2Nb-2Cr (at %) TiAl-based alloy. Specimen resulting from both investment-casting and powder-metallurgy routes were used. Their initial microstructures are shown in Figure 1. As-cast (AC) samples were elaborated by investment casting followed by a HIPing step. They are mostly composed of very large and elongated grains with alternate  $\alpha_2$ - $\gamma$  lamellae; powder metallurgy (PM) microstructure results from high-temperature HIPping then slow cooling, thus it shows small  $\gamma$  grains with a small amount of  $\alpha_2$  phase at their triple junctions. In the following, PM samples will be used to analyze the mechanisms of  $\gamma_m$  destabilization in order to avoid any texture effect, while texture evolution during heat treatments will be studied using AC samples.



**Figure 1:** Initial microstructures of Ti-48Al-2Nb-2Cr (at %) samples elaborated through (a) investment-casting- low magnification optical micrograph and the insert is high magnification micrograph of the cast microstructure (b) powder-metallurgy routes.

## 2.1 Heat treatments

Both AC and PM samples ( $\phi 16\text{mm} \times 40\text{mm}$  for AC and  $15\text{mm} \times 15\text{mm} \times 40\text{mm}$  for PM) were quenched in brine water maintained around  $-5^\circ\text{C}$ , after an isothermal treatment for 15 min under argon in the  $\alpha$  domain ( $\sim 1365^\circ\text{C}$ ). Due to thermal gradient and to possible surface contamination by oxygen, the resulting microstructure was heterogeneous at the sample scale: only  $\alpha_2$  phase was present close to the surface of the specimen; completely massive microstructure was found in its inner part, with a very small amount of  $\gamma$ -feathery structure at the center. Samples were extracted from a completely massive zone to perform Differential Scanning Calorimetry (DSC) experiments using a DSC 404 Pegasus apparatus from Netzsch. They were subjected to two successive thermal cycles from room temperature to  $1100^\circ\text{C}$ , using heating and cooling rates of  $20\text{ K/min}$ . From the results obtained by DSC, different heat treatments were designed and performed. All brine water quenched samples were heated at  $5^\circ/\text{min}$ , then isothermally heat treated at different temperatures during different times, and finally quenched in air. All heat treatments were performed in a constant flow of argon. The different heat-treatment parameters used in the present work are reported in Table 1. PM samples were treated at low temperatures and for rather short times in both  $\alpha_2-\gamma$  and  $\alpha-\gamma$  domains, whereas AC samples received longer isothermal heat treatments in  $\alpha_2-\gamma$  and  $\alpha-\gamma$  domains.

**Table 1:** Sample dimensions and heat treatments performed on AC and PM TiAl alloy.

Processing Technique	Initial Sample Dimensions	Heat treatment 1	Heat treatment 2
As-cast sample	16 mm $\phi$ , height 40mm	Ice Quenching $\rightarrow$ Massive microstructure	i) $1050^\circ\text{C}$ , 2hrs ii) $1250^\circ\text{C}$ , 2hrs
Powder Metallurgy	15 mm x 15 mm x 40 mm	Ice Quenching $\rightarrow$ Massive microstructure	i) $900^\circ\text{C}$ , 30 sec ii) $1100^\circ\text{C}$ , 30 sec iii) $1100^\circ\text{C}$ , 20 min

Hardness measurements were carried out on each treated sample, using a Vickers microhardness tester applying a load of 500g. At least 10 indentations were performed per sample.

## 2.2 Microstructure characterization

All heat treated samples were mechanically polished and electrolytically etched in a solution of 90% methanol and 10% perchloric acid, under 17 V for 70 sec. They were observed using a Scanning Electron Microscope (SEM) equipped with a Field Emission Gun (FEG). Quantitative analysis of phase volume fraction was carried out using the APHELION image treatment software [22]. The different phases present in the microstructure were discriminated on the basis of their grey-level contrast on high resolution backscattered electron (BSE) images. Crystallographic orientation mapping was performed through Electron BackScattered Diffraction (EBSD), using either low resolution ( $20\ \mu\text{m}$ ) or high resolution ( $0.2\ \mu\text{m}$ ) step sizes. EBSD technique gave information concerning local texture and orientation relationships between phases, but also grain size distributions as a function of heat treatments. Note that the low tetragonality of the face centered tetragonal  $\gamma$  phase ( $c/a$  ratio equal to 1.016), which is associated with long-range ordering, cannot be detected

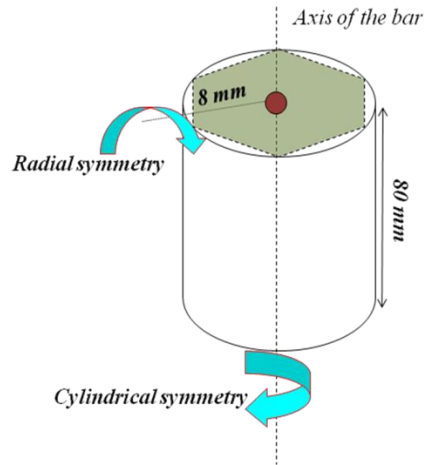


through SEM/EBSD technique performed under standard mapping conditions [23-24]. Therefore, any single  $\gamma_m$  grain detected by EBSD is considered to have a cubic symmetry and may contain three ordered domain variants.

Transmission Electron Microscopy (TEM) was used to image the different phases at higher magnification and to determine their individual crystallographic orientations. It was performed on thin foils electrolytically prepared in a solution of 60% methanol, 35% butylglycol and 5% perchloric acid under 17 V. In that case, the different order variants of  $\gamma$  phase can be discriminated by indexing the sub-lattice bands of their Kikuchi patterns. This was performed using a software called Euclid's Phantasies (EP), which has already been presented in detail elsewhere [25].

### **2.3 Texture measurement**

The crystallographic texture of the  $\gamma$  phase was measured by X-Ray Diffraction (XRD) on samples issued from the as-cast material through the different heat treatments reported in Table 1. These AC samples were cut perpendicular to a cylinder of diameter 16 mm. For all samples having undergone the massive transformation, grain size was small and texture was accurately measured directly on flat surfaces perpendicular to the cylinder axis. Texture measurement was more delicate for the as-cast sample. As illustrated in Figure 1(a), the initial microstructure was very coarse and exhibits a strong anisotropy resulting from the solidification process. Except for the small equiaxed zone of about 1.5 mm diameter in the center of the sample, the ( $\alpha_2$ - $\gamma$ ) lamellar grains were mostly columnar with lengths of several hundred micrometers extending along the radial direction. Therefore, pole figures measured on perpendicular surfaces were not significant since they only concerned a few grains. In order to obtain statistically reliable results, an as-cast specimen was machined in the shape of a cylinder with hexagonal basis as represented in Figure 2. Pole figures were measured along the six tangential planes parallel to the bar axis. Assuming that these planes are equivalent, 'mean' pole figures were obtained by the addition of the six measured sets. For an easier comparison with other samples, texture of the as-cast material was simulated from this tangential measurement by taking into account the cylindrical bar symmetry. This finally permitted to use the same representation for all pole figures from the different samples. As experimental conditions for the X-ray measurements are different for the sample before and after massive transformation, they are summarized in Table 2.



**Figure 2:** Schematic representation of the as-cast specimen used for the texture measurement. The specimen was cut along the six faces and the measurements were done perpendicular to the axis of the bar.

**Table 2:** Experimental conditions for X-ray texture measurement of different samples.

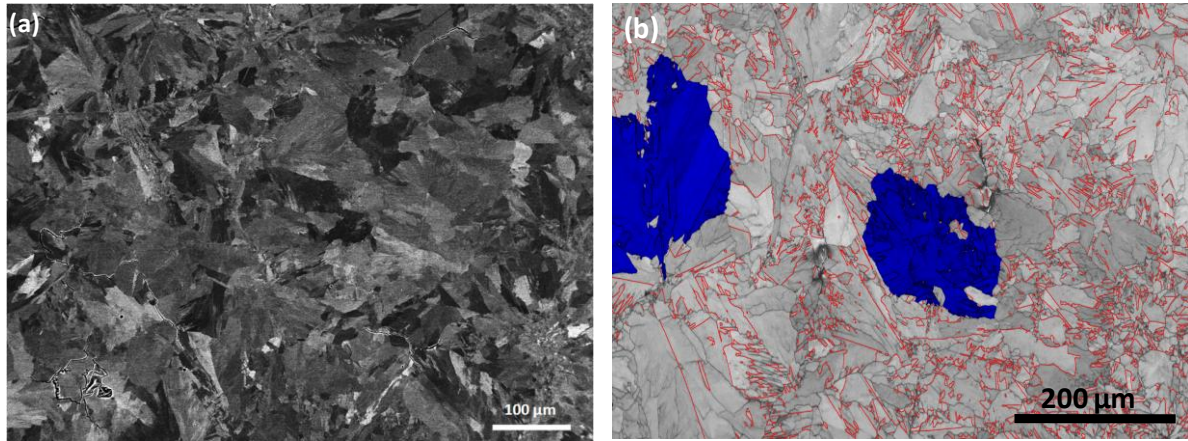
Microstructure	Apparatus Type	Detector	Radiation	Step Size	Area scanned
As-Cast	Self built goniometer based on a Microcontrol-Nex port cradle and a RIGAKU rotating anode	INEC	Cu-K $\alpha$	Azimuth: 5° Declination 5°	$\phi$ 0.8 mm x 5mm (on each face (ref. Fig 2) totally six faces)
Massive Massive + 1050°C Massive + 1250°C	Self- built Huber Goniometer	LYNXEYS Bruker	Co-K $\alpha$	Azimuth: 5° Declination 2.5°	$\phi$ 0.8 mm x 10mm (on three different area)

### 3. Results and Discussion

#### 3.1 Structure and stability of $\gamma_m$ phase

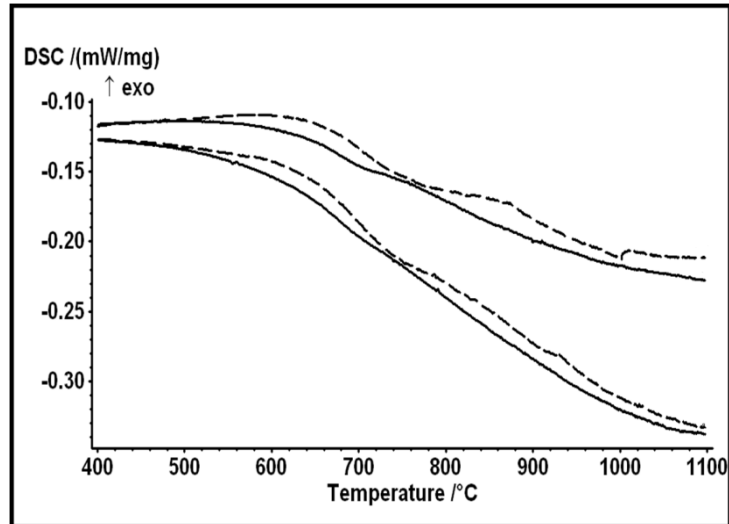
Figure 3 shows the gamma-massive microstructure of the PM sample quenched in brine-water, when observed in two different imaging modes. These micrographs illustrate the main features of  $\gamma_m$  phase which have been largely discussed in previous works [13-16, 26]. At SEM scale,  $\gamma_m$  phase is formed of small equiaxed grains with a large size distribution: their average size is about 35  $\mu\text{m}$ , with a large number of grains ranging between 1 $\mu\text{m}$  and 60 $\mu\text{m}$  and a few ones with a size up to 100 $\mu\text{m}$  (volume fraction around 15%). The boundaries of massive grains appear blur and irregular. EBSD mapping (Figure 3 (b)) makes it possible to define the grain limits and shows that two neighboring  $\gamma_m$  grains are often in twin relationship over their  $\{111\}_\gamma$  planes (as explained in § 2.2,  $\gamma$  phase is considered to have a cubic symmetry). This relationship results from the specific  $\gamma_m$  transformation mechanisms which involve successive twinning events during growth [13, 14]. Order domains can be imaged using transmission microscopy [12]. At the TEM scale,  $\gamma_m$  grains are also found to

contain a large number of crystal defects such as dislocations, stacking faults and anti-phase boundaries [15].



**Figure 3:-** Massive microstructure observed using different modes: (a) Low magnification BSE micrographs (b) EBSD micrograph ('band-contrast' representation); the red lines corresponds to boundaries between neighboring grains in twin relationship; the blue regions correspond to sets of  $\gamma$ -massive grains which have grown by the process of successive twinning (see the text for details).

Several DSC experiments were performed to detect the  $\gamma_m$  de-stabilization temperature range. Examples of DSC curves recorded during heating from room temperature up to 1100°C are given in Figure 4. Although small, a difference was systematically detected between the thermal flux recorded during the first and the second heating steps performed on the same sample. This perturbation always takes place between 500°C and 950°C. Observation of samples heat treated at 900°C confirmed that the massive structure is no more stable at this temperature (see next paragraph). These results are in agreement with the previous ones obtained by Clemens *et al.* [7] on two different but similar TiAl-based alloys: from the analysis of XRD peaks measured on samples heat treated every 100°C starting from 400°C, these authors evaluated the  $\gamma_m$  de-stabilization temperature range around 800°C, i.e. in the  $\alpha_2/\gamma$  domain.

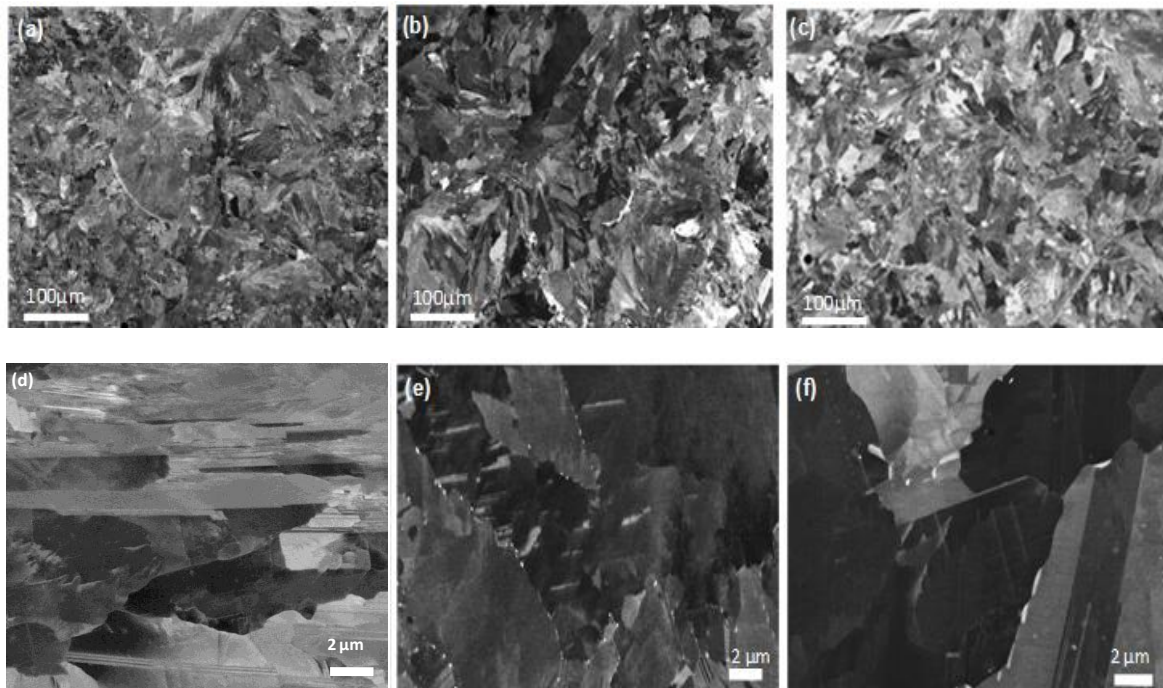


**Figure 4:-** DSC curves during successive heating at 20 °C/min. of two different samples initially presenting a gamma-massive microstructure: dotted lines are recorded for the first heating stages ( $\gamma_m$  structure) whereas plain lines correspond to the second heating stages (stabilized microstructure)

## 3.2 Mechanisms of phase transformation

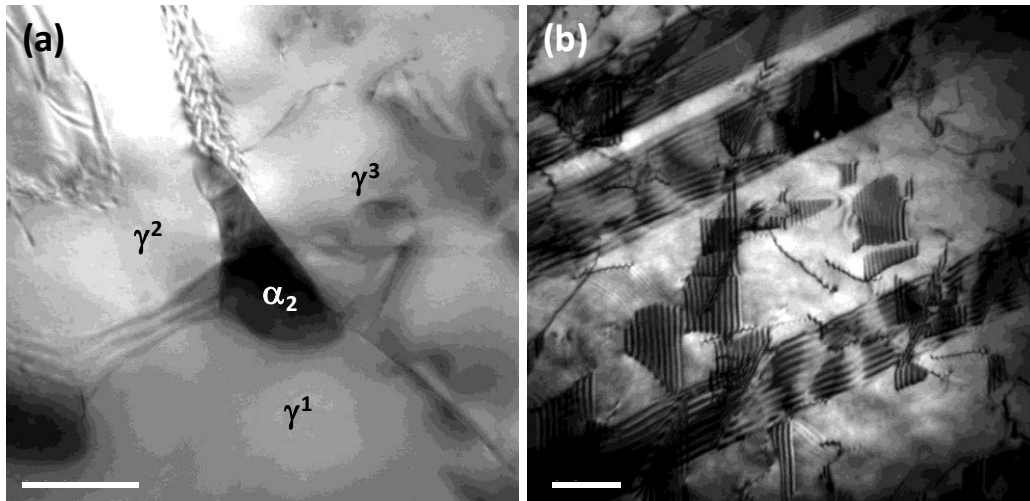
### 3.2.1 Nucleation sites and characteristics of the $\alpha_2$ phase

Figure 5 (a-c) shows low magnification SEM micrographs of different heat treated PM samples: as-quenched (a) and aged for 30 sec. at 900°C (b) and 1100°C (c). At this scale, there is no significant grain size evolution as a result of heat treatment.



**Figure 5:-** SEM microstructures of the samples analyzed (a) massive microstructure (b) massive +900°C, 30 sec, (c) massive + 1100°C, 30 sec, (d) (e) and (f) are the corresponding high resolution images.

At higher magnifications, Figure 5 (d-f),  $\alpha_2$  precipitation is detected in all heat treated samples. At 900°C,  $\alpha_2$  precipitates with a globular morphology and of the order of few nanometers in size can be seen along certain grain boundaries. TEM investigations show that the precipitation of these globular  $\alpha_2$  takes place predominantly along triple junctions of grain boundaries, along high angle  $\gamma_m/\gamma_m$  grain boundaries and at triple junctions formed between Ordered Domain Boundaries (ODB) and high angle boundaries. These  $\alpha_2$  precipitates follow a strict Blackburn Orientation Relationship (BOR), i.e.  $\{111\}_\gamma // \{0002\}_{\alpha_2}$  and  $\langle 110 \rangle_\gamma // \langle 11\bar{2}0 \rangle_{\alpha_2}$  [27], with one of the  $\gamma_m$  grains. As an example the  $\alpha_2$  precipitate shown in Figure 6 (a) follows a strict BOR with the  $\gamma_3$  grain (parent grain), which was deduced from their corresponding Kikuchi patterns. In term of morphology, this relationship linking the  $\alpha_2$  precipitate and its  $\gamma_3$  parent grain is also manifested by the existence of a  $\{111\}_\gamma$  inter-phase boundary (or ‘facet’) between them. It is also worthwhile to note that numerous defects present in the massively transformed phase, such as the stacking faults illustrated in Figure 6(b), were still present after the heat treatment at 900°C.



**Figure 6:-** TEM micrographs taken from specimen heat treated at 900°C for 30 sec (a)  $\alpha_2$  precipitate at a  $\gamma_m$  triple junction; (b) stacking faults generated during the massive transformation.

The isothermal heat treatment at 1100°C for 30 sec. resulted in the coarsening of the globular  $\alpha_2$  (Figure 5(f)), accompanied by a relative smoothing of the initially irregular  $\gamma/\gamma$  grain boundaries. In addition, thin acicular  $\alpha_2$  precipitates are detected in the interior of  $\gamma_m$  grains. These  $\alpha_2$  platelets have a mean width of about 200 nm (Figure 7(a)). TEM investigations showed that they all present a strict BOR with their host  $\gamma_m$  grain (see patterns of Figure 7 (a)). In some cases these  $\alpha_2$  platelets cross the whole  $\gamma$  grain, but they are also often stopped at ODB's, as in the case of plates A and B in Figure 7(b).  $\alpha_2$  plates with different orientations can also be found in a given grain.

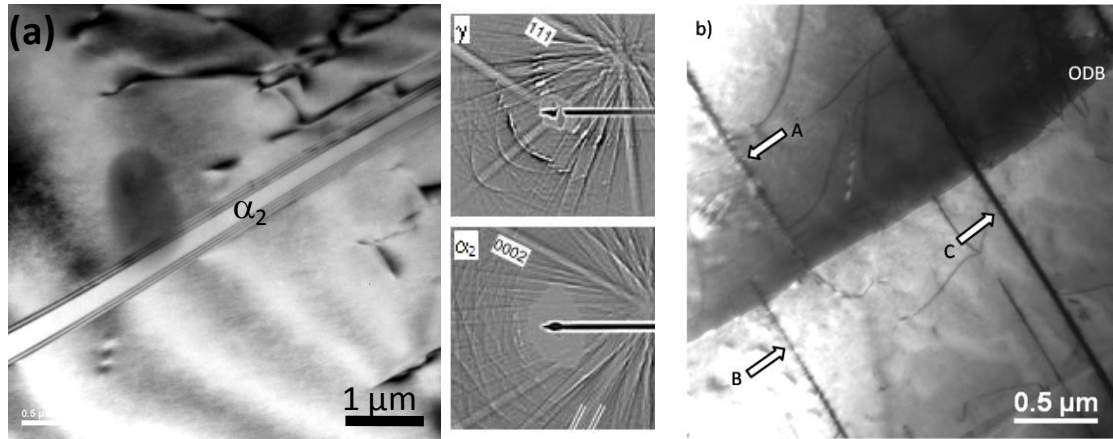
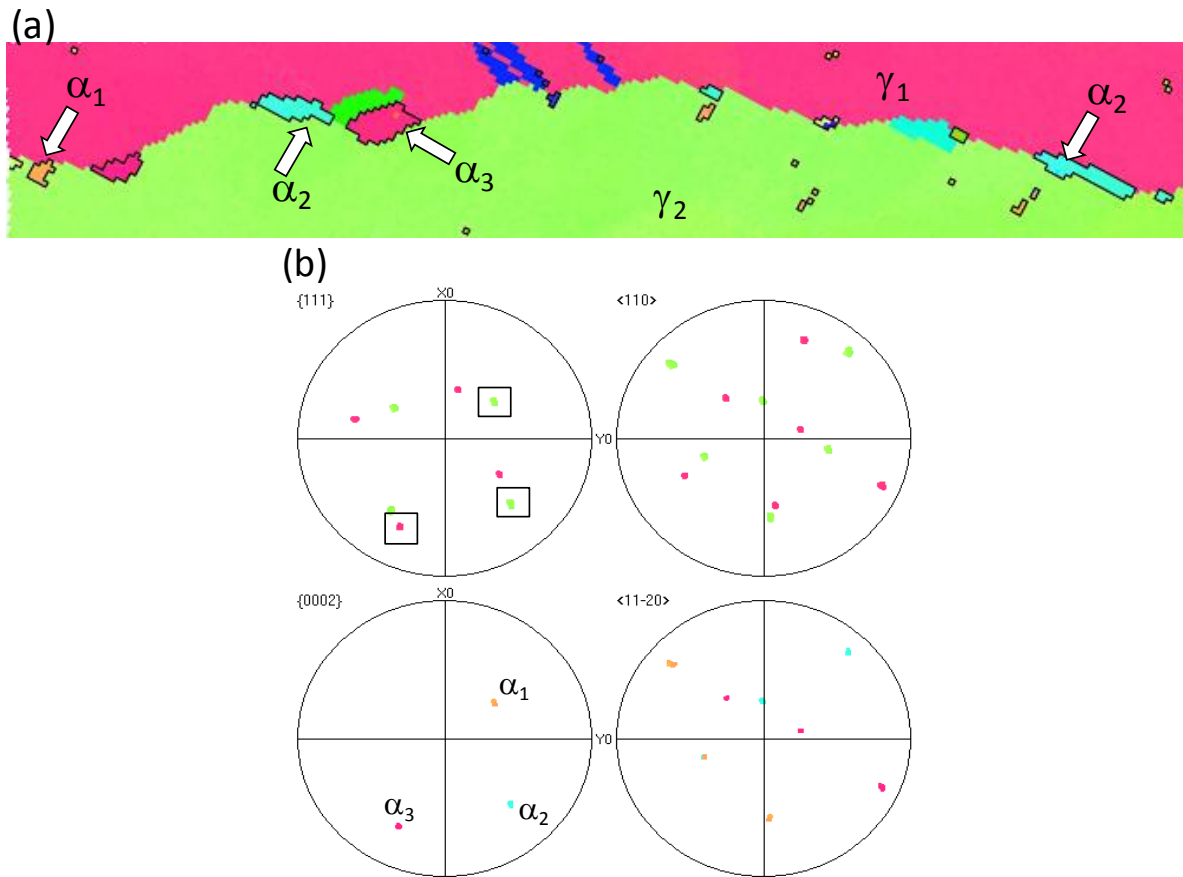


Figure 7: TEM micrographs from the sample heat treated at 1100°C for 30 sec after massive transformation: a) acicular  $\alpha_2$  precipitate inside  $\gamma$  grain interiors, with their corresponding Kikuchi patterns. (b)  $\alpha_2$  platelets pinned at an ODB

The nucleation sites of globular  $\alpha_2$  precipitates observed in the present study are mostly  $\gamma_m/\gamma_m$  high angle grain boundaries and triple junctions, which is in agreement with the observations of Kumagai *et al.* [17]. Zhang *et al.* [18] also reported nucleation of globular  $\alpha_2$  precipitates on stacking faults, on dislocations and within  $\gamma$  grains. However, these authors studied the destabilization of massive phase when rapidly heated and treated for different times in the  $\alpha$  domain. In that case, the driving force for the  $\gamma_m \rightarrow \gamma + \alpha$  transformation should be very high, thus all defects are expected to be possible nucleation sites. In the case of massive phase heat treated at 900°C, we have no statistical evidence that others sites than grain boundaries could be activated, although a few globular  $\alpha_2$  precipitates were occasionally spotted over stacking faults. A globular  $\alpha_2$  precipitate located along a grain boundary or at a triple junction always shows a  $\{111\}_\gamma$  facet with the neighboring  $\gamma$  grain with which it is in BOR (Figure 6(a)). Four different orientation variants of  $\alpha_2$  can form *a priori* in BOR with one  $\gamma_m$  grain, thus eight  $\alpha_2$  variants are expected along a  $\gamma_m/\gamma_m$  grain boundary, provided that the two neighboring  $\gamma_m$  grains do not share any specific orientation relationship. When several variants are possible at a given grain boundary, Lee and Aaronson [28] inferred from theoretical considerations that the one with its habit plane closest to the grain boundary plane has the lowest nucleation energy. This theory, called ‘minimum angle criterion’, was experimentally validated in several systems. In particular, in the case of  $\gamma_m$  nucleation at  $\alpha/\alpha$  grain boundaries of TiAl-based alloys, it allowed to explain that an orientation variant is often dominant along a given grain boundary plane [14]. This criterion appeared to be realistic (see for instance Figure 6(a) where the trace of the precipitate facet is close to the trace of the  $\gamma_m/\gamma_m$  grain boundary) and has been often observed by EBSD in many cases. As noted before,  $\gamma_m/\gamma_m$  grain boundaries are very irregular. This means that the local orientation of grain boundary plane changes from place to place. Therefore, several orientation variants can be expected along a given grain boundary, even if the ‘minimum angle criterion’ is locally valid. This situation is illustrated in Figure 8(a); it was effectively often observed.



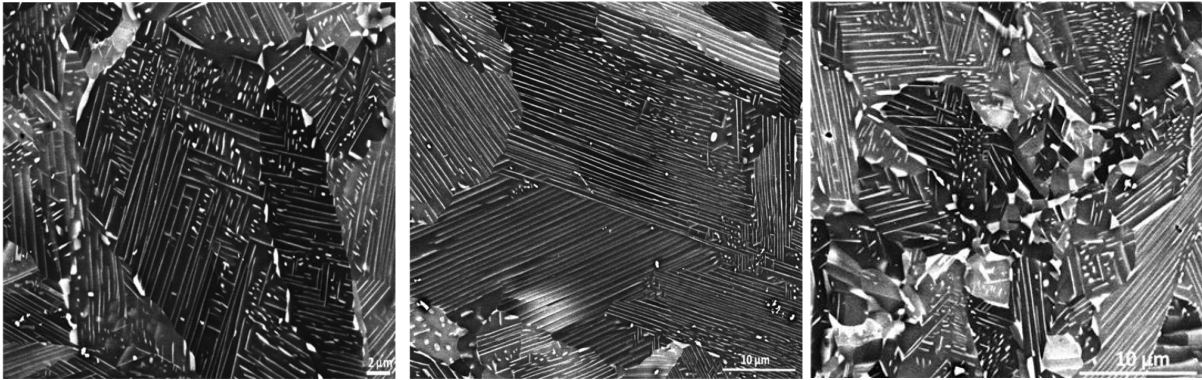
**Figure 8:-** EBSD map and the corresponding pole figures of the  $\alpha_2$  and  $\gamma$  phases, showing that the  $\alpha_2$  precipitates always follow a strict BOR with one of the  $\gamma$  grain and that several variants of  $\alpha_2$  precipitates are formed along the same grain boundary.

TEM investigations showed that the density of stacking faults (SF) was considerably reduced during ageing at 1100°C when compared to 900°C. The  $\alpha_2$  platelets seem to form over the SF's, which was viewed in the specimen heat treated at 900°C. These observations are similar to those made by Brooks *et al.* in stainless steel during a similar phase transformation [29]. Generally in FCC,  $\frac{a}{2}\langle 110 \rangle$  unit dislocations can dissociate to give a stacking fault on  $\{111\}$  separated by two Shockley partials. These SF's are actually closed packed layers of HCP. Therefore, they are potential nucleation sites for the  $\alpha_2$  phase. The thickening of the resulting platelets is expected and verified to be very slow, because of the coherent character of their interfaces. On the other hand, their development in both sides along the SF is more efficient. Thus, they lengthen until they reach a grain boundary, another  $\alpha_2$  platelet or an ODB.

### **3.2.2 $\alpha_2$ coarsening and morphological evolution**

Figure 9 shows some SEM micrographs typical of the PM sample heat treated at 1100° C for 20 min. When compared with the sample treated for 30 sec at the same temperature, it is evident that the same types of  $\alpha_2$  precipitates are present but that their coarsening has taken place during ageing. These results are in contradiction with those of Kumugai *et al.* [17] who reported the nucleation of a second population of thin  $\alpha_2$  platelets after 1 hr ageing, and noted that the thickness of the initially formed platelets hardly

increased. The number of orientations, as well as the relative volume fraction of  $\alpha_2$  platelets differs from one  $\gamma$  grain to another. Certain grains enclose two or three tangled families of platelets (Figure 9 (a)), whereas others present a morphology similar to the lamellar microstructure, with large areas showing only one orientation of the  $\alpha_2$  platelets (Figure 9 (b)). The density and volume fraction of globular  $\alpha_2$  precipitates also appear heterogeneous. In comparison with Figure 9 (a) and (b), Figure 9 (c) shows a region with a higher number of coarser globular precipitates. This increase in  $\alpha_2$  globular precipitates is associated with a local depletion of  $\alpha_2$  platelets and with the presence of smaller  $\gamma$  grains. A careful analysis of these regions suggests that they could be mainly located near the ex- $\alpha/\alpha$  grain boundaries.

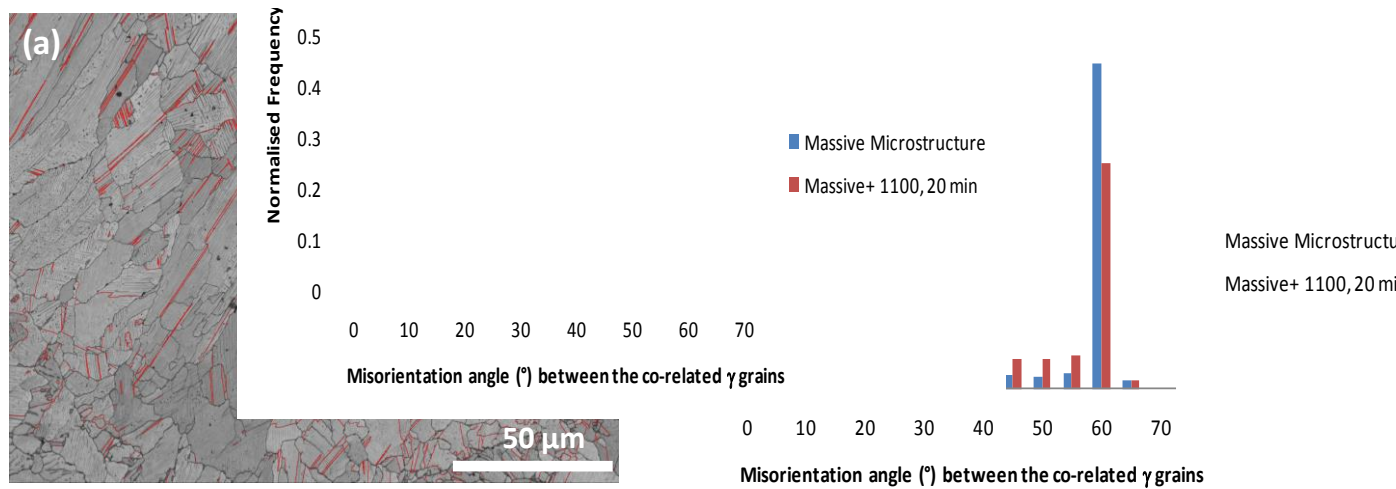


**Figure 9:-** SEM micrographs of the specimen heat treated at 1100°C for 20 min showing (a) (b) two typical grain structures with  $\alpha_2$  globular precipitates and  $\alpha_2$  platelets, and (c) a region with a high amount of coarse globular precipitates.

One explanation of this non-expected heterogeneity in the  $\alpha_2$  phase spatial distribution could be found in the crystallographic features of the initial massive structure. It has been previously showed that this structure develops by nucleation of numerous small  $\gamma_m$  grains at the  $\alpha/\alpha$  grain boundaries, a part of which subsequently grows within the  $\alpha$  grains through a mechanism involving several successive  $\{111\}_\gamma$  twinning steps [13, 14]. Consequently, a lot of  $\gamma_m/\gamma_m$  grain boundaries within the ex- $\alpha$  grains are low-energy twin boundaries. Using a dedicated SEM/EBSD procedure, it is even possible to detect 'sub-domains' constituted of  $\gamma_m$  grains, all resulting from the same nucleus through this twinning process [13, 14]. As an example, Figure 3 (b) highlights twin boundaries in red and two sub-domains in blue on an EBSD map of the massive PM sample. It is worthwhile to note that the density of twin boundaries appears lower on the EBSD maps of the PM sample heat treated at 1100°C for 20 min as can be seen from Figure 10. With regard to these observations and remarks, we propose that  $\alpha_2$  globular precipitates nucleate preferentially at high-energy  $\gamma_m/\gamma_m$  grain boundaries, rather than at twin boundaries. Therefore, due to the massive transformation process, the density of such favorable nucleation sites would be higher near the ex- $\alpha/\alpha$  grain boundaries. During further heating and ageing, these globular precipitates are expected to grow more rapidly to the detriment of platelets, especially because of the higher diffusion kinetics along misoriented boundaries. In the meantime, their presence also hinders the movement of grain boundaries, which finally tends to conserve small grain sizes. On the other hand, the nucleation density of  $\alpha_2$  globular precipitates is expected to be lower in the interior of the ex- $\alpha$  grain, since restricted to the boundaries between sub-domains. Consequently, the population of platelets would be higher and their evolution during ageing would contribute to the development of larger



multi-lamellae grains. This transformation model also suggests that the size distribution –or at least the mean size- of  $\gamma_m$  sub-domains (rather than of  $\gamma_m$  grains) in the initial massive structure could be an important quantitative characteristic to forecast the grain size after ageing.



**Figure 10:** (a) Band contrast EBSD map showing the reduced number of  $\gamma$ -massive sub-domain in a sample heat treated at 1100°C for 20 min. (b) Histogram showing the misorientation between the neighboring  $\gamma$  grains in a massive microstructure and massive microstructure heat treated at 1100°C for 20 min.

### 3.3 Texture evolution

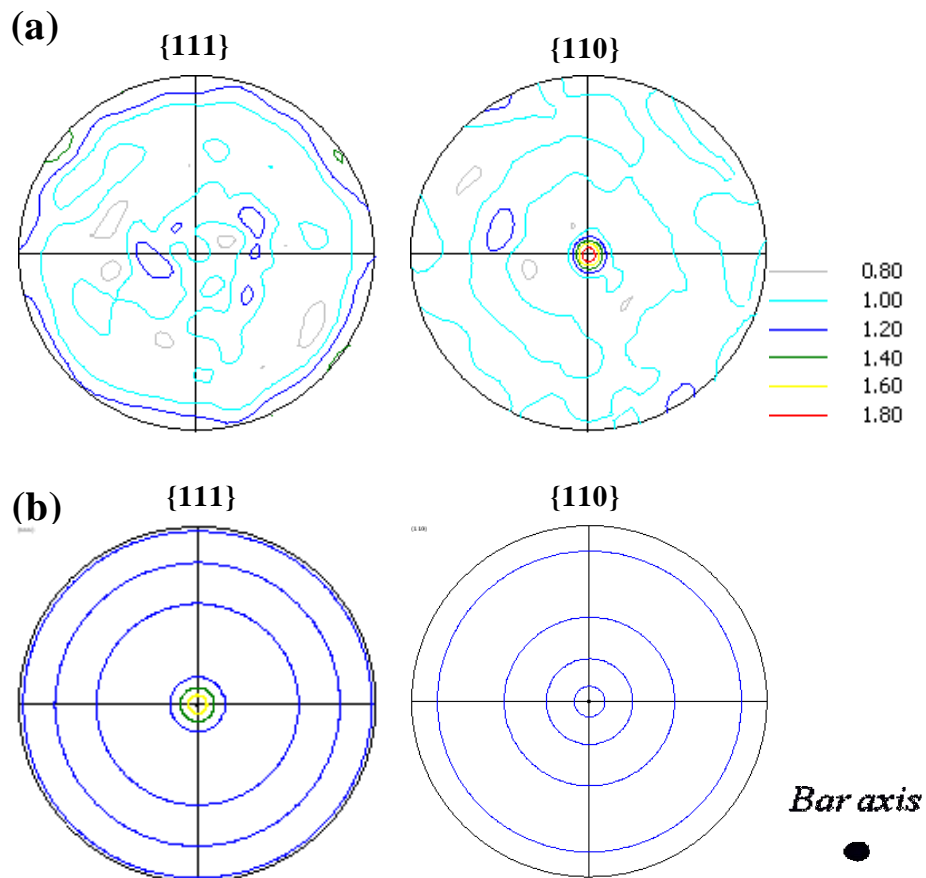
This part mainly focuses on the crystallographic texture evolution during ageing treatments made in the  $\alpha_2 + \gamma$  and  $\alpha + \gamma$  phase field, starting from a  $\gamma$  massive microstructure as a precursor. For this purpose, we worked with samples resulting from the conventional casting route (AC). Their textures were analyzed at successive steps of the heat treatment: a) initial state ('as-cast' sample, initial microstructure illustrated in Figure 1 (a)), b) after quench inducing massive transformation (microstructure similar to the one of Figure 3) and after long isothermal ageing treatments made either c) in the  $\alpha_2 + \gamma$  phase field (1050°C for 2 h) or d) in the  $\alpha + \gamma$  phase field (1250°C for 2h). For comparison, an as-cast sample was also heat treated at 1250°C for 2h, leading to a conventional 'duplex' structure. Due to the low amount of  $\alpha_2$  phase present in the different samples, only the texture of  $\gamma$  phase was investigated, considering it as a cubic phase.

#### 3.3.1 As-cast structure

The texture was analyzed in a volume mainly composed of columnar grains extending along the radial direction from the border towards the center of the sample, with a mean length of around 1 mm and a mean width of about 80 μm. Low amount of monolithic  $\gamma$  grains were found interspaced between the  $\gamma$  grains which are induced by the HIPping stage (Figure 1.a). The equiaxed zone in the center was not considered for the texture analysis. The columnar grains presented a  $\alpha_2 + \gamma$  lamellar microstructure. Therefore, in order to obtain statistically reliable results, the pole figures were measured along six tangential planes according to the procedure explained in Section 2.3. Significant amount of the sample has been removed from the surface to avoid any effect in the texture from the

chill zone. The poles figures reported in Figure 11 (a) correspond to a fiber texture where the  $\{110\}_\gamma$  planes are perpendicular to the radial direction. However, the maximum of pole density is only 1.90 times the random distribution, indicating that the texture is not very prominent. Except for the as-cast texture measurement, all the other pole figures were measured on a section perpendicular to the bar axis. Hence for an easier comparison, the as-cast texture of the bar was simulated from the pole figures measured along the tangential planes by taking into account the cylindrical bar symmetry. The corresponding  $\{111\}_\gamma$  and  $\{110\}_\gamma$  pole figures represented in the section perpendicular to the bar axis are displayed in Figure 11 (b).

The texture obtained is similar to the one reported by Clemens *et al.* [30] for an as-cast Ti-48Al alloy. However, it differs in both the nature and the sharpness from the texture measured by A. Bartels *et al.* [31] on a Ti-48Al-2Cr. Indeed the latter was a relatively strong fiber texture with the  $\{111\}_\gamma$  planes perpendicular to the radial direction. This kind of texture is characteristic of TiAl alloys solidifying through the  $\alpha$  domain. In that case, hexagonal  $\alpha$  dendrites grow with their [0001] direction parallel to the heat flow direction. The subsequent solid phase transformation produces a lamellar microstructure with a BOR between  $\gamma$  and  $\alpha_2$ , resulting in a fiber texture with the  $\{111\}_\gamma$  planes perpendicular to the radial direction. However, the solidification and solid-phase transformation path of TiAl-based alloys is known to be dependent not only on alloy composition, [32, 33] but also on residual oxygen content, solidification rate and geometry of the solidification mold [34].



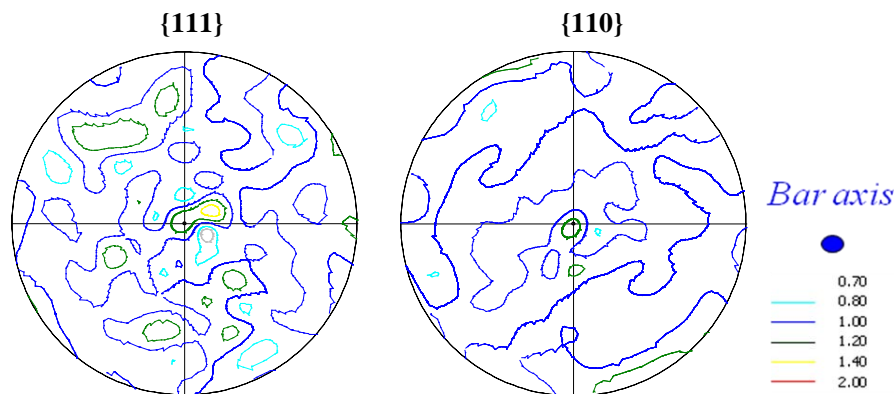
**Figure 11:-** (a) Pole figures of the as-cast specimen measured along the tangential directions. (b) Simulated pole figures of  $\{111\}$  and  $\{110\}$  parallel to the axis of the bar.

In particular, the low solidification texture intensity observed in the present work could result from a solidification path passing through the ( $\beta$  + liquid) peritectic domain.

Indeed, in a binary Ti-48Al alloy, the solidification path first crosses the peritectic  $\beta$ + liquid domain (until the composition of Al is 49 at %) [34]. Ternary alloying elements have a major influence on the initial solidification phase. While considering from a thermodynamic point of view, in the case of GE alloy, having alloying elements like Cr and Nb, which are  $\beta$  stabilizers excludes, the possibility of passing through  $\alpha$  as its first solidification phase. The effect of oxygen on the transformation temperature and phase domain is not significant since the alloy contains less than 1500 ppm of oxygen [20]. From the kinetics point of view, the solidification rate must be as high as 300 mm/h to have  $\alpha$  as the first transformation phase from liquid [35]. But from the pole figure which shows a  $\{110\}$  fiber texture, it is clear that the first transformation phase is not  $\alpha$  but could be  $\beta$ , because solidification through  $\alpha$  domain will result in a  $\{111\}_\gamma$  fiber texture. During transformation through  $\beta$  the preferential growth direction is along  $[100]_\beta$  [32]. Following the Burger's orientation relationship during transformation to  $\alpha$  ( $\{110\}_\beta // \{0002\}_\alpha$ ,  $\langle 111 \rangle_\beta // \langle 11\bar{2}0 \rangle_\alpha$ ) one  $\beta$  orientation can give 12 crystallographic  $\alpha$  orientations. Then, during the transformation from  $\alpha \rightarrow \gamma$ , one  $\alpha$  orientation can give six distinct orientations of  $\gamma$  [36]. Hence, solidification through  $\beta$  should result in spreading of  $\gamma$  orientations at room temperature, therefore in a weak texture. Since the purpose of the present work was not to explain the origin of the solidification texture, no deeper investigation was performed in this direction.

### 3.3.2 Gamma-massive structure

Figure 12 shows the  $\{111\}_\gamma$  and  $\{110\}_\gamma$  pole figures measured after complete massive transformation. As expected, the texture has been weakened, although it is still possible to distinguish some characteristics from the as-cast alloy texture, in particular the  $\{111\}$  pole density maximum along the bar axis. The maximum of pole density reach only  $1.40^5$  times the one of random distribution.



**Figure 12:-**  $\{111\}_\gamma$  and  $\{110\}_\gamma$  pole figures of the massive specimen

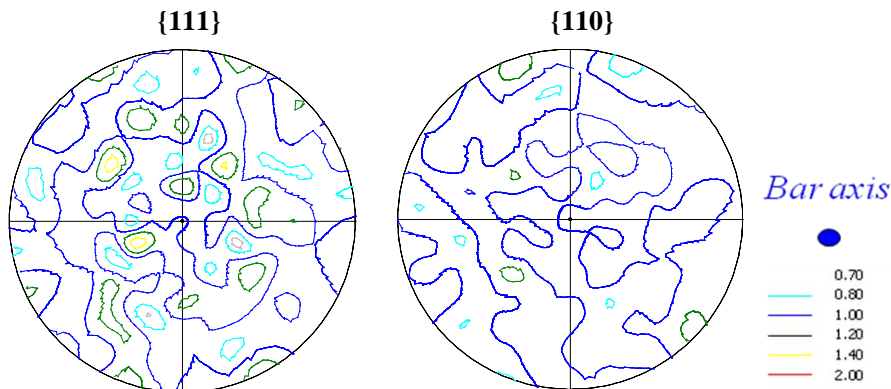
Ice water quenching from the alpha domain results in a diffusionless phase transformation forming massive microstructure with grains, equiaxed, highly irregular and

<sup>5</sup> The standard error for pole figure density was calculated by the method applied by Matthies [39]. Using this method, the confidence ranges obtained are  $1.40 \pm 0.16$  for the massive sample and  $1.9 \pm 0.28$  for the as-cast one. Since there is no overlapping of intervals, it is considered that the massive grains clearly takes part in the reducing the texture of the ac-cast alloy

sometimes faceted. As discussed before, these massive grains mainly nucleate along triple junctions and grain boundaries, in BOR with one of the neighboring  $\alpha$  grains, then grow in other  $\alpha_2$  grains with no specific orientation relationship. The growth of the massive grains always proceeds by successive twinning [13, 14]. Consequently, it is expected that the texture becomes more and more random with the development of the different generations of twins. However, there is a strong twin variant selection according to [14], which could explain the presence of some large  $\gamma_m$  grains and the fact that the texture is not as random as expected.

### 3.3.3 Structure after tempering in the $\alpha_2+\gamma$ phase field

The microstructure of the massive AC sample tempered for 2hrs at 1050°C appeared similar to the one illustrated in Figure 5 (c) and (f), with two populations of  $\alpha_2$  globular precipitates and thin  $\alpha_2$  platelets. The  $\gamma$  grain size distribution was close to the one of the massive microstructure. Figure 13 reports the  $\{111\}_\gamma$  and  $\{110\}_\gamma$  pole figures of this sample. It can be seen that there is no significant change in texture between both structures and that the poles density maximum are similar. These results are in accordance with the microstructural evolution, since the precipitation of the different forms of  $\alpha_2$  was showed not to affect very much the microstructure of the  $\gamma$  phase.

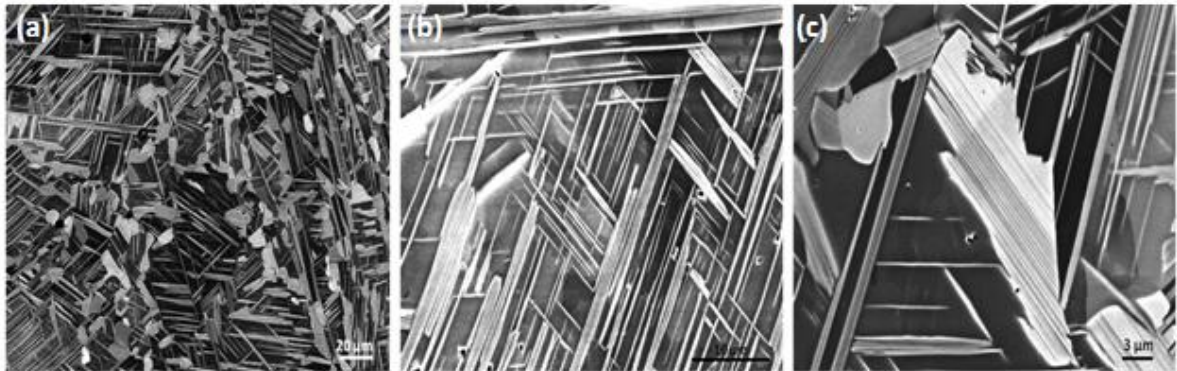


**Figure 13:-**  $\{111\}_\gamma$  and  $\{110\}_\gamma$  pole figure of the sample tempered for 2 hrs at 1050°C

### 3.3.4 Structure after tempering in the $\alpha+\gamma$ phase field

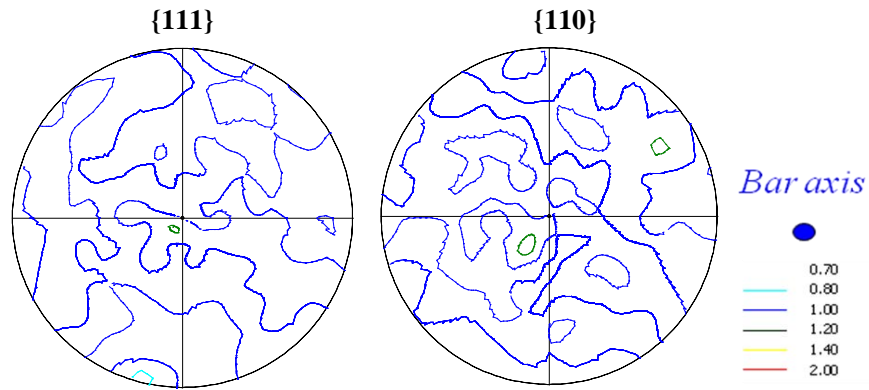
Figure 14 (a-c) shows some micrographs of the massive AC sample tempered for 2hrs at 1250°C, i.e. in the  $\alpha+\gamma$  phase field. This microstructure was reported as ‘convoluted structure’ in [37, 38]. It is of a duplex type, with rather large grains (mean size about 26 $\mu\text{m}$ ) showing a coarse lamellar or ‘basket-weave’ structure (Figure 14 (b)) and smaller ones ((mean size about 8 $\mu\text{m}$ ) with a very fine lamellar structure (Figure 14 (c)). The surface area fraction of these equiaxed small lamellar structures is approximately 9%. In the light of the microstructural evolution analyzed in Section 3.2, it is clear that the former result from the subsequent development of ( $\gamma+\alpha_2$  platelets) grains formed during heating, while the latter correspond to high-temperature  $\alpha$  grains which encountered a lamellar transformation during final air quench. These  $\alpha$  grains are likely to be initiated by globular  $\alpha_2$  precipitates observed at lower temperatures, which explains why they appear to surround the grains with coarse inner plates. In the following, we refer to this duplex structure originated from a

massive one as 'M-duplex structure'. The global  $\alpha_2$  volume fraction of this M-duplex structure, measured on high magnification BSE images, was found to be  $30 \pm 2$  %. This value is close to the volume fraction measured for the conventional duplex structure treated in the same conditions, which is  $33 \pm 4$  %. However, it is worthwhile to remember that the distribution of  $\alpha_2$  phase is actually completely different in both cases. In the conventional duplex structure, it is only located in fine lamellar grains co-existing with monolithic  $\gamma$  grains, whereas in M-duplex, it is also present in the form of tangled plates inside the  $\gamma$  grains. In terms of mechanical properties, this microstructure is expected to be more isotropic.

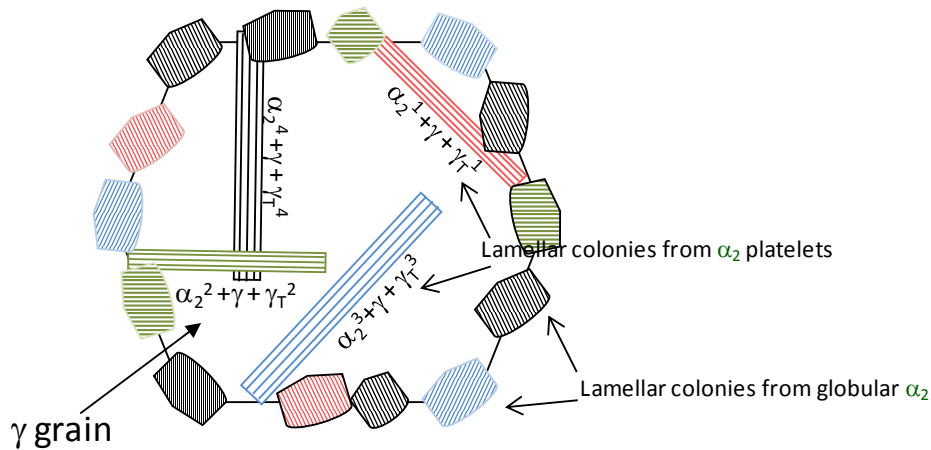


**Figure 14:-** SEM micrographs of sample tempered 2hrs at 1250°C (a) low magnification observation (b) image of a 'basket-weave' structure developed during tempering (c) image of a fine lamellar structure developed from a grain during air quench

The  $\{111\}_\gamma$  and  $\langle 110 \rangle_\gamma$  pole figures of the M-duplex structure are reported in Figure 15. They show that the crystallographic texture is still smoothed with regard to the texture of the massive structure. In order to understand why, it is necessary to come back to the crystallography of the phase transformations during tempering and subsequent quenching. During heating then tempering in the  $\alpha+\gamma$  phase field,  $\alpha$  grains forms in BOR with the  $\gamma$  grains. Consequently, there are four  $\alpha$  variants associated with the four crystallographically equivalent  $\{111\}_\gamma$  planes. During a quench, this  $\alpha$  phase re-transforms into a  $(\alpha_2+\gamma)$  lamellar structure. Each  $\alpha$  orientation can give rise to two  $\gamma$  orientations, according to the BOR, which are in twin relation with each other. One of these two orientations is the same orientation as that of the  $\gamma$  grain but the other is a new one. Hence, for a given  $\gamma_m$  grain, four new  $\gamma$  orientations are generated according to this mechanism which is schematically represented in Figure 16.

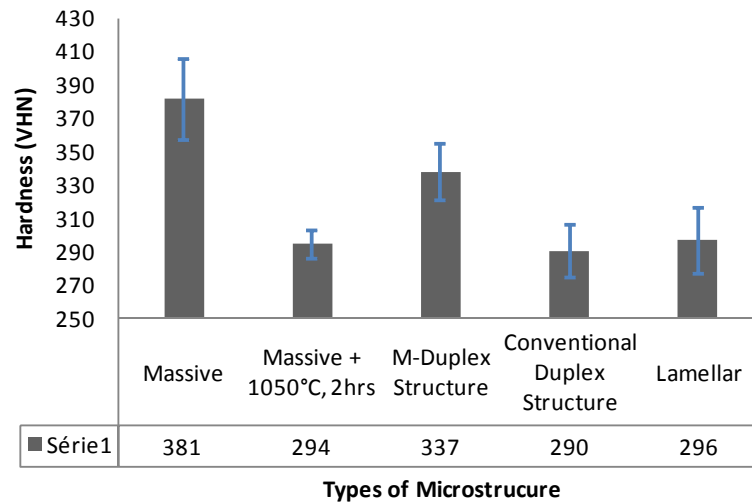


**Figure 15:-**  $\{111\}_\gamma$  and  $\{110\}_\gamma$  pole figure of specimen tempered for 2hrs at 1250°C.



**Figure 16:-** Schematic representation explaining the generation of different  $\gamma$  orientation during the heat treatment at 1250°C for 2hrs on a massive microstructure.

Figure 17 reports the results of Vickers hardness measurements performed on the different structures of the present study. Apart from the metastable massive structure, the M-duplex structure appears to be the hardest one. In particular, it shows a superior hardness (about  $337 \pm 17$  VH) when compared to the conventional duplex structure ( $290 \pm 16$  VH) with similar  $\alpha_2$  volume fraction. This might be due to the more homogeneous spatial distribution of the  $\alpha_2$  phase. Wu *et al.* and Saage *et al.* [37, 38] discussed the mechanical properties of these type of structures and reported that their tensile properties are far better than those of duplex structures and of as-cast structures, with enhanced ductility and tensile strength.



**Figure 17:-** Results of hardness measurement made on massive and different tempered microstructures with as-cast + HIP as its initial microstructure.

#### 4. Summary

DSC, SEM, TEM, EBSD and X-Ray diffraction experiments were applied on a Ti-48Al-2Nb-2Cr (at %) alloy with the objective of analyzing the evolution of microstructure and crystallographic texture during tempering of a gamma-massive ( $\gamma_m$ ) structure in both  $\alpha_2 \rightarrow \gamma$  and  $\alpha \rightarrow \gamma$  phase fields. The main results and conclusions are:

- The evolution of the metastable  $\gamma_m$  phase towards a binary structure occurs above 500°C in the  $\alpha_2 \rightarrow \gamma$  domain.
- Two types of  $\alpha_2$  precipitates develop in the ex- $\gamma_m$  grains: i) globular intergranular precipitates, which always present a Blackburn Orientation Relationship (BOR) with one of the adjacent  $\gamma_m$  grains; ii) acicular intragranular precipitates, in BOR with their host grain (four orientation variants in a given grain). For the heating conditions used in the present study (5°C/min.), globular precipitation precedes the acicular one during heating.
- Subsequent ageing in  $\alpha_2 + \gamma$  or  $\alpha + \gamma$  domains results in coarsening and rearrangement of both populations of  $\alpha/\alpha_2$  precipitates. The coarsening kinetics of globular precipitates appears faster along high angle grain boundaries, which brings out the frontiers of the ex- $\alpha$  grains.
- Massive transformation reduces the crystallographic texture issued from solidification process. However, the most isotropic texture is measured after a massive transformation followed by an isothermal ageing in the  $\alpha + \gamma$  domain, then a slow cooling down to room temperature ('M-duplex' or 'convoluted' microstructure).

#### Acknowledgments

A. Sankaran would like to thank the research council of Région Lorraine for the financial support of her Ph.D. The authors would like to thank J. Zollinger for his help and insightful discussions.

## References

- [12] Kim YW, Microstructural evolution and mechanical properties of a forged gamma titanium aluminide alloy, *Acta Metall. Mater.* 10 (1992) 1121-1134.
- [13] Takeyama M, Microstructural evolution and tensile properties of titanium-rich TiAl alloy, *Mater. Sci. and Eng., A*, 152 (1992) 269-276.
- [14] Usta M, Wolfe H, Dequette DJ, Stoloff NS, Wright RN, Thermo-mechanical grain refinement in gamma ( $\gamma$ ) based TiAl intermetallics, *Mater. Sci. Eng., A*, 359 (2003) 168-177.
- [15] Sastry SML, Mahapatra RN, Grain refinement of intermetallics by severe plastic deformation, *Mater. Sci. Eng., A*, 329-331 (2002) 872-877.
- [16] Ramanujam RV, The transformation between the  $\gamma$  and  $\alpha$  phases in binary and ternary  $\gamma$ -based titanium aluminides, *Acta Metall. Mater.* 42 (1994) 2313-22.
- [17] Helmut Clemens and Heinrich Kestler, Processing and applications of Intermetallic  $\gamma$ -TiAl- based alloys, *Advanced Engineering Materials*, 2 (2000) 551-570.
- [18] Clemens H, Bartels A, Bystrzanowski S, Chladil H, Leitner H, Dehm G, Gerling R, Schimansky FP, Grain refinement in  $\gamma$ -TiAl-based alloys by solid state phase transformations, *Intermetallics*, 14 (2006) 1380-1385.
- [19] Liss K-L, Bartels A, Clemens H, Bystrzanowski S, Stark A, Buslaps T, Schimansky F-P, Gerling R, Scheu C, Schreyer A, Recrystallization and phase transitions in a  $\gamma$ -TiAl-based alloy as observed by ex situ and in situ high-energy X-ray diffraction, *Acta Mater.* 54 (2006) 3721-3735.
- [20] Wang JN, Yang J, Wang Y, Grain refinement of a Ti-47Al-8Nb-2Cr alloy through heat treatments, *Scripta Mater.* 52 (2005) 329-334.
- [21] Dey SR, Bouzy E, Hazotte A, Features of feathery  $\gamma$  structure in a near- $\gamma$  TiAl alloy, *Acta Mater.* 56 (2008) 2051-2062.
- [22] Dey SR, Hazotte A, Bouzy E, Naka S, Development of Widmanstätten laths in a near- $\gamma$  TiAl alloy, *Acta Mater.* 53 (2005) 3783-3794.
- [23] Dey SR, Morawiec A, Bouzy E, Hazotte A, Fundenberger JJ, A technique for determination of  $\gamma/\gamma$  interface relationships in a ( $\alpha_2 + \gamma$ ) TiAl base alloy using TEM Kikuchi patterns, *Materials letters* 60 (2006) 646-50.
- [24] Dey SR, Bouzy E, Hazotte A, EBSD characterization of massive  $\gamma$  nucleation and growth in a TiAl-based alloy, *Intermetallics*, 14 (2006) 444-449.
- [25] Sankaran A, Bouzy E, Humbert M, Hazotte A, Variant selection during nucleation and growth of  $\gamma$ -massive phase in TiAl-based intermetallic alloys, *Acta Mater.*, 57 (2009) 1230-1242.
- [26] Wang P, Veeraraghavan D, Kumar M, Vasudevan VK, Massive-parent interphase boundaries and their implications on the mechanisms of the ( $\alpha$ ) $\rightarrow$ ( $\gamma$ (M)) massive transformation in Ti-Al alloys *Metall. Mater. Trans. A*, 33A (2002) 2353-2371.
- [27] Wittig JE, The massive transformation in titanium aluminides: Initial stages of nucleation and growth, *Metall. Mater. Trans. A*, 33A (2002) 2373-2379.
- [28] Kumagai T, Abe E, Takeyama M, Nakamura M, Microstructural evolution of massively transformed  $\gamma$ -TiAl during isothermal aging, *Scripta Mater.* 36 (1997) 523-529.
- [29] Zhang WJ, Chen GL, Evangelista E, Formation of alpha phase in the massive and feathery gamma-TiAl alloys during aging in the single alpha field, *Metall. and Mater. Trans. A* 30A (1999) 2591-2598.



- [30] Wen CE, Chen CQ, New microstructure-property approach: Quenching/tempering treatment in gamma TiAl alloy, *Scripta Metall. et Mater.* 33 (1995) 1283-1288.
- [31] A. Huang, M.H. Loretto, D. Hu, K. Liu, Xinhua Wu, The role of oxygen content and cooling rate on transformations in TiAl-based alloys, *Intermetallics*, 14 (2006) 838-847.
- [32] D. Hu, A.J. Huang, X. Wu, On the massive phase transformation regime in TiAl alloys: The alloying effect on massive/lamellar competition, *Intermetallics*, 15 (2007) 327-332.
- [33] Aphelion - copyright ADCIS S.A. (F) and A.A. Imaging (USA)
- [34] Dey SR, Hazotte A, Bouzy E, Multiscale  $\gamma$  variant selection in a quaternary near- $\gamma$  Ti-Al alloy, *Philosophical Magazine A*, 86 (2006) 3089-3112.
- [35] Pouchou JL, Ferrini A, Denquin A, Boivin D, Renollet Y, Gallais C. In: Pouchou JL editor. 'L'analyse EBSD - Principes et applications', EDP Sciences, 2003, 51.
- [36] Fundenberger JJ, Morawiec A, Bouzy E, Lecomte JS, Polycrystal orientation maps from TEM, *Ultramicroscopy* 96 (2003) 127-137.
- [37] Dey SR, Bouzy E, Hazotte A, Intragranular nucleation sites of massive  $\gamma$  grains in a TiAl-based alloy, *Scripta Mater.* 57 (2007) 365-368.
- [38] Blackburn M J, In: Jaffee, Promisel N E, editors. *The Science, Technology and Applications of Titanium*. Pergamon Press, Oxford; 1970: 633.
- [39] Lee JK and Aaronson HI, Influence of faceting upon the equilibrium shape of nuclei at grain boundaries—I. Two-dimensions, *Acta Metall.* 23 (1975) 799-808.
- [40] Brooks JW, Loretto MH, Smallman RE, Direct observations of martensite nuclei in stainless steel, *Acta Metall.* 27 (1979) 1839-1847.
- [41] Clemens H, Chladil HF, Wallgram W, Zickler GA, Gerling R, Liss KD, Kremmer S, Güther V Smarsly W, In and ex situ investigations of the  $\beta$ -phase in a Nb and Mo containing  $\gamma$ -TiAl based alloy, *Intermetallics*, 16 (2008) 827-833.
- [42] Bartels A, Schillinger W, Micromechanical mechanism of texture formation in  $\gamma$ -TiAl, *Intermetallics* 9 (2001) 883-889.
- [43] Yamaguchi M, Johnson DR, Lee HN, Inui H, Directional solidification of TiAl-base alloys, *Intermetallics* 8 (2000) 511-517.
- [44] Kim MC, Oh MH, Lee JH, Inui H, Yamaguchi M, Wee DM, Composition and growth rate effects in directionally solidified TiAl alloys, *Mater. Sci. Eng., A*, 239-240 (1997) 570-576.
- [45] Zollinger J., Influence de l'oxygène sur le comportement à la solidification d'alu-miniures de titane binaires et alliés au niobium basés sur le composé intermétallique  $\gamma$ -TiAl, PhD report, Inst. Nat. Polytech. de Lorraine (2008).
- [46] Johnson DR, Inui H, Yamaguchi M, Crystal growth of TiAl alloys, *Intermetallics*, 6 (1998) 647-652.
- [47] Germain L, Dey SR, Humbert M, Gey N, Determination of parent orientation maps in advanced titanium-based alloys, *Journal of Microscopy*, 227 (2007) 284-291.
- [48] Wu X, Hu D, Microstructural refinement in cast TiAl alloys by solid state transformations, *Scripta Mater.* 52(2005) 731-734.
- [49] Saage H, Huang AJ, Hu D, Loretto MH and Wu X, Microstructures and tensile properties of massively transformed and aged Ti46Al8Nb and Ti46Al8Ta alloys, *Intermetallics* 17 (2009) 32-38.
- [50] Matthies S, Vinel GW, Helming K, *Standard Distributions in Texture Analysis*, Volume 1, Akademie-Verlag Berlin 1987.

Annexe D

**First attempt to  
theoretically  
calculate the  $\gamma$ -  
massive texture in  
a TiAl based alloy**

# First attempt to theoretically calculate the $\gamma$ -massive texture in a TiAl based alloy

## 1. Introduction

Rapid quenching from the single  $\alpha$  domain of the TiAl-based alloys generates  $\gamma$  grains through massive transformation, mostly over the prior  $\alpha/\alpha$  grain boundaries [1], with a few massive grains found in the interior of the  $\alpha$  grains [2-3]. The massive transformation is a diffusionless transformation, and forms by the process of nucleation and growth. The  $\gamma$  massive nucleus maintains a strict Blackburn orientation relationship (BOR) with one of the  $\alpha$  grains [1-2]. The BOR related nucleus generates along the prior  $\alpha/\alpha$  grain boundary sharing BOR with one  $\alpha$  grain and starts growing inside the neighboring attached  $\alpha$  grain with which it has no orientation relation. Once the nucleus is formed, the growth of  $\gamma$  massive nucleus progresses by the twinning along its {111} planes, finally generating several massive  $\gamma$  ( $\gamma_m$ ) grains [1, 4].

The development of the  $\gamma_m$  grains has been widely studied [1-12]. It has been the subject of interest due to generation of various small size  $\gamma_m$  grains with different orientations, which are believed to generate a smooth texture with isotropic properties after subsequent heat treatment [6]. All the earlier reported works are mostly based at small scale area observations and hence, lack in the study on the development of texture of  $\gamma_m$  grains.

The present work makes an attempt to theoretically calculate the  $\gamma_m$  nuclei obtained from their BOR related  $\alpha$  grains and the further twinning on the {111} planes of the  $\gamma_m$  nuclei into  $\gamma_m$  grains, producing several generations. An experimental orientation image map (OIM) containing several  $\alpha$  grains with  $\gamma_m$  grains was obtained through the technique of Electron Backscatter Diffraction (EBSD). The local texture of  $\gamma_m$  grains was theoretically calculated from the EBSD map starting with the orientation of the  $\alpha$  grains and was then compared with the experimentally measured texture of  $\gamma_m$  grains. Finally, the experimental and theoretically calculated textures are compared and the reasons for their discrepancies are discussed.

## 2. Different Orientation Relationships

It has been established by Veeraraghavan *et al.*, [5] that the massive transformation takes place between a range of temperatures depending on the under cooling rates between  $\sim 1125$  and  $1025^\circ\text{C}$ . Therefore, they are formed in the  $\alpha + \gamma$  domain and sometimes in the  $\alpha_2 + \gamma$  domain. During cooling from the  $\alpha + \gamma$  domain to the  $\alpha_2 + \gamma$  domain, the orientation of the  $\alpha$  phase is retained by the  $\alpha_2$  phase as there is only an ordering transformation taking place between the two phases. As for the  $\gamma$  phase formed from the  $\alpha$  phase, it follows a strict orientation relationship during the phase transformation. In the present study, careful emphasis has not been made on the temperature of massive transformation, but since the orientation of the  $\alpha$  phase and the  $\alpha_2$  phase are the same, the orientation of the room temperature  $\alpha_2$  phase is used for the texture calculation.

A  $\gamma_m$  nucleus follows a strict Blackburn orientation relationship (BOR) [13] with its parent  $\alpha$  grain.

$$(0002)_\alpha // \{111\}_\gamma$$

$$[1\bar{1}\bar{2}0]_\alpha // [\bar{1}\bar{1}0]_\gamma$$

The lattice parameters of the  $\alpha_{\text{hcp}}$  and  $\gamma_{\text{tetragonal}}$  is given in Table 1.

**Table 1:** Lattice parameter of the room temperature  $\gamma$  and the  $\alpha_2$  phase.

Phase	Laue Group	a(nm)	c(nm)
$\gamma$ -tetragonal	4/mmm	0.4005	0.4070
$\alpha_2$ -Hexagonal	6/mmm	0.5782	0.4629

During the transformation from the  $\alpha$  to  $\gamma$  phase, one orientation of  $\alpha$  can give rise to six orientations of  $\gamma$ , which arises due to the tetragonality of the  $\gamma$  phase [14].

For the validation of the model, a reference image taken from EBSD is used. During orientation mapping by EBSD, the tetragonal phase of  $\gamma$  is indexed as a cubic phase because of the small  $c/a$  ratio of the  $\gamma$  phase. Hence, the lattice parameters used with a cubic assumption is  $a_0 = 0.4030$  for the  $\gamma$  phase.

With this assumption, during the transformation from the  $\alpha$  to  $\gamma$  phase, orientation relation between them can be give by

$$\Delta g = (30.0^\circ, 54.73^\circ, 45^\circ)$$

This is the rotation which permits to superimpose the co-ordinate of the  $\alpha$  with the co-ordinate of  $\gamma$ .

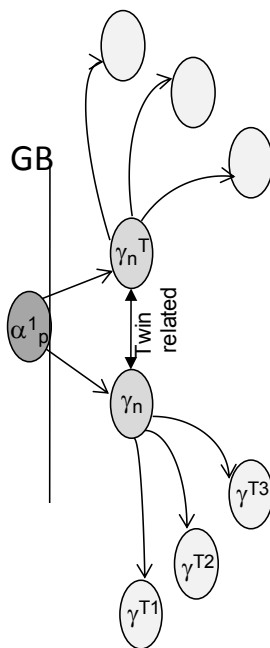
With this transformation, each  $\alpha$  orientation gives one  $\gamma$  orientation which is the nucleus of the  $\gamma$ -massive grain. After the nucleation, the  $\gamma$  grain propagates by the process of twinning, showing a misorientation of  $60^\circ$  along the  $[111]$  axis. Therefore from the  $\gamma$  nucleus, four different twin orientations are possible with the twinning planes  $(\bar{1}11)$ ,  $(1\bar{1}1)$ ,  $(11\bar{1})$  and  $(111)$ .

### 3. $\gamma$ -Orientation determination from the $\alpha$ parent:

During the massive phase transformation, the  $\gamma_m$  phase forms by the process of nucleation along the the grain boundaries. From our previous study [1] we found that the most preferred site of nucleation of the  $\gamma_m$  grains are the triple junctions. With the experimental conditions used, almost 65% of the triple junctions resulted in bearing a  $\gamma_m$  domain. In contrast, only 15% of the grain boundaries showed to bear a  $\gamma_m$  domain. For a grain boundary nucleation, a  $\gamma_m$  nucleus is formed when the grain boundary plane is parallel or nearly parallel with one of the (0002) plane of the  $\alpha_2$  phase. The chance for this type of configuration is higher near a triple junction. This is because, there are three grain

boundaries taking part in the nucleation process; so there are six possibilities to form a nucleus, whereas in a  $\alpha/\alpha$  grains boundary, it has only two chance to form a  $\gamma_m$  nucleus. . And since the number of  $\alpha/\alpha$  grain boundary taking part in the nucleation is quite less, only triple junctions are considered for the calculation of the texture.

As shown in the previous section, a  $\gamma$  orientation can be obtained from the parent  $\alpha$  orientation by applying the transformation matrix  $\Delta g$ . This will result in the orientation of the  $\gamma_{nuclei}$ . More often, the  $\gamma$  nucleus orientation calculated with  $\Delta g$  does not exactly match with the experimental orientation. There is sometimes a slight deviation in the values. This deviation in the orientation can be because of orientation variation from point to point which might be due to the presence of ordered domains and internal stresses. After calculating the  $\gamma_n$  orientation, the orientation of its variants with which it has a twin relation is easily calculated, by applying a  $60^\circ$  rotation along each of its  $\{111\}$  plane. So from each  $\gamma$  orientation four different  $\gamma$  orientations can be obtained, which are in twin relation with the  $\gamma_{nuclei}$ , and the fourth one being the other potential nucleus which twins along the  $(111)$  plane. A schematic representation of the nucleation and growth processes is given in Figure 1.



**Figure 1:-** Schematic representation of the nucleation and growth mechanism of the  $\gamma_m$  grains.

Considering the two  $\gamma$  orientations that have a BOR with the parent  $\alpha$  grain, as nuclei, the first generation of the  $\gamma$  variants are the grains that share a twin relation with the  $\gamma$  nucleus. Each  $\gamma$  nucleus gives three  $\gamma$  variants; therefore the first twin generation of  $\gamma$  grains is comprised of six different orientations. Consecutively, each  $\gamma$  orientation from the 1<sup>st</sup> generation can give rise to another three different orientations of  $\gamma$  variants which have a twin relation with its  $\gamma_{parent}$  thereby producing 18 different orientations of  $\gamma$  arising from the six 1<sup>st</sup> generation  $\gamma$  variants. They form the 2<sup>nd</sup> generation. The  $\gamma_m$  grains spread over their  $\alpha$  host grain in similar fashion to form several generations of  $\gamma$  variants. Here we consider that triple junctions are the only nucleation points for the  $\gamma$  massive grain. Studies by orientation image mapping have shown that during most of the triple junction nucleation, each  $\alpha$  grain taking part in forming the triple junction gives rise to at least one  $\gamma$  massive nucleus [1, 16].

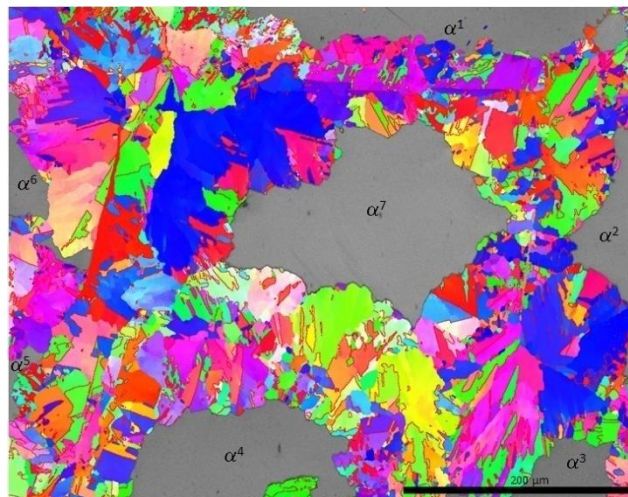
Therefore if assuming that all the triple junction bears a  $\gamma$  massive domain, then each triple junction consists of at least three  $\gamma$  nuclei arising from each  $\alpha$  grain.

#### 4. Application:

In order to validate the texture calculation, an EBSD map was taken on a Ti- 48 Al- 2Cr- 2Nb sample, which was ice quenched rapid enough to stop the complete massive transformation with some remnant ex- $\alpha$  grain. Figure 2 shows the EBSD map used for calculating the theoretical texture of the massive phase. One can see from the figure that the massive transformation is not complete and at the centre of each ex- $\alpha$  grain, there is still some  $\alpha_2$  phase helping us to identify the orientation of the parent  $\alpha_2$  grain. Seven different orientations of the  $\alpha_2$  grains can be taken and their orientations are given in Table 2. A comparison is done between the theoretically obtained orientations of the  $\gamma$  grains and the experimentally obtained orientations and is given in Table 3. Analysis of the EBSD map showed that the massive domains have formed up to two generations and some of the  $\gamma$  grains has given rise to the 3<sup>rd</sup> generation of the  $\gamma$  variants. Therefore, for the theoretical calculation up to two generation of  $\gamma$  orientations have been calculated. Including the orientation of the  $\gamma$  nucleus, each  $\alpha$  grain results in 26 orientations of  $\gamma$  (up to second generation). In the map taken, there are seven  $\alpha$  grains, therefore, calculating  $\gamma$  variants from each  $\alpha$  grain up to the second generation results in 182 different  $\gamma$  orientations.

**Table 2:-** The seven  $\alpha_2$  orientations used for the calculation

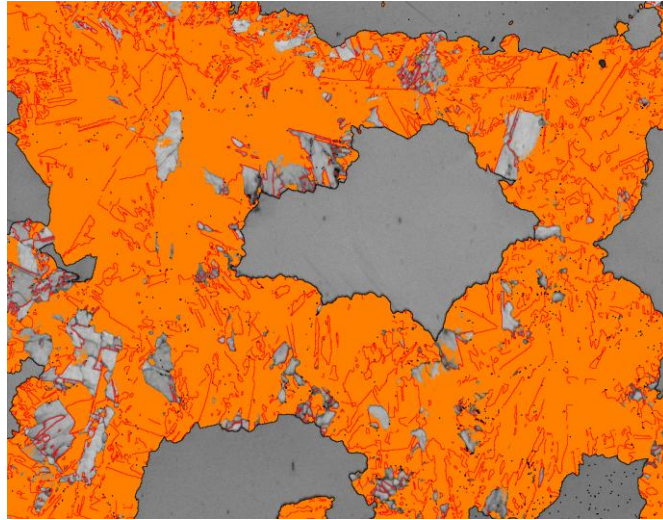
	Euler angles
$\alpha^1$	50.8 128.2 31.6
$\alpha^2$	89.5 29.6 21.0
$\alpha^3$	134.4 44.1 3.1
$\alpha^4$	166.5 52.9 11.3
$\alpha^5$	22.0 163.3 18.4
$\alpha^6$	41.8 142.5 24.1
$\alpha^7$	56.1 87.9 43.4



**Figure 2:-** EBSD map used for calculating the local texture of the  $\gamma$  phase.**Table 3:-** Euler angle of experimental and theoretically calculated  $\gamma$  orientations and their misorientation angles.

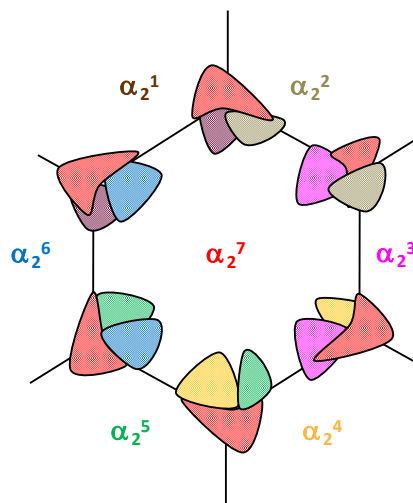
	Experimental	Theoretical	Misorientation angle
$\alpha_2$ (Parent)	134.4 44.1 3.1	-	-
$\gamma_{\text{nucleus}}$	32.4 27.2 78.6	33.53 27.01 347.88	0.62
$\gamma_{\text{nucleus}}^{\text{T}}$	242.55 22.88 99.09	235.9 20.0 14.3	3.89
$\gamma_2^{\text{T}}$	148.1 30.8 6.60	244.39 86.40 30.69	0.66
$\gamma_3^{\text{T}}$	291.1 36.6 27.5	324.58 121.97 18.28	1.02
$\gamma_4^{\text{T}}$	260.5 47.3 25.1	76.28 131.03 64.08	0.71

In order to verify, if the orientation calculated are in agreement with the actual orientations of the  $\gamma$  grains formed, the theoretically calculated orientations were entered in the Channel 5 software [17] with a misorientation dispersion of  $3^\circ$ . This dispersion is considered ideal after comparing a number of theoretically and experimentally calculated  $\gamma$  orientations as can be seen from Table 3. As mentioned the small misorientation can arise due to the transformation conditions, ordered domains and internal stresses during the time of massive transformation. The map obtained is given in Figure. 3. The red lines show the grain that has twin relation with the neighboring grain and the black lines denotes the  $\gamma/\alpha$  phase boundaries. From the map we can see that almost all the  $\gamma$  variants are being reconstructed by the theoretically calculated orientations. But at some places there are some  $\gamma$  grains that are not indexed at all. Careful examination shows that these grains either share a twin boundary with the indexed  $\gamma$  grains or are the grains that have intra-grain misorientation higher than the dispersion given. Hence, these grains are either third generation  $\gamma$  variants or  $\gamma$  grains with higher misorientation dispersion.



**Figure 3:-** Band contrast EBSD with theoretically calculated  $\gamma$  orientation. The orange zone corresponds to the  $\gamma$  grains indexed by the theoretically calculated  $\gamma$  orientations, the red lines corresponds to the  $\gamma$  grains that has a twin relation with the neighboring  $\gamma$  grains and the black lines denote the  $\alpha/\gamma$  inter phase boundaries.

After calculating the  $\gamma$  orientations and indexing it with the EBSD map taken as reference, the pole figures obtained experimentally and theoretically calculated were also compared. For calculating the pole figures theoretically, different assumptions have been considered. A schematic representation of the seven  $\alpha$  orientations considered for the calculation has been given in Figure 4. The centre grain  $\alpha_2^7$ , gives rise to a  $\gamma$  nucleus six times since it takes part in forming a triple junction six times. Whereas the other  $\alpha$  grains  $\alpha_2^{(1-6)}$  takes part in forming a triple junctions only two times as can be seen in Figure. 4. Therefore, the weight given for the orientations coming out of the centre grain  $\alpha_2^7$  is thrice when compared to the weight of the orientation coming out of the other  $\alpha$  grains ( $\alpha_2^{(1-6)}$ ). With this assumption the pole figures were calculated; the two sets of  $\{110\}$ ,  $\{111\}$  and  $\{100\}$  pole figures are given in Figure. 5.

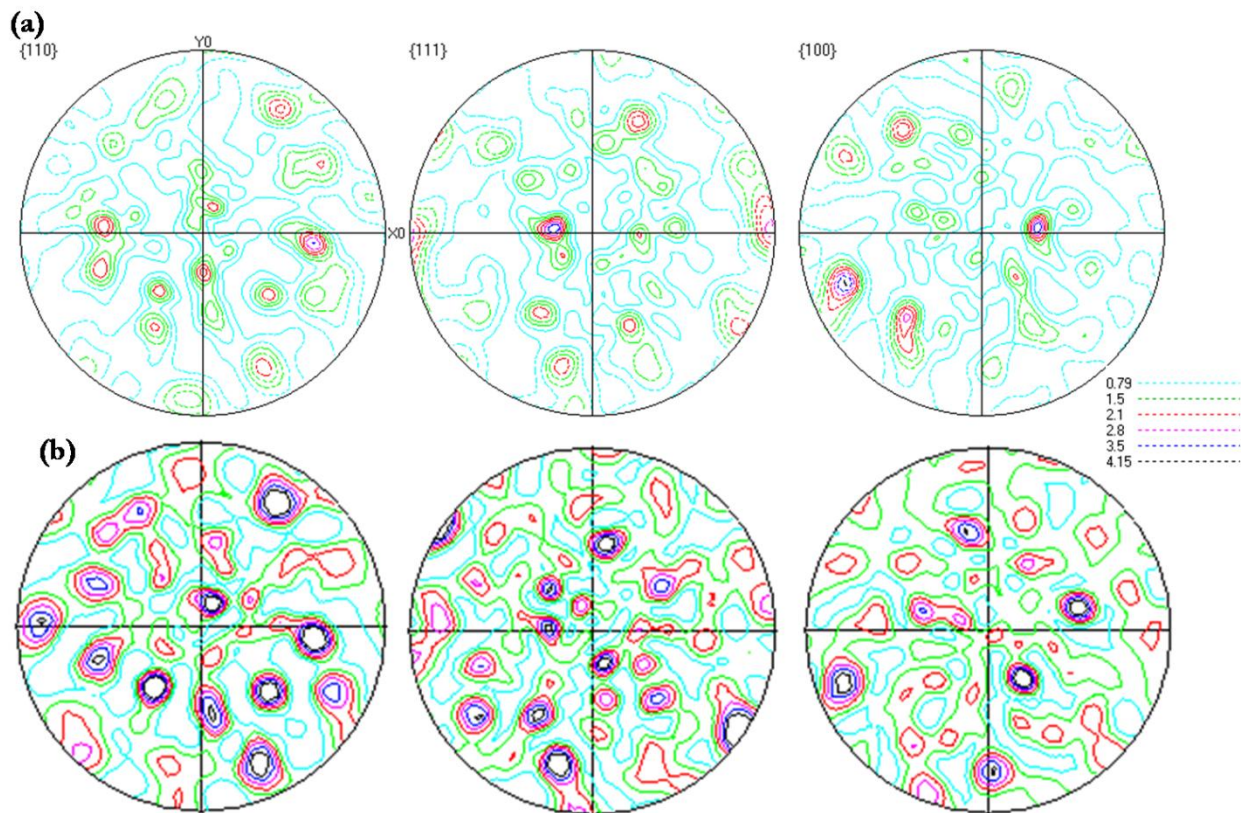




**Figure 4:-** Schematic representation of the EBSD map shown in Figure 2, showing the possible number of  $\gamma$  nucleus possible from each  $\alpha$  grain.

Comparing the two sets of pole figures we can see that though all the dominant poles seen in the experimental pole figures can be traced with the theoretical calculation, there are a number of poles that are formed in the theoretical calculation, but not seen in the experimental figures, also the intensity of the poles are different between the theoretical and experimental pole figures. These differences between the experimental pole figure and the theoretical pole figures can be attributed to more than one reason.

- i. The EBSD investigation is done on a two-dimensional surface. There might be a number of  $\gamma$  variants that are formed but do not lie in the surface of investigation. This has been proved by the three dimensional investigation of the  $\gamma$  massive domains (Appendix A2).
- ii. The second and the major reason attributing to the difference in experimental and theoretically calculated pole figure is the variants selection. From the Figure 2, it is clear that all the  $\gamma$  grains do not have the same surface fraction. Some of the grains have higher surface fraction while the others have lower surface fraction. Three-dimensional analysis of the  $\gamma$  domains showed that the dominant variant that is seen on a particular area of investigation remains the dominant variants throughout the bulk of the material (Appendix A2) Therefore the weight of each grains largely differs because of the variant selection.



**Figure 5:-** (a) Experimental pole figures of  $\gamma$  phase, taken from the EBSD map shown in Fig. 2. (b) Theoretical pole figures calculated from the orientations of the  $\alpha$  grains taken from the EBSD map shown in fig. 2.

After the nucleation of possible  $\gamma_m$  nucleus (Figure 1), from our previous study [1] we found that out of the two BOR related nuclei, one of the nuclei always grows to the detriment of the other. There is a strong selection of variant occurring in the growth between these two nuclei. The influence of variant selection on the texture calculation is rather high because the nucleus with the highest volume fraction can influence the intensity of the poles. Also during the growth of the  $\gamma$  variants, there are a few variants that are formed preferentially over the other  $\gamma$  variants. Several authors have discussed the phenomenon of growth in a massive microstructure in terms of their interface mobility. This is because, the rate controlling step in a massive transformation is the nucleation, once the nucleation occurs, growth of the massive grains occurs rapidly [7]. Therefore, it is assumed that the influence of the interface mobility is more preponderant than other energy factors. Many authors reported that the growing interface is mainly incoherent but sometimes with facets in different level (micro or nano facets) [8, 10]. Studies by HRTEM on a similar alloy [9] and on different alloys [8] show that the growing massive interface is mainly incoherent. But they also form a number of facets scaling various lengths. They argued that formation of these facets does not mean there is a rational orientation relationship between the host and the growing interface. The relationship is mainly irrational. Although, many authors saw a one dimensional row of atoms matching between the growing and the host phase and this phenomenon they termed as edge-to-edge matching. These set of matching atoms are accurately aligned and they do not form a repetitive pattern [11]. They stated that even though these one –dimensional matching does not effectively reduce the free energy as in the case of plane-plane matching, they take part in the reduction of the interfacial energy and thereby reducing the  $\Delta G^*$  [8-12]. Although a number of explanations have been given regarding the growth of the  $\gamma$  grains, there is still not a concrete growth mechanism that can be statistically validated. After establishing a strong mechanism for variant selection of the  $\gamma$  variants, the calculation can be fine tuned to have a more precise theoretically calculated  $\gamma$  texture.

So, to conclude, an attempt has been made to theoretically calculate the  $\gamma$  texture of the massive grains in a TiAl alloy based on the orientation relationships followed during the nucleation and the growth. The different  $\gamma$  orientations has been successfully calculated and compared with the experimental results and a good agreement between the both has been obtained, even though, there is some disagreement between the actual texture between the experimental and theoretical results. This can be attributed to the lack of growth mechanisms established during the growth of the  $\gamma$  grains which results in a strong variant selection.

### References:

- [1] Sankaran A, Bouzy E, Humbert M, Hazotte A, Acta Mater., 2009; 57: 1230.
- [2] Wittig JE, Metall. Mater. Trans. A, 2002; 33A: 2373.
- [3] Dey SR, Bouzy E, Hazotte A, Scripta Mater. 2007; 57: 365.
- [4] Dey SR, Bouzy E, Hazotte A, Intermetallics, 2006; 14: 444.
- [5] Veeraraghavan D, Ping Wang, Vasudevan VK, Acta Mater. 1999; 47: 3313.
- [6] Sankaran A, Bouzy E, Fundenberger JJ, Hazotte A, Accepted to be published in Intermetallics.
- [7] Kittl JE and Massalski TB, Acta Metall. 1967; 15: 161.

- [8] Yanar C, Wiezorek JMK, Radmilovic V, Soffa WA, Metall. Mater. Trans. A, 2002;33A:2413.
- [9] Howe JM, Reynolds WT, Vasudevan VK Metall. Mater. Trans. A, 2002; 33A:2391.
- [10] Massalski TB, Soffa WA, Laughlin DE, Metall. Mater. Trans. A, 2006; 37A:825.
- [11] Aaronson HI, Metall. Mater. Trans. A, 2006; 37A: 803.
- [12] Aaronson HI, Mahajan S, Purdy GR, Hall MG, Metall. Mater. Trans. A, 2002; 33A:2347.
- [13] Blackburn M J, In: Jaffee, Promisel N E, editors. The Science, Technology and Applications of Titanium. Pergamon Press, Oxford; 1970: 633.
- [14] Zghal S, Naka S, Couret A, Acta Mater. 1997; 45: 3005.
- [15] Wang P, Veeraraghavan D, Kumar M, Vasudevan VK, Metall. Mater. Trans. A, 2002, 33A: 2353.
- [16] Veeraraghavan D, Wang P, Vasudevan VK, Acta Mater. 2003; 51: 1721.